

## ABSTRACT

YAN, HONGPING. Correlating Interfacial and Bulk Nanostructure with Performance of Organic Electronic Devices. (Under the direction of Prof. Harald Ade.)

Resonant soft X-ray reflectivity and scattering (R-SoXR and R-SoXS) are used to investigate the interfacial and bulk nanomorphology of organic electronics including organic solar cells (OSCs), organic field-effect transistors (OFETs) and organic light-emitting diodes (OLEDs). Nanomorphology changes as function of fabrication conditions are revealed with the aid of R-SoXR and R-SoXS techniques. The morphology characterizations are correlated to device performances to better understanding of the device physics. A self-consistent method of measuring the complex index of refraction,  $\mathbf{n} = 1 - \delta + i\beta$  with high accuracy yet without complicated instrumentation is also developed to facilitate the device characterization. With the guidance of the measured index of refractions of the organic materials, R-SoXR and R-SoXS are productively applied to measure interfacial width of buried interfaces of multilayer systems and domain properties in phase separated polymer blend systems, respectively. The results assist the organic electronic community to better understand the influence of processing method on the nanomorphology and hence the device performance. These discoveries provide both physicists and engineers in this field with instructions both to better understand the working mechanism and to improve the device efficiency.

© Copyright 2012 by Hongping Yan

All Rights Reserved

Correlating Interfacial and Bulk Nanostructure with Performance of  
Organic Electronic Devices

by  
Hongping Yan

A dissertation submitted to the Graduate Faculty of  
North Carolina State University  
in partial fulfillment of the  
requirements for the Degree of  
Doctor of Philosophy

Physics

Raleigh, North Carolina

2012

APPROVED BY:

---

Prof. David Aspnes

---

Prof. Gregory Parsons

---

Prof. Albert Young

---

Prof. Harald Ade  
Chair of Advisory Committee

## DEDICATION

with love to my families.

## BIOGRAPHY

Hongping Yan was born on April 14, 1983, in Jiaonan, Shandong, China to Wenying Zhou and Jinbao Yan. He received his Bachelor of Science degree in Materials Science and Engineering from University of Science and Technology of China in July 2002. In the same year, he came to United States and started his graduate studies in the Department of Physics at NC State University, working towards his Ph.D. degree under the direction of Prof. Harald Ade.

## ACKNOWLEDGEMENTS

First of all, I would like to thank my advisor Prof. Harald Ade for all his support and help. He has been a great mentor with passion and tremendous patience to me. It was a pleasure for me to be a part of our stimulating discussions. His elucidating approach to physical problems is exemplary and I hope it will be reflected in my future scientific career.

I am also thankful to all current and former members of our NCSU research group, namely Brian Collins, Wei Ma, John Tumbleston, Eliot Gann, Sen Li, Terry McAfee, Anne Watson, Ziran Gu, Lewis Guignard, Cheng Wang, Benjamin Watts, Sufal Swaraj, Jaewook Seok, and Aric Meyer.

Thanks to my committee members, Dr. David Aspnes, Dr. Albert Young, and Dr. Gregory Parsons.

I would like to thank the Physics Department at large: faculty, staff and fellow students, especially to Prof. John Blondin, Prof. Michael Paesler, Rebecca Savage, Chastity Buehring, and Kevin Dudley.

I would also like to thank Advanced Light Source, Lawrence Berkeley National Lab, for offering the wonderful opportunity to be part of the greatest research community. Special thanks to Cheng Wang, Eric Gullikson, David Kilcoyne, Tony Young, Alex Hexemer and Tolek Tyliczszak for the fruitful discussions and their tremendous support on the beamtimes.

I would also like to thank my collaborators, Chris McNeill (Monash University, Australia), Torben Schuettfort, Auke Kronemeijer (Cambridge), Andres Garcia, Thuc-Quyen Nguyen, Guillermo C. Bazan, Karen E. Sohn, and Edward J. Kramer from (UCSB), for their contributions to some exciting applications of R-SoXR and R-SoXS.

Thanks for the support by DOE grants, including the Advanced Light Source Doctoral Fellowship.

Special thanks goes to my wife Yongxing Hu for her love and unlimited support.

Last but certainly not least, thanks to my parents Jinbao Yan and Wenying Zhou for their immeasurable support of my education throughout my life and their encouragement and guidance which has proven to be invaluable.

# TABLE OF CONTENTS

<b>List of Tables</b> . . . . .	<b>viii</b>
<b>List of Figures</b> . . . . .	<b>ix</b>
<b>Chapter 1 Introduction</b> . . . . .	<b>1</b>
1.1 Organic solar cells . . . . .	1
1.1.1 Device working mechanism . . . . .	1
1.1.2 Device characterization . . . . .	3
1.2 Organic field-effect transistors . . . . .	6
1.3 Organic light-emitting diodes . . . . .	9
1.4 Morphology characterization of organic electronics . . . . .	10
1.4.1 Conventional useful techniques and methods . . . . .	10
1.4.2 Soft X-rays and near edge X-ray absorption fine structures (NEXAFS) . . . . .	12
1.4.3 Scanning transmission X-ray microspectroscopy (STXM) . . . . .	13
1.4.4 Resonant soft X-ray reflectivity and scattering overview . . . . .	17
<b>Chapter 2 Accurate determination of the index of refraction of organic thin films near the carbon 1s absorption edge</b> . . . . .	<b>28</b>
2.1 Abstract . . . . .	29
2.2 Introduction . . . . .	29
2.3 Results and discussion . . . . .	32
2.4 Conclusion . . . . .	34
2.5 Acknowledgements . . . . .	36
2.6 Supplemental information . . . . .	36
2.6.1 Doubly Subtractive Kramers-Kronig relation . . . . .	36
2.6.2 Determination of film density . . . . .	38
2.6.3 Experimental details . . . . .	39
<b>Chapter 3 Interfaces in organic devices studied with resonant soft X-ray reflectivity</b> . . . . .	<b>41</b>
3.1 Abstract . . . . .	42
3.2 Introduction . . . . .	43
3.3 Experimental methods . . . . .	45
3.3.1 PFNBr/MEH-PPV bilayers and multilayer . . . . .	45
3.3.2 PFB/F8BT bilayers . . . . .	46
3.3.3 Dielectric/P(NDI2OD-T2) bilayers . . . . .	46
3.3.4 Data acquisition . . . . .	47
3.4 Results and discussion . . . . .	47
3.4.1 CPE/MEH-PPV bilayers . . . . .	47
3.4.2 PFB/F8BT bilayers . . . . .	55
3.4.3 Dielectric/P(NDI2OD-T2) bilayers . . . . .	58
3.5 Conclusion . . . . .	58
3.6 Acknowledgments . . . . .	61

<b>Chapter 4 Influence of annealing and interfacial roughness on the performance of bilayer donor/acceptor polymer photovoltaic devices . . .</b>	<b>62</b>
4.1 Abstract . . . . .	63
4.2 Introduction . . . . .	63
4.3 Results and discussion . . . . .	65
4.3.1 Characterization of interface width . . . . .	65
4.3.2 Photoluminescence quenching . . . . .	66
4.3.3 Device properties . . . . .	69
4.3.4 Mobility characterization . . . . .	69
4.3.5 Monte Carlo simulations . . . . .	71
4.4 Conclusions . . . . .	78
4.5 Experimental section . . . . .	79
4.5.1 Materials, sample and device preparation . . . . .	79
4.5.2 Resonant soft X-ray reflectivity measurements . . . . .	79
4.6 Acknowledgements . . . . .	80
4.7 Supporting information . . . . .	80
<b>Chapter 5 Influence of dielectric-dependent interfacial widths on device performance in top-gate P(NDI2OD-T2) field-effect transistors . . . . .</b>	<b>82</b>
5.1 Abstract . . . . .	83
5.2 Introduction . . . . .	83
5.3 Results and discussion . . . . .	85
5.4 Conclusion . . . . .	90
5.5 Acknowledgements . . . . .	90
5.6 Supporting information . . . . .	91
5.6.1 Experimental details . . . . .	91
<b>Chapter 6 Correlating the efficiency and nanomorphology of polymer blend solar cells utilizing resonant soft X-ray scattering . . . . .</b>	<b>93</b>
6.1 Abstract . . . . .	94
6.2 Introduction . . . . .	95
6.3 Results and discussion . . . . .	97
6.4 Conclusions . . . . .	111
6.5 Experimental section . . . . .	112
6.5.1 Materials . . . . .	112
6.5.2 Optical characterization . . . . .	112
6.5.3 Device fabrication . . . . .	112
6.5.4 Device characterization . . . . .	113
6.5.5 Resonant soft X-ray scattering measurements . . . . .	113
6.5.6 Grazing-incidence wide-angle X-ray scattering (GI-WAXS) . . . . .	114
6.5.7 Scanning transmission X-ray microscopy . . . . .	114
6.6 Acknowledgement . . . . .	114
6.7 Supplemental information . . . . .	114
<b>Chapter 7 Future outlook . . . . .</b>	<b>119</b>

7.1	Polarization-dependent resonant soft X-ray reflectivity for molecular orientation depth profiling of organic thin films . . . . .	119
7.2	Polarization-dependent resonant soft X-ray scattering for molecular ordering study in organic thin films . . . . .	122
7.3	Quantatively determination of the domain purity by scattering invariant calculation	129
7.4	Index-matched soft X-ray scattering . . . . .	130
7.5	R-SoXS at high- $q$ range for interfacial study of the domain boundaries . . . . .	133
<b>References . . . . .</b>		<b>136</b>
<b>Appendix . . . . .</b>		<b>155</b>
	Appendix A Kramers-Kronig relations . . . . .	156

## LIST OF TABLES

Table 3.1	Surface and interface roughness of PFNBr/MEH-PPV/Si bilayers and MEH-PPV reference layer as determined from fits shown in Figures 3.1 and 3.2.	49
Table 3.2	R-SoXR sensitivity to particular interface and dominant fringe spacing of R-SoXR data of PFNBr/MEH-PPV/PEDOT:PSS/ITO/glass multilayer device (see Figure 3.3) as a function of photon energy; nominal layer thickness, and quantitative results of layer thickness. Shaded areas indicate no particular sensitivity to this layer. Unit for $\Delta q$ of fringes spacing is $\text{nm}^{-1}$ .	53
Table 3.3	Fitting results from R-SoXR measurements of PFB/F8BT/Si bilayers at 282.4 eV and 284 eV, assuming an error function interface profile. . . . .	56
Table 4.1	Fitting results from R-SoXR measurements at 282.4 eV and 284 eV assuming an error function interface profile. . . . .	66
Table 4.2	Summary of fitting parameters used to fit the space-charge limited expression (Equation 4.1) to the data of Figure 4.4. . . . .	71

## LIST OF FIGURES

Figure 1.1	An illustration of the working mechanism of an OSC device. . . . .	2
Figure 1.2	A schematic of bulk heterojunction film (a) and a schematic of a bulk heterojunction device (b). . . . .	4
Figure 1.3	Schematic of $J - V$ measurement and typical $J - V$ curve in dark (dashed line) and under illumination (solid line) of OSC. . . . .	5
Figure 1.4	An illustration of the equivalent circuit of an OSC device. Figure reproduced from Reference [1]. . . . .	5
Figure 1.5	Schematic of the geometry of major types of organic field-effect transistors.	7
Figure 1.6	Schematic diagram of the OFET current flow $I_D - V_{SD}$ curve with the regions of operation noted. . . . .	8
Figure 1.7	Schematic diagram of the OFET $\sqrt{I_D} - V_{SG}$ curve showing the derivation of $V_t$ by extrapolation. The $V_{SD}$ at which the curve is acquired is indicated in Figure 1.6 with dashed line. . . . .	8
Figure 1.8	Schematic representation of a typical structure of organic light-emitting diode. . . . .	10
Figure 1.9	Schematic representation showing energy ranges of soft X-rays among other radiations. Figure courtesy of D. Attwood [2]. . . . .	13
Figure 1.10	Schematic of the photo-absorption processes occurring in a NEXAFS experiment. An incident photon, whose energy corresponds to a NEXAFS resonance, excites an electron from a core level (1s) into an unoccupied, anti-bonding level. (Figure created by A.P. Smith) . . . . .	14
Figure 1.11	Schematic of the scanning transmission X-ray microspectroscopy (STXM). The incident intensity is denoted as $I_0$ , and the transmitted intensity as $I$ .	14
Figure 1.12	(a) Absorption spectra of P3HT, P(NDI2OD-T2) and the blend film studied in this work scaled to mass absorption coefficient of each species. (b) and (c) Chemical structure of P3HT and P(NDI2OD-T2), respectively. . .	16
Figure 1.13	STXM images of P3HT: P(NDI2OD-T2) blend at (a) the C-1s $\rightarrow \pi_{C=C}^*$ resonance 285.3 eV and (b) off resonance at 350 eV. Color scales are in optical densities whose average values have been normalized to 1. . . . .	16
Figure 1.14	Interface geometry for incident ( $\mathbf{k}$ ), reflected ( $\mathbf{k}''$ ), and refracted waves ( $\mathbf{k}'$ ).	17
Figure 1.15	Diagram of a multilayer stack containing $N$ layers, where the optical constants, thickness, propagation angle, and interface roughness/diffuseness parameter of the $i$ th layer are $\mathbf{n}_i$ , $d_i$ , $\theta_i$ and $\sigma_i$ , respectively. The ambient (i.e., the region above the film) has optical constants $\mathbf{n}_a$ , and the substrate has optical constants $\mathbf{n}_s$ . . . . .	21
Figure 1.16	Sketch of the interface profile function $p(z)$ , which describes a rough or diffuse interface. . . . .	24
Figure 1.17	Schematic of resonant soft X-ray scattering (R-SoXS). . . . .	25

Figure 1.18	Relative scattering intensity (SI) for a PFB/F8BT thin film with pure domains and with a fixed thickness of a fraction of an absorption length ( $< 30$ nm). Inset shows the theoretical scattering intensity for PFB/F8BT and the absorption coefficient $\beta$ of PFB and F8BT near the carbon absorption edge. The chemical structures of PFB and F8BT are provided above the graph. Figure reproduced from Reference [3]. . . . .	26
Figure 2.1	Absorption spectra $\beta$ calculated from transmission NEXAFS and Henke's atomic scattering factors. . . . .	33
Figure 2.2	Overplot of R-SoXR data and fits for PMMA single layer, showing the quality of fits at energies, from top to bottom, 270.3, 282.3, 284.3, 286.3, 287.9, 288.3, 288.5, 288.9, 289.3, 294.3, and 310.3 eV. . . . .	33
Figure 2.3	Fitting results (dot) of optical constants, dispersion part, $\delta$ (A), and absorption part $\beta$ (B), for PMMA and calculation (solid line) using Kramers-Kronig relation. The corresponding values as derived from Henke's database are shown for comparison. . . . .	35
Figure 2.4	The data points (circles) and linear fit (line) to derive the film density. . .	38
Figure 2.5	Comparison of fitted and calculated $\delta$ (A), $\beta$ (B) of PS, and R-SoXR data (circle) and fits (solid line) for 80 nm PS thin film for selected photon energies, from top to the bottom, 278 eV, 280 eV, 281 eV, 282 eV, 283 eV, 285 eV, 288 eV, 290 eV, 293 eV. . . . .	40
Figure 3.1	R-SoXR fits and data acquired at 285.6 eV for PFNBr/MEH-PPV bilayers, which had the PFNBr cast from methanol:THF mixtures as indicated. The numbers at the right of the reflectance traces are the layer thicknesses in nm as derived from the fits. Note the scaling by $q^4$ . . . . .	48
Figure 3.2	Reflectance acquired from (a) MEH-PPV single layer pre-annealed at 240 °C (270 eV), (b) as cast bilayer (285.6 eV), (c) as cast bilayer on pre-annealed MEH-PPV (285.6 eV), and (d) bilayer annealed at 230 °C. The numbers at the left of the reflectance traces are the layer thicknesses in nm as derived from the fits. Note the scaling by $q^4$ . Data offset for clarity. . . . .	50
Figure 3.3	Reflectance of PFNBr/ MEH-PPV/ PEDOT:PSS /ITO /glass multilayer at selected photon energies. Note the scaling by $q^4$ . Data offset for clarity. . . . .	51
Figure 3.4	Fits of multilayer data 284.6 and 285. 4 eV and simulation of 270 eV data. Note the scaling by $q^4$ . Data offset for clarity. . . . .	55
Figure 3.5	Representative R-SoXR data at 282.4 eV (open circle) and numerical fits (solid line) of Si/PFB/F8BT samples as a function of annealing. (1) As-prepared, (2) 100 °C, (3) 120 °C, (4) 140 °C, (5) 160 °C, and (6) 200 °C. The loss of the fringe modulations at higher annealing temperatures directly indicates an increase in polymer/polymer interfacial width. Note the scaling by $q^4$ . Data offset for clarity. . . . .	56
Figure 3.6	R-SoXR reflectance (open circle) and fits (solid line) of (1) PFB as-spun, (2) PFB 200 °C annealed, (3) F8BT as-spun, and (4) F8BT 200 °C annealed single layers. Data offset for clarity. . . . .	57

Figure 3.7	R-SoXR data acquired at a number of photon energies to show the selective sensitivity of the method to different interfaces for PS/P(NDI2OD-T2), PMMA/P(NDI2OD-T2), and CYTOP/P(NDI2OD-T2) bilayers at the carbon and fluorine absorption edges. Traces are offset for easy viewing. Data offset for clarity. . . . .	59
Figure 3.8	Data and fits for bilayers of: (1) CYTOP/P(NDI2OD-T2) at 688 eV; (2) CYTOP/P(NDI2OD-T2) at 285 eV; (3) PS/P(NDI2OD-T2) at 281.4 eV; and (4) PMMA/P(NDI2OD-T2) at 286.0 eV. Note that data and fits are scaled for better viewing in a single graph. Note the scaling by $q^4$ . Data offset for clarity. . . . .	60
Figure 4.1	(a) Representative R-SoXR data at 282.4 eV (circles) and numerical fits (solid line) of Si/PFB/F8BT samples as a function of annealing. (1) as-prepared, (2) 100 °C, (3) 120 °C, (4) 140 °C, (5) 160 °C, and (6) 200 °C. The loss of the fringe modulations at higher annealing temperatures directly indicates an increase in polymer/polymer interfacial width. Note the scaling of the reflectance by $q^4$ for easier comparison. (b) Schematic showing the shape of the error function used to fit the data in part (a) in relation to rough and diffuse interfaces. . . . .	67
Figure 4.2	(Squares) Changes in the relative number of excitons dissociated at the PFB/F8BT interface with annealing; (Circles) Changes in the interface width of the PFB/F8BT bilayer with annealing determined from the R-SoXR data of Figure 1. . . . .	68
Figure 4.3	(a) Current voltage characteristics of PFB/F8BT bilayer devices as a function of annealing temperature. (b) Reverse bias dependence of photocurrent of PFB/F8BT bilayer devices. . . . .	70
Figure 4.4	(a) Current voltage characteristics of hole-only PFB devices and fits to the space-charge limited expression. (b) Current voltage characteristics of electron-only F8BT devices and fits to the space-charge limited expression. . . . .	72
Figure 4.5	Optical absorption profile of the bilayer device under AM1.5G illumination computed using the matrix formalism and used for the Monte Carlo simulations. . . . .	75
Figure 4.6	Experimental (lines) and Monte Carlo simulated (symbols) current-voltage characteristics of as-spun (solid line, squares), 100 °C annealed (dashed, circles), and 140 °C annealed (dots, triangles) devices. . . . .	76
Figure 4.7	(a) Photoluminescence spectra of neat F8BT films as a function of annealing. (b) Photoluminescence spectra of PFB / F8BT bilayers annealed at different temperatures. . . . .	80
Figure 4.8	(a) UV-vis absorption spectra of PFB / F8BT bilayers as a function of annealing. (b) Normalized external quantum efficiency spectra of PFB / F8BT bilayer devices. . . . .	81

Figure 4.9	(a) Current voltage scans taken of the 140 °C annealed device under AM1.5G illumination demonstrating the stability of the device under high reverse bias. (b) A series of dark current voltage curves taken before and after the light current voltage curves in part (a) demonstrating reproducibility and the absence of breakdown. Note the different current scales, with the dark current 400 times lower than the photocurrent at $-14$ V. . . . .	81
Figure 5.1	R-SoXR data (thicker lines) of bilayers on silicon substrates with various dielectrics as top layers acquired at individual energies: (1) PMMA, 275.0 eV, (2) PMMA, 285.9 eV, (3) PS, 275.0 eV, (4) PS, 281.4 eV, (5) CYTOP, 275.0 eV, and (6) CYTOP, 688.0 eV. The model refinements (fits) to the data are plotted on top of each data traces as thinner black solid lines. Data are offset vertically and (5) and (6) are scaled by a factor of 0.2 and 2, respectively, for clarity. . . . .	86
Figure 5.2	R-SoXR data and fits of single layers: (1) PMMA, (2) PS, (3) CYTOP, and (4) P(NDI2OD-T2). . . . .	87
Figure 5.3	(A) Average interfacial widths of the three types of bilayer systems measured and from the surface of the P(NDI2OD-T2) single reference layer. For simplicity, “Vac” stands for “Vacuum” and the commercial name “N2200” is used for “P(NDI2OD-T2)”. The dielectric constants, transport activation energies, and mobilities for OFETs based on each type of dielectric are plotted in (B) to provide context. For clarity, note that they are plotted on their own individual y-axes, with values labeled beside each data point. . . . .	88
Figure 5.4	Chemical structures of the active layer P(NDI2OD-T2), and the dielectrics PMMA, PS, and CYTOP. . . . .	91
Figure 6.1	(a) Chemical structures of P3HT, F8TBT, and P(NDI2OD-T2). (b) Absorption spectra of neat films. . . . .	98
Figure 6.2	Evolution of the absorption spectra of blend films with annealing: (a) P3HT:F8TBT; (b) P3HT: P(NDI2OD-T2). (c) Changes in P3HT vibronic structure with annealing in the P3HT:F8TBT blend; (d,e) changes in P3HT and P(NDI2OD-T2) vibronic structure in the P3HT:P(NDI2OD-T2) blend with annealing. . . . .	100
Figure 6.3	Evolution of the device characteristics of ITO / PEDOT:PSS/ P3HT: F8TBT /Al (a,c,e) and ITO/ PEDOT:PSS/ P3HT: P(NDI2OD-T2)/Al (b,d,f) devices with annealing. (a,b) Changes in the external quantum efficiency spectra, (c,d) plot of the current voltage characteristics under $100 \text{ mW/cm}^2$ AM1.5G illumination, and (e,f) summary of the evolution in short-circuit current, open-circuit voltage, fill factor, and power conversion efficiency with annealing temperature. . . . .	101
Figure 6.4	R-SoXS of P3HT:P(NDI2OD-T2) blend thin films prepared at various conditions: as-cast, 120, 160, 180, and 200 °C annealed. Inset: Domain spacing calculated from the fitted scattering peak locations of the smaller domains. . . . .	102

Figure 6.5	R-SoXS of P3HT:F8TBT blend thin films prepared at various conditions: as-cast and annealed at 100, 120, 140, 160, and 200 °C. . . . .	104
Figure 6.6	Evolution of the photoluminescence spectrum of P3HT:F8TBT blends with annealing. Solid lines depict the blend; while dashed lines correspond to the spectrum of neat films. The magnitude of the F8TBT spectrum has been reduced 20-fold. . . . .	105
Figure 6.7	In-plane GI-WAXS data of P3HT:P(NDI2OD-T2) samples prepared at various conditions: as-spun, 100, 120, 140, 160, and 180 °C annealed (a), and crystal sizes along the (100) direction derived from a Scherrer analysis (b). . . . .	107
Figure 6.8	In-plane GI-WAXS data of P3HT:F8TBT samples prepared at various conditions: as-spun, 140, and 200 °C annealed. . . . .	108
Figure 6.9	Comparison of UV-Vis absorption spectra of as-cast chloroform and xylene P3HT:F8TBT blends. The red-shift in the xylene-processed absorption spectrum is evidence for increased P3HT ordering following spin-coating. . . . .	115
Figure 6.10	In-plane GI-WAXS data of P3HT:P(NDI2OD-T2) blend films annealed at 180 °C and 200 °C, showing that 200 °C annealed sample is much less crystalline. The intensity of 180 °C annealed sample has been scaled to match the other data set in main article text, and the 200 °C annealed sample is then scaled accordingly. . . . .	115
Figure 6.11	Optical contrast plots of P3HT/ P(NDI2OD-T2), vacuum/P3HT, and vacuum / P(NDI2OD-T2). The energy at which the data were acquired is indicated with the vertical dark line. . . . .	116
Figure 6.12	Optical contrast plots of P3HT/F8TBT, vacuum / P3HT, and vacuum / F8TBT. The vertical dark line indicates the energy at which the R-SoXS data were acquired. . . . .	117
Figure 6.13	STXM images taken at 285.3 eV and histogram results of the images, showing no contrast difference observed for: (a) As-spun, and (b) 120 °C, (c) 200 °C annealed samples. . . . .	118
Figure 7.1	Schematic of the molecular orientation of P(NDI2OD-T2) polymer (one repeating unit shown) on a substrate. Green arrows indicate the polarization direction of the soft X-ray beam and the stacking direction of the green arrows is actually the propagating direction of the beam. Yellow arrows represent the transition dipole moment of the molecule. . . . .	120
Figure 7.2	Preliminary polarization-dependent R-SoXR data acquired at beamline 11.0.1.2 comparing with data from 6.3.2 with <i>s</i> -polarized X-ray. Data are acquired at 281.4 eV on PS/P(NDI2OD-T2) bilayer. From top to bottom: reflectivity data from beamline 6.3.2 for comparison ( <i>s</i> -polarized); data from beamline 11.0.1.2 with <i>s</i> -polarized X-ray; and data from beamline 11.0.1.2 with <i>p</i> -polarized X-ray. The various colors indicate the data acquired at several angle ranges and they are stitched to obtain the whole range data. . . . .	121

Figure 7.3	Angle-dependent NEXAFS of P3HT and P(NDI2OD-T2). The insets illustrate the relative orientations of the molecules to the incident soft X-ray beam. Green arrows in the insets indicate the polarization direction of the beam and the stacking direction of these arrows is actually the propagating direction of the beam. It is worth noting that the insets just show the extreme situations. Practically in a real film, the large population of molecules employ orientational preferences of alignment rather than aligning perfectly. . . . .	123
Figure 7.4	Polarization-dependent STXm images of P3HT: P(NDI2OD-T2) blend acquired at photon energy of 285.3 eV. Polarizations of the soft X-rays are (from top to bottom) <i>s</i> -, <i>p</i> - and circular, respectively, indicated with arrows in the images. The insets in each images show the Fourier transformation of each image to show the ordering of the patterns observed in the images. Zoomed-in images are shown beside the images from each polarization, with dashed lines highlighting some of the domains to show how the domain brightness varies from linear polarizations to circular. . . . .	124
Figure 7.5	P-SoXS of P3HT:P(NDI2OD-T2) blend films. (a),(b), Anisotropic scattering patterns obtained using linear horizontally (a) and vertically (b) polarized photons at an energy of 285.3 eV. The linear intensity scale bar is in arbitrary units, blue represents low intensity and white represents high intensity. (c), Radial scattering profiles at non-resonant (black) and resonant (green) energies. Darker lines are averages over the entire azimuth whereas lighter lines are from 30° sectors along the azimuth as indicated by white dashes in (a). (d), $I(\phi)$ for $q = 0.04 \text{ nm}^{-1}$ (colour-coded circles in (a) and (b) ). Figure authorized by and reproduced from Reference [4]. . . . .	125
Figure 7.6	Morphology and mechanism of scattering anisotropy in P3HT: P(NDI2OD-T2) films. (a), Scattering contrast between randomly oriented P3HT and oriented P(NDI2OD-T2) as a function of the photon electric-field alignment with the P(NDI2OD-T2) transition dipole moment (TDM). Two data sets from actual optical constants are shown as red and blue and intermediate traces are calculated and coloured using a linear interpolation. Energy used for scattering is shown with the arrow. (b), Top-down schematics depicting (left to right) a view of the mesoscale phase composition of the film, a view of the contrast for horizontally polarized X-rays and a view of the contrast for vertically polarized X-rays. Colours for P(NDI2OD-T2) represent TDMs orientation mimicking those used in (a). Blue regions, therefore, have TDMs oriented perpendicular to the electric field. (c), Molecular-scale perspective at the blend interface formed in the phase-separated materials. The green line on the grey substrate represents the interface between material phases. P(NDI2OD-T2) TDMs (shown in yellow) determine how the molecules scatter resonant X-ray photons and in this sample are aligned radially along the curved interface. Figure authorized by and reproduced from Reference [4]. . . . .	126

Figure 7.7	Angle-dependent contrast functions between P3HT and P(NDI2OD-T2) for an ordered matrix of P3HT. Angles are defined to be between the ordered molecule's transitions dipole moment and that of the photon electric field. Arrows indicate the photon energies used in scattering data presented in Figure 7.8. Figure authorized by and reproduced from Reference [4]. . . . .	127
Figure 7.8	Radial scattering profiles processed identically as in Figure 7.5 at different photon energies. Figure authorized by and reproduced from Reference [4].	128
Figure 7.9	Schematic diagram of an IM-SoXS setup. A polymer bilayer on a substrate is illustrated as the sample examined. The green arrows indicates the out-of-plane scattering and the red ones indicates the in-plane scattering. The center of the red circle is where the direct beam should reach the detector.	131
Figure 7.10	Optical constants of PMMA. . . . .	132
Figure 7.11	An illustration of the comparison between the length scales probed in low- $q$ and high- $q$ scattering data. . . . .	134
Figure A.1	$f^0$ represented in the complex $\omega$ -plane. for $\gamma \ll \omega_s$ , the function $f^0(\omega)$ has poles at $\pm\omega_s - i(\gamma/2)$ in the lower half plane and is analytic in the upper half plane. . . . .	156

# Chapter 1

## Introduction

The potential use of conjugated semiconducting polymers in modern organic electronics have motivated exceptional research interest in past three decades. Tremendous efforts have been made to develop new materials for related applications. The potential applications of these materials are mainly inspired by i) low cost of manufacturing and ii) flexibility of the devices. Organic semiconducting materials can be processed from solutions close to room temperatures and some of the fabrication processes can even be performed in ambient atmosphere, which cuts the energy usage and confers organic devices the advantage of low cost over its inorganic counterparts.

There are three major types of organic electronic devices that are considered in this thesis: a) organic solar cells (OSCs), b) organic field-effect transistors (OFETs) and c) organic light-emitting diodes (OLEDs). Organic solar cells are the devices that harvest the solar energies and turn them into electric power. Organic field-effect transistors are used as components of computing circuits and switches. Organic light-emitting diodes are the devices that give out light by consuming electric power.

### 1.1 Organic solar cells

#### 1.1.1 Device working mechanism

Initiated with employing small molecules that has photovoltaic effects, organic solar cells nowadays have achieved outstanding efficiency getting close to 9% [5] comparing to its pioneers. While the physics of the conventional solar cells composed of p-n junction materials is reasonably well understood, there is far less understanding of the underlying physics about the organic solar cells in terms. Nevertheless, the working mechanism of organic solar cells is usually described by four steps, with Figure 1.1 as a simplified illustration:

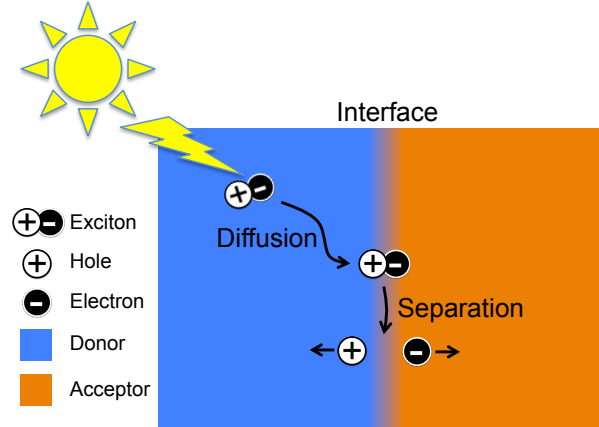


Figure 1.1: An illustration of the working mechanism of an OSC device.

1. Optical absorption and exciton generation. When the photon gets absorbed, the  $\pi$ -conjugated system of the polymer get excited and relaxes down to the bottom of the potential energy surface of the lowest excited state, the excited state reaches its equilibrium geometry, and an exciton forms. The exciton is a bound electron-hole pair with a typical bonding energy of a few tens of one electron volts (eV), which is distinguishing from what happens in inorganic semiconductors. Instead of creating free charges, the absorption of photons in an organic semiconductor creates electronically neutral bound electron-hole pairs that needs to be separated at the heterojunction of donor/acceptor.
2. Exciton diffusion. Before the excitons (the bound electron-hole pairs) can be separated into free charges, they have to travel through the active material to reach the interfaces of the donor and the acceptor, which is the process of exciton diffusion. The challenge is that the excitons have to get to the donor/acceptor interface before they decay to the ground state (recombination). The exciton diffusion length,  $L = \sqrt{D * \tau}$ , with  $D$  the diffusion coefficient and  $\tau$  the lifetime of the exciton, gives the longest distance that an exciton can travel before decaying, which is on the length scale of 10 nanometers (nm).
3. Exciton dissociation. Once the excitons reach the donor/acceptor interface, they can dissociate provided their energy is higher than that of charge-transfer or charge-separated states. The dissociation process is so complicated that currently no clear picture has been recognized to describe it throughly. However, the general simplified hypothesis describes the process as involving a transition from the exciton state down to the lowest charge transfer state, which corresponds to the situation where the hole sits on the highest occupied molecular orbitals (HOMO) of a donor molecule and the electron on the lowest unoccupied molecular orbitals (LUMO) of an adjacent acceptor molecule.

4. Charge transporting and collection. The separated free charges can drift and diffuse towards the corresponding electrodes with efficiency depending on their mobilities in the materials. Due to the large electron-vibration coupling in  $\pi$ -conjugated materials and the disorder effects, each charge is associated to a local geometry relaxation and constitutes a polaron (radical-ion in chemical terminology) which hops from molecule to molecule [6]. These charges are then collected at the electrodes and form photocurrent. Because of the defects existing within the semiconducting materials, it is worth noting that not all free charges can be extracted as photocurrent. The trapped charges will cause build-up potentials that hinder the charge transfer process.

The excitonic character of organic semiconductors is a signature feature, and it has impacted the design and geometry of the devices for the past several decades. With a planar geometry, the thickness of the active organic layers are required to be comparable to the exciton diffusion length  $L$ , which means the organic layer has to be as thin as  $\sim 10 - 20$  nm to avoid dramatic exciton recombination. However, to get the incident light absorbed sufficiently, a thickness of at least  $\sim 100$  nm is required. Hence, if the planar geometry is employed for a device, an optimal compromise has to be found regarding the thickness of the active layer for efficient exciton dissociation and sufficient absorption of incident light. This limitation of the planar geometry has stimulated the development of the new active layer geometry based on bulk heterojunctions (BHJ), in which the donor and acceptor components are mixed together and form an interpenetrating, bicontinuous phase-separated network with nanoscale morphology, as shown in Figure 1.2(A). A device is completed by sandwiching this active layer with hole and electron transport layers and electrodes as shown in Figure 1.2(B). In such devices, the donor/acceptor heterojunction is distributed throughout the bulk of the composite film, enabling efficient exciton dissociation and leaving holes in the donor component and electrons in the acceptor component of the phase-separated network. Because of the intimate mixing of the donor and acceptor materials, the morphology control is extremely critical to extract the charge carriers efficiently.

### 1.1.2 Device characterization

When an organic solar cell is in operation, it is illuminated with light, and if there is a load connecting the cathode and anode, there will be a potential drop across the load and the photocurrent flows from anode to cathode. To characterize the performance of an OSC device, the general protocol is to apply a bias across the device and record the current flowing when sweeping the bias voltage applied on an illuminated device with certain light flux (usually using a solar simulator that generates similar spectrum and intensity as what the sun does). The generated plot of current ( $I$ ) vs. bias voltage ( $V$ ) is the so-called  $I - V$  curve. Conventionally for the sake of easier comparison, the current is normalized to per area, thus ending up with

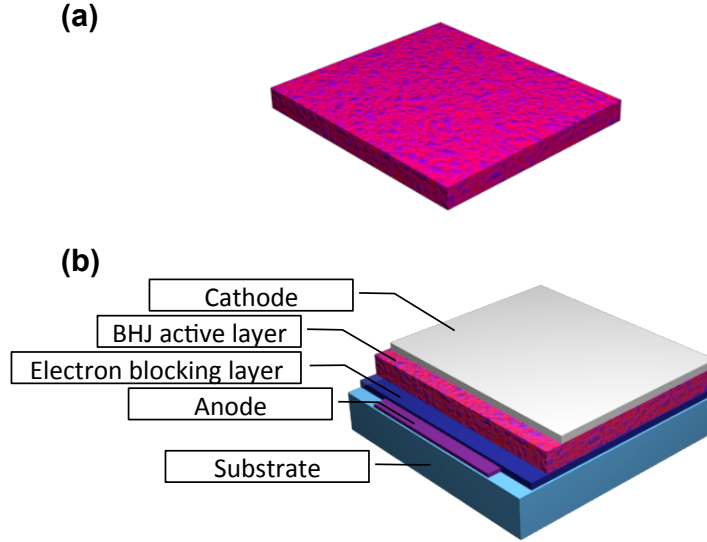


Figure 1.2: A schematic of bulk heterojunction film (a) and a schematic of a bulk heterojunction device (b).

$J - V$  curve, in which  $J$  is the current density with a unit of  $\text{mA}/\text{cm}^2$  usually. A typical  $J - V$  curve is shown in Figure 1.3. In this plot, the dashed line is the  $J - V$  curve in black and the solid line is when the solar cell is illuminated. Point A marks the short circuit current  $J_{SC}$  and point B marks the open circuit voltage  $V_{OC}$ .  $J_{SC}$  is the maximum current when there is zero load connected to the cell and  $V_{OC}$  is the maximum voltage one can get from an OSC device with infinite load connected at a certain illumination condition. At a given bias  $V_{max}$ , corresponding to a current density  $J_{max}$  (marked with point C in Figure 1.3), the output power from the solar cells reaches its maximum  $J_{max} \times V_{max}$ . The ratio of the maximum power and the input power from the light gives the power conversion efficiency of the device:

$$\eta = \frac{J_{max}V_{max}}{P_{in}} = FF \frac{J_{SC}V_{OC}}{P_{in}} \quad (1.1)$$

where  $P_{in}$  is the incident power density and  $FF$  denotes the fill factor,

$$FF = \frac{J_{max}V_{max}}{J_{SC}V_{OC}} \quad (1.2)$$

The  $J - V$  curve can be modeled by the Shockley equation with the simplified equivalent circuit as shown in Figure 1.4 [7, 8, 9] comprised of (i) a diode with reverse saturation current density  $J_0$  (current density in the dark at reverse bias) and ideality factor  $n$ ; (ii) a current source  $J_{ph}$ , which corresponds to the photocurrent upon illumination; (iii) a series resistance  $R_S$ , which has to be minimized and takes account of the finite conductivity of the semiconducting

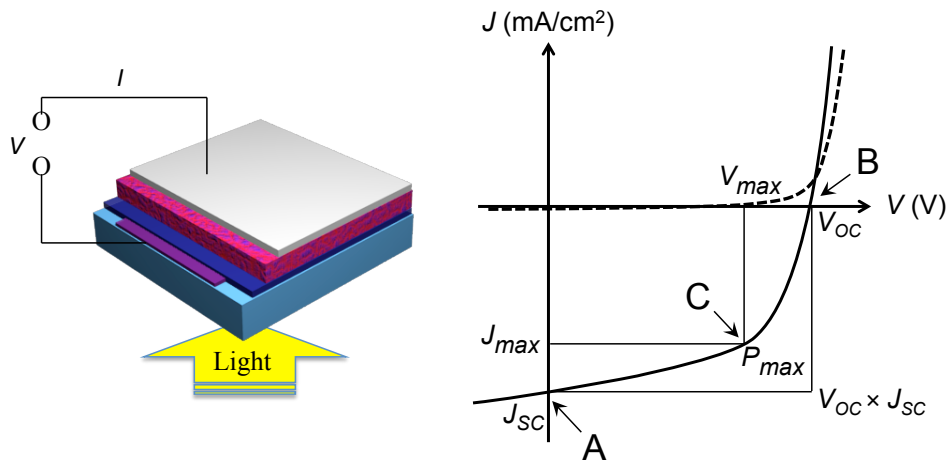


Figure 1.3: Schematic of  $J - V$  measurement and typical  $J - V$  curve in dark (dashed line) and under illumination (solid line) of OSC.

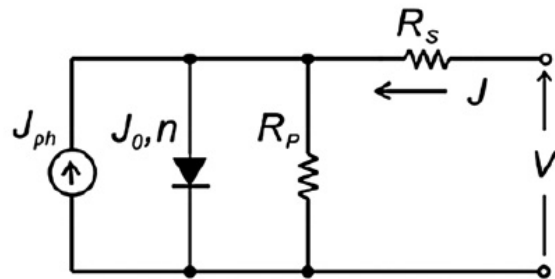


Figure 1.4: An illustration of the equivalent circuit of an OSC device. Figure reproduced from Reference [1].

material, the contact resistance between the semiconductors and the adjacent electrodes, and the resistance associated with electrodes and interconnections; and (iv) a shunt resistance  $R_P$ , which needs to be maximized and takes into account the loss of carriers *via* possible leakage paths; the latter include structural defects such as pinholes in the film, or recombination centers introduced by impurities:

$$J = \frac{1}{1 + R_S/R_P} \left[ J_0 \left\{ \exp \left( \frac{V - JR_S A}{nkT/e} \right) - 1 \right\} - \left( J_{ph} - \frac{V}{R_P A} \right) \right] \quad (1.3)$$

where  $e$  denotes the elementary charge,  $kT$  the thermal energy, and  $A$  the active area of the cell.

Fill factor  $FF$ , open-circuit voltage  $V_{OC}$  and short-circuit current  $J_{SC}$  are the most commonly examined parameters when considering performance across devices. The fill factor provides semi-quantitative measurement of the efficiency at which the device makes use of the charges before recombination. The open-circuit voltage depends on the energy difference between the ionization potential of the donor component and the electron affinity of the acceptor component forming the heterojunction [10, 11]. The short-circuit current is affected by the optical band gap of the materials and the nanomorphology of the active layer.

## 1.2 Organic field-effect transistors

Field-effect transistors (FETs) are important building blocks for electronic industries, especially some modern electronics like computing chips. The FETs based on inorganic materials have been proved to be reliable and highly efficient. Manufacturing of these inorganic devices, however, are usually demanding in terms of material growth, temperature control, vacuum control, and packaging. In contrast, the organic field-effect transistors (OFETs) can be fabricated by solution processing in room temperature and normal pressure. Besides, the capability of being able to be fabricated on bendable substrates recognize OFETs the potential of much more applications [12]. In this sense, OFETs have promising advantages for designated uses in plenty low-performance radio-frequency technologies, sensors, and light emission.

One of the most common OFET device configurations is that of the thin-film transistor (TFT), in which a thin film of the organic semiconductor is deposited and employed as the active channel layer of the device. Depending on the relative position of the gate/dielectric and source-drain contacts to the active layer, there are three type of organic thin-film transistor architectures being mostly utilized: (i) top-contact, bottom-gate, (ii) bottom-contact, bottom-gate and (iii) bottom-contact, top-gate, as illustrated in Figure 1.5. Minimal current between source and drain electrodes is measured when no voltage is applied between the source and gate ( $V_{SG}$ ) electrodes (device “off”). When a voltage is applied to the gate, electrons or holes

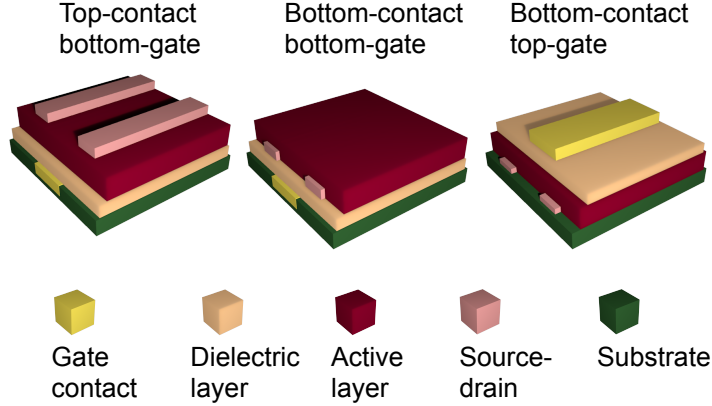


Figure 1.5: Schematic of the geometry of major types of organic field-effect transistors.

(depending on either n- or p-type) can be induced at the semiconductor-dielectric interface and the source-drain current increases (device “on”) with fixed source-drain voltage ( $V_{SD}$ ). The basic equations describing the OFET drain current are given as:

$$(I_{SD})_{linear} = \frac{W}{L} \mu C_i \left( V_{SG} - V_T - \frac{V_{SD}}{2} \right) V_{SD} \quad (1.4)$$

$$(I_{SD})_{saturate} = \frac{W}{2L} \mu C_i (V_{SG} - V_T)^2 \quad (1.5)$$

where  $\mu$  is the field-effect carrier mobility of the semiconductor,  $W$  the channel width,  $L$  the channel length,  $C_i$  the capacitance per unit area of the insulator layer, and  $V_T$  the threshold voltage. On increasing the magnitudes of  $V_{SD}$  and  $V_{SG}$ , a linear current regime is initially observed at low drain voltages ( $V_{SD} < V_{SG}$ ), followed by a saturation regime when the drain voltage exceeds the gate voltage. Note that OFETs normally operate in the accumulation mode, where a  $V_{SG}$  with bigger magnitude enhances channel conductivity, in contrast to conventional Si transistors. The mobility  $\mu$  is the relationship between the carrier speed in a material and the applied electric field. Microscopically, carriers accelerate due to the force applied by the electric field and periodically scatter and experience other momentum transfer phenomena which dissipate the acquired momentum. This occurs rapidly and across a large number of carriers which averages the observed effect.

To examine the performance of a device, typical characterizations include output characteristic (drain sweep) and transfer characteristic (gate sweep):

1. **Output characteristic.** Holding  $V_{SG}$  at several values, the transistor action is measured by sweeping  $V_{SD}$  values, as shown in Figure 1.6, with linear and saturation regions denoted. The output characteristic is almost universally presented as the qualitative proof

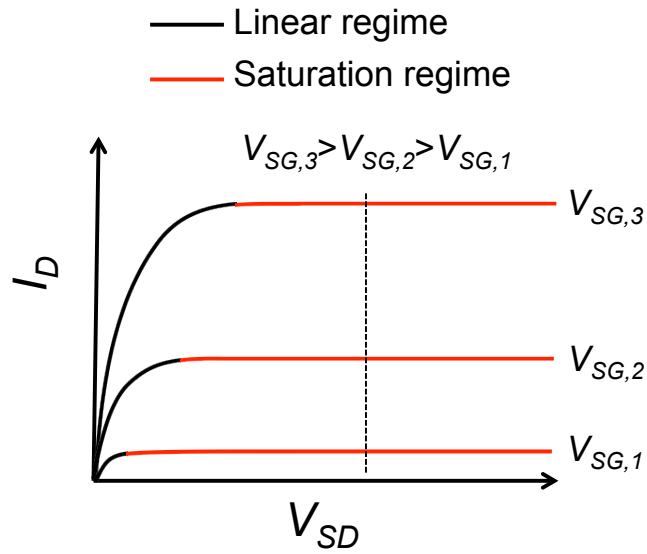


Figure 1.6: Schematic diagram of the OFET current flow  $I_D - V_{SD}$  curve with the regions of operation noted.

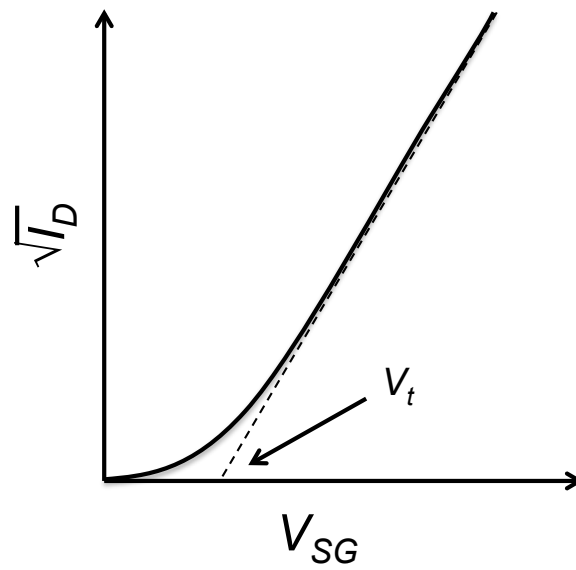


Figure 1.7: Schematic diagram of the OFET  $\sqrt{I_D} - V_{SG}$  curve showing the derivation of  $V_t$  by extrapolation. The  $V_{SD}$  at which the curve is acquired is indicated in Figure 1.6 with dashed line.

confirming that a transistor has been formed.

- 2. Transfer characteristic.** The transistor action is measured by holding  $V_{SD}$  constant at a few values and sweeping the gate voltage  $V_{SG}$ . At least one value of  $V_{SD}$  is selected to test the device in the linear region. According to the relation between the current and the voltage as in Equation 1.5, the threshold voltage  $V_t$  can be obtained by a plot of  $\sqrt{I_D} - V_{SG}$  as shown in Figure 1.7. The linear region measurement should ideally be taken at a  $V_{SD}$  as low as possible. It is only for low values of  $V_{SD}$  that the electric field and charge density in the channel is uniform and the measurement of mobility is valid. Mobility varies significantly as a function of gate voltage, it is often measured and reported as a function of  $V_{SG}$  by taking the slope tangent at each  $V_{SG}$  individually.

### 1.3 Organic light-emitting diodes

Organic light-emitting diodes (OLEDs) are novel organic electronic that have been predicted to revolutionize the display industry. OLEDs provide superior brightness and color purity, markedly lower drive voltages, as well as increased viewing angles, which surmount conventional cathode ray tubes and liquid crystal displays (LCDs). Small area OLEDs have been successfully commercialized in the markets for some of the consumer digital products such as cell phones and music players, while for big area applications such as HDTVs, improvements on manufacturing are still highly demanded to lower the cost. The device structure of a model multilayer OLED is presented in Figure 1.8. The device consists of transparent conducting oxide (TCO) anode, hole-transport layer (HTL), emissive layer (EML), electron-transport layer (ETL), and metallic low work function electrode (LWE) as the cathode. Under forward bias, the HTL is oxidized as holes are injected (electrons extracted) from the anode into its highest occupied molecular orbital (HOMO), and the ETL is reduced as electrons are injected from the cathode into its lowest unoccupied molecular orbital (LUMO). Charge carriers migrate under the applied electric field and recombine to form singlet and triplet excitons within the EML. These excited-state species can return to the ground state via both radiative and nonradiative decay pathways. Energy level offsets of the anode and cathode work functions from the HTL HOMO and ETL LUMO energies, respectively, strongly influence the intrinsic carrier injection barriers [13]. To improve the performance of a OLED device, one needs to optimize three electronic processes: (i) charge injection, (ii) transport, and (iii) recombination.

Interfacial phenomena represent a challenging and important area of OLED science and technology and have been the subject of much recent theoretical and experimental study [14, 15], because the carrier transport in most OLED heterostructures is largely injection-limited. Considering that typical OLED carrier populations are electron-limited, most interfacial modifica-

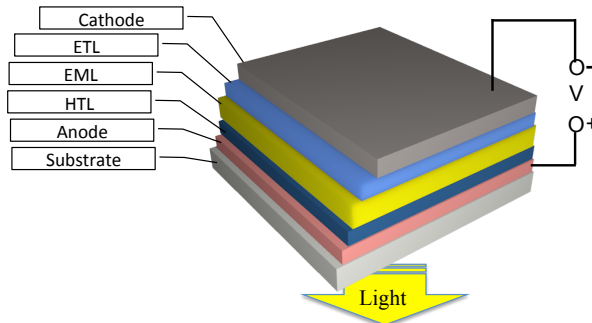


Figure 1.8: Schematic representation of a typical structure of organic light-emitting diode.

tion efforts have focused on hole injection/fluence attenuation and electron flux enhancement. Modifications have been applied to both cathode-organic and anode-organic interfaces, all influence charge injection and afford varying degrees of enhanced device response (e.g., in turn-on voltage, maximum luminance, and/or quantum efficiency). Notably, the exact interfacial structures and mechanistic roles remain incompletely defined [16].

## 1.4 Morphology characterization of organic electronics

The performance of the organic electronics, e.g. OSCs, OFETs and OLEDs, are largely determined by the nanoscale morphology of their compositing materials as introduced above. This nanomorphology includes not only the bulk phase separation and domain morphology, but also interfacial nanostructures at the interfaces between components within devices. However, despite the significance of the nanomorphology for understanding and improving the performance of organic electronic devices, only very limited aspects [17, 18, 19, 20, 21] have been known of the relation between the morphology and the performance. This is mainly due to the difficulty to characterize the soft-condensed matters composing these organic systems, especially at sub-100 nm scale. A wide range of conventional well-developed characterization techniques in materials research keep playing important roles in investigating organic electronic materials, as briefly introduced in the following. Many of these techniques are powerful and can obtain significant information of the interfacial and bulk nanomorphology of organic species.

### 1.4.1 Conventional useful techniques and methods

Atomic Force Microscopy (AFM) are widely used to characterize the surfaces of vast variety of organic materials. [22, 23, 24]. It's an extremely powerful techniques since the imaging can be conducted under ambient conditions and does not require vacuum or dry environments to operate. This enables one to perform characterizations in situ, which is critically important

when the systems under investigation involve liquids or elevated/reduced temperatures. For most studies, AFM is used to quantify surface topographic features ranging from sub-nanometer to a few microns. However, variants of the AFM technique do allow spatially resolved surface chemical composition to be determined. AFM is also a platform for development of many dedicated techniques in organic electronic research such as conductive-AFM (c-AFM) for current map study and electrostatic force microscopy (EFM) for photoinduced charge study of OSCs [25, 26]. The limitation of AFM technique is obvious. It is a surface sensitive method and can only characterize the interface of the vacuum and the soft matter. It cannot provide bulk morphology information such as domain purity in a phase separated organic blend thin films.

Neutron techniques are also very powerful to examine soft matters in terms of the sensitivity to different species in a phase separated system, because the contrast between constituents can be enhanced by deuterating one of the species. Neutron reflectivity [27] is commonly used to investigate surfaces and interfaces between immiscible and partially miscible organic materials because of its inherent sub-nanometer resolution. The length-scales probed by the reflection experiment are sensitive to structural features perpendicular to the plane of the film with length scales between 0.5 nm and 500 nm. The very large penetration power of neutron beam makes it straightforward to study *buried* interfaces. The large difference in neutron scattering length density between deuterium and hydrogen enables contrast enhancement or “highlighting” by isotopic substitution. Neutron scattering is another powerful technique for structural and dynamic properties study in polymeric research. The length and timescales accessed by neutron scattering simultaneously match those of typical molecular processes. Therefore, neutron scattering has been a tool used to elucidate structure and dynamics of increasingly complex, multi-component materials. With the ability of high penetration of the neutron particle, in situ measurements can be performed, so that structural changes can be followed mimicking processing conditions [28]. However, the deuteration is usually very expensive and the underlying physical and chemical properties of the material might be disturbed [29, 30].

The closely related techniques are X-ray reflectivity and scattering. X-ray reflectivity have been used for decades to characterize the surface and buried interface of inorganic thin films [31]. It is also commonly used to study the surfaces and interfaces in some organic systems. In contrast to neutrons, X-ray reflectivity experiments are sensitive to the average electron density fluctuations along the sample normal. The general experimental and analysis approach is analogous to the neutron reflectivity (so is resonant soft X-ray reflectivity which will be discussed later) with many of the standard optical equations identical for both techniques but with neutron scattering length density being replaced with electron density. X-ray reflectivity technique can be used if sufficient contrast in electron density between the polymer phases is present. With the same contrast mechanism plus more sensitive to molecular ordering, X-ray scattering has been playing more and more important role in organic material study nowadays. X-ray

scattering can be used to investigate the microstructure of polymer films, yielding quantitative information about degree of crystallinity and detailed information about the molecular packing structure, the orientation of crystalline regions, and potentially information about structural defects [32, 33]. These information are extremely important for the performance of OFETs and OSCs [34, 35, 36]. For instance, one of the major impediments to the use of polymers is their low field-effect mobility, which is intimately related to the electronic coupling of the molecules in a thin film [37, 38]. The detailed picture of the molecular organization obtained from X-ray scattering is helpful to interpret differences in the behavior of materials. It is difficult to obtain single crystalline films of semiconducting polymers and polycrystalline films are studied in most cases. Transport in most organic solids is anisotropic due to the dependence of the electronic coupling on the packing geometry, therefore it is important to determine the orientation of the molecules relative to the direction of transport. For example, in thin-film transistor structures, it is advantageous to have the best transport between two electrodes on the substrate surface.

However, it is hard to use conventional X-ray techniques to access the phase separation and domain properties between organic components in a system. That's because for most organic materials that mostly contain only low-atomic-number (low- $Z$ ) elements, the electron density are very similar, thus the inherent contrast are usually too low to be detectable.

#### 1.4.2 Soft X-rays and near edge X-ray absorption fine structures (NEXAFS)

In order to access the chemical sensitive information of the organic systems with low- $Z$  materials such as polymers, techniques that can distinguish the constituents better need to be utilized. In the work included in this thesis, we use resonant soft X-ray techniques, i.e. resonant soft X-ray reflectivity (R-SoXR) and resonant soft X-ray scattering (R-SoXS), to investigate several types of polymer systems employed in organic electronic devices, presenting informations that are very difficult/impossible to derive with conventional techniques as demonstrated above.

Soft X-rays are electromagnetic waves with energies covering the range of several eV to several hundreds eV (Figure 1.9), which is a region where a large number of atomic resonances fall in. As a consequence, the absorption of radiation occurs in very short length scales, typically measured in nanometers or micrometers (microns,  $\mu\text{m}$ ), in all materials. These resonances provide mechanisms for both elemental and chemical identification due to the finger-print absorption edges of different elemental atoms and chemical environments (such as molecular bonding) around them in both inorganic and organic chemical compounds. This phenomenon allows for the advances in both science and technology.

Carbonaceous materials, such as synthetic and natural polymers, exhibit rich carbon (nitrogen, oxygen, sulfur, fluorine and/or other hetero-atoms for some polymers) K-edge NEXAFS spectra. This is primarily due to the essentially covalent nature of the chemical bonds in these

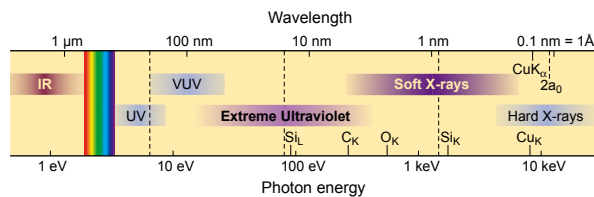


Figure 1.9: Schematic representation showing energy ranges of soft X-rays among other radiations. Figure courtesy of D. Attwood [2].

materials and the numerous possible combinations of single and multiple bonds between carbon atoms as well as hetero-atoms. NEXAFS spectroscopy measures the photoabsorption cross-section for the excitation of tightly bound core electrons. These spectra are element specific, as each element has a characteristic core binding energy (i.e. Carbon 1s (C-1s):  $\sim 290$  eV, Nitrogen 1s:  $\sim 400$  eV, Oxygen 1s:  $\sim 530$  eV, etc.). The spectral features correspond to transitions from the ground state to a core excited state. In general, this must be treated as a multielectron process. However, it is convenient to describe X-ray absorption in closed-shell molecules with an orbital approximation as a one-electron transition ( $C\ 1s \rightarrow \pi^*$ ) perturbed by the creation of the core hole. Figure 1.10 presents a schematic of the X-ray photoabsorption process for the carbon 1s NEXAFS spectrum of several different polymers. NEXAFS is an absorption spectroscopy in which a core electron is excited into empty states near the photo-ionization threshold [39]. It is thus inherently element specific due to the special elemental binding energies of core electrons. In addition, because of the intimate relationship between molecular bonding and the structure of the empty electronic states, NEXAFS is very sensitive to the detailed chemical structure of the sample as well. Figure 1.10 demonstrates Carbon 1s NEXAFS spectra of a number of common conjugated polymers that can be used in vast variety of organic electronics [40], showing the ability of this spectroscopy to differentiate materials on the basis of relatively subtle bonding and structural differences.

### 1.4.3 Scanning transmission X-ray microspectroscopy (STXM)

The need for detailed compositional and chemical analysis at high spatial resolution has motivated the development of the scanning transmission X-ray micro spectroscopy (STXM). In order to scan the photon energy at high resolution for NEXAFS, a synchrotron radiation facility as a tunable light source is required for this instrument.

In a STXM microscope setup, as shown in the schematic diagram in Figure 1.11, a small spot of X-rays is raster scanned relative to the sample to create an image one pixel at a time while both the incident and transmitted photon flux signal is monitored simultaneously under computer control. In order to acquire useful information in a reasonable time, high photon flux

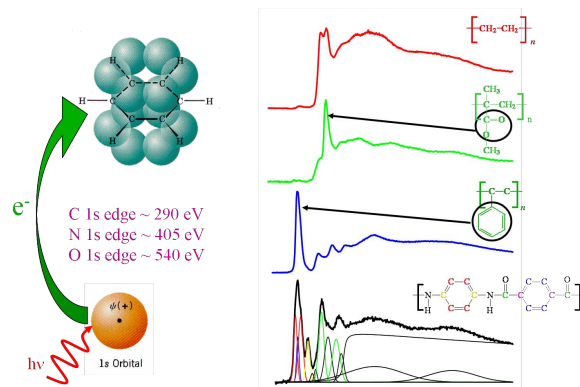


Figure 1.10: Schematic of the photo-absorption processes occurring in a NEXAFS experiment. An incident photon, whose energy corresponds to a NEXAFS resonance, excites an electron from a core level (1s) into an unoccupied, anti-bonding level. (Figure created by A.P. Smith)

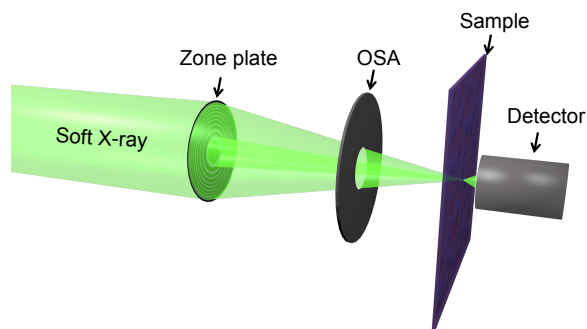


Figure 1.11: Schematic of the scanning transmission X-ray microspectroscopy (STXM). The incident intensity is denoted as  $I_0$ , and the transmitted intensity as  $I$ .

in a small spot is required. A zone-plate, the device to focus lights with diffraction instead of refraction or reflection, is used as lens to get soft X-rays focused. In order to suppress unwanted diffraction orders that would decrease the available signal-to-background ratio, the zone plate is fabricated with a central stop. A slightly smaller pinhole, the order selection aperture (OSA), is placed between the zone plate and the sample. The moving of the sample stages are precisely controlled with laser interferometer, combining with the focused light spot, to gain high spacial resolution up to  $\sim 40$  nm [41].

According to *Beer's Law*, the relation between the incident intensity  $I_0$  and the transmitted intensity  $I$  can be written as

$$I = I_0 e^{-\frac{4\pi\beta}{\lambda}z} \quad (1.6)$$

or

$$I = I_0 e^{-\mu\rho z} \quad (1.7)$$

where  $z$  is the thickness of the film,  $\lambda$  is the wave length of the light,  $\mu$  is the mass absorption coefficient, and  $\rho$  is the density of the film. The final format of a NEXAFS spectrum can be presented in various ways, such as the optical density (*OD*) or mass absorption coefficient  $\mu$ , where

$$OD = -\ln \frac{I}{I_0} \quad (1.8)$$

and

$$\mu = \frac{OD}{\rho z} \quad (1.9)$$

As examples, sample NEXAFS spectra of two semiconductive polymers, poly(3-hexylthiophene) (P3HT) and poly [N,N'-bis(2-octyldodecyl)-naphthalene-1,4,5,8-bis(dicarboximide)-2,6-diy]-alt-5,5'-(2,2'-bithiophene) (P(NDI2OD-T2)), and 2D scan images of a blend of them are presented in Figure 1.12 and Figure 1.13, respectively. Differences in the absorption spectra of the two polymers are obvious. The images show that at 285.3 eV, where the C-1s  $\pi_{C=C}^*$  absorption is, the absorption difference between polymers results in the visibility of the blend composition morphology in Figure 1.13(a). However, there is no feature seen in image acquired at 350 eV, resulting from the very similar absorption ability of the two polymers at this energy far away from the absorption edge. Much other study has been done on the composition of organic semiconductive materials utilizing this capability of STXM [42, 43, 44, 45, 46, 47, 48]

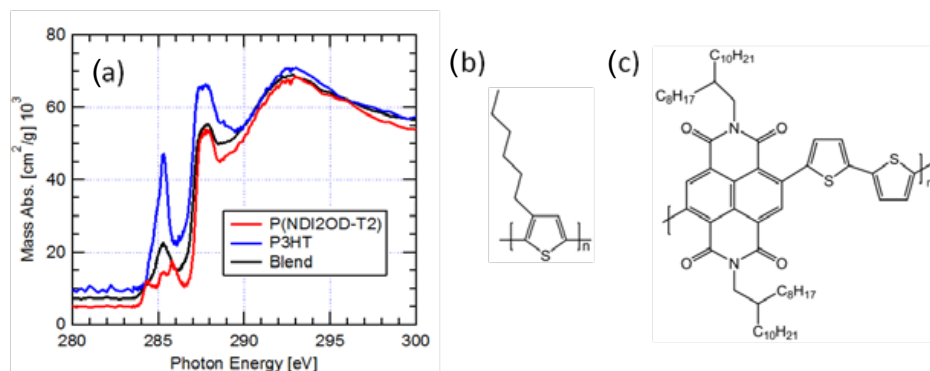


Figure 1.12: (a) Absorption spectra of P3HT, P(NDI2OD-T2) and the blend film studied in this work scaled to mass absorption coefficient of each species. (b) and (c) Chemical structure of P3HT and P(NDI2OD-T2), respectively.

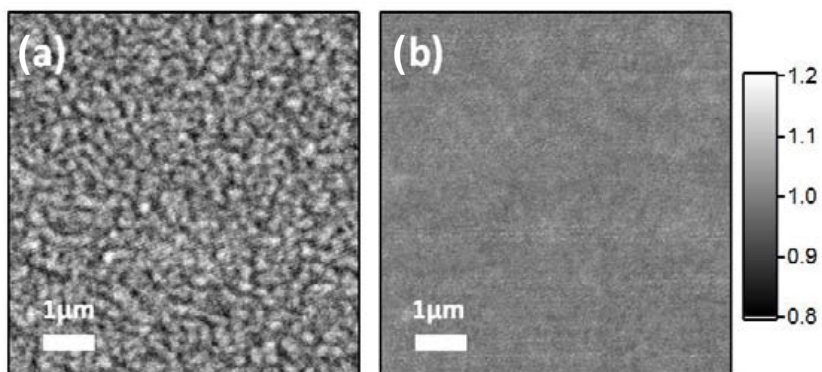


Figure 1.13: STXM images of P3HT:P(NDI2OD-T2) blend at (a) the C-1s  $\rightarrow$   $\pi_{C=C}^*$  resonance 285.3 eV and (b) off resonance at 350 eV. Color scales are in optical densities whose average values have been normalized to 1.

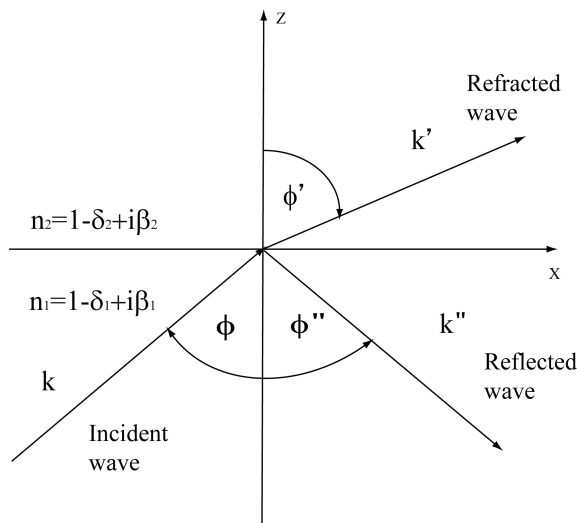


Figure 1.14: Interface geometry for incident ( $\mathbf{k}$ ), reflected ( $\mathbf{k}''$ ), and refracted waves ( $\mathbf{k}'$ ).

#### 1.4.4 Resonant soft X-ray reflectivity and scattering overview

In order to make use of the techniques of R-SoXR and R-SoXS productively, optical properties of the materials at soft X-ray energy range need to be known. NEXAFS spectra can be used to derive the optical constants of the materials (see details in Chapter 2), so that they can be utilized to guide the experiments. The optical constants are also required as the initial values for numerical model refinement to extract physical film parameters, e.g. film thickness and interfacial roughnesses. Assuming that a material is isotropic, the complex index of refraction can be written as  $\mathbf{n} = 1 - \delta + i\beta$ , where  $\delta$  is the dispersion part and  $\beta$  the absorption part of the index of refraction. The imaginary part,  $\beta$ , can be derived from NEXAFS spectra directly, and the real part,  $\delta$ , is usually difficult to measure directly in soft X-ray range due to the high absorption. We develop a new method to accurately determine  $\delta$  and  $\beta$ , which will be demonstrated with details and related maths in Chapter 2. In order to understand the physics of how the optical constants, i.e.  $\delta$  and  $\beta$ , affects the reflectivity phenomena and the contrast mechanism, we start with looking at the reflection and refraction at an interface.

#### X-ray reflection and refraction at an interface

When an electromagnetic wave reaches an interface of two materials, reflection and refraction occur at that interface. Figure 1.14 shows a schematic of the phenomena of reflection and refraction at the interface of material 1 and material 2 with complex index of refraction  $\mathbf{n}_1 = 1 - \delta_1 + i\beta_1$  and  $\mathbf{n}_2 = 1 - \delta_2 + i\beta_2$ , respectively. The incident plane wave function is

$$\mathbf{E} = \mathbf{E}_0 e^{-i(\omega t - \mathbf{k} \cdot \mathbf{r})} \quad (1.10)$$

the refracted wave is

$$\mathbf{E}' = \mathbf{E}'_0 e^{-i(\omega t - \mathbf{k}' \cdot \mathbf{r})} \quad (1.11)$$

and the reflected wave is

$$\mathbf{E}'' = \mathbf{E}''_0 e^{-i(\omega t - \mathbf{k}'' \cdot \mathbf{r})} \quad (1.12)$$

Here we assume all waves have the same frequency,  $\omega$ , and  $|\mathbf{k}| = |\mathbf{k}'| = \frac{\omega}{c}$ , and the refracted wave has

$$k' = |\mathbf{k}'| = \frac{\omega}{c} \mathbf{n} = \frac{\omega}{c} (1 - \delta + i\beta) \quad (1.13)$$

At interface ( $z = 0$ ), from the Maxwell's equation, the boundary conditions must be satisfied,  $\mathbf{E}$  and  $\mathbf{H}$  components parallel to the interface must be continuous:

$$\mathbf{z}_0 \times (\mathbf{E}_0 + \mathbf{E}''_0) = \mathbf{z}_0 \times \mathbf{E}'_0 \quad (1.14)$$

and

$$\mathbf{z}_0 \times (\mathbf{H}_0 + \mathbf{H}''_0) = \mathbf{z}_0 \times \mathbf{H}'_0 \quad (1.15)$$

$\mathbf{D}$  and  $\mathbf{B}$  components perpendicular to the interface must be continuous:

$$\mathbf{z}_0 \times (\mathbf{D}_0 + \mathbf{D}''_0) = \mathbf{z}_0 \times \mathbf{D}'_0 \quad (1.16)$$

and

$$\mathbf{z}_0 \times (\mathbf{B}_0 + \mathbf{B}''_0) = \mathbf{z}_0 \times \mathbf{B}'_0 \quad (1.17)$$

Continuity of parallel field components requires

$$(\mathbf{k} \cdot \mathbf{x}_0 = \mathbf{k}' \cdot \mathbf{x}_0 = \mathbf{k}'' \cdot \mathbf{x}_0) \text{ at } z = 0 \quad (1.18)$$

$$k_x = k'_x = k''_x \quad (1.19)$$

and as shown in figure 1.14

$$k \sin \phi = k' \sin \phi' = k'' \sin \phi''. \quad (1.20)$$

Since  $k$  and  $k''$  propagate in the same material  $\mathbf{n}_1$ , we can write

$$\sin \phi = \sin \phi'', \quad (1.21)$$

which states that the angle of incidence equals the angle of reflection. For the refracted wave  $k'$ ,

$$k \sin \phi = k' \sin \phi'. \quad (1.22)$$

Because both waves has the same frequency  $\omega$ , from 1.13, we can get the *Snell's law* that describes the refractive turning for complex  $\mathbf{n}$

$$\frac{\sin \phi}{\mathbf{n}_2} = \frac{\sin \phi'}{\mathbf{n}_1} \quad (1.23)$$

### Reflection coefficients at an interface

For the S-polarized wave ( $\mathbf{E}_0$  perpendicular to the plane of incidence), following the boundary condition, the scalar field amplitude at the interface (subscript zero) must satisfy the condition that the tangential electric fields be continuous, i.e.

$$E_0 + E_0'' = E_0' \quad (1.24)$$

and the tangential magnetic fields be continuous, i.e.

$$H_0 \cos \phi - H_0'' \cos \phi = H_0' \cos \phi' \quad (1.25)$$

Recalling that for plane waves propagating in a medium of refractive index  $\mathbf{n}$ ,  $\mathbf{E}$  and  $\mathbf{H}$  are related by

$$\mathbf{H}(\mathbf{r}, t) = \mathbf{n} \sqrt{\frac{\epsilon_0}{\mu_0}} \mathbf{k}_0 \times \mathbf{E}(\mathbf{r}, t) \quad (1.26)$$

and the amplitudes are related by

$$H = \mathbf{n} \sqrt{\frac{\epsilon_0}{\mu_0}} E \quad (1.27)$$

After doing the math, 1.25 can be written as

$$\mathbf{n}_1 (E_0 - E_0'') \cos \phi = \mathbf{n}_2 E_0' \cos \phi'. \quad (1.28)$$

Combing 1.23, 1.24, and 1.28, we get

$$(\mathbf{n}_1 \cos \phi - \mathbf{n}_2 \cos \phi')E_0 = (\mathbf{n}_1 \cos \phi + \mathbf{n}_2 \cos \phi')E_0'' \quad (1.29)$$

so that the ratio of field amplitude is

$$\frac{E_0''}{E_0} = \frac{\mathbf{n}_1 \cos \phi - \mathbf{n}_2 \cos \phi'}{\mathbf{n}_1 \cos \phi + \mathbf{n}_2 \cos \phi'}. \quad (1.30)$$

The reflectivity  $R$ , defined as the ratio of reflected to incident intensity (at the surface), is determined to be

$$R = \frac{\bar{I}''}{\bar{I}_0''} = \frac{|\bar{S}''|}{|\bar{S}|} = \frac{\frac{1}{2}Re(\mathbf{E}_0'' \times \mathbf{H}_0''^*)}{\frac{1}{2}Re(\mathbf{E}_0 \times \mathbf{H}_0^*)}, \quad (1.31)$$

with the same  $\mathbf{n}$  for both incident and reflected waves,

$$R = \frac{|\mathbf{E}_0''|^2}{|\mathbf{E}_0|^2}. \quad (1.32)$$

For the S-polarized wave, the reflection coefficient is

$$R_s = r_s^2 = \frac{|\mathbf{n}_1 \cos \phi - \mathbf{n}_2 \cos \phi'|^2}{|\mathbf{n}_1 \cos \phi + \mathbf{n}_2 \cos \phi'|^2}, \quad (1.33)$$

where  $r_s$  is the Fresnel reflection coefficient for S-polarized wave. Using the same derivation, we can get the reflection coefficient and Fresnel coefficient for the P-polarized wave,

$$R_p = r_p^2 = \frac{|\mathbf{n}_2 \cos \phi - \mathbf{n}_1 \cos \phi'|^2}{|\mathbf{n}_1 \cos \phi + \mathbf{n}_2 \cos \phi'|^2}, \quad (1.34)$$

where  $\mathbf{n}_1$  and  $\mathbf{n}_2$  are the complex index of refraction of the two materials. Knowing the values of  $\delta$  and  $\beta$  as function of photon energy, one can now calculate the reflectance, at an arbitrary angle of incidence. Alternatively, angle dependent reflectance can be used to experimentally determine values of  $\delta$  and  $\beta$  via numerical model refinement. We used this method to measure the optical constant ( $\delta$  and  $\beta$ ) of polymers poly(methyl methacrylate) (PMMA) and polystyrene (PS) in the photon energy near the Carbon 1s edge,  $\sim 285$  eV. This will be discussed in chapter 2.

Considering an extreme condition at normal incidence, i.e.  $\phi = \phi' = 0^\circ$ , from Equation 1.33 (the same for Equation 1.34) one can have

$$R = \frac{|\mathbf{n}_1 - \mathbf{n}_2|^2}{|\mathbf{n}_1 + \mathbf{n}_2|^2}. \quad (1.35)$$

Combining with  $\mathbf{n}_1 = 1 - \delta_1 + i\beta_1$  and  $\mathbf{n}_2 = 1 - \delta_2 + i\beta_2$ ,  $R$  can be written as

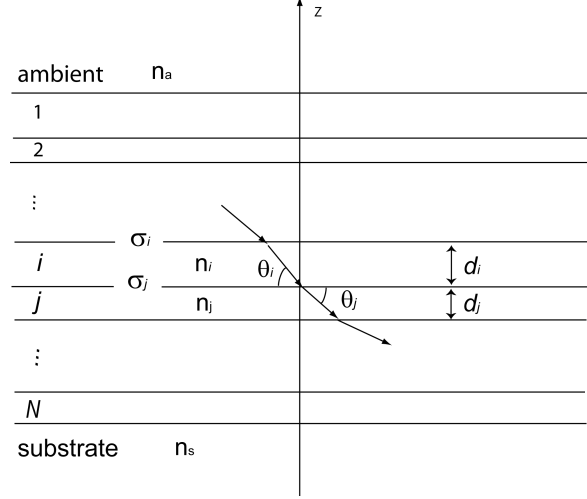


Figure 1.15: Diagram of a multilayer stack containing  $N$  layers, where the optical constants, thickness, propagation angle, and interface roughness/diffuseness parameter of the  $i$ th layer are  $\mathbf{n}_i$ ,  $d_i$ ,  $\theta_i$  and  $\sigma_i$ , respectively. The ambient (i.e., the region above the film) has optical constants  $\mathbf{n}_a$ , and the substrate has optical constants  $\mathbf{n}_s$ .

$$R = \frac{|\delta_2 - \delta_1 - \mathbf{i}(\beta_1 - \beta_2)|^2}{|2 - \delta_1 - \delta_2 + \mathbf{i}(\beta_1 + \beta_2)|^2} = \frac{\Delta\delta^2 + \Delta\beta^2}{(2 - \delta_1 - \delta_2)^2 + (\beta_1 + \beta_2)^2} \quad (1.36)$$

Since the values of  $\delta$  and  $\beta$  are usually small at soft X-ray range (on the order of  $\sim 10^{-3}$ ), we can see that at this situation  $R \approx (\Delta\delta^2 + \Delta\beta^2)/4$ . The reflectivity is sensitive to differences in the index of refraction across an interface and is proportional to  $\Delta\delta^2 + \Delta\beta^2$ . The term  $\Delta\delta^2 + \Delta\beta^2$  can therefore be considered the quantitative measure of the *contrast* between materials.

### Reflection from multiple interfaces, recursive method

Starting with the simpler case, we consider a single layers that contains two interfaces, in which a thin film (medium 1) of thickness  $d$  is now interposed between a vacuum (medium 0) and a substrate (medium 2), as shown in Figure 1.15. In this case the reflected radiation consist not only of rays reflected at the 0-1 interface but also of rays transmited from medium 1 to medium 0 after having been reflected at the 1-2 interface once, twice, etc.

To track all these contributions systematically, the single interface between medium  $i$  and medium  $j(= i + 1)$  will be first studied. The amplitude of wave incident in medium  $i$  and strike the  $i - j$  interface will be partly reflected back into medium  $i$  and partly transmitted to medium  $j$ . Recalling Equation 1.33 and 1.34, the fraction of the amplitude that is reflected back to medium  $i$  is  $r_{ij}$ , which is referred as the Fresnel reflection coefficient, and the fraction of

amplitude that is transmitted to medium  $j$  is  $t_{ij}$ , which is referred as the Fresnel transmission coefficient.

The overall coefficient  $r$  of reflection is then the sum of amplitudes of all the beams (Figure 1.15) emerging from the 0-1 interface, and is given by

$$r = r_{01} + t_{01}r_{12}t_{10}e^{-i2\phi_1} + \dots + t_{01}r_{12}(r_{10}r_{12})^{m-1}t_{10}e^{-i2m\phi_1} \quad (1.37)$$

where  $\phi_i = 2\pi d_i n_i \sin \theta_i / \lambda$ ,  $m$  ( $= 1 \dots \infty$ ) is the number of times the beam has been reflected at the 1-2 interface before emerging to medium 0. Equation 1.37 can be summed to give

$$r = \frac{r_{01} + r_{12}e^{-i\phi_1}}{1 + r_{01}r_{12}e^{-i\phi_1}} \quad (1.38)$$

Now, we consider the reflection from a system consisting of a large number of thin parallel layers, that is, a series of  $N$  layers (and  $N + 1$  interfaces), where the  $i^{th}$  layer has thickness  $d_i$ , interfacial roughness/diffuseness  $\sigma_i$ , and optical constant  $\mathbf{n}_i$  as shown in Figure 1.15. The region above the multilayer stack – the ambient – has optical constants  $\mathbf{n}_a$ , and the region below the film – the substrate – has optical constant  $\mathbf{n}_s$ . Under these circumstances, the net reflection,  $r$  of the  $i^{th}$  layer is given by

$$r = \frac{r_{ij} + r_{jk}e^{-i\phi_i}}{1 + r_{ij}r_{jk}e^{-i\phi_i}} \quad (1.39)$$

where  $\phi_i = 2\pi d_i n_i \sin \theta_i / \lambda$ . The procedure to compute the net reflection coefficients for a multilayer is to apply Equation 1.39 recursively, starting from the bottom most layer, and the reflectance is  $|r|^2$ .

### Reflection coefficient at a rough interface

The scattering of electromagnetic radiation from a non-ideal interface has been an important problem. When the interface between two media is smooth, a plane wave incident on the interface at angle  $\theta$  is specularly reflected, meaning the reflected wave vector lies in the same plane and the scattered angle is also  $\theta$ , i.e along the specular direction. When such a smooth interface becomes rough, some of the wave will be diffusely scattered out of the specular direction. The net result is that the intensity of the specular component gets reduced. The amount of reduction of the specular component should indicate the degree of roughness of the interface. In our case, the interfacial roughness at polymer/polymer interface is the key point we want to study. Here how the interfacial roughness will be presented in the specular reflectivity measurement will be discussed.

In order to account for the loss in specular reflectance due to the interface imperfections

(i.e., interfacial roughness and/or diffuseness), we now consider the case where the change in index across the interface is not abrupt, but can be described by an interface profile function  $p(z)$ . We define  $p(z)$  as the normalized, average value along the  $z$  direction of the dielectric function,  $\epsilon(x)$ , (with  $n = \sqrt{\epsilon}$ )

$$p(z) = \frac{\iint \epsilon(x) dx dy}{(\epsilon_i - \epsilon_j) \iint dx dy}, \quad (1.40)$$

where

$$\epsilon(x) = \begin{cases} \epsilon_i, & z \rightarrow +\infty \\ \epsilon_j, & z \rightarrow -\infty. \end{cases} \quad (1.41)$$

In the case of non-abrupt interfaces, the resultant loss in specular reflectance can be approximated by multiplying the Fresnel reflection coefficients (1.33 and 1.34) by the function  $\tilde{w}(q)$ , the fourier transform of  $w(z) = dp/dz$ . The modified Fresnel reflection coefficients are given by

$$r'_{ij} = r_{ij} \tilde{w}(q) \quad (1.42)$$

where  $q = 4\pi \sin \theta / \lambda$ ,  $\theta$  is the grazing incident angle and  $\lambda$  is the wavelength of light. Note that the loss in specular reflectance depends only on the average variation (over  $x$  and  $y$ ) in index of refraction across the interface. Consequently, the reflectance can be reduced equally by a rough interface, in which the transition between the two materials is abrupt at any point  $(x, y)$ , or a diffused interface, in which the index varies smoothly along the  $z$  direction (or by an interface that can be described as some combination of the two cases.) This means that, it is hard to distinguish the rough interface from the diffuse interface by just using specular reflectivity. Use of non specular scattering (diffuse scattering) can solve this problem. There are several models of the interface profile  $p(z)$ . The appropriate choice of model is dictated largely by the nature of the interface. For instance, the classical diffusion of two materials produces a variation in composition at the interface described by an error function. The profile  $p(z)$  is modeled as an error function, then  $w(z)$  is a Gaussian. In contrast, the mixing at an interface produced by bombardment of the surface by energetic atoms during sputter deposition might be better described by a linear compositional variation, and consequently  $w(z)$  is the rectangle function. In the case of a rough interface, it has been suggested that the distribution of surfaces about the mean position, which in equivalent to  $w(z)$ , is best described by an error function. In this work we are interested in the polymer/polymer interface. From the mean field theory, the interface between two immiscible polymers has a Hyperbolic Tangent function profile, it is commonly replaced using a error function since they are very close and it is easier for the calculation, the error function considering an interface of roughness  $\sigma$ , as shown in Figure 1.16,

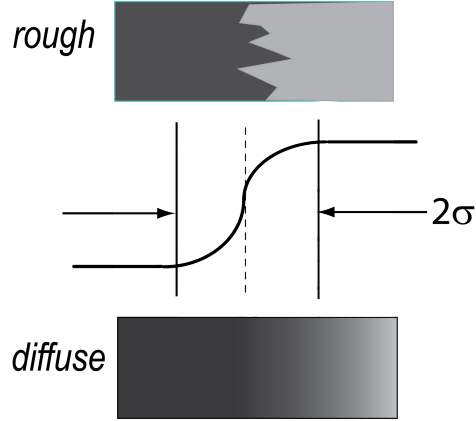


Figure 1.16: Sketch of the interface profile function  $p(z)$ , which describes a rough or diffuse interface.

$$p(z) = \frac{1}{\sqrt{\pi}} \int_{-\infty}^z e^{-t^2/2\sigma^2} dt. \quad (1.43)$$

Then the derivative  $w(z)$  is the Gaussian function,

$$w(z) = \frac{1}{\sqrt{2\pi\sigma^2}} e^{-z^2/2\sigma^2}, \quad (1.44)$$

with a Fourier transform given by

$$\tilde{w}(q) = e^{-\sigma^2 q^2/2}. \quad (1.45)$$

Substitution into 1.42 yields the modified Fresnel reflection coefficient

$$r'_{ij} = r_{ij} e^{-\sigma^2 q^2/2} \quad (1.46)$$

and so the reflectivity becomes

$$R'_{ij} = R_{ij} e^{-\sigma^2 q^2}, \quad (1.47)$$

which indicates a damping of the reflectivity amplitude towards higher  $q$  at higher angles in an reflectivity experiment.

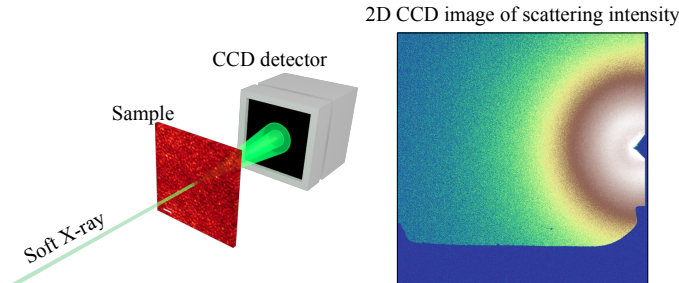


Figure 1.17: Schematic of resonant soft X-ray scattering (R-SoXS).

### Resonant soft X-ray scattering

Characterization of the three-dimensional structure of organic blends with sub-10-nm resolution is a key technical challenge in understanding the relationship of morphology and performance of organic electronics. Due to the lower photon energy of soft X-rays that match the energy of core levels of the constituent atoms and specific spectral transitions, R-SoXS provides greatly enhanced scattering contrast and scattering intensity over conventional hard X-ray small angle scattering and also, in contrast to neutron scattering, does not require deuteration [49, 50]. Furthermore, differences in the optical constants at soft X-ray energies of the constituent materials in the blend provides information regarding domain purity in addition to characterizing the distribution of domain sizes down to a few nanometers. This allows the investigation of polymer/fullerene and polymer/polymer systems and their direct comparison.

The schematic representation and a 2D data image of R-SoXS set up are shown in Figure 1.17. Significantly nuanced and high spatial resolution information than available real space techniques can be achieved with R-SoXS experiments. A detailed overview of X-ray scattering as a technique is available in ref. [51]. The advantage of R-SoXS stems from the ability to achieve much higher scattering intensities in relation to hard X-ray small angle scattering and thus is able to characterize the bulk of very thin films in transmission. The energy dependence of the measured intensity  $I(E)$  in a small angle or long wavelength limit X-ray scattering experiment is given as

$$I(E) \propto F^2(E) \propto E^4 |\Delta\delta(E) + i\Delta\beta(E)|^2 \quad (1.48)$$

Here,  $E$  is the photon energy and  $F$  is the scattering factor. In the soft X-ray region, one is operating in the long wavelength limit and the scattering vector  $q = 4\pi \sin \theta / \lambda$  dependence of  $F$  can be neglected.  $F$  can be described in terms of  $\Delta\delta$  and  $\Delta\beta$ , the differences in the dispersive and absorptive components, respectively, of the complex index of refraction between two phases. Given that hard X-rays have energy much larger than the energy of the deepest core levels of

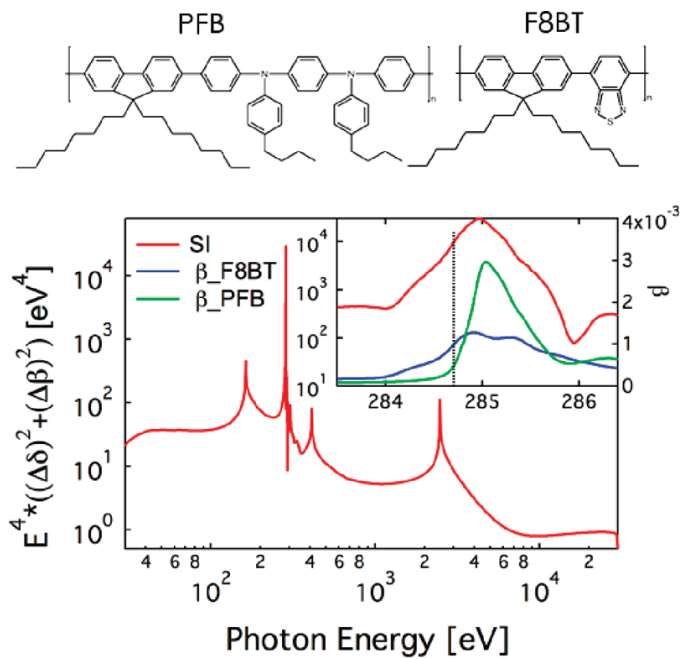


Figure 1.18: Relative scattering intensity (SI) for a PFB/F8BT thin film with pure domains and with a fixed thickness of a fraction of an absorption length ( $< 30$  nm). Inset shows the theoretical scattering intensity for PFB/F8BT and the absorption coefficient  $\beta$  of PFB and F8BT near the carbon absorption edge. The chemical structures of PFB and F8BT are provided above the graph. Figure reproduced from Reference [3].

constituent atoms in most polymers, Equation 1.48 implies that the scattering intensity for hard X-rays is mostly determined by the total electron density contrast between polymeric materials. Near resonance, however, the intensity is modulated strongly by the rapid changes in either dispersion or absorption and can even be dominated by absorption, i.e.,  $\Delta\beta^2$ . Furthermore scattering is vastly enhanced near an absorption edge for soft X-rays as the  $\Delta\delta^2 + \Delta\beta^2$  factor can overcome the  $E^4$  factor. In order to exemplify this strength in the context of materials important to organic device research Figure 1.18 demonstrates the relative scattering intensity of a PFB:F8BT (a polymer donor:acceptor blend) thin film with pure domains and with a fixed thickness that is a fraction of the photon absorption length ( $< 30$  nm). Experiment utilizing the maximum scattering peak near the carbon absorption edge yield orders of magnitude higher scattering intensities than at other energies. Additionally, the relative purity of the domains in the films can be ascertained as the absolute and relative scattering intensity at constant energies scales with  $\Delta\delta^2 + \Delta\beta^2$ , which in turn reflects the purity of the domains. For example, domains with PFB:F8BT composition of 75/25 and 25/75 for the two phases, respectively, will only yield 1/4th the scattering intensity of samples with pure domains.

## Chapter 2

# Accurate determination of the index of refraction of organic thin films near the carbon 1s absorption edge

The complex index of refraction describes the fundamental interaction, i.e. absorption and dispersion, of electromagnetic radiations with materials. These interactions in turn afford and support a plethora of materials characterization tools. In this chapter, we discuss a manuscript of the demonstration of a practical and accurate method to obtain the complex index of refraction,  $\mathbf{n} = 1 - \delta + \mathbf{i}\beta$ , near soft x-ray carbon 1s absorption edge. Combining Near Edge X-ray Absorption Fine Structure (NEXAFS) spectroscopy scaled to the Henke atomic scattering factor database, the use of Doubly Subtractive Kramers-Kronig method, and high precision specular reflectivity measurements from thin films, we were able to determine  $\delta$ , the notoriously difficult to measure index of refraction decrement, with high accuracy and without extra instrumentation for measuring the density or thickness of the film. The accurate optical constants determined by this method will greatly improve the simulation and interpretation of resonant soft X-ray scattering and reflectivity data. The method was demonstrated using thin films of the polymers poly(methyl methacrylate) and polystyrene (PS), respectively, and should be extendable to all organic materials.

This is a manuscript by Hongping Yan, Cheng Wang, Allison R. McCarn, and Harald Ade (in preparation). In this work, I took the PMMA NEXAFS and reflectivity data and did the data analysis for them. I successfully applied and coded the Doubly Subtractive Kramers-Kronig method to calculate  $\delta$  from  $\beta$  directly, avoiding the more complex way involving scattering factors. Cheng Wang initiated this project before he graduated from Ade research group and took the first data for PS thin film. The previous undergraduate student Allison R. McCarn helped with initial reflectivity profile fitting for PS data. The perspective and analysis is significantly

advanced from the work performed by Cheng Wang.

## 2.1 Abstract

A practical and accurate method to obtain the index of refraction, especially the decrement,  $\delta$ , across the carbon 1s absorption edge is demonstrated. The combination of absorption spectra scaled to the Henke atomic scattering factor database, the use of Doubly Subtractive Kramers-Kronig relations, and high precision specular reflectivity measurements from thin films allowed the notoriously difficult to measure  $\delta$  to be determined with high accuracy. No independent knowledge of the film thickness or density is required. High confidence interpolation between relatively sparse measurements of  $\delta$  across an absorption edge has been achieved. Accurate optical constants determined by this method will greatly improve the simulation and interpretation of resonant soft X-ray scattering and reflectivity data. The method was demonstrated using poly(methyl methacrylate) and should be extendable to all organic materials.

## 2.2 Introduction

The complex index of refraction describes the fundamental interaction, i.e. absorption and dispersion, of electromagnetic radiations with materials. These interactions in turn afford and support a plethora of materials characterization tools. Quite often, the quality of the analysis and optimization of experimental procedures or the exploitation of materials in applications ranging from devices to optical elements greatly benefit from an accurate knowledge of the complex index of refraction of the materials investigated. For this reason, optical constants of atoms and materials are catalogued and tabulated over the full range of the electromagnetic spectrum. In the energy range of 50 – 30,000 eV, the optical constants have been compiled by Henke *et al.* in the form of atomic scattering factors  $f(\omega) = f_1(\omega) - \mathbf{i}f_2(\omega)$  [52], which can be related to the scalar complex index of refraction,  $\mathbf{n}(E) = 1 - \delta(E) + \mathbf{i}\beta(E)$ , if the material is disordered. A well-known limitation of the Henke data is the lack of fine spectral details to describe the optical properties near absorption edges. This is true for atoms, but even more so for compounds, for which the molecular bonding has to be taken into account. For organics, materials of primary concern here, the Near Edge X-ray Absorption Fine Structure (NEXAFS) has been compiled for numerous substances by a number of researchers as a supplement and complement to Henke [53, 54, 40, 55, 56, 57, 58]. Despite the remarkable richness of spectral features in these materials shown in NEXAFS spectra, corresponding databases and compilations for the dispersion properties are entirely lacking, other than a few reports on characterizing the dispersion of polyimide and amorphous carbon [59, 60, 61]. In this letter, a facile yet accurate method to determine the index of refraction of a polymer material near the carbon 1s absorp-

tion edge is presented. This method takes advantage of the fact that NEXAFS of polymers can be relatively easily measured and, most importantly, that optical properties, i.e.  $\delta$  and  $\beta$ , are directly fitted in model refinements of thin film reflectivity data. This allows the use of *Doubly* Subtractive Kramers-Kronig (DSKK) method to calculate  $\delta$  from  $\beta$  accurately, with the required values of  $\delta$  for DSKK measured by reflectivity with high accuracy.

The absorption part of the index of refraction,  $\beta$ , can be easily measured in transmission geometry by applying Beer's Law,  $I = I_0 \exp(-4\pi\beta z/\lambda)$ , where  $I_0$  is the incident intensity,  $I$  is the transmitted intensity through the film of a thickness  $z$ , and  $\lambda$  is the wavelength in vacuum. If  $z$  is accurately known,  $\beta$  can be measured directly. The relative absorption can also be measured indirectly by using total electron yield measurements, although such a measurement is only semi-quantitative [39, 62, 55, 63, 64, 65]. In contrast, the real (dispersion) part of the index of refraction,  $\delta$ , is significantly more difficult to measure with high accuracy and high signal/noise ratio, especially for the fine structures near an absorption edge. Interferometry, ellipsometry, and reflectivity have been previously utilized to determine  $\delta$ , and to a lesser extent  $\beta$ , for a limited number of materials [66, 67, 68, 59, 60, 69]. The direct measurement of  $\delta$  is complicated by the short wavelength (relative to visible light), the small value of  $\delta$ , and the relatively strong absorption of soft X-rays. Several types of interferometers have been developed to measure  $\delta$  by measuring the phase shift of transmitted light through a thin film of the material of interest [66, 59, 70, 60]. However, due to the high attenuation of soft X-rays in general, particularly at the absorption edge, it is difficult to make interferometric measurements close to an absorption edge [70]. These measurements also require an independent determination of the mass thickness of the film. An alternative way of measuring  $\delta$  is by fitting the reflectance profile of a solid's surface to the Fresnel reflectivity and to extract values for both  $\delta$  and  $\beta$ . However, sample roughness and high absorption are known to affect the accuracy of these results [65] and the accuracy is also decreased for larger  $\beta/\delta$  values.

The recent development and utilization of Resonant Soft X-ray Reflectivity (R-SoXR) and Resonant Soft X-ray Scattering (R-SoXS) [50, 71, 49, 72, 73, 3, 74, 75, 76, 77] has posed a greater need for precise knowledge about optical constants of materials that are involved. The strength of R-SoXR and R-SoXS is based on the strong elemental and chemical specific oscillations of the complex index of refraction of polymers near the absorption edge. Within the resonant region, both the relative dispersive *and* the absorptive properties of matter are important and can be selectively employed by simply tuning to the corresponding photon energies. Accurate knowledge of the complex index of refraction is a key aspect of utilizing R-SoXR and R-SoXS productively. Detailed knowledge of  $\delta$  for a large range of materials will not only benefit R-SoXR and R-SoXS applications, but should be of wider interest including phase sensitive X-ray imaging methods [78].

The real and imaginary parts of the index of refraction are related through Kramers-Kronig

(KK) relations within a semi-classical description of photon-material interaction[79] (see Supplemental Information for mathematical details). Considering the relatively large error brought about by the slow converging when applying KK relation directly because of the finite energy range that can be attained in practice, we choose to employ the subtractive method first introduced by Bachrach and Brown [80]. Specifically, we use *Doubly* Subtractive Kramers-Kronig (DSKK) method to calculate  $\delta$  from  $\beta$  [81]:

$$\begin{aligned} & \frac{\delta(E)}{(E^2 - E_a^2)(E^2 - E_b^2)} - \frac{\delta(E_a)}{(E^2 - E_a^2)(E_a^2 - E_b^2)} - \frac{\delta(E_b)}{(E_b^2 - E^2)(E_a^2 - E_b^2)} \\ &= -\frac{2}{\pi} P_C \int_{E_{Min}}^{E_{Max}} \frac{E' \beta(E')}{(E'^2 - E^2)(E'^2 - E_a^2)(E'^2 - E_b^2)} dE' \end{aligned} \quad (2.1)$$

In this equation, the infinite integration interval is substituted by the finite range from  $E_{Min}$  to  $E_{Max}$ , and the error introduced by this substitution is minimized by the subtractive method. The required two known values of  $\delta$  at  $E_a$  and  $E_b$  can be measured from reflectivity experiments as discussed later.

To further reduce the error caused by limited energy range, Henke's atomic scattering factors are utilized to expand the energy range of the integration variable. The NEXAFS absorption spectrum in the form of optical density,  $O.D. = -\ln(I/I_0)$ , is measured in transmission. This spectrum is then expended using a "molecular scattering factor" (see below) constructed from Henke's atomic scattering factors to span the 10 eV to 30 KeV range. Once the density of the film,  $\rho$ , is derived from reflectivity measurements,  $\beta$  can be calculated. Accurate values of  $\delta$  can be derived from reflectivity measurement by using energies far from the edge. Using several values of  $\delta$ ,  $\rho$  can be derived with high accuracy by a linear fit (see Supplemental Information for details).

The overall procedure is as follows:

1.  $\beta$  is calculated from NEXAFS and Henke with a multiplicative scaling factor, which is basically the density,  $\rho$ .
2. This preliminary  $\beta$  is used to predict the energy dependence of  $\delta$ , which will then needs to be scaled with the same scaling factor required for the correcting of  $\beta$ , i.e. the density.
3. The actually density and hence the correct scaling factor is obtained by comparing measured  $\delta$  at energies far away from absorption edge (from reflectivity) to predicted  $\delta$ .
4. The corrected  $\beta$  and measured  $\delta$  are then used for the DSJK calculations to calculated  $\delta$  accurately for energies in between the values corresponding to the  $\delta$  utilized.

## 2.3 Results and discussion

The materials utilized to demonstrate the methodology is the ubiquitous polymer poly(methyl methacrylate) (PMMA), which is an amorphous polymer that does not show any anisotropy in the index of refraction and can be readily processed into a thin film. NEXAFS spectra of PMMA were acquired at beamline 5.3.2.2 at the Advanced Light Source (ALS) [41]. PMMA was spun-cast from n-butyl-acetate with a thickness of  $\sim 70$  nm. The film was then floated off in deionized water and picked up with a TEM grid for NEXAFS spectra data acquisition. The absorption spectrum was measured from 270 eV to 400 eV in transmission. The samples for the reflectivity measurements were prepared from the same solution but on freshly cleaned silicon substrates. Reflectivity ( $\theta - 2\theta$  geometry) data were acquired at ALS beamline 6.3.2 in a high vacuum [82], following previously established protocols [71, 72] that includes precautions to avoid radiation damage which cause spectral changes [83]. Simulations and fits of reflectance were performed using the non-commercial program IMD [84] using a least-squared algorithm.

A molecular scattering factor  $f_{2,C_5H_8O_2}$  for PMMA (chemical formula  $C_5H_8O_2$ ) is the sum of Henke's atomic scattering factors of 5 C, 8 H, and 2 O atoms. The calculated  $\beta_S = \beta/(\rho/\rho_0)$ , with  $\rho_0 \equiv 1 \text{ g/cm}^{-3}$ , from experimental NEXAFS spectrum and from  $f_{2,C_5H_8O_2}$  are plotted in Fig. 2.1. The NEXAFS data covers an energy range of 270 eV to 400 eV, while  $f_{2,C_5H_8O_2}$  ranges from 10 eV to 30 KeV. The step at  $\sim 285$  eV, also referred to an absorption edge, is due to the excitation of the core electron into the vacuum continuum. Since no molecular structure is considered in Henke's data, the edge looks like a step function with no details near the edge. The  $\beta_S$  calculated from  $f_{2,C_5H_8O_2}$  was then used to expand the NEXAFS spectra for energies lower than 270 eV and higher than 400 eV (see inset). The real part of the index of refraction,  $\delta$ , then needs to be calculated using KK relations. To determine the density  $\rho$  mentioned above, R-SoXR was performed on a  $\sim 70$  nm PMMA film on silicon substrate. Reflectance measurements with  $\theta$  from  $0^\circ$  to  $20^\circ$  were performed for a set of energies spanning the 270 – 320 eV range (Fig.2.2). Due to the strong energy dependence of the index of refraction, the resultant resonant aspects can be readily observed in the reflectance profiles. Below 285 eV, the reflectance profiles have strong Kiessig fringes at all angles. The onset of the first dip in the reflectance profile relates to the critical angle,  $\theta_c$ , of the vacuum/PMMA interface, with  $\theta_c \approx \sqrt{2\delta}$ . For energies above the absorption edge, the reflectance profiles appear less modulated, especially at low grazing angles. This is due to the high absorption of the polymer at these energies and the long optical path the X-rays need to travel at small grazing angles. The reflected intensity corresponding to the polymer/substrate interface is reduced, leading to the small Kiessig fringe amplitudes at small angles. At higher angle, the optical path is shorter and less light is absorbed, which leads to better visibility of the interference fringes.

The experimental reflectance profiles are fitted through model refinements of a single layer by

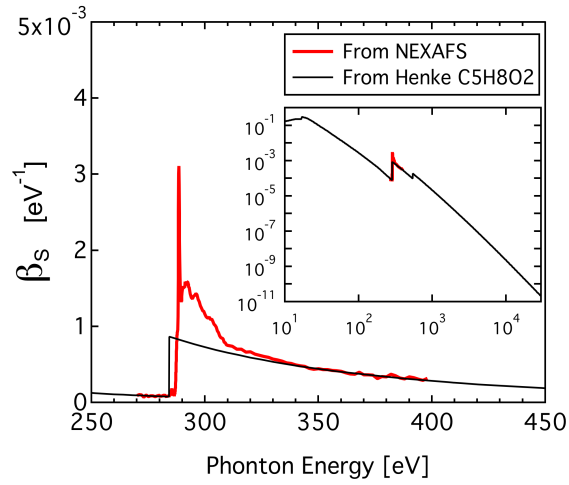


Figure 2.1: Absorption spectra  $\beta$  calculated from transmission NEXAFS and Henke's atomic scattering factors.

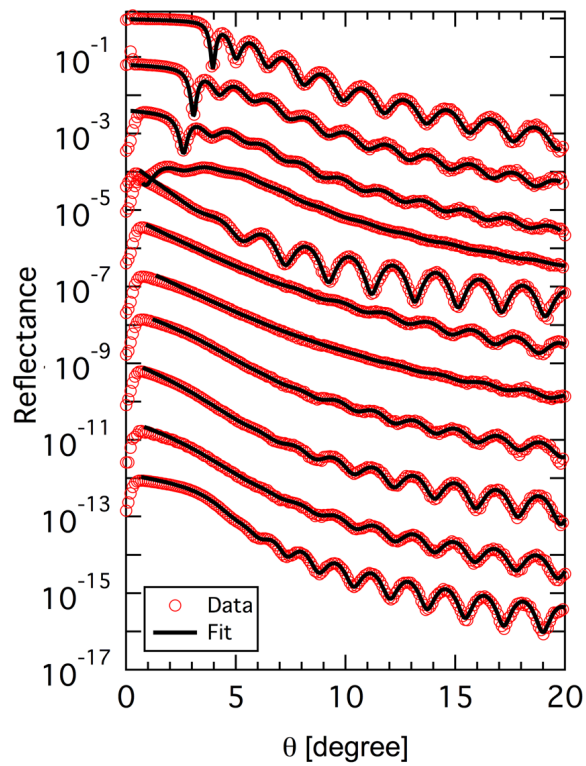


Figure 2.2: Overplot of R-SoXR data and fits for PMMA single layer, showing the quality of fits at energies, from top to bottom, 270.3, 282.3, 284.3, 286.3, 287.9, 288.3, 288.5, 288.9, 289.3, 294.3, and 310.3 eV.

means of a least-square algorithm. It is most advantageous to start by fitting the reflectance data acquired at photon energies far below the absorption edge, e.g. 270.3 eV, where the sensitivity to  $\delta$  is high. Parameters that describe the property of the film, such as the film thickness, roughness of the surface, and roughness at the polymer/substrate interface can be extracted with high accuracy. Since all data were obtained from the same sample, these structural parameters can then be used for fitting the reflectance profiles at all other energies. Therefore, only two variables,  $\delta$  and  $\beta$ , are left as free parameters to be determined by a least-square fit.

With the values of  $\delta$  obtained, the density of the PMMA thin film is determined by comparing the values derived from the reflectivity measurement (see Supplemental Information). From this linear fit, the density of the film is determined to be 1.20 g/cm<sup>3</sup> (according to Equation 13 in Supplemental information), which is very close to the tabulated values 1.18 g/cm<sup>3</sup>. The value of the density is then subsequently used to calculate the accurate  $\beta$  with  $\beta = (\rho/\rho_0)\beta_S$ , followed by the application of DSJK method for the calculation of  $\delta$ .  $\beta$  and  $\delta$  are plotted in Fig. 2.3, along with the experimental results from fits of the reflectance measurements at key energies. Error bars in the experimental  $\delta$  and  $\beta$  are reflecting the data scatter from fitting results obtained at multiple sample locations, which capture both the error of the fits themselves and the variations that come from the sample. Below the absorption edge, in the energy range of 270.3 – 287.9 eV, the values of  $\delta$  and  $\beta$  from the experiment and from the Kramers-Kronig calculations match well, and the experimental scatter for  $\delta$  is small. For energies between 290 and 310 eV, systematic errors are observed. The present reflectivity fits slightly overestimate  $\beta$  and underestimated  $\delta$ . This systematic error can be clearly seen by comparing the fits and data at the onset of the visibility of the Kiessig fringes in Fig. 2.2. The data shows the onset of fringes at smaller angles than the fit, indicating that the model fits overestimate the absorption in the actual films. For comparison,  $\delta$  and  $\beta$  as derived from Henke’s database are also shown in Fig. 2.3. The good agreement of experimental results and the calculation at large number of energy points especially the near-edge region shows the accuracy of the calculation and the validity of calculated value through the whole energy range. The optical constants of another sample polymer, polystyrene (PS), were also calculated and compared to experimentally derived values with good overall correspondence, indicating that the method is generally applicable. For details see Supplemental Information.

## 2.4 Conclusion

In conclusion, the indexes of refraction of a PMMA and a PS thin film were measured accurately for soft X-ray energies across the carbon 1s absorption edge using the inherent interferometric aspects of a reflectivity measurement from a thin film. Such a measurement is simpler and more straightforward to accomplish than a number of prior methods utilized to measure  $\delta$ . The values

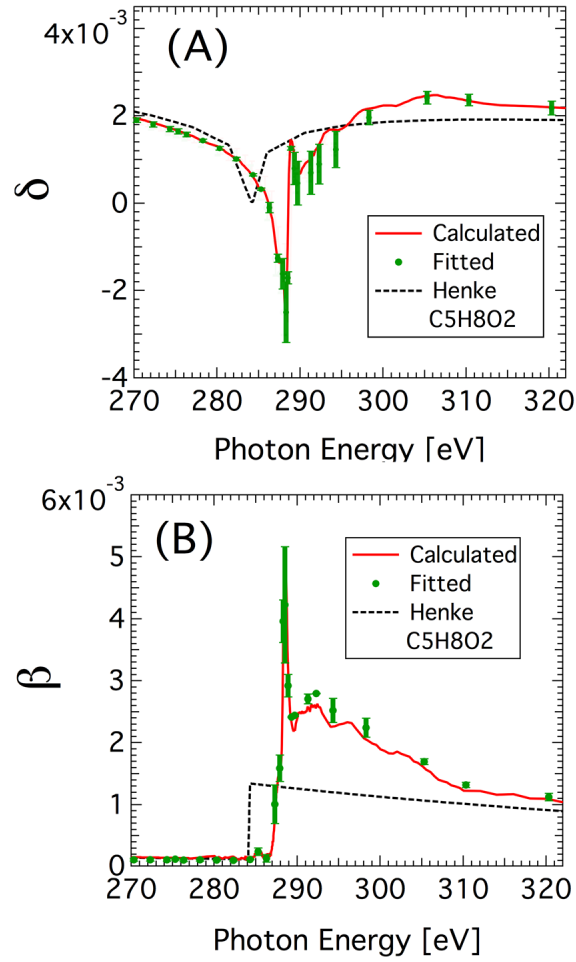


Figure 2.3: Fitting results (dot) of optical constants, dispersion part,  $\delta$  (A), and absorption part  $\beta$  (B), for PMMA and calculation (solid line) using Kramers-Kronig relation. The corresponding values as derived from Henke's database are shown for comparison.

of  $\delta$  calculated with the DSKK method from measured  $\beta$  and a few calibrated  $\delta$ 's, and hence indirectly the accuracy of the NEXAFS spectrum, were verified at several energies by comparing with the experimental values of  $\delta$  and  $\beta$  obtained from fitting the reflectance data using a least square fitting algorithm. The use of DSKK method is straightforward, yet decreases the error due to the limited energy range of  $\beta$ . By utilizing the presented method that combines NEXAFS measurements, Henke's atomic scattering factor database, reflectivity measurements, and Kramers-Kronig calculations, the index of refraction of polymer thin films can be determined with good accuracy in a self-consistent fashion without the need of independent mass thickness measurements. The dispersive properties of organic materials can now be tabulated in analogy to the databases already existing for  $\beta$ . The generality of this method should be applicable to a broad range of soft/hard materials.

## 2.5 Acknowledgements

The authors are grateful for fruitful discussions with and help from Eric Gullikson (ALS 6.3.2, CXRO) and David Kilcoyne (ALS 5.3.2.2). Work at NCSU is supported by the U. S. Department of Energy (DE-FG02-98ER45737). Data acquired at beamlines 5.3.2.2 and 6.3.2 at the ALS, which is supported by the Director of the Office of Science, Department of Energy, under Contract No. DE-AC02-05CH11231.

## 2.6 Supplemental information

### 2.6.1 Doubly Subtractive Kramers-Kronig relation

The real and imaginary parts of the index of refraction are related through Kramers-Kronig relations (see Appendix A):

$$\delta(E) = -\frac{2}{\pi} \mathcal{P}_c \int_0^\infty \frac{E' \beta(E')}{E'^2 - E^2} dE' \quad (2.2)$$

$$\beta(E) = -\frac{2E}{h\pi} \mathcal{P}_c \int_0^\infty \frac{\delta(E')}{E'^2 - E^2} dE' \quad (2.3)$$

in which  $\mathcal{P}_c$  denotes the Cauchy Principle Value and  $h$  is the Plank constant.

If the values of  $\delta$  are known at two energies from direct measurements as  $\delta(E_a)$  and  $\delta(E_b)$ , according to Equation 2.2, one has

$$\delta(E_a) = -\frac{2}{\pi} \mathcal{P}_c \int_0^\infty \frac{E' \beta(E')}{E'^2 - E_a^2} dE' \quad (2.4)$$

and

$$\delta(E_b) = -\frac{2}{\pi} \mathcal{P}_c \int_0^\infty \frac{E' \beta(E')}{E'^2 - E_b^2} dE' \quad (2.5)$$

From Equations 2.2, 2.4, and 2.5, the Doubly Subtractive Kramers-Kronig relation can be derived as following:

$$\begin{aligned} & \frac{\delta(E)}{(E^2 - E_a^2)(E^2 - E_b^2)} - \frac{\delta(E_a)}{(E^2 - E_a^2)(E_a^2 - E_b^2)} - \frac{\delta(E_b)}{(E_b^2 - E^2)(E_a^2 - E_b^2)} \\ &= -\frac{2}{\pi} \mathcal{P}_c \int_{E_{Min}}^{E_{Max}} \frac{E' \beta(E')}{(E'^2 - E^2)(E'^2 - E_a^2)(E'^2 - E_b^2)} dE' \end{aligned} \quad (2.6)$$

To further reduce the error, Henke's atomic scattering factors are utilized to expand the energy range of the integration variable [52]. The NEXAFS absorption spectrum in the form of optical density,  $O.D. = -\ln(I/I_0)$  with  $I$  the incident intensity and  $I_0$  the transmitted intensity, is measured in transmission with small energy step size around the absorption edge. According to Beer's Law  $I = I_0 \exp(-4\pi\beta z/\lambda)$ , where  $\lambda(= hc/E)$  is the wave length of the light in vacuum, the relation between  $O.D.$  and  $\beta$  can be written as

$$\beta = \frac{hc}{4\pi z E} O.D. \quad (2.7)$$

where  $c$  is the speed of light in vacuum and  $z$  is the thickness of the film used for NEXAFS experiments. To expand the energy range of  $\beta$  using Henke's atomic scattering factor database, the "molecular scattering factor" in the energy range of 10 eV to 30 KeV for a repeating unit of the polymer,  $f_{2,monomer}$ , is constructed by summing up the atomic scattering factors of each atom:

$$f_{2,monomer} = \sum_j N_j f_{2,j} \quad (2.8)$$

where  $N_j$  is the number of the  $j^{th}$  type of atoms in the monomer. Considering the relation between  $\beta$  and  $f_2$  [2]

$$\beta = \frac{N_A r_e h^2 c^2 \rho}{2\pi M_W E^2} f_{2,monomer} \quad (2.9)$$

the NEXAFS spectrum can be scaled to  $f_{2,monomer}$  according to the relation

$$f_{2,monomer} = \frac{M_W E}{2N_A r_e h c \rho z} O.D. \quad (2.10)$$

with a scale factor  $M_W/(2N_A r_e h c \rho z)$  obtained. This ends up with a  $f_{2,monomer}$  spanning 10 eV to 30 KeV with fine structures around carbon 1s absorption energies.  $\beta$  can then be calculated according to Equation 2.9, with  $\rho$  kept unknown until being derived with further assistance of

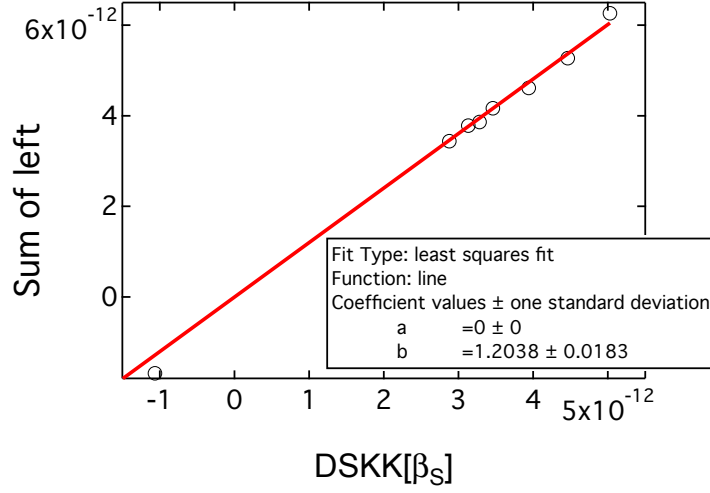


Figure 2.4: The data points (circles) and linear fit (line) to derive the film density.

reflectivity data.

### 2.6.2 Determination of film density

To determine the film density so that the optical constants can be derived more accurately, a simple linear fit was performed. Considering  $\beta = (\rho/\rho_0)\beta_S$  ( $\rho_0 \equiv 1 \text{ g/cm}^3$ ), where  $\beta_S$  denotes the  $\beta$  with assumed density  $\rho = 1 \text{ g/cm}^3$ . Equation 2.6 can be rewritten as

$$\frac{\delta(E_j)}{(E_j^2 - E_a^2)(E_j^2 - E_b^2)} - \frac{\delta(E_a)}{(E_j^2 - E_a^2)(E_a^2 - E_b^2)} - \frac{\delta(E_b)}{(E_b^2 - E_j^2)(E_a^2 - E_b^2)} = (\rho/\rho_0) \cdot DSKK[\beta_S(E)]|_{E=E_j} \quad (2.11)$$

where  $E_j$  is the energy at which the value of  $\delta$  is measured, and

$$DSKK[\beta_S(E)]|_{E=E_j} = -\frac{2}{\pi} \mathcal{P}_c \int_{E_{Min}}^{E_{Max}} \frac{E' \beta_S(E')}{(E'^2 - E_j^2)(E'^2 - E_a^2)(E'^2 - E_b^2)} dE' \quad (2.12)$$

According to Equation 2.11, the right-sided integral are calculated for  $\beta$ 's at several energies far away from the absorption edge. The corresponding left-sided values are calculated and a linear fit is performed to derive the unknown  $\rho$ . The data points and the fit are shown in Figure 2.4. The Density of PMMA film is determined to be  $1.20 \text{ g/cm}^3$  according to the fitted slope, comparing to the tabulated value of  $1.18 \text{ g/cm}^3$ .

Following the identical protocol, as another example of determining  $\delta$  from  $\beta$  with high accuracy, polystyrene (PS) thin film is used as the model layer here. The results are summarized in Figure 2.5, with a film density  $1.03 \text{ g/cm}^3$  derived, comparing to tabulated value  $1.05 \text{ g/cm}^3$ .

### 2.6.3 Experimental details

NEXAFS spectra of PS and PMMA were acquired at beamline 5.3.2 at the Advanced Light Source (ALS) [41, 82]. PS (Polymer Source,  $M_W=138 \text{ kg/mol}$ ,  $M_W/M_n=1.05$ ,  $T_g \sim 100 \text{ }^\circ\text{C}$ ) was spun-cast from toluene (Sigma-Aldrich) onto the silicon substrate with a thickness of  $\sim 80 \text{ nm}$ . PMMA (Sigma-Aldrich,  $M_W=120 \text{ kg/mol}$ ,  $M_W/M_n=1.05$ ,  $T_g \sim 125 \text{ }^\circ\text{C}$ ) was spun-cast from n-butyl-acetate with a thickness of  $\sim 75 \text{ nm}$ . The film was then floated off in deionized water and picked up with a TEM grid for NEXAFS spectra data acquisition. The absorption spectrum was measured from 270 eV to 400 eV in transmission.

The samples for the reflectivity measurements were prepared on silicon (100) wafers (Wafer World), which were cleaved into  $2.5 \text{ cm} \times 2.5 \text{ cm}$  substrates, cleaned in Baker Clean JTB-111 (J.T. Baker), and washed with deionized (DI) water. They were subsequently etched with 10% (volume/volume fraction) hydrofluoric acid and rinsed with DI water to produce a hydrogen passivated silicon surface (Si-H).  $\sim 80 \text{ nm}$  thick PS layer was spun-cast from toluene (Sigma-Aldrich) on top of the substrates, annealed in vacuum at  $T = 135 \text{ }^\circ\text{C}$  for 24 hours and quenched to room temperature through simple removal from the oven. PMMA was spun-cast from n-butyl-acetate with a thickness of  $\sim 75 \text{ nm}$ , annealed and quenched following the same protocol as used for PS. After quenching, the films were characterized using visible light microscopy and AFM to ensure against dewetting. Layer thicknesses were measured with a Rudolph AutoEL-3 ellipsometer. Reflectivity ( $\theta - 2\theta$  geometry) data were acquired at ALS beamline 6.3.2 [82] in a high vacuum, following previously established protocols [71]. Simulations and fits of reflectance were performed using the non-commercial program IMD [84] using a least-squared algorithm. The ellipsometer-derived thickness was used as starting value when fitting the reflectivity data.

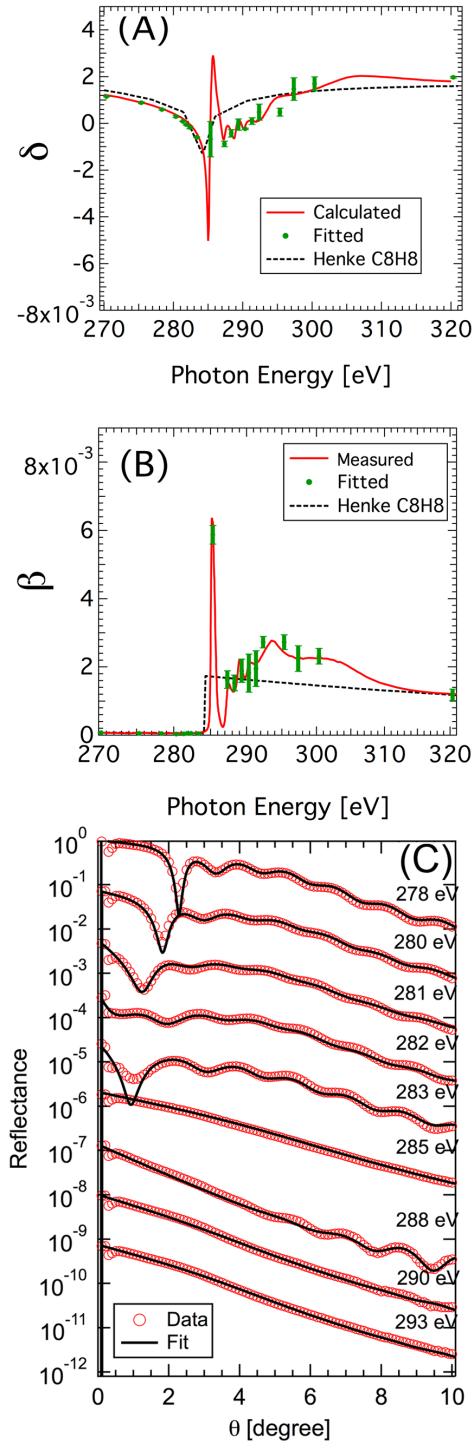


Figure 2.5: Comparison of fitted and calculated  $\delta$  (A),  $\beta$  (B) of PS, and R-SoXR data (circle) and fits (solid line) for 80 nm PS thin film for selected photon energies, from top to the bottom, 278 eV, 280 eV, 281 eV, 282 eV, 283 eV, 285 eV, 288 eV, 290 eV, 293 eV.

## Chapter 3

# Interfaces in organic devices studied with resonant soft X-ray reflectivity

Interface study has been becoming more and more important for organic devices, such as polymer light emitting diodes (PLEDs), organic solar cells (OSCs) and organic thin-film transistors (OTFTs). Enclosed in chapter are our successful measurements of surface and interface roughnesses of bilayer polymer thin films with Resonant Soft X-ray Reflectivity (R-SoXR). These bilayer systems cover all the three fields of OLED, OSC, and OTFT. Importantly, we present for the first time the buried interface measurement of bilayer system of dielectric on top of P(NDI2OD-T2), which is a high electron-mobility polymer utilized in TFTs. What's also exciting is that we have successfully extended the application of R-SoXR method from x-ray energy around carbon to fluorine absorption edge, which will enhance the ability of soft x-ray in scientific research and benefit a lot of related fields.

This work has been published on *Journal of Applied Physics* with DOI: 10.1063/1.3661991. This is an article by [Hongping Yan](#), Cheng Wang, Andres Garcia, Sufal Swaraj, Ziran Gu, Christopher R. McNeill, Torben Schuettfort, Karen E. Sohn, Edward J. Kramer, Guillermo C. Bazan, Thuc-Quyen Nguyen, and Harald Ade. In this work, Cheng Wang took the reflectivity data for CPE/MEH-PPV bilayers study (see following article contents for more details) and completed the analysis of the bilayer data as well. Sufal Swaraj helped taking the initial data for the PFB/F8BT bilayer data. Other collaborators provided the samples and device characterizations.

My contributions in this work include 1) developing a new data taking protocol to take high quality reflectivity data for PFB/F8BT bilayer study; 2) completing the nontrivial multilayer reflectivity data analysis to identify the layer thickness and roughness semi-quantitatively; 3) taking the reflectivity data for P(NDI2OD-T2) bilayer system with extending R-SoXR method to fluorine (F) K absorption edge energies; and 4) reference NEXAFS data taking of the poly-

mers and the optical constants calculations of them.

Our previous protocol of taking R-SoXR data involved the use of a photodiode as the detector. The photodiode has the advantage of quick linear response up to high intensity even for a direct beam, which makes it suitable as a detector for reflectivity experiments especially when the sample angle ( $\theta$ ) is low. However, the background of a photodiode is relatively large comparing to the flux signal due to the reflected beam at higher angles ( $\theta > 40^\circ$  or  $q > 1.82 \text{ nm}^{-1}$ ) depending on the condition of the samples, because the reflectivity intensity is proportional to  $q^{-4}$ . This does not only reduce the quality of the data but also make the normalization very difficult because the signal is so low that it is too sensitive to the subtraction of the background. For a better signal-noise ratio at angles higher than  $40^\circ$  and simpler data processing, a channeltron is used as the detector instead of the photodiode. The channeltron has the capability of single-photon count with zero background counts in dark. With the combination of the use of a small pin-hole to cut down the beam intensity at lower angles to avoid saturation of the channeltron at high intensity when sample angle is lower than several degrees, the channeltron detector can give high quality data over the whole  $0 - 60^\circ$  range or higher sample  $\theta$ . This does not only improve the overall data for better and simpler data reduction, but also enhances the fit quality because the use of small pin-hole increases the angular resolution at low- $\theta$  region, which the optical constants fit is sensitive to. Furthermore, because the roughness of the interface adds a damping to the reflectivity profile, with these higher quality data of bigger range, it is possible to fit interfacial widths below 1 nm accurately.

One of the critical points to measure the interfacial widths of buried interfaces is to find a suitable energy where the contrast between two materials is high enough but the absorption of these materials is still low so that sufficient intensity can get through the film. However, for the bilayer of CYTOP/P(NDI2OD-T2) investigated in this work, the contrast is not high enough within carbon K absorption energy region, as it can be seen in the data presented later in this chapter. I have been motivated by this to use energies around fluorine K absorption edge, noticing that the majority of the non-carbon atoms in CYTOP is fluorine. It worked very well at 688 eV to measure the buried interface, demonstrating the successful extension of R-SoXR method to absorption edges other than carbon.

### 3.1 Abstract

Interfaces between donor and acceptor semiconducting polymers are critical to the performance of polymer light-emitting diodes and organic solar cells. Similarly, interfaces between a conjugated polymer and a dielectric play a critical role in organic thin-film transistors. Often, these interfaces are difficult to characterize with conventional methods. Resonant soft x-ray reflectivity (R-SoXR) is a unique and relatively simple method to investigate such interfaces. R-SoXR

capabilities are exemplified by presenting or discussing results from systems spanning all three device categories. We also demonstrate that the interfacial widths between active layers can be controlled by annealing at elevated temperature, pre-annealing of the bottom layer, or casting from different solvent mixtures. The extension of R-SoXR to the fluorine K absorption edge near 698 eV is also demonstrated.

## 3.2 Introduction

Conjugated semiconducting polymers and their applications have been attracting considerable attention in recent years. They are materials that are reshaping technologies, such as light emitting diodes (LEDs), solar cells (SCs), and thin-film transistors (TFTs), because of a tremendous interest in low-cost flexible electronics<sup>1</sup> and photovoltaic solar energy conversion [85, 86]. Many of the organic semi-conducting materials can be processed from solutions, thus offering the potential for cost advantages. In all three classes of devices, the interface between constituent polymers is critically important, and a better understanding of the interfacial structure is required to better control the device performance.

In polymer LEDs (PLEDs), two different polymers are often used that allow greater flexibility in optimizing the injection and transport of electrons and holes. Laterally phase separated blends can be used for PLEDs, but polymer multilayers are frequently employed [87, 18, 88, 89, 90]. The fabrication of multilayer PLEDs is tremendously simplified with the use of charged conjugated polyelectrolytes (CPE). These are polar electron transport materials that can be cast from a polar solvent onto non-polar hole transport materials, such as poly[2-methoxy-5-(20-ethylhexyloxy)-p-phenylene vinylene] (MEH-PPV). Various devices have been made using CPEs and MEH-PPV, but interfaces in CPE-based structures have not yet been characterized extensively.

A related but essentially reverse photo-physics to that of PLEDs occurs in polymer-based SCs [91]. A bound electron-hole pair, known as an exciton with a binding energy of  $\sim 0.4$  eV, is created when a photon is absorbed. The exciton then diffuses and is required to reach an interface between two materials with different electron affinity and ionization potential. Exciton dissociation occurs via electron transfer from the donor to the acceptor material (or via hole transfer from the acceptor to the donor), and photocurrent is generated when these charges are separated and reach the device electrodes. Although many studies have been done with polymer/fullerene blends as active material [92, 93] and the efficiency of fullerene-based devices is indeed higher than polymer/polymer devices [94], the latter is still of interest, due to its higher open-circuit voltage and potential to create well-ordered nanostructures through the use of block-copolymers. Polymer/polymer devices in bilayer geometry also offer the advantage that the influence of the interfacial structure on device performance can be most readily measured

and assessed [74].

In TFTs, charge transport occurs essentially along a 1 nm deep accumulation layer in the semiconducting polymer at the interface with a dielectric layer [95]. Polymer dielectrics are being increasingly used in polymer TFTs, as they lead to less electron trapping [96] and allow for top gate devices to be fabricated via sequential solution deposition from orthogonal solvents. Besides molecular interactions, which determine the packing geometry of the semiconducting polymer, the charge transport performance is highly influenced by the microstructure of the film [97]. The surface and interfacial roughness is an important parameter when characterizing the microstructure. For example, the mobility of crystalline organic semiconductors is highly sensitive to the roughness of the surface of inorganic dielectric layers [98, 99, 100].

Despite the desirability for more in-depth structural knowledge, relatively little is known about the interfacial structure of organic devices and how it affects optoelectronic properties. Interfacial width, the root-mean-square (RMS) deviation of the physical roughness and chemical composition gradient normal to the interface, can be characterized by well-established techniques, such as neutron reflectivity (NR)[101, 102] and x-ray reflectivity (XR). XR has been used extensively to investigate polymer thin films and their interfaces, including some organic devices [103, 104]. Most of the time, however, the electron density contrast for polymers in conventional XR is rather small [105, 106]. Neutron reflectivity has superior sensitivity to carbonaceous soft-condensed matter if one of the components is deuterated. This may be impractical or too expensive for many of the polymers used in organic devices, with materials costing up to \$4,000 per gram, even if not deuterated. Consequently, only a very limited number of NR studies on optoelectronic relevant polymers have been carried out [102, 107, 108]. For fullerene-based devices, sufficient natural contrast exists for neutron scattering [109, 110]. As an alternative, resonant soft x-ray reflectivity (R-SoXR) is a promising tool to characterize interfacial properties of organic thin films, due to high intrinsic material contrast that exists for most of the organic materials at soft x-ray energies [111, 112, 72, 71, 113]. Here, we present the use of R-SoXR to characterize the interfaces between active materials in all three categories of organic devices, i.e., polymer LEDs (PLED), polymer solar cells (PSCs), and polymer TFTs (PTFTs).

The assumption that the direct casting of the CPE layer on top of the MEH-PPV does not disrupt the MEH-PPV layer and that sharp interfaces are required for good performance of organic LEDs (OLEDs) was underlying the synthesis, development, and use of these CPE materials. Initial transmission electron microscopy (TEM) studies [114] have indeed shown that only materials of opposite polarity cast from solvents of matching polarity yield sharp interfaces and well-developed bilayer structures. Quantitative measurements of the interfacial width are, however, difficult with TEM, and the interface could only be characterized as being  $\sim 2$  nm in width. Recent high precision R-SoXR studies on model bilayers have shown that the differential

casting of CPEs on top of MEH-PPV yields sharp and smooth interfaces with an RMS width of 0.8 nm [115]. We extend these studies and show how the interfacial width can be controlled in bilayers by either the use of solvent mixtures for casting or a number of annealing protocols.

In addition, a detailed analysis of an almost complete OLED device consisting of a multilayer of PFNBr/ MEH-PPV/poly(3,4 ethylene dioxythiophene): poly(styrene- sulfonate)/indium tin oxide/glass (PEDOT:PSS/ITO/glass) substrate's structure is presented. The interfacial widths of all five interfaces in this device (without the top electrode) are quantitatively determined or estimated from R-SoXR data. A simplified and incomplete analysis of this multilayer has been reported previously [106]. It is demonstrated that the interfacial widths between the active CPE/MEH-PPV layers in the actual device are slightly larger than in the model bilayers. They are sufficiently similar to each other, though, that the more simple bilayer structures can be used as a proxy to investigate the influence of fabrication methods and procedures on the interfacial width between active layers.

The use of R-SoXR to study planar photovoltaic heterojunctions based on the polyfluorene co-polymers poly(9,9-dioctylfluorene-co-bis(N,N' - (4-butylphenyl))bis(N,N' - phenyl-1,4-phenylene)diamine) (PFB) and poly(9,9-dioctyl- fluorene-co-benzothiadiazole) (F8BT) is also discussed. By obtaining quantitative information of morphology, photoluminescence quenching, and device performance, it is possible to examine the competing effects of exciton and charge dissociation and to show that sharp, non-equilibrium interfaces produce the best device performance [74].

The first R-SoXR results on TFT bilayers are presented. The devices consist of a dielectric top layer of either polystyrene (PS), poly (methyl methacrylate) (PMMA), or CYTOP CTL-809M (Asahi Glass) and a bottom layer of poly{[N,N'- bis(2-octyldodecyl)-naphthalene-1,4,5,8-bis(dicarboximide)-2,6- diyl]-alt-5-5' -(2,2' -bithiophene)} (P(NDI2OD-T2), Polyera Corporation). P(NDI2OD-T2) is a newly developed high- mobility electron transporting polymer [116, 117]. Furthermore, the R-SoXR method can be successfully extended from the carbon 1s absorption edge to the fluorine 1s absorption edge.

### 3.3 Experimental methods

#### 3.3.1 PFNBr/MEH-PPV bilayers and multilayer

MEH-PPV and PFNBr were synthesized following previously published protocols [89]. PEDOT:PSS (Baytron P) was used as received. The multilayer device was prepared on an ITO coated glass substrate (Thin Film Devices), onto which a  $\sim 6$  nm thick PEDOT:PSS film was spun cast. The multilayer structure was completed by casting an  $\sim 80$  nm MEH-PPV layer from toluene on the PEDOT:PSS, followed by spin casting a  $\sim 20$  nm PFNBr layer from methanol.

The nominal layer thicknesses are derived by spin casting single layers from the same solution and determining their thicknesses with an ellipsometer. Deposition of a metal cathode on top would complete this structure into an actual device.

PFNBr/MEH-PPV bilayers were prepared on SiO<sub>2</sub> substrates by casting an  $\sim 80$  nm MEH-PPV layer first from toluene on the SiO<sub>2</sub> followed by spin casting a  $\sim 20$  nm PFNBr layer from methanol or a tetrahydrofuran (THF):methanol solution. Methanol is a poor solvent for MEH-PPV, so the MEH-PPV layer surface should not be disturbed. In an attempt to disturb the smooth MEH-PPV surface during casting, a mixed solution with THF and methanol was used, because THF can dissolve both PFNBr (top layer) and MEH-PPV (bottom layer). Three different concentrations of THF were used (1%, 10%, 20% THF). To assess the effect of annealing, bilayers were annealed for 20 min at 150 °C and 230 °C, respectively.

Differences in annealing protocols were as follows from a different batch of materials: (1) direct casting of both layers without annealing; (2) casting and annealing at 230 °C of bottom MEH-PPV with subsequent casting of the PFNBr and no further annealing; and (3) differential casting of a bilayer with subsequent annealing at 230 °C. A complementary set of samples from this batch of materials was made as complete devices.

### 3.3.2 PFB/F8BT bilayers

Materials and sample preparation: PFB and F8BT were supplied by Cambridge Display Technology Ltd. and used as received. PFB had a molecular weight ( $M_W$ ) and polydispersity (PDI) of 168 kg mol<sup>-1</sup> and 2.8, respectively, while the  $M_W$  of F8BT was 190 kg mol<sup>-1</sup> and PDI 1.9. Films were spin-coated from p-xylene with a thickness of typically 60 nm. PFB/F8BT bilayers were prepared by first spin casting F8BT onto the silicon wafer, and PFB was then spun cast onto a cleaned and oxygen plasma-treated glass slide and floated off onto de-ionized water. The F8BT-coated substrate was then lowered and laminated onto the air-side of the floating PFB film and picked up. Substrates were then placed overnight to dry in a vacuum chamber with pressure of less than 10<sup>-6</sup> mbar. Samples were annealed by placing on a hotplate in the glove-box at the desired temperature for 10 min, and subsequently quenched to room temperature.

### 3.3.3 Dielectric/P(NDI2OD-T2) bilayers

P(NDI2OD-T2) was purchased from the Polyera Corporation, USA, and specified with a number average molecular weight ( $M_n$ ) and polydispersity index (PDI) of 25.4 kg mol<sup>-1</sup> and 4.03, respectively. The gate dielectrics poly(methyl methacrylate) (PMMA) and polystyrene (PS) with a weight average molecular weight ( $M_W$ ) of 1000 kg mol<sup>-1</sup> and 120 kg mol<sup>-1</sup>, respectively, were purchased from Sigma-Aldrich. CYTOP CTL-809M was used as received from Asahi Glass.

P(NDI2OD-T2) thin films were prepared by spin casting from a 20 g/L dichlorobenzene solution onto electron-conducting (antimony-doped) silicon wafers. The film thickness was determined using a profilometer (Veeco Dektak 3) to be around 55 nm. The P(NDI2OD-T2) films were subsequently annealed at 110 °C for 20 min in nitrogen atmosphere and quickly cooled to room temperature. Deposition of the gate material was also performed by spin casting from orthogonal solvents (n-butyl-acetate for PS and PMMA) using the same spin-conditions, which yielded a film thickness of 75 nm measured with the profilometer on a pristine silicon wafer. After deposition of the gate material, no further heat treatment was performed on the bilayers.

### 3.3.4 Data acquisition

Near edge x-ray absorption fine structure (NEXAFS) spectra of reference samples were acquired at beamline 5.3.2 at the Advanced Light Source (ALS) [41]. These spectra are used to derive optical constants of the materials to predict contrast and provide initial optical constants for the fits and simulation.

R-SoXR data were acquired at beamline 6.3.2 at the ALS in a high vacuum ( $\sim 10^{-7}$  Torr) [82], following previously established protocols [72]. To detect and avoid radiation damage, which can cause mass loss and spectral change [83, 118], some scans were repeated and the sample was occasionally translated to expose a fresh sample area. Simulations and fits were performed using the non-commercial program IMD [84].

The R-SoXR data and fits sometimes show some discrepancy in the low q-region that has been traced to spectral contamination. The q range used to extract parameters from the fits is therefore sometimes restricted to  $\sim 0.2 - 2.5 \text{ nm}^{-1}$  [74].

## 3.4 Results and discussion

### 3.4.1 CPE/MEH-PPV bilayers

In order to employ simple sample preparation procedures and use the least complex R-SoXR analysis, a smooth silicon substrate was used instead of a relatively rough PEDOT:PSS/ITO/glass substrate for the majority of structures investigated. PFNBr/MEH-PPV/Si model bilayers were prepared by sequential casting from non-polar and polar solvents using established protocols. Methods to control the interfacial width were investigated by preparing PFNBr/MEH-PPV/Si bilayers by casting the PFNBr with 100% methanol or a THF:methanol mixture directly onto the MEH-PPV. In addition, PFNBr/MEH-PPV bilayers with PFNBr spun with 100% methanol were annealed at 150 °C and 230 °C for 20 min. MEH-PPV and PFNBr were also cast sequentially on PEDOT:PSS/ITO/glass substrates to simulate a complete device.

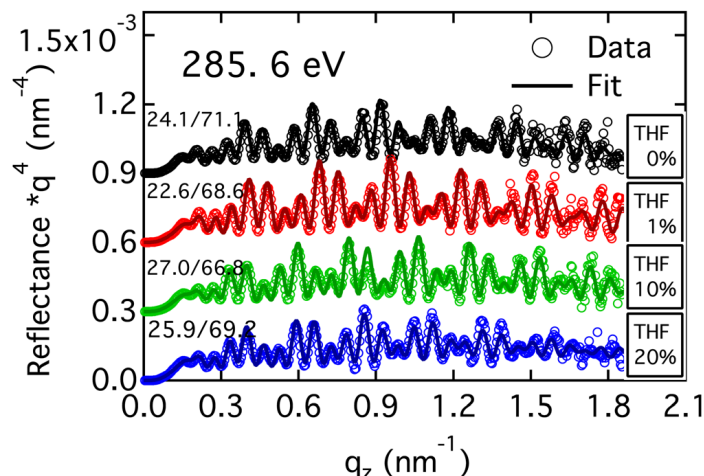


Figure 3.1: R-SoXR fits and data acquired at 285.6 eV for PFNBr/MEH-PPV bilayers, which had the PFNBr cast from methanol:THF mixtures as indicated. The numbers at the right of the reflectance traces are the layer thicknesses in nm as derived from the fits. Note the scaling by  $q^4$ .

R-SoXR results at 285.6 eV of the PFNBr/MEH-PPV/Si bilayers cast from the different solvent mixtures are displayed in Figure 3.1. Qualitatively, the reflectance profiles exhibit clear fringe modulations with two  $\Delta q$ 's, indicating a bilayer structure. The quantitative results for the interfacial and surface widths, and the layer thicknesses from fits to the data in Figure 3.1 are summarized in Table 3.1. The interfacial width changed appreciably as a function of solvent polarity only for the highest THF content, i.e., the 20%:80% THF:methanol mixture. In this case, the width increases from 0.8 nm to 1.2 nm. The 1% and 10% THF solutions yield essentially the same sample as the use of a pure methanol solvent. These results are not unexpected. PFNBr has been specifically designed to allow differential casting from methanol, a poor solvent for MEH-PPV. The MEH-PPV layer surface is not disturbed much with the use of methanol, which has been previously demonstrated [115] and is confirmed with the present results. Since THF can dissolve both PFNBr (top layer) and MEH-PPV (bottom layer), sufficient THF (i.e., 20%) during casting of the PFNBr does indeed broaden the interface.

The effect of different sample preparation procedures was also explored. In Figure 3.2, R-SoXR results and fits of PFNBr/MEH-PPV bilayers prepared with the following procedures are plotted: direct casting without any further annealing (Figure 3.2(b)), pre-annealing of the bottom MEH-PPV layer at 230 °C for 20 min, followed by casting the top PFNBr layer (Figure ??(c)), and a bilayer made by direct casting both layers one-by-one and subsequent annealing of the entire bilayer at 230 °C (Figure 3.2(d)). Clear, qualitative differences can be readily observed and interpreted: The more extensive the annealing and processing, the rougher the

Table 3.1: Surface and interface roughness of PFNBr/MEH-PPV/Si bilayers and MEH-PPV reference layer as determined from fits shown in Figures 3.1 and 3.2.

Sample	Surface Roughness RMS (nm)	Interfacial Roughness RMS (nm)
Standard	0.9	0.8
THF 1%	1.0	0.7
THF 10%	0.9	0.8
THF 20%	1.2	1.2
Annealed MEH-PPV single layer	1.7	0.0
Bilayer with pre-annealed MEH-PPV layer	1.6	2.0
Annealed bilayer @ 150 °C	1.1	0.9
Annealed bilayer @ 230 °C	1.1	4.0

surface and interface. The quantitative values of surface and interfacial roughnesses from fits are summarized in Table 3.1. As expected from the raw data, the surface and interfacial widths are greatly affected by the different sample preparation procedures and the interfacial roughness increases from 0.8 nm to 2.0 nm for the preannealed sample and to  $\sim$  nm for the annealed bilayer. R-SoXR of an annealed single layer MEH-PPV sample is shown in Figure 3.2(a) and yields a surface roughness of 1.7 nm. Previous R-SoXR results on as-cast MEH-PPV reported a very smooth surface with an RMS surface roughness of 0.52 nm and an increase of about 0.35 nm to 0.88 nm for the interfacial width upon casting of a PFNBr layer [115]. The present R-SoXR measurements thus indicate that the PFNBr/MEH-PPV interface further roughens slightly during the casting of the PFNBr, even for the preannealed MEH-PPV, with an increase of  $\sim$  0.3 nm. This is very comparable to the increase observed for the as-cast MEH-PPV layer. Since the  $\sim$  20 nm thin top layer is differentially spun cast onto a solid bottom layer, there would be no capillary waves during casting [119]. The present and prior results strongly suggest that the casting of the CPE does not significantly result in chemical interdiffusion and that the major contribution to the 2.0 nm width observed for the bilayer with a preannealed MEH-PPV bottom layer is due to the initial physical roughness of the MEH-PPV layer on which the PFNBr is cast. Whether or not there is a contribution from capillary waves to the roughness during the annealing of the entire bilayer is not relevant, as we are not interested in understanding thermodynamic interface properties, but the effects of processing on the interfacial width.

Figure ?? shows the R-SoXR data for the PFNBr/MEH-PPV/PEDOT:PSS/ITO/glass multilayer device at five photon energies. Complicated reflectance patterns arise as a function of

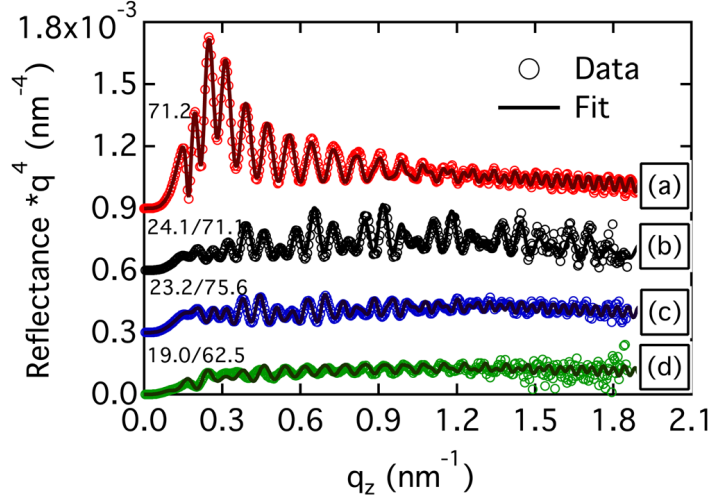


Figure 3.2: Reflectance acquired from (a) MEH-PPV single layer pre-annealed at 240 °C (270 eV), (b) as cast bilayer (285.6 eV), (c) as cast bilayer on pre-annealed MEH-PPV (285.6 eV), and (d) bilayer annealed at 230 °C. The numbers at the left of the reflectance traces are the layer thicknesses in nm as derived from the fits. Note the scaling by  $q^4$ . Data offset for clarity.

photon energy, since the reflections from each interface interfere and their respective reflectivity is photon energy dependent. In addition, absorption can play an important and dominant role in R-SoXR. Considering intrinsic materials contrast and taking absorption into account, the following picture can be deduced: (For simplicity, the vacuum/PFNBr, PFNBr/MEH-PPV, MEH-PPV/PEDOT:PSS, PEDOT:PSS/ITO, and ITO/glass interfaces will be referred to for the multilayer device as interface #1, #2, #3, #4, and #5, respectively.) At 285.4 eV, the top three interfaces have relatively strong reflections and the 4th and 5th interface is not efficiently probed, due to absorption. At 284.6 eV, interface #3 has very low contrast and relatively strong absorption in the MEH-PPV and PEDOT:PSS prevents probing of interfaces #4 and #5. Only interfaces #1 and #2 contribute. At 283.8 eV, interface #1 (the top surface) has a minimum in contrast. The contrast for the second interface is also low, yet this is an energy where there is little absorption and the third, fourth, and fifth interfaces are probed effectively. At 270 eV, primarily, interfaces #1, #3, #4, and #5 contribute. At 282.6 eV, primarily, interfaces #1, #4, and #5 are probed, with a minor contribution from interface #3. Hence, at these latter two energies, information about the total film thickness and the deeper interfaces is encoded in the complex reflectance profiles. Interface #2, at which charge combination and light emission occur, is most efficiently probed at 284.6 and 285.4 eV.

Having identified the contributing interfaces as a function of photon energy, the layer thickness of each layer can now be derived from the  $\Delta q$ 's, as measured from the various fringe

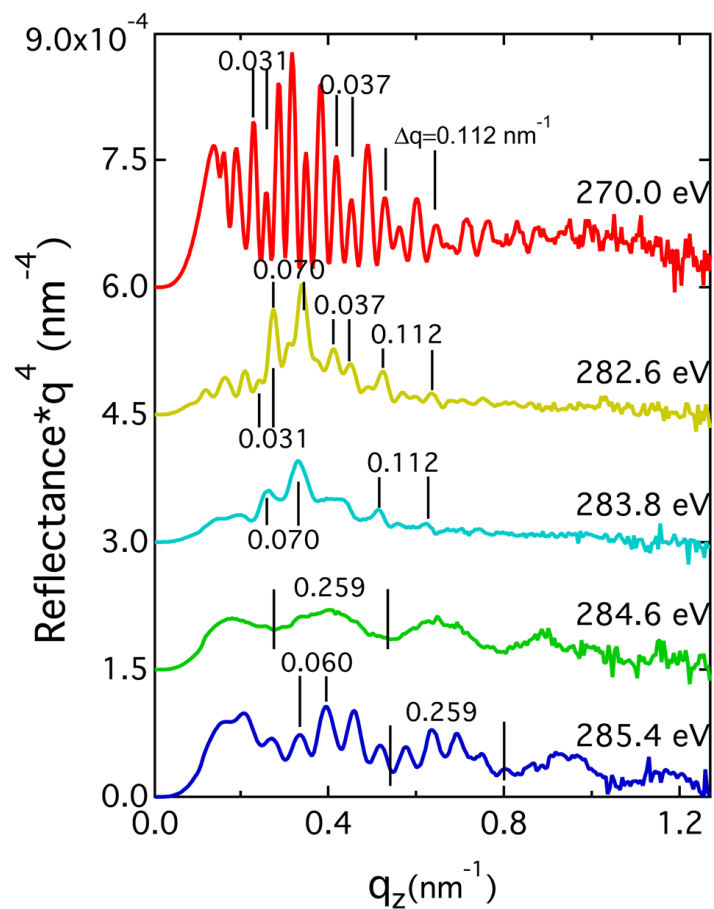


Figure 3.3: Reflectance of PFNBr/ MEH-PPV/ PEDOT:PSS /ITO /glass multilayer at selected photon energies. Note the scaling by  $q^4$ . Data offset for clarity.

spacings indicated in Figure 3.3. At 284.6 eV, there are only well-defined fringes with a  $\Delta q$  of approximately  $0.259 \text{ nm}^{-1}$ , corresponding to a derived thickness of  $d \approx 2\pi/\Delta q = 24.2 \text{ nm}$ . At 285.4 eV, modulations of the Kiessig fringes corresponding to two  $\Delta q$  values are clearly visible, similar to those observed for polymer bilayers on Si substrates [72, 71]. The smaller  $\Delta q$  equals  $\sim 0.060 \text{ nm}^{-1}$  and corresponds to a thickness of  $\sim 104 \text{ nm}$ . The larger  $\Delta q = 0.259 \text{ nm}^{-1}$  yields the same information as the 284.6 eV data. A third  $\Delta q$  cannot be detected in the 285.4 eV data, directly indicating that only three of the five interfaces dominate this data. Photon energies of 282.6 eV and 270 eV yield dominant fringes with two different  $\Delta q$ 's. For  $q$  values less than  $\sim 0.4 \text{ nm}^{-1}$ , the average  $\Delta q$  is  $\sim 0.031 \text{ nm}^{-1}$ , corresponding to a thickness of  $\sim 203 \text{ nm}$ , while, for  $q$  values larger than that, the average  $\Delta q$  is  $\sim 0.037 \text{ nm}^{-1}$ , corresponding to a thickness of  $\sim 170 \text{ nm}$ . Furthermore, a regular pattern for higher  $q$ 's is observed that corresponds to  $\Delta q \approx 0.112 \text{ nm}^{-1}$ . At 283.8 eV, a  $\Delta q \approx 0.070 \text{ nm}^{-1}$  is observed at low  $q$ , corresponding to a thickness of  $\sim 90 \text{ nm}$ , and a  $\Delta q \approx 0.111 \text{ nm}^{-1}$ , corresponding to  $\sim 56 \text{ nm}$ , is observed at high  $q$ . The results of this analysis in conjunction with the dominant interface reflections are summarized in Table ???. A self-consistent picture with only minor differences in layer thicknesses emerges. The average derived thicknesses for the top four layers are:  $\sim 24 \text{ nm}$ ,  $\sim 80 \text{ nm}$ ,  $\sim 56 \text{ nm}$ , and  $\sim 30 \text{ nm}$ , for a total of  $\sim 200 \text{ nm}$ .

Table 3.2: R-SoXR sensitivity to particular interface and dominant fringe spacing of R-SoXR data of PFNBr/MEH-PPV/PEDOT:PSS/ITO/glass multilayer device (see Figure 3.3) as a function of photon energy; nominal layer thickness, and quantitative results of layer thickness. Shaded areas indicate no particular sensitivity to this layer. Unit for  $\Delta q$  of fringes spacing is  $\text{nm}^{-1}$ .

		Semi-qualitative analysis from fringe spacing (nm)												
Photon energy		270.0 eV			282.6 eV				283.8 eV	284.6 eV	285.4 eV			
Interfaces observed:		1,5	1,4	3,4	1,5	1,4	3,5	3,4	3,5	3,4	1,2	1,3	1,2	Fits/
$\Delta q$ of fringes spacing:		0.031	0.037	0.112	0.032	0.036	0.070	0.112	0.070	0.112	0.259	0.060	0.259	sim. (nm)
Layer	Nom. $t$ (nm)													
PFNBr	25											24		23.5
MEH-PPV	80		172			175						104		78.8
PEDOT:PSS	60	203		56	196			56						60
ITO	30						90		90					30

Through fits or simulations, one can extract more precise quantitative information for thicknesses and, more importantly, the interfacial widths from the various reflectance profiles. Figure 3.4 shows such fits or simulation for photon energies of 270, 284.6, and 285.4 eV, respectively. In contrast to the prior incomplete analysis [106], a complete multi-layer model was used here along with improved optical constants previously derived from independent measurements. Thickness, roughness, and optical constants can be fitted. The individual fits for the 284.6 eV and 285.4 eV reflectance yield a surface roughness of 0.9 nm and roughnesses of 1.1 nm and 3.5 nm for the PFNBr/MEH-PPV and the MEH-PPV/PEDOT:PSS interfaces, respectively. The layer thicknesses derived from the fits are 23.5 nm and 78.8 nm, in close agreement to the semi-quantitative estimates derived above. This is in agreement with prior fits using a simplified bilayer model [106]. Furthermore, the data at energies below 283.9 eV contains information about the interfacial widths or roughnesses of the PEDOT:PSS/ITO and the ITO/glass interfaces. For the 270 eV data, a complete fit over the full  $q$  range with all adjustable parameters is not converging, due possibly to some background and normalization issues in that data. Instead, we have used simulations for the 270 eV data that were visually optimized to match the  $\Delta q$  observed and the damping at the correct  $q$ . These simulations constrain the top three interfaces to those measured from the 284.6 eV and 285.4 eV data and use only measured optical constants. The only free parameters that are adjusted are the width of interfaces #4 and #5. These optimized simulations indicate that these interfaces have widths of 4.0 nm and 3.5 nm, respectively. The results of the fits and the simulation are summarized in Table ???. In most experimental situations, one would often have enough processing flexibility to measure the surface roughness and any change in the first buried interfacial width after each processing step. We find it nonetheless interesting to use this multilayer sample as an example of what could be accomplished with R-SoXR if such flexibility did not exist or is operationally too complicated or time consuming.

Interestingly, the PEDOT:PSS/ITO interface (i.e., #4) is by far the roughest. Also, the width of the MEH-PPV/ PEDOT:PSS interface is not significantly reduced from that observed for PEDOT:PSS/ITO. This implies that the casting of the PEDOT:PSS did not significantly smooth out the ITO roughness or that the PEDOT:PSS surface roughened during the casting of the MEH-PPV. The latter is relatively unlikely. By the time the last layer is cast, a very smooth surface of 0.9 nm is achieved. The CPE/MEH-PPV interface was rather sharp with a width of 1.1 nm. This is larger by  $\sim 0.2$  nm than the width measured on bilayers cast on smooth substrates and must be caused by the larger initial roughness of the MEH-PPV in the multilayer. This difference is nonetheless relatively small compared to the overall width and, in particular, to the large changes in interfacial width observed as a function of annealing or even the 0.4 nm increase observed for 20% THF. Hence, the more simple bilayer structures can be used to characterize the interface as a function of sample preparation protocol, and any future correlation to device performance can be made from bilayer data and does not require the more

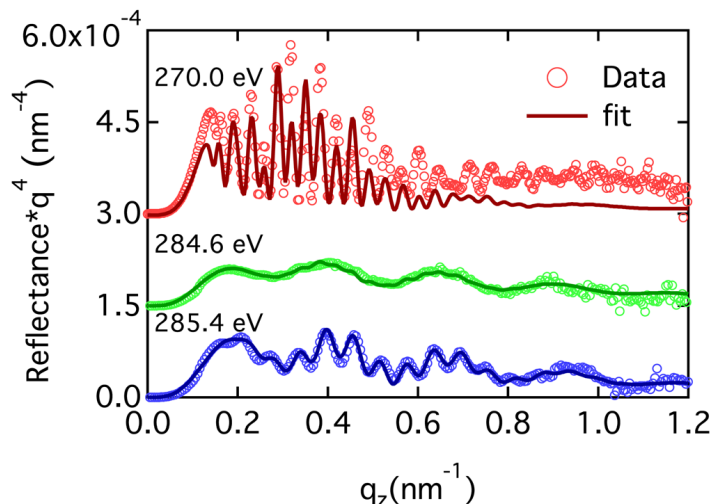


Figure 3.4: Fits of multilayer data 284.6 and 285.4 eV and simulation of 270 eV data. Note the scaling by  $q^4$ . Data offset for clarity.

complex analysis of the multilayers.

### 3.4.2 PFB/F8BT bilayers

Bilayer PFB/F8BT/Si heterojunctions were initially fabricated by floating, which minimizes material intermixing, and were subsequently annealed. Figure 3.4 shows the R-SoXR data acquired at 282.4 eV of such PFB/F8BT/Si bilayers. Fits of the reflectance profiles yield quantitative values for the width of the polymer/polymer interface and the surface. Table ?? summarizes the interfacial RMS roughness of average results for the interfacial width from at least three spots measured at 282.4 and 284 eV, at which the soft x-ray is sensitive to both the interface and the surface (180 °C data value from only two spots). As shown in the table, the as-prepared (no annealing), laminated bilayers have sharp interfaces with the 0.68 nm interfacial width consistent with the surface roughness of the initially spin-coated films. This value increases to 0.70 nm and 1.0 nm, even when the film is annealed at lowest temperatures of 100 and 120 °C, respectively. The interfacial widths quoted are averages from several spots, increasing the accuracy of the measurement. A discussion of the number of samples characterized and error analysis can be found in Ref. 12. When the films are annealed near or above the glass transition temperatures of the polymers ( $\sim 140$  °C), substantial increases in the interfacial width are observed, with a jump to 2.6 nm for 140 °C and  $\sim 6.7$  nm for 200 °C.

In order to differentiate interface roughness from interface interdiffusion indirectly, surface roughness measurements on as-cast and 200 °C annealed single layer PFB and F8BT films were compared to the measured surface roughness of the bilayer films. As shown in Figure 3.6,

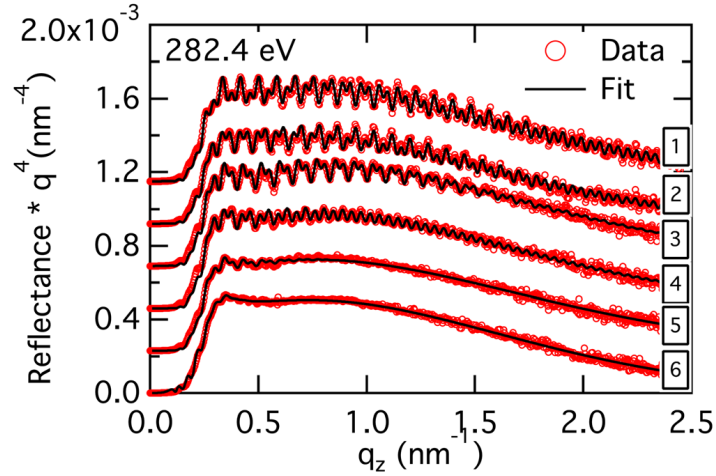


Figure 3.5: Representative R-SoXR data at 282.4 eV (open circle) and numerical fits (solid line) of Si/PFB/F8BT samples as a function of annealing. (1) As-prepared, (2) 100 °C, (3) 120 °C, (4) 140 °C, (5) 160 °C, and (6) 200 °C. The loss of the fringe modulations at higher annealing temperatures directly indicates an increase in polymer/polymer interfacial width. Note the scaling by  $q^4$ . Data offset for clarity.

Table 3.3: Fitting results from R-SoXR measurements of PFB/F8BT/Si bilayers at 282.4 eV and 284 eV, assuming an error function interface profile.

Sample	Interfacial root mean square (RMS) roughness (nm)
As-prepared	0.68
100 °C	0.70
120 °C	1.0
140 °C	2.6
160 °C	3.6
180 °C	6.5
200 °C	6.7

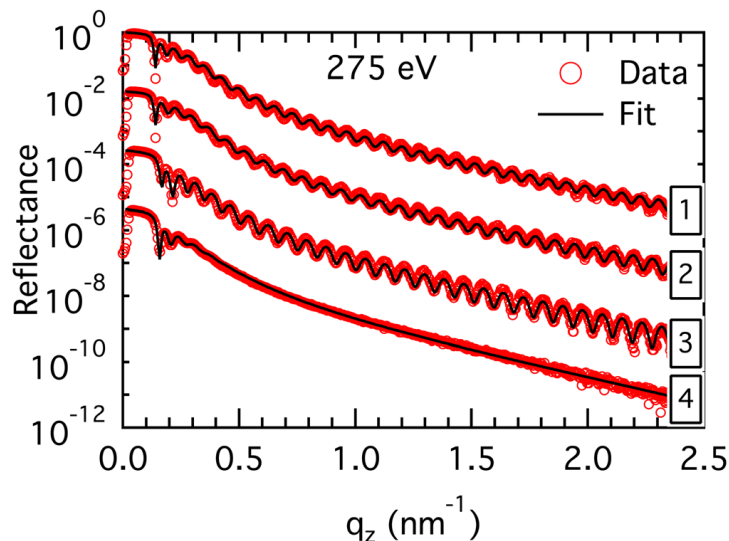


Figure 3.6: R-SoXR reflectance (open circle) and fits (solid line) of (1) PFB as-spun, (2) PFB 200 °C annealed, (3) F8BT as-spun, and (4) F8BT 200 °C annealed single layers. Data offset for clarity.

unannealed films are very sharp, with a surface roughness of  $\sim 0.46$  nm for both F8BT and PFB. Annealing significantly roughened the surfaces, with measured roughnesses of  $\sim 1.8$  nm for the 200 °C annealed PFB single layer,  $\sim 5.8$  nm for the 200 °C annealed F8BT single layer, and  $\sim 6.7$  nm for the 200 °C annealed Si/F8BT/PFB bilayer. The PFB surface roughness decreases with annealing to  $\sim 0.3$  nm, annealing out features arising from casting [72]. Two important aspects are apparent: i) The bilayer surface, which has PFB on top, is rougher than the surface of the single layer PFB; and ii) the interface and surface roughnesses of the Si/F8BT/PFB bilayer have similar magnitude and are close to the single layer F8BT roughness. This strongly implies that F8BT roughens when annealed (presumably due to its liquid crystalline/semi-crystalline nature) and that this roughening determines the interface roughness and surface roughness in the Si/F8BT/PFB bilayer [74].

A combination of R-SoXR characterization,  $J-V$  device data, photoluminescence quenching measurements, and Monte Carlo simulations revealed that only the sharpest interface yields the best device performance. The lower efficiency for the annealed device is attributed to decreased interfacial charge separation efficiency, which is partly due to a decrease in the bulk mobility of the constituent materials upon annealing, but also (and significantly) due to the increased interface roughness [74]. This could have profound implication for polymer/polymer device processing if the results are confirmed to be general for all polymer/polymer systems. New processing strategies that produce sharp non-equilibrium interfaces and increased use of block

copolymers are indicated by these results.

### 3.4.3 Dielectric/P(NDI2OD-T2) bilayers

R-SoXR is successfully applied to dielectric/ P(NDI2OD-T2) systems and extended to photon energies near the fluorine absorption edge at 698 eV [52]. Figure 3.7 shows the reflectivity data at various energies of the following three systems: 1) PMMA on top of P(NDI2OD-T2); 2) PS on top of P(NDI2OD-T2); and 3) CYTOP (a fluorinated polymer) on top of P(NDI2OD-T2). The sensitivity of soft x-rays to the surface and interface of two polymers is clearly strongly dependent on photon energy. At 275 eV, the total thickness of the bilayers is seen. In contrast to this, at 286 eV and 281.4 eV, the PMMA and PS surfaces are “turned off”, respectively, and the bottom P(NDI2OD-T2) layer is probed almost exclusively. Significantly, R-SoXR also yields excellent tunable contrast near the fluorine absorption edge. As seen in Figure 3.7, R-SoXR is very sensitive to the buried interface between CYTOP and P(NDI2OD-T2) at a photon energy around 688 eV. The slow modulation observed in the PS/P(NDI2OD-T2) and PMMA/P(NDI2OD-T2) bilayers arises from a thin silicon oxide layer of the substrates. Figure 3.8 shows some of these data along with a fit. By averaging at least three measured spots on each sample, we can derive the interfacial widths of the interfaces we are interested in. For PS/P(NDI2OD-T2) and PMMA/P(NDI2OD-T2) bilayers, the buried interface widths between polymers are measured to be 0.9 nm and 0.4 nm, respectively, with a surface roughness of 0.4 nm and 0.6 nm, respectively. For the CYTOP/P(NDI2OD-T2) bilayer, the surface and interface roughness are measured as 1.2 nm and 1.0 nm, respectively, around 285 eV(carbon edge). Fits to the reflectance acquired around 688 eV (fluorine edge) yield a surface roughness of 1.0 nm and interface roughness of 1.1 nm. Considering that the C- and F-edge data are acquired at different spots on the same sample, the difference between measured results at the C-edge and the F-edge is likely due to variations across the sample. Variations between samples of nominally the same type and different locations on the same sample need to be assessed carefully before conclusions about relation to device performance can be drawn. The data here simply demonstrate that experimental conditions have been identified that allow now the various P(NDI2OD-T2)-based TFT systems and details of their processing to be assessed. Due to the very small interfacial width measured in some cases, the systematic influence of the substrate roughness to the error budget needs to be assessed further.

## 3.5 Conclusion

R-SoXR is a unique and productive complement to conventional XR and NR. For most materials systems investigated to date, there are photon energies experimentally accessible, at which

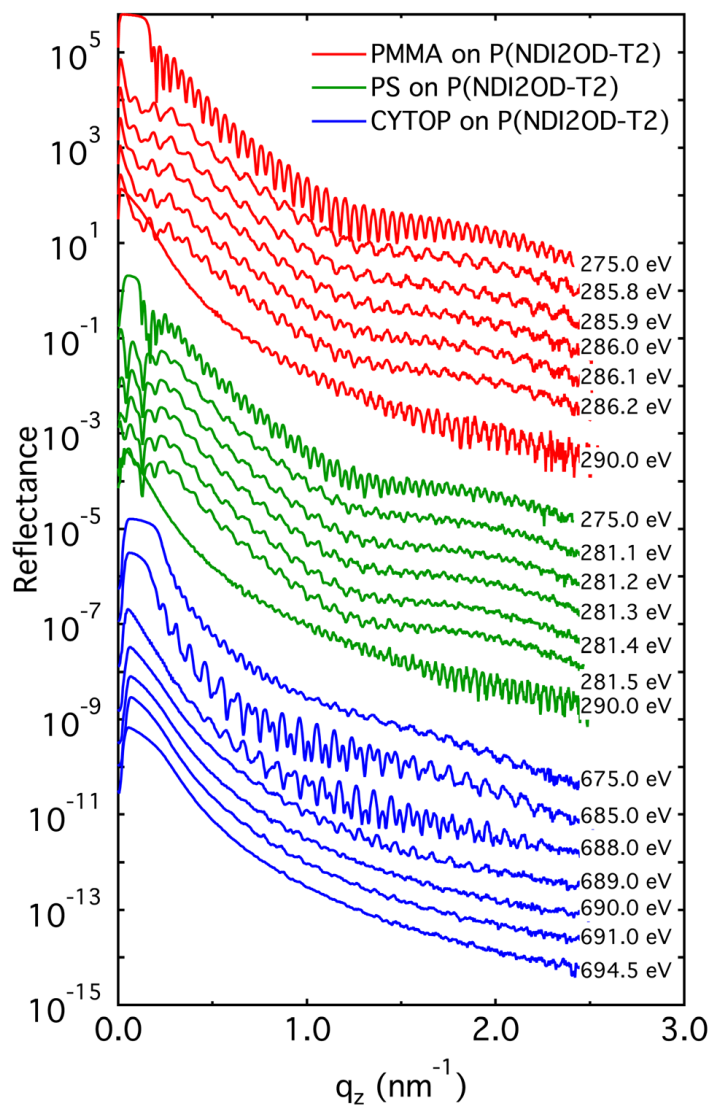


Figure 3.7: R-SoXR data acquired at a number of photon energies to show the selective sensitivity of the method to different interfaces for PS/P(NDI2OD-T2), PMMA/P(NDI2OD-T2), and CYTOP/P(NDI2OD-T2) bilayers at the carbon and fluorine absorption edges. Traces are offset for easy viewing. Data offset for clarity.

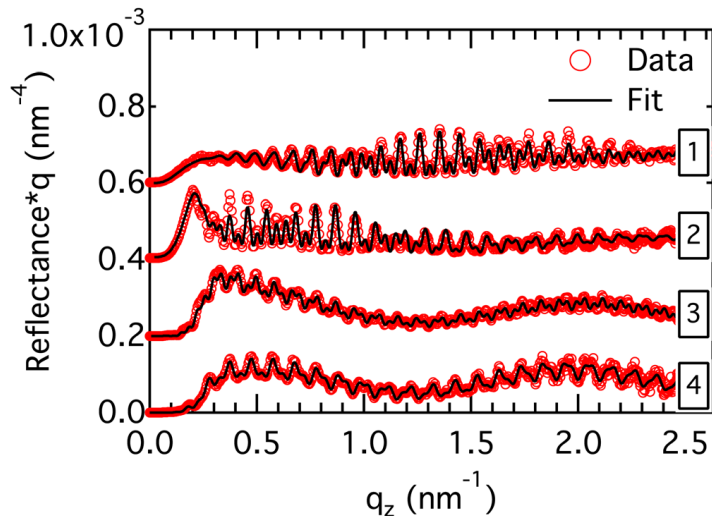


Figure 3.8: Data and fits for bilayers of: (1) CYTOP/P(NDI2OD-T2) at 688 eV; (2) CYTOP/P(NDI2OD-T2) at 285 eV; (3) PS/P(NDI2OD-T2) at 281.4 eV; and (4) PMMA/P(NDI2OD-T2) at 286.0 eV. Note that data and fits are scaled for better viewing in a single graph. Note the scaling by  $q^4$ . Data offset for clarity.

sufficient contrast between materials exists to provide high quality data that will allow the quantitative determination of interfacial widths. Examples from three types of organic devices in which interfaces play a critical role have been presented.

The interfacial widths between active layers in a PFNBr/ MEH-PPV optoelectronic device were shown to be tunable by annealing at elevated temperature, pre-annealing of the bottom layer, or casting from different solvent mixtures. Adding up to 20% THF to the PFNBr casting solution had the smallest effect. The interfacial width can be significantly broadened either by pre-annealing of the MEH-PPV bottom layer or post-annealing of a bilayer. The effects of sample preparation procedures on interfacial width can be readily characterized with R-SoXR, and comparison to device performance is now possible without having to deuterate one of the components.

Similarly for PFB/F8BT, it is shown that the interfacial width systematically increases with annealing temperature from 0.68 nm for pristine laminated bilayers to 6.7 nm with annealing at 200 °C. Combined with photoluminescence and device performance data, this study helps to partially explain the relatively poor efficiency of all-polymer systems. The results suggest that non-equilibrium, sharp interfaces are optimal for charge separation and that control of interface structure in solution-processed blends should be considered in order to maximize device efficiency. Novel processing routes and device fabrication processes that provide superior morphological control will have to be developed to harness the high  $V^{OC}$  potential exhibited

by all-polymer devices.

Lastly, the R-SoXR method has been successfully applied to TFT bilayer systems consisting of the recently developed high-mobility electron-transporting polymer P(NDI2OD-T2). The interface roughness of the buried P(NDI2OD-T2) interface in PS- and PMMA-based bilayers has been measured. Furthermore, with results from the CYTOP/P(NDI2OD-T2) bilayer, we have demonstrated that R-SoXR has been extended from the carbon 1s edge to the fluorine 1s absorption edge.

### **3.6 Acknowledgments**

The authors are grateful for fruitful discussions with and help from E. Gullikson (CXRO), B. Watts, E. Gann, B. Collins, and T. Araki (NCSU). Work at NCSU was supported by the U. S. Department of Energy (DE-FG02-98ER45737). Work at UCSB was supported by the Materials Research Laboratory funded by the National Science Foundation under the MRSEC program (UCSB MRL, DMR-1121053), the NSF CAREER Award (DMR# 0547639), and the Department of Energy, Office of Basic Energy Sciences (DE- SC000-2368). K.E.S. was supported by a NSF Graduate Fellowship. Work at Cambridge was supported by the Engineering and Physical Sciences Research Council, U.K. (Advanced Research Fellowship EP/E051804/1). The authors thank Cambridge Display Technology Ltd. for supplying PFB and F8BT. Data were acquired at beamlines 5.3.2 and 6.3.2 at the ALS, which is supported by the Director of the Office of Science, Department of Energy, under Contract No. DE-AC02-05CH11231.

## Chapter 4

# Influence of annealing and interfacial roughness on the performance of bilayer donor/acceptor polymer photovoltaic devices

To investigate how annealing affects the performance of all polymer organic solar cell devices based on PFB/F8BT donor/acceptor bilayers (detailed chemical names and structures later), R-SoXR are used to measure the interfacial width, indicating a systematically increase with annealing temperature. Combining photoluminescence measurement, device characterization, and Monte Carlo simulation of device performance, the behavior of device performance with annealing is explained. Our results indicate that non-equilibrium, sharp interfaces are optimal for charge separation and that control of interface structure in solution-processed blends should be considered in order to maximize device efficiency.

This is a published work on *Advanced Functional Materials* by [Hongping Yan](#), Sufal Swaraj, Cheng Wang, Inchan Hwang, Neil C. Greenham, Chris Groves, Harald Ade and Christopher R. McNeill, with DOI: 10.1002/adfm.201001292. In this collaborative work, I finished the complete reflectivity data analysis to draw the final conclusions. Sufal Swaraj took the R-SoXR data at Advanced Light Source, Cheng Wang helped with data analysis and discussions. Inchan Hwang and Neil C. Greenham provided Monte Carlo simulation results. Chris Groves, and Christopher R. McNeill provided the samples and device characterizations. All coauthors contributed to the discussions and the finalizing of the conclusions.

## 4.1 Abstract

Through controlled annealing of planar heterojunction (bilayer) devices based on the polyfluorene copolymers poly(9,9-dioctylfluorene-co-bis(N, N'-(4-butylphenyl))bis(N,N'-phenyl-1,4-phenylene)diamine) (PFB) and poly(9,9-dioctylfluorene-co-benzothiadiazole) (F8BT) we study the influence of interface roughness on the generation and separation of electron - hole pairs at the donor/acceptor interface. Interface structure is independently characterized by resonant soft X-ray reflectivity with the interfacial width of the PFB/F8BT heterojunction observed to systematically increase with annealing temperature from 1.6 nm for unannealed films to 16 nm with annealing at 200 °C for ten minutes. Photoluminescence quenching measurements confirm the increase in interface area by the three-fold increase in the number of excitons dissociated. Under short-circuit conditions, however, unannealed devices with the sharpest interface are found to give the best device performance, despite the increase in interfacial area (and hence the number of excitons dissociated) in annealed devices. The decrease in device efficiency with annealing is attributed to decreased interfacial charge separation efficiency, partly due to a decrease in the bulk mobility of the constituent materials upon annealing but also (and significantly) due to the increased interface roughness. We present results of Monte Carlo simulations that demonstrate that increased interface roughness leads to lower charge separation efficiency, and are able to reproduce the experimental current-voltage curves taking both increased interfacial roughness and decreased carrier mobility into account. Our results show that organic photovoltaic performance can be sensitive to interfacial order, and heterojunction sharpness should be considered a requirement for high performance devices.

## 4.2 Introduction

Polymer-based solar cells are an attractive new technology due to the ability to quickly process large-area uniform thin films of the active layer at low temperature. Power conversion efficiencies have steadily increased over the last decade and are currently at 6 – 7% but still need to increase further to ensure commercial viability [92, 94]. Our understanding of the operating principles of polymer solar cells has also steadily improved but there is more to be understood. The mechanisms of charge generation, separation and transport in organic semiconductors are fundamentally different to inorganic semi- conductors. The primary photoexcitations of organic semiconductors are in general tightly bound excitons, necessitating the use of donor/acceptor heterojunctions of electron-accepting and electron-donating materials [120]. Due to the small exciton diffusion length of conjugated polymers, a bulk-heterojunction architecture is generally favored over a planar or bilayer geometry. In the bulk-heterojunction architecture, a three-dimensional phase-separated network is utilized, ensuring that all excitons generated within

the bulk of the film are able to reach a donor/acceptor heterojunction and dissociate. A bicontinuous morphology of donor and acceptor phases ensures that separated electrons and holes may traverse the bulk of the film and be collected at the electrodes.

The process of the separation of geminate electron-hole pairs at the donor/acceptor interface must also be considered in order to explain the behavior of many organic photovoltaic devices [121, 122]. Due to the low dielectric constant of organic semiconductors, electron-hole pairs created at donor-acceptor interface following exciton dissociation must overcome their mutual Coulomb attraction in order to separate. The separation of interfacial electron-hole pairs can be described as a field-dependent Onsager-type process [121, 122, 123, 124]. The field required to separate the majority of electron-hole pairs varies considerably with donor/acceptor combination [125]. This variation can be partially attributed to differences in material electron/hole mobilities, though local rather than bulk mobilities should be considered. Film micro-structure also plays a critical role in determining whether geminate electron-hole pairs not only escape their mutual Coulomb attraction but also negotiate a path away from the interface instead of inadvertently meeting again and recombining [123, 126, 127, 128]. Recently, we studied [127] the influence of nanoscale phase-separation on the device performance of polymer blends showing that the optimum morphology is coarser than one may expect if considering the need to maximize exciton dissociation yield alone. Rather, a coarser phase-separated structure is required in order to balance the processes of charge generation and separation. A similar conclusion was reached by Veldman et al. who studied polymer/fullerene blends [123]. Monte Carlo simulations of charge separation in phase-separated blends further showed that increasing the domain size from 4 to 16 nm improves the charge separation yield [126]. This observation is explained in terms of finer blends having fewer possible routes available to separate charges further, making it likely for initially separated charge pairs to meet again and recombine.

In addition to domain size, the nature of the donor/acceptor interface is also expected to be important in determining the efficiency of charge separation. While the length scale of phase separation in polymer/polymer and polymer/fullerene blends is considered to be critical in optimizing device performance, little consideration has been given to the sharpness of the donor/acceptor heterojunction. Here we study planar heterojunctions based on the polyfluorene co-polymers poly(9,9-dioctylfluorene-co-bis(N,N'-(4-butylphenyl))bis(N,N'-phenyl-1,4-phenylene) diamine) (PFB) and poly(9,9-dioctylfluorene-co-benzothiadiazole) (F8BT). Annealing of PFB/F8BT bilayers leads to a roughening of the heterojunction interface as characterized by resonant soft X-ray reflectivity (R-SoXR) and increased photoluminescence quenching. While a relatively inefficient photovoltaic system, PFB and F8BT demonstrate good contrast in soft X-ray experiments [129] making them ideally suited to R-SoXR studies. PFB and F8BT also have high photoluminescence quantum efficiencies and clearly separated emission bands enabling quantitative analysis of photoluminescence quenching [127]. Furthermore PFB and F8BT are some

of the most characterized conjugated polymers in terms of their electronic and photophysical properties enabling as many independent parameters to be specified in our device modeling. By obtaining quantitative information regarding morphology, photoluminescence quenching and charge transport allows us to examine very closely the competing effects of exciton dissociation and charge separation.

## 4.3 Results and discussion

### 4.3.1 Characterization of interface width

Planar PFB/F8BT heterojunctions were fabricated by spin-coating 60 nm thick PFB and F8BT layers, floating one film off in de-ionized water and laminating on the other. This method minimizes material intermixing that often happens when bilayers are fabricated by sequential spin-coating, even from nominally orthogonal solvents. Bilayers for devices were fabricated on ITO/PEDOT:PSS-coated glass substrates, whereas bilayers for interfacial characterization were prepared on silicon (for X-ray reflectivity studies) or quartz (for photoluminescence studies). Bilayers were annealed for 10 minutes at the indicated temperature on a hotplate in a nitrogen glovebox. Full details of sample and device preparation can be found in the experimental section. To quantitatively assess the width of the buried PFB/ F8BT interface we have employed Resonant Soft X-ray Reflectivity (R-SoXR). Due to the high intrinsic material contrast that exists for most polymer pairs at soft X-ray energies [71, 72], R-SoXR is capable of providing quantitative interface characterization without the need for deuteration [107]. The enhanced contrast afforded by soft X-rays has also been recently exploited in the use of resonant soft X-ray scattering to study the nanomorphology of polymer/polymer and polymer/fullerene blends [3]. Figure 4.1a presents representative R-SoXR reflectance measurements acquired at 284 eV of PFB/F8BT bilayers prepared on silicon substrates in a similar fashion to the devices. Fits of the reflectance profiles yield quantitative values for the width of the polymer/polymer interface and the surface. An error function was used for the fits, with this parameterization capturing the interfacial diffusion processes [130]. An error function furthermore approximates very well the expected arctan profile of an equilibrium polymer/polymer interface [131] and roughness with a Gaussian distribution (see Figure 4.1b). Average results for the interfacial width from at least three spots measured at 282.4 and 284.0 eV on each sample, with the exception of the 180 °C for which only two spots were measured, are summarized in Table 1 tabulating the square root of the variance,  $\sigma$ , and the full width half maximum (FWHM) of the corresponding Gaussian distribution. The FWHM values will be used for the following discussion. The as-prepared, laminated bilayers have sharp interfaces with the 1.6 nm interface consistent with the surface roughness of the initially spin-coated films. A measurable increase in width to 1.7 nm and 2.4

Table 4.1: Fitting results from R-SoXR measurements at 282.4 eV and 284 eV assuming an error function interface profile.

Sample	Interfacial RMS roughness [nm]	Interfacial FWHM width [nm]
As-prepared	0.68	1.6
100 °C	0.70	1.7
120 °C	1.0	2.4
140 °C	2.6	6.2
160 °C	3.6	8.4
180 °C	6.5	15
200 °C	6.7	16

nm is observed at even the lowest annealing temperatures of 100 and 120 °C, respectively. Substantial increases in the interfacial width are measured for annealing temperatures near or above the glass transition temperatures of the polymers ( $\sim 140$  °C) with a substantial jump to 6.2 nm observed for annealing at 140 °C and to  $\sim 16$  nm for annealing at 200 °C. We note that our analysis cannot directly distinguish between diffuse, molecular intermixing and interface roughening (see Figure 4.1(b) for a schematic differentiating these two structures). In order to indirectly differentiate interface roughness from interface interdiffusion, surface roughness measurements on as-cast and 200 °C annealed single layer PFB and F8BT films were compared to the measured surface roughness of the bilayer films. Unannealed PFB and F8BT films are very sharp with a surface roughness of 1.1 nm. Annealing significantly roughened the surface for the 200 °C annealed F8BT single layer to 14 nm, and to 12 nm for the 200 °C annealed Si/F8BT/PFB bilayer. In contrast, the 200 °C annealed PFB single layer smoothed out to measured roughnesses of 0.70 nm. Two important aspects are apparent: i) The bilayer surface, which has PFB on top, is much rougher than the surface of the single layer PFB and ii) the interface and surface roughnesses of the Si/F8BT/PFB bilayer have similar magnitude and are close to the single layer F8BT roughness. This strongly implies that the F8BT interface and surface roughens when annealed (presumably due to its liquid crystal- line/semi-crystalline nature) and that this roughening determines the interface roughness and surface roughness in the Si/F8BT/PFB bilayer.

### 4.3.2 Photoluminescence quenching

Figure 4.2 presents the results of the photoluminescence quenching study (see supporting information for raw data). In Figure 4.2, the relative number of excitons diffusing to and dissociating at the PFB/F8BT interface is calculated by comparing the photoluminescence signal of the

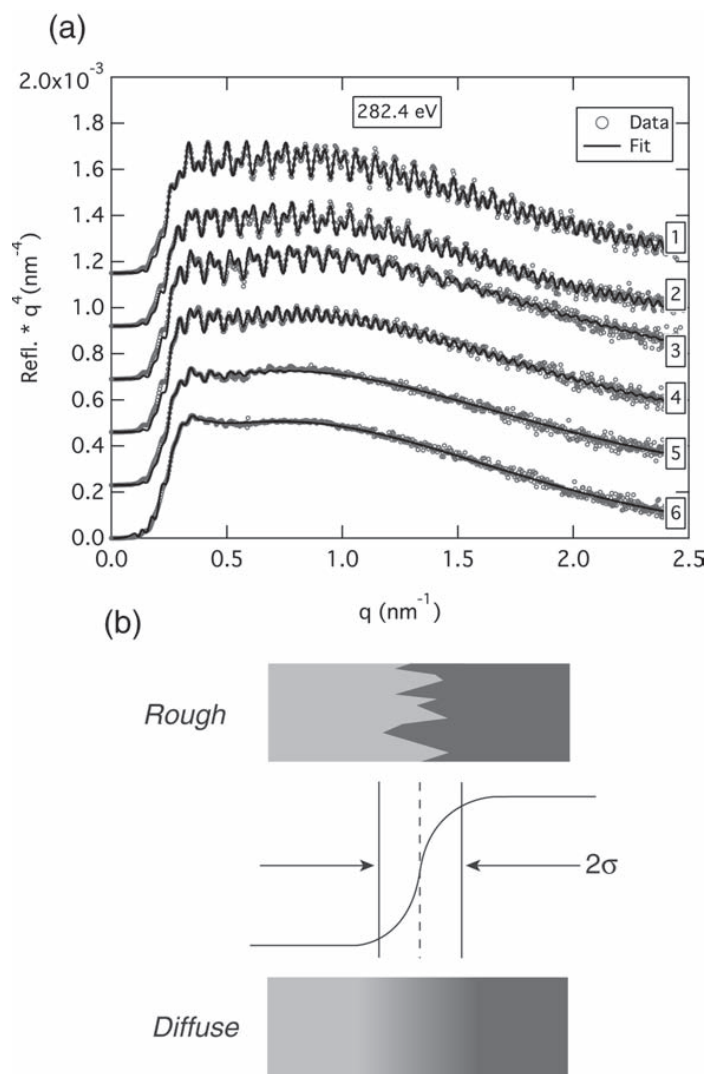


Figure 4.1: (a) Representative R-SoXR data at 282.4 eV (circles) and numerical fits (solid line) of Si/PFB/F8BT samples as a function of annealing. (1) as-prepared, (2) 100 °C, (3) 120 °C, (4) 140 °C, (5) 160 °C, and (6) 200 °C. The loss of the fringe modulations at higher annealing temperatures directly indicates an increase in polymer/polymer interfacial width. Note the scaling of the reflectance by  $q^4$  for easier comparison. (b) Schematic showing the shape of the error function used to fit the data in part (a) in relation to rough and diffuse interfaces.

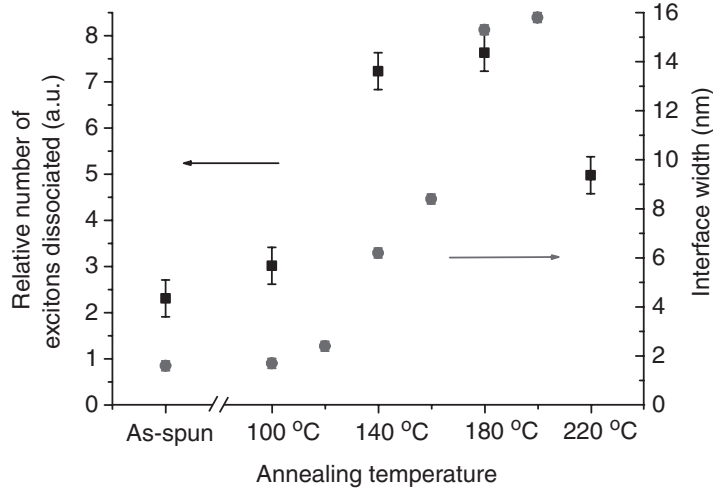


Figure 4.2: (Squares) Changes in the relative number of excitons dissociated at the PFB/F8BT interface with annealing; (Circles) Changes in the interface width of the PFB/F8BT bilayer with annealing determined from the R-SoXR data of Figure 1.

PFB/F8BT bilayers to that of a pristine F8BT films. These reference pristine F8BT films were also annealed in order to account for changes in F8BT photoluminescence quantum efficiency with annealing [132] (see Figure 4.7 in the supporting information). Figure 4.2 shows that there is a modest (30%) increase in photoluminescence quenching with annealing at 100 °C, followed by a large increase (nearly 200%) with annealing at 140 °C, signifying a significant increase in exciton dissociation efficiency. Interestingly annealing above 140 °C does not bring about any further significant increases in quenching, with the quenching efficiency actually decreasing with annealing at 220 °C, despite increases in interface width as measured by R-SoXR. This observation suggests that there may be molecular interdiffusion at low annealing temperatures followed by roughening at higher annealing temperatures. Conversely, the increase and then decrease in photoluminescence quenching with annealing may be consistent with roughening, with the decrease in quenching at higher annealing temperatures attributed to lateral coarsening of the interface with a length scale larger than the exciton diffusion length. Given the success we have below in modeling the device characteristics with roughened as opposed to diffuse interfaces, we consider interface roughening to be the dominant mechanism. Future photoluminescence studies (notably time-resolved studies) and modeling of exciton diffusion may be able to complement R-SoXR helping to differentiate interface roughening and diffusion.

### 4.3.3 Device properties

Figure 4.3 presents device characteristics of ITO/PEDOT:PSS/PFB/ F8BT/Al bilayer devices. Despite the increase in exciton dissociation efficiency with annealing, a systematic decrease in photovoltaic efficiency with annealing is observed. All devices maintain a similar open-circuit voltage, with the as-spun device showing a noticeably higher fill factor compared to annealed devices suggestive of superior charge separation yield at low electric fields. Figure 4.3b presents current voltage curves under extended reverse bias (note that the devices are stable under reverse bias and the current-voltage curves reproducible. Please see Figure 4.9 for examples of sequentially acquired current-voltage curves.) for which the dark current has been subtracted (which even at  $-14$  V is less than 0.5% of the light current). Therefore Figure 4.3b plots the voltage dependence of photocurrent generation. The  $140$  °C annealed device has a higher photocurrent yield than the unannealed device at high reverse bias, showing that the additional exciton dissociation in this device can be realized as photocurrent, however a larger electric field is required to separate the interfacial electron-hole pairs that are produced and consequently the fill factor is lower. Even at  $-14$  V the photocurrent yield in the  $140$  °C-annealed device has not saturated and is only 36% higher than the photocurrent yield of the unannealed device under the same bias conditions. We note that changes in the efficiency of charge collection are not likely to account for the decreased efficiency of the annealed devices. Once electrons and holes have been separated from the donor and acceptor interface they are constrained to their respective phases with diffusion and electric field gradients inhibiting bimolecular recombination at the donor/acceptor interface. We also note that the optimum annealing temperature of PFB/F8BT blends is found to be  $140$  °C, demonstrating that mild heat-treatment does not otherwise have a significantly adverse impact on device operation [127]. For the remainder of this paper we focus on explaining the performance of the as-spun,  $100$  °C-annealed and  $140$  °C-annealed devices where device performance systematically decreases despite increases in interface width and exciton dissociation efficiency.

### 4.3.4 Mobility characterization

In order to account for variations in the bulk mobility of the materials with annealing, we have measured the mobility of hole-only and electron-only diodes annealed at different temperatures. Figure 4.4 presents the raw data for as-spun,  $100$  °C- and  $140$  °C-annealed devices along with fits to the space-charge limited current expression

$$J_{SCL} = \frac{9}{8} \epsilon \mu_0 e^{0.891\gamma} \sqrt{V_{int}/L} \frac{V_{int}^2}{L^3} \quad (4.1)$$

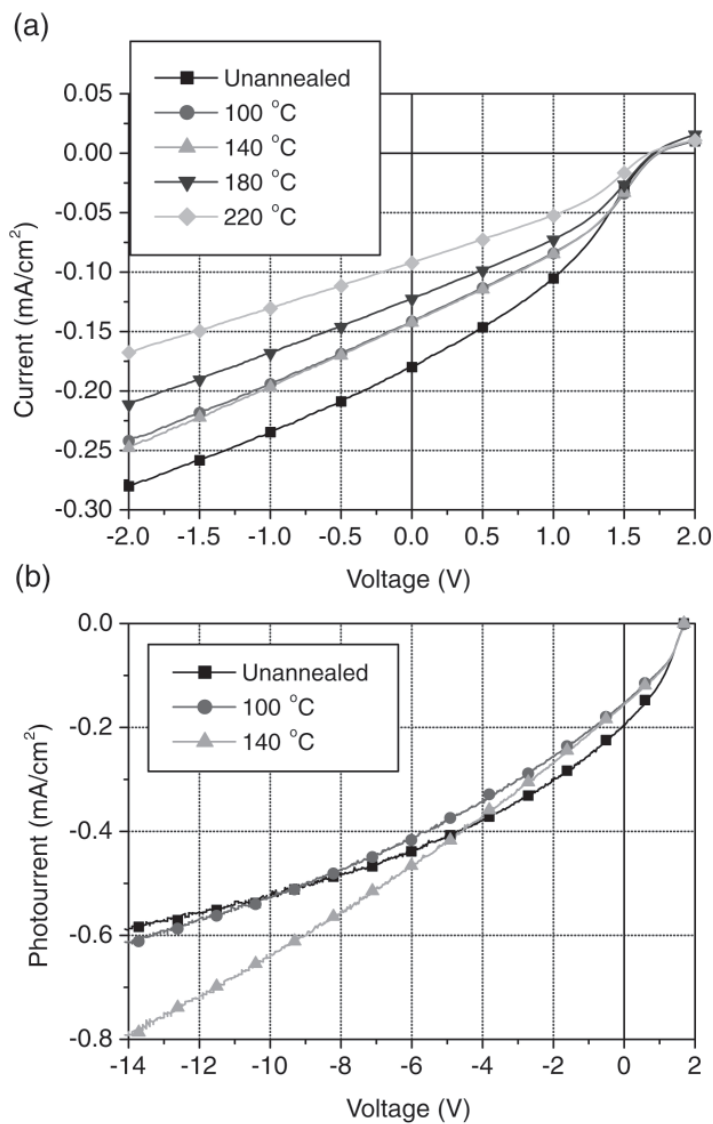


Figure 4.3: (a) Current voltage characteristics of PFB/F8BT bilayer devices as a function of annealing temperature. (b) Reverse bias dependence of photocurrent of PFB/F8BT bilayer devices.

Table 4.2: Summary of fitting parameters used to fit the space-charge limited expression (Equation 4.1) to the data of Figure 4.4.

	$\mu_0[\times 10^{-7} \text{ cm}^2\text{V}^{-1}\text{s}^{-1}]$	$V_{int}$ [V]	$\gamma [\times 10^{-3} (\text{mV}^{-1})^{0.5}]$
PFB As-spun	3.5	-0.75	0.48
PFB 100 °C	2.1	-0.6	0.48
PFB 140 °C	2.3	-0.35	0.50
F8BT As-spun	0.80	-0.05	1.05
F8BT 100 °C	0.80	-0.75	0.90
F8BT 140 °C	0.23	0.25	0.75

that accounts for a field-dependent mobility of the form  $\mu = \mu_0 \exp(\gamma\sqrt{E})$  where  $\mu_0$  is the zero-field mobility,  $\gamma$  the field activation parameter,  $E$  the electric field strength,  $J_{SCL}$  the current density,  $\varepsilon$  the permittivity,  $V_{int}$  the internal voltage and  $L$  the film thickness. The fitted values for mobility,  $\gamma$  and  $V_{int}$  are tabulated in Table 2; a value of  $\varepsilon_r = 4$  was used for all fits. For both PFB and F8BT the respective hole and electron mobilities decrease with annealing consistent with previous observations [132, 133]. The zero-field hole mobility of PFB is observed to decrease from  $3.5 \times 10^{-7} \text{ cm}^2 \text{ V}^{-1}\text{s}^{-1}$  for the as-spun film to  $2.3 \times 10^{-7} \text{ cm}^2 \text{ V}^{-1}\text{s}^{-1}$  with annealing at 140 °C, while the zero-field electron mobility of F8BT is observed to decrease from  $0.80 \times 10^{-7} \text{ cm}^2 \text{ V}^{-1}\text{s}^{-1}$  for the as-spun film to  $0.23 \times 10^{-7} \text{ cm}^2 \text{ V}^{-1}\text{s}^{-1}$  with annealing at 140 °C.

### 4.3.5 Monte Carlo simulations

Since we see both an increase in structural disorder at the donor/acceptor interface and a decrease in electron and hole mobilities with annealing, we have performed Monte Carlo simulations to examine the influence of these two factors on device performance. The model used is similar to that reported previously [134, 135, 136], in which the morphology of the device is represented by a 1 nm spaced Cartesian lattice that has either electron- or hole-transporting character, corresponding to F8BT and PFB respectively. The energetic disorder experienced by charges is randomly assigned to each site from a Gaussian distribution of width,  $\sigma_d$ . We assume that the values of energetic disorder experienced by an electron and hole on the same conjugated segment are correlated, and thus the site energy for excitons is a factor of  $\sqrt{2}$  larger than that for charges. Here excitons are injected at random positions within the simulation volume at a rate which corresponds to the incident light intensity and the absorption strength of the polymers. Excitons then undergo a random walk of nearest-neighbor hops at a rate determined

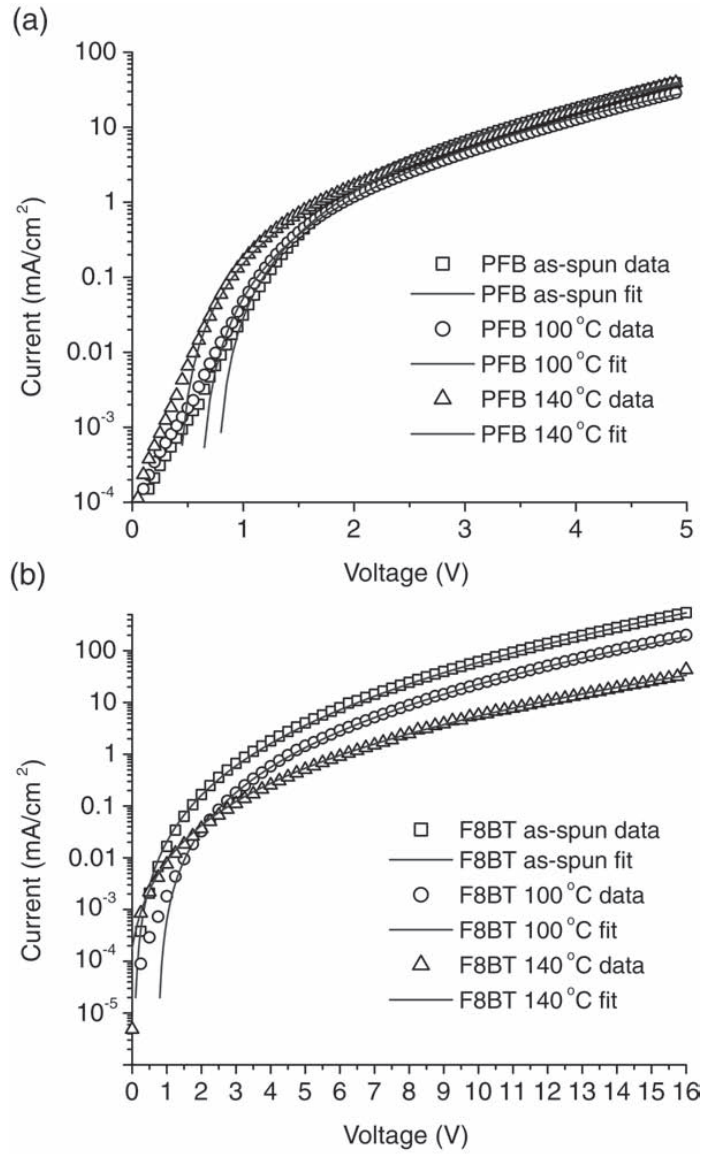


Figure 4.4: (a) Current voltage characteristics of hole-only PFB devices and fits to the space-charge limited expression. (b) Current voltage characteristics of electron-only F8BT devices and fits to the space-charge limited expression.

by a Miller-Abrahams expression [137],

$$\omega_{ij} = \omega_{ex} \exp\left(-\frac{E_j - E_i}{kT}\right), E_j > E_i \quad (4.2)$$

$$\omega_{ij} = \omega_{ex} E_j < E_i$$

where  $E_i$  and  $E_j$  are the energies of sites  $i$  and  $j$  respectively. If an exciton diffuses to the edge of an F8BT or PFB domain, i.e. a heterojunction, the exciton dissociates into a geminate pair. Excitons can also decay with a rate  $1/\tau_{ex}$ . Charges hop from current site  $i$  to nearest neighbor sites of the appropriate transporting material (F8BT for electrons and PFB for holes),  $j$  at a rate given by a Marcus expression [138]

$$\omega_{ij} = \nu \exp\left(-\frac{(E_j - E_i + E_R)^2}{4E_R kT}\right) \quad (4.3)$$

where  $E_R$  is the reorganization energy of the molecules, here equal to half the polaron energy, and the prefactor includes information regarding the electronic coupling between molecules. When calculating the hopping rates for the charges, the energetic disorder of the sites, internal electric field and all Coulombic interactions between carriers and image charges are included assuming  $\epsilon_r = 4$ . Recombination between adjacent electron-hole pairs occurs at a constant rate,  $1/\tau_R$ . Events are ordered using the first reaction method [139], which has recently been shown to work well over the range of energetic disorder of interest in OPVs [140]. The photocurrent is calculated by noting the average rate of charge extraction from the contacts. To avoid confusion between the behaviors of the dark and photocurrent, we do not include dark current here and analyze only those parts of the  $J - V$  curve that are dominated by the photocurrent ( $V < 1.3$  V). The simulation terminated at a time which was 50 times longer than the longest time constant in the system, which depending upon the conditions chosen was either the inverse photoinjection rate, carrier transit time, or inverse recombination rate.

Before we discuss the parameters used in the simulation, it should be noted that there is much information regarding nanoscale processes which will have an effect upon device performance (for example the degree of charge trapping [134], differences between on and off chain mobility [141, 142], or the local charge recombination rate [143]) that elude precise determination by bulk measurements. Therefore the task of simulating OPV device performance is generally underdetermined and more than one set of parameters will fit the data. However, F8BT and PFB are among the better characterized polymers for OPV applications which allows us to keep the number of fitted parameters to a minimum.

The exciton and geminate charge-pair lifetimes,  $\tau_{ex}$  and  $\tau_R$ , have been determined to be 500 ps [144] and 31 ns [145] respectively in the PFB/F8BT system. We maintain the value of  $\tau_R$  over all of the morphologies examined since Hodgkiss et al. [146] have shown that the

lifetime of geminate pairs in poly[(9,9- dioctylfluorene)-2,7-diyl-alt-[4,7-bis(3-hexylthien-5-yl)-2,1,3- benzothiadiazole] -2,2-diyl] (F8TBT) and poly(3-hexylthiophene) (P3HT) blends cast from different solvents, and thus with different morphologies, is relatively constant. The degree of energetic disorder reported in PFB [147, 148] and F8BT [147, 149] is typically around 100 meV, with some variations with molecular weight and processing conditions, and so we choose  $\sigma_d = 100$  meV for both materials. Given these values, we set  $w_{ex} = 4 \times 10^{10} \text{ s}^{-1}$  to obtain an exciton diffusion length of 9 nm in good agreement with experiment [150]. The temperature,  $T$  for all the simulations was taken to be 298 K while  $E_R$  is taken to be 0.25 eV as for other polymer systems [134]. Simulation of the optical absorption profile of the device (see Figure 4.5) was performed using the transfer matrix formalism as applied previously to organic photovoltaic devices by Inganäs and co-workers [151, 152] using the known optical constants of PFB, F8BT and other layers in the device [153]. The optical absorption profile was calculated for wavelengths over the range of 300 to 800 nm and integrated with the AM1.5G solar spectrum to determine the exciton generation profile in the device under illumination. The optical constants are assumed not to change significantly with annealing as supported by UV-vis absorption measurements of annealed bi-layer films and the similar shape of EQE curves, particularly for annealing temperatures up to 140 °C (see supporting information). The degree of exciton dissociation at the heterojunction affected  $dJ/dV$  during fitting since the absolute value of geminate separation efficiency, and in turn its voltage dependence, has to change in sympathy. To fit  $dJ/dV$  we took the generation rate of excitons to be  $1.6 \times 10^{27} \text{ m}^{-3} \text{ s}^{-1}$ , which is similar to the average generation rate of excitons in the region of the heterojunction in Figure 4.5. The internal voltage of the device is ill-defined since the work function of Al can vary over the range  $-4.3$  eV to  $-3.4$  eV depending on the degree of oxidation [154], while the PEDOT:PSS workfunction can vary between  $-5.2$  eV and  $-4.8$  eV [155]. Thus we arbitrarily chose the voltage at which the dark current began to increase rapidly (1.3 V) as the internal voltage, which is commensurate with the expected range of electrode workfunction variation.

Monte Carlo models require an input morphology that is defined on a nanometer length scale, hence we cannot use the current experimental data directly and instead we must simulate or construct the morphology used in the simulations. Ideally we would mimic the experimental processes by first defining a bilayer and then annealing the device to roughen the interface. However, the Ising-type model that is generally used to simulate the annealing process [156] naturally converges on “blocky” morphologies [157] that do not roughen to extent measured in experiment. We instead expect the annealed devices to have an interface with a mean roughness as predicted by R-SoXR measurements with texture on a nanometer lengthscale since the degree of exciton dissociation increases upon annealing. To qualitatively reproduce this morphology we here assume a “sandwich” type structure in which two equally thick pure F8BT and PFB layers sandwich a 1:1 blend layer [156] of characteristic feature size 10 nm and thickness  $d$ , and it is

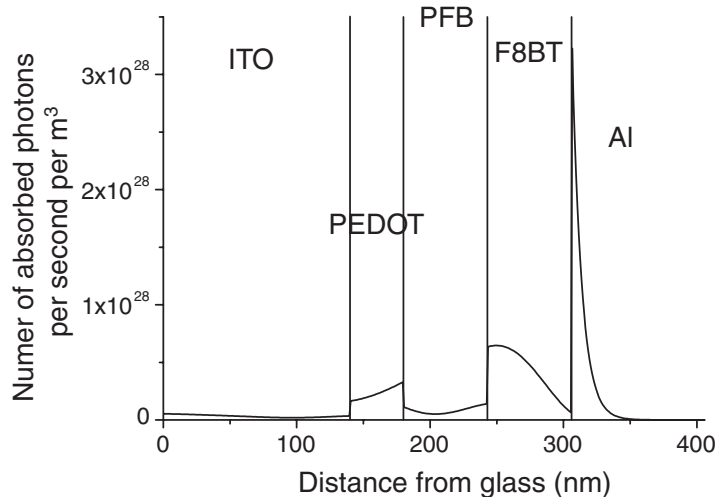


Figure 4.5: Optical absorption profile of the bilayer device under AM1.5G illumination computed using the matrix formalism and used for the Monte Carlo simulations.

this blended layer that represents the roughened interface of the bilayer. The thickness of the F8BT and PFB layers are chosen such that the total device thickness is 120 nm. Note that this approach implies an abrupt compositional profile, i.e. 50:50 in the “rough interface” blended layer and pure material either side, which differs from that which is expected (see above). The question of how to predict blend formation during annealing or solvent evaporation in a quantitative manner that would reproduce the composition profile expected from experiment is not straightforward but is under active investigation by the authors. Since the interfacial roughness determined by R-SoXR measurements are given to the nearest 0.1 nm whilst the size resolution of the model is 1 nm, we simulate two bilayers with values of  $d$  that are the R-SoXR measured interfacial width rounded up or rounded down to the nearest nanometer, before averaging the data in proportion to obtain effective data for an arbitrary  $d$ . For example, the current density for the  $d = 1.6$  nm as-spun device is a 60:40 weighted average of the current density for a  $d = 2$  nm and a  $d = 1$  nm bilayer respectively. The choice of a blend layer with a 10 nm characteristic feature size is a result of fitting, as it was found that the feature size had a weak effect on the gradient of the photocurrent voltage curves.

For the as-spun devices we set  $\nu_e/\nu_h = 1.30$ , which is the average ratio of F8BT electron to PFB hole mobility measured over the field range of interest (we fit to field-average values here as fitting the field-dependence of mobility raises some issues. We find that the field-dependence of mobility is only slightly dependent upon  $\sigma$  over physically realistic values. By contrast, the spatial arrangement of energetic disorder (i.e. whether it is correlated), and the range of hopping (i.e. variable range hopping), can exert a more significant influence upon the field-

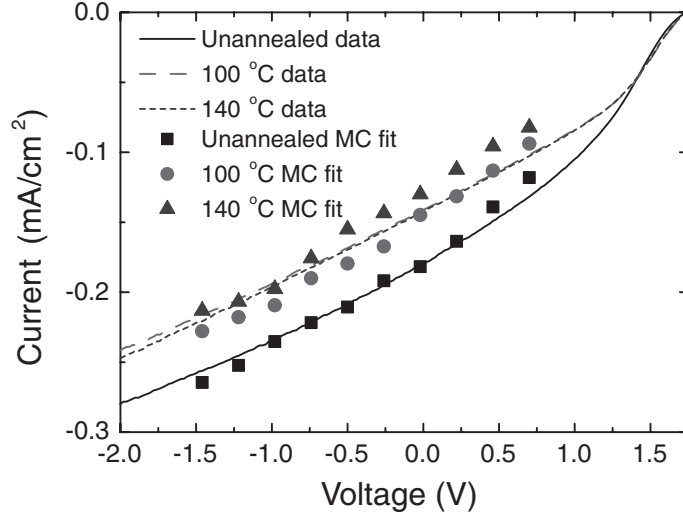


Figure 4.6: Experimental (lines) and Monte Carlo simulated (symbols) current-voltage characteristics of as-spun (solid line, squares), 100 °C annealed (dashed, circles), and 140 °C annealed (dots, triangles) devices.

dependence of mobility. However, we do not possess any experimental data for correlation of energetic disorder or the delocalization of the charge wave functions for either F8BT or PFB.) and  $d = 1.6$  nm, as in Table 1. As can be seen in Figure 4.6, good agreement is obtained when  $\nu_e = 2.6 \times 10^{10} \text{ s}^{-1}$  and  $\nu_h = 2.0 \times 10^{10} \text{ s}^{-1}$  ( $\nu_e/\nu_h = 1.30$ ). These prefactors correspond to mobilities in pristine material that are larger than those determined at low charge-carrier density on SCLC diodes [147]. This may indicate that geminate separation in this system is determined primarily by the larger on-chain mobility of F8BT [142] rather than the “average” of on- and off- chain mobilities probed by bulk measurements. For the 100 °C annealed devices the measured field-average electron mobility in F8BT and hole mobility in PFB reduce by a factor of 0.5 ( $\nu_e/\nu_h = 1.30$ ), while  $d$  increases to 1.7 nm. In accordance with these measured values, we set  $\nu_e = 1.3 \times 10^{10} \text{ s}^{-1}$ ,  $\nu_h = 1.0 \times 10^{10} \text{ s}^{-1}$ , and  $d = 1.7$  nm. Again we can see that the agreement between experiment and the model is very good, especially when one considers the absence of additional fitting. Upon further annealing to 140 °C, the field-average electron mobility in F8BT is reduced by a further factor of 0.2 when compared to the 100 °C annealed device, while the hole mobility in PFB stays substantially similar ( $\nu_e/\nu_h = 0.26$ ), and  $d$  increases to 6.2 nm. Following the same procedure, we modify the electron and hole mobility prefactors by the amount seen in experiment to  $\nu_e = 2.6 \times 10^{10} \text{ s}^{-1}$ ,  $\nu_h = 1.0 \times 10^{10} \text{ s}^{-1}$  ( $\nu_e/\nu_h = 0.26$ ) to obtain the good agreement seen in Figure 4.6.

As an aside, it should be noted that the  $J - V$  curves for the as-spun, 100 °C and 140 °C

annealed devices were reproduced to better than  $0.02 \text{ mA cm}^{-2}$  accuracy using only 3 common fitted parameters, namely the characteristic feature size of the blend used to construct the bilayer, the mobility prefactor for the as-spun device, and the choice of the exciton generation rate. This shows that despite the shortcomings of mesoscopic Monte Carlo models in comparison to their more detailed counterparts [158], they still retain sufficient detail to allow quantitative analysis.

Returning to the data, when increasing the annealing temperature from  $100 \text{ }^\circ\text{C}$  to  $140 \text{ }^\circ\text{C}$ , the F8BT electron mobility drops significantly and, on this basis, one would expect that the short-circuit current and fill factor would reduce due to increased geminate recombination [126]. Furthermore, the  $140 \text{ }^\circ\text{C}$  annealed bilayer has a wider, blend-like interface that is not optimal for charge separation since the carriers are spatially confined in their respective phases that hinders the charge separation process. This is reflected in the carrier collection efficiency measured by the simulation,  $\eta_{cc}$ , which at  $-1.2 \text{ V}$  (where simulated data matches experiment very well) for the  $100 \text{ }^\circ\text{C}$  annealed device  $\eta_{cc} = 36.7\%$ , whereas for the  $140 \text{ }^\circ\text{C}$  annealed device  $\eta_{cc} = 24.9\%$ .

To examine the relative contributions of increased interfacial roughness and reduced mobility to the reduction in collection efficiency  $\eta_{cc}$ , we also simulated the  $J - V$  curve for a bilayer with  $6.2 \text{ nm}$  interfacial roughness, as in the  $140 \text{ }^\circ\text{C}$  annealed device, but with the same mobility parameters as the  $100 \text{ }^\circ\text{C}$  annealed device, and found the carrier collection efficiency at  $-1.2 \text{ V}$  to be  $29.8\%$ . Thus, by comparing the  $100 \text{ }^\circ\text{C}$  and  $140 \text{ }^\circ\text{C}$  annealed devices discussed immediately above, approximately half of the reduction in  $\eta_{cc}$  at short circuit from the  $100 \text{ }^\circ\text{C}$  device to the  $140 \text{ }^\circ\text{C}$  annealed device is attributed to the decrease in charge carrier mobility, whilst the remaining half of the loss in  $\eta_{cc}$  is due to the increased roughening of the interface. It is perhaps surprising that only a  $6.2 \text{ nm}$  thick interfacial layer, which is much shorter than the lengthscale over which geminate charges experience a strong Coulombic attraction ( $\sim 15\text{-}20 \text{ nm}$ ), can have such a profound effect on the separation efficiency. This is a key result, as it shows that rough interfaces in bilayers and blends will severely hamper their performance, and as such identifies clean and sharp interfaces as a key requirement for high-efficiency solar cells. Noting the identical short-circuit currents of the  $100 \text{ }^\circ\text{C}$  and  $140 \text{ }^\circ\text{C}$  annealed device, the drop in geminate separation efficiency for increased annealing at  $140 \text{ }^\circ\text{C}$  is balanced by the rougher interface providing better exciton dissociation.

Our combined experimental-modeling study has therefore shown that the device performance of polymer heterojunction solar cells is sensitive to the structure of the donor/acceptor interface. While increased interface width can be beneficial to device performance in terms of increased exciton dissociation probability, such benefits can be offset by decreases in charge separation efficiency due to the confinement of electron-hole pairs at the interface. Thus while domain size and morphology are key structural considerations when optimizing device per-

formance, the structure of the domain interfaces should also be considered. Interestingly our results indicate a preference for non-equilibrium sharp interfaces as produced by the lamination method that will not naturally be produced by solution-processed blends. The observation that non-equilibrium, sharp interfaces afford higher charge separation efficiencies than “natural” interfaces has significant implications. As the interfacial width of solution-processed and annealed blends will always be larger than that of laminated bilayers, a sub-optimum charge separation efficiency can always be expected in polymer/polymer blends. Interestingly, due to the spherical geometry and rigid nature of C60 and related fullerene molecules, polymer/fullerene composites are likely to have locally sharper interfaces than polymer/polymer composites. Furthermore, pure crystalline domains, at least in P3HT, might lead to relatively sharp interfaces and may also play a critical role in fullerene-based devices. Of course there are other factors that may explain the superior operation of polymer/fullerene devices such as the higher electron affinity and charge mobility of fullerene derivatives compared to polymers. Nevertheless, microstructurally all-polymer blends may have an intrinsic interfacial disadvantage over polymer/fullerene blends. To promote sharp interfaces in all-polymer blends, highly incompatible polymer pairs (high  $\chi$ ) or highly non-equilibrium processing methods should be favored; however, since high  $\chi$  polymer pairs cannot be co-dissolved, new processing methods such as differential solvent casting may need to be developed, and may require a new synthesis perspective for PV materials similar to that already practised for organic light-emitting diodes [159, 115].

#### 4.4 Conclusions

We have investigated the influence of annealing on the device performance of PFB/F8BT donor/acceptor bilayers. The interfacial width has been measured to systematically increase with annealing temperature from 1.6 nm for pristine laminated bilayers to 16 nm with annealing at 200 °C. Photoluminescence was also observed to increase with annealing, with a three-fold increase in the number of excitons dissociated in films annealed at 140 °C and 180 °C compared to the unannealed bilayer. Despite increases in exciton dissociation efficiency due to increases in interfacial area, device performance is observed to systematically decrease with annealing. With the aid of a Monte Carlo simulation this decrease in device performance with annealing is attributed partly to a decrease in the electron and hole mobilities of F8BT and PFB respectively, but is also significantly due to a decrease in the separation probability of interfacial electron-hole pairs due to increased disorder at the interface. Our results indicate that non-equilibrium, sharp interfaces are optimal for charge separation and that control of interface structure in solution-processed blends should be considered in order to maximize device efficiency.

## 4.5 Experimental section

### 4.5.1 Materials, sample and device preparation

PFB and F8BT were supplied by Cambridge Display Technology Ltd. and used as received. PFB had a molecular weight ( $M_w$ ) and polydispersity (PDI) of  $168 \text{ kg mol}^{-1}$  and 2.8 respectively, while the  $M_w$  of F8BT was  $190 \text{ kg mol}^{-1}$  and PDI 1.9. Films were spin-coated from p-xylene with thickness of typically 60 nm. PFB/ F8BT bilayers were prepared by first spin-coating PFB onto the desired substrate (Spectrosil quartz for photoluminescence studies or poly(3,4- ethylenedioxythiophene):polystyrene sulfonic acid (PEDOT:PSS)-coated indium-tin oxide/glass substrates for device fabrication). F8BT was then spin-coated onto a cleaned and oxygen plasma-treated glass slide and floated off onto deionized water. The PFB-coated substrate was then lowered and laminated onto the air-side of the floating F8BT film and picked up. Substrates were then placed overnight to dry in a vacuum chamber with pressure of less than  $10^{-6}$  mbar. Devices were completed by transferring to a nitrogen glove box and evaporating 100 nm of aluminum in a vacuum of better than  $10^{-6}$  mbar. Samples were annealed by placing on a hotplate in the glove box at the desired temperature for 10 minutes then quenching to room temperature. The results presented here are for devices annealed after aluminum deposition, however devices were also made that were annealed before aluminum evaporation with the same results observed. Hole-only PFB devices were fabricated by spin-coating a 170 nm thick PFB layer on top of an ITO/PEDOT:PSS electrode and evaporating a gold top electrode. Electron-only F8BT devices were fabricated by evaporating an aluminum electrode onto a PEDOT:PSS-coated ITO substrate (the underlying PEDOT:PSS layer helps to smooth the evaporated aluminum electrode [160]) followed by a spin-coated 390 nm thick F8BT layer and evaporation of a calcium electrode with a protective aluminum over-layer. Devices were encapsulated before removal and testing. Current-voltage measurements were performed using a Keithley 237 SMU under  $100 \text{ mW cm}^{-2}$  AM1.5G irradiation (Oriel 81160-1000 solar simulator) or in the dark for electron- and hole- only measurements. Photoluminescence spectra and efficiencies were measured at room temperature in a nitrogen-purged integrating sphere with excitation from an argon ion laser at 488 nm that selectively excites F8BT and detection with an Oriel Instaspec IV spectrometer.

### 4.5.2 Resonant soft X-ray reflectivity measurements

R-SoXR data were acquired at beamline 6.3.2 at the Advanced Light Source (ALS) in Berkeley, CA [82], following previously established protocols that avoid radiation damage [72]. To achieve higher sensitivity, the more aromatic PFB was laminated on top of F8BT that was pre-coated onto a silicon substrate. Simulations and fits were performed using the non-commercial program

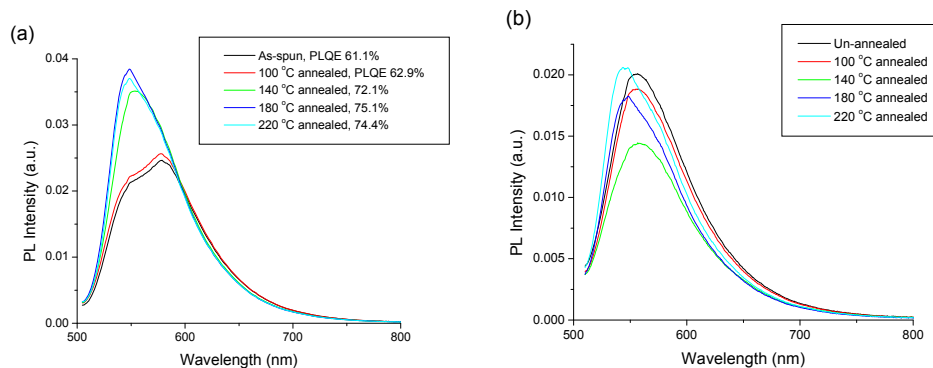


Figure 4.7: (a) Photoluminescence spectra of neat F8BT films as a function of annealing. (b) Photoluminescence spectra of PFB / F8BT bilayers annealed at different temperatures.

IMD [84]. The data and fits show a discrepancy in the low  $q$ -region that has been traced to spectral contamination. The  $q$  range used to extract parameters for the fits has therefore been restricted to  $0.2\text{-}2.5\text{ nm}^{-1}$ . At least five spots  $100\text{ }\mu\text{m}$  by  $300\text{ }\mu\text{m}$  in size were characterized on each sample at 282.4 and 284 eV, except for the 180 °C sample for which only two spots were measured. Some data sets had obvious outlayer data points. They were always much larger than those that clustered at lower values. Since the films were prepared by floating with the laminated film crinkled in parts, the large widths measured in some spots are likely to correspond to these areas. Hence, averages for the interfacial width have been calculated from the spots with the three smallest interfacial widths for each of the two photon energies utilized.

## 4.6 Acknowledgements

This work was supported at the University of Cambridge by the Engineering and Physical Sciences Research Council, U.K. (Advanced Research Fellowship EP/E051804/1). Work by NCSU supported by the US Department of Energy, Office of Science, Basic Energy Science, Division of Materials Science and Engineering for support under contract DE-FG02-98ER45737. ALS is supported by the US Department of Energy, Office of Basic Energy Science. The authors thank Cambridge Display Technology Ltd. for the supply of conjugated polymers used in this study. Simulations were carried out on the Durham University “Hamilton” Supercomputing cluster.

## 4.7 Supporting information

This section includes Figure 4.7, 4.8, and 4.9.

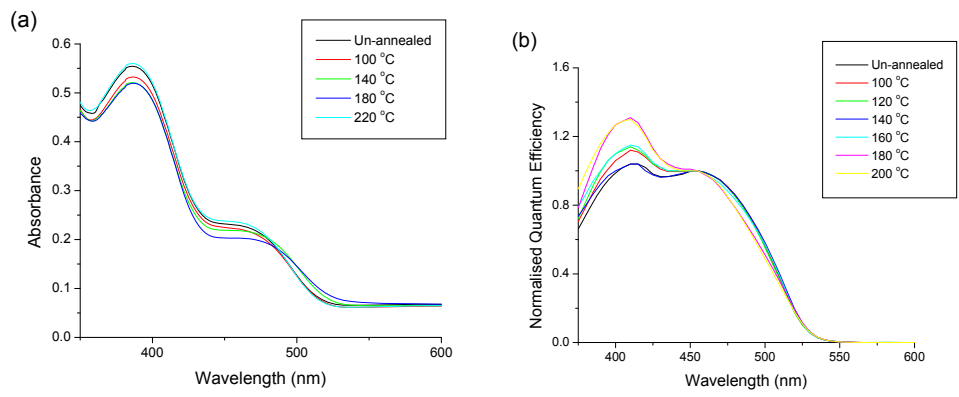


Figure 4.8: (a) UV-vis absorption spectra of PFB / F8BT bilayers as a function of annealing. (b) Normalized external quantum efficiency spectra of PFB / F8BT bilayer devices.

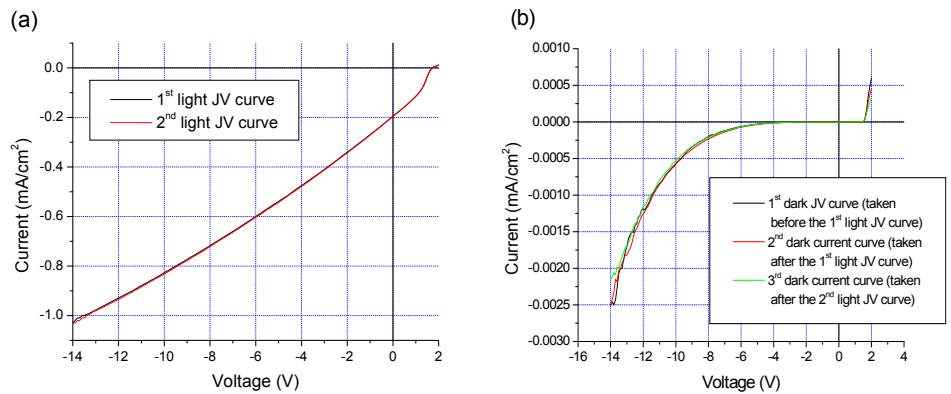


Figure 4.9: (a) Current voltage scans taken of the 140 °C annealed device under AM1.5G illumination demonstrating the stability of the device under high reverse bias. (b) A series of dark current voltage curves taken before and after the light current voltage curves in part (a) demonstrating reproducibility and the absence of breakdown. Note the different current scales, with the dark current 400 times lower than the photocurrent at  $-14$  V.

## Chapter 5

# Influence of dielectric-dependent interfacial widths on device performance in top-gate P(NDI2OD-T2) field-effect transistors

The physical properties of the semiconductor/dielectric interface in an OFET are critically important to the device performance. For example, the interfacial roughness of the semiconductor/dielectric interface induces structural disorder, resulting trap states that will reduce the charge transport efficiency. Despite this importance, few studies have ever attempted to measure the interfacial structure and relate it to device performance. This is mainly because of the difficulty to probe the buried interface, especially the interfaces between polymers, due to the low contrast between the constituents. In addition, in P(NDI2OD-T2)-based top-gate field-effect transistors, previous reports observed an absence of the expected dipolar disorder effect on the performance of the OFETs in this novel high mobility n-type devices, but the reason has never been understood beyond hypothesis. Our work presented in this chapter for the first time determine with high precision the interface roughnesses of the buried semiconductor/dielectric interfaces in an OFET. We demonstrate that the deposition of the polymer dielectric on top of the semiconducting polymer significantly affects the interface structure, even when the dielectric is cast from the same orthogonal solvent. This exposes explicit and implicit assumptions about device fabrication as problematic. Our measurements explain the relative negligible effect of dipolar disorder on the mobility in P(NDI2OD-T2)-based OFETs, which has confounded

the field so far as the interpretation of device performance was based on the assumption that differential casting will not affect interfacial properties. Our discoveries challenge assumptions in the field and will lead to better control over OFET interfacial properties and thus to higher performance devices.

This work has been submitted to *Applied Physics Letters*. Authors of this article include Hongping Yan, Torben Schuettfort, Auke J. Kronemeijer, Christopher R. McNeill, and Harald Ade. I took the R-SoXR data and completed the full analysis of them. The high quality numerical fits of the reflectivity profiles are successfully achieved, even at energies around fluorine 1s absorption edge. I also took the NEXAFS spectra and performed the optical constants calculations of the polymers as reference of experiments and initial values of numerical fits. Torben Schuettfort and Christopher R. McNeill provided the samples used in this study. All coauthors contribute to the discussions and the finalizing of the article.

## 5.1 Abstract

Resonant Soft X-ray Reflectivity (R-SoXR) is employed to determine the interfacial widths of the semiconductor/dielectric interface in P(NDI2OD-T2)-based top-gate organic field-effect transistors (OFETs). It is shown that the deposition of a polymer dielectric on top of a semiconducting polymer layer can affect the interface structure, even when cast from an orthogonal solvent. The observed differences in the interfacial widths for different dielectrics explain the insensitivity of OFET performance to dielectric choice for OFETs fabricated using an identical fabrication protocol. The R-SoXR results demonstrates that differences in the physical interface structure should be taken into account when considering the influence of polymer dielectrics on the performance of all solution-processed OFETs. Specifically, the importance of the choice of solvent for the deposition is highlighted.

## 5.2 Introduction

Organic field-effect transistors (OFETs) have received significant attention due to their potential application in low-cost flexible electronics [161, 162]. Polymer dielectrics are being increasingly used in OFETs as they facilitate n-type operation[96] and allow for top-gate transistors to be fabricated via sequential solution deposition from orthogonal solvents. Due to the geometry and electrostatics of OFETs, charge transport occurs in a few nanometer thick accumulation layer at the semiconductor/dielectric interface [95]. Charge transport is thus governed not only by the energetic disorder introduced by the randomly oriented static dipoles in the dielectric, but also by the structural disorder introduced by interfacial roughness [163]. The extent of this so-called dipolar disorder is governed by the dielectric constant,  $k$ , of the dielectric and the interaction

strength with the conjugated backbone. Indeed, it is reported in the seminal work of Veres et al. that the hole mobility decreased by a factor of  $\sim 20$  upon increasing the dielectric constant from  $\sim 2.0$  to  $\sim 3.6$  in OFETs based on the amorphous polymer polytriarylamines (PTAA) [164]. The influence of the dielectric on the performance of OFETs has been the subject of much other study as well [165, 166, 167].

Despite the critical importance of both the physical and energetic structure of the semiconductor/dielectric interface in OFETs, very few studies have been devoted to the physical structure of the polymer semiconductor/polymer dielectric interface as employed in top-gate OFETs [108, 168]. Instead, it is generally assumed that the use of orthogonal solvents does not lead to changes in the structure of the interface [165]. Variation in device performance is generally explained solely in terms of differences in the dielectric permittivity [169, 170]. Recent work on organic light-emitting bilayers has shown that the interface structure can, however, change slightly even with the use of orthogonal solvents [115, 171]. Here we determine the quality, i.e. the interfacial widths, of the semiconductor/dielectric interface in poly([N,N'- bis(2-octyldodecyl)- naphthalene- 1,4,5,8- bis(dicarboximide)- 2,6- diyl]- alt- 5,5'- (2,2'-bithiophene)) (P(NDI2OD-T2)) based top-gate OFETs and relate these measured interfacial widths to device performance. It is shown for various dielectrics that the deposition of a polymer dielectric on top of a semiconducting polymer layer affects the interface structure even when the dielectric is deposited from an orthogonal solvent. The observed differences explain the previously reported absence of the dipolar disorder effect on the performance of OFETs that were fabricated using an identical fabrication protocol [170]. Consequently, differences in the physical interface structure need to be taken into account when evaluating the influence of polymer dielectrics on the performance of top-gate OFETs.

The polymer P(NDI2OD-T2) is a recently-developed n-type semiconductor demonstrating electron mobilities of up to  $0.85 \text{ cm}^2 \text{ V}^{-1} \text{ s}^{-1}$  in bottom-contact, top-gate transistors [116]. In contrast to reports of the dependence of mobility on dielectric permittivity for other organic semiconductors, Yan et al. reported that the electron mobility of P(NDI2OD-T2) in OFETs was relatively insensitive to the dielectric constant of the polymer dielectric. It was speculated that the long 2-octyldodecyl side chains decoupled the semiconductor core from the dipoles in the dielectrics. Caironi et al. observed a similar insensitivity of the electron mobility, noting that “the substantial insensitivity of the mobility to the degree of dipolar energetic disorder at the dielectric-semiconductor interface is intriguing” [170]. In contrast, in a more recent study using high- $k$  dielectrics Li et al. observed a strong dielectric-dependence of the mobility of P(NDI2OD-T2) in OFETs with a face-on packing of the P(NDI2OD-T2) molecules in the thin films [117]. Furthermore, by using methyl ethyl ketone rather than n-butyl-acetate as a differential solvent, Li et al. achieved higher mobilities than Caironi et al. when using PMMA and PS as dielectrics [172]. In order to understand the observed differences, the effect of solvent

casting on the buried interfacial structure has to be characterized by an in-situ method after the deposition of the dielectric. Atomic Force Microscopy (AFM), which is typically used for characterizing interfacial roughness, is unsuitable for in-situ characterization [172].

### 5.3 Results and discussion

Here we use Resonant Soft X-ray Reflectivity (R-SoXR) to directly determine the interfacial widths of semiconductor/dielectric interfaces in top-gate P(NDI2OD-T2) based field-effect transistors [71]. By tuning the soft X-ray energy, we are able to selectively modulate the reflected intensity at various interfaces and quantitatively characterize the interfacial widths and thicknesses of the polymer films, without deuteration as required for neutron reflectivity yet with higher material-contrast than possible with hard X-rays. Bilayer structures were fabricated by sequentially spin-coating  $\sim 55$  nm P(NDI2OD-T2) and  $\sim 75$  nm dielectric layers (poly(methyl methacrylate) (PMMA), polystyrene (PS) or CYTOP, see Figure 5.4 in Supporting Information for chemical structures) on silicon wafers using the same materials and mirroring the process conditions for fabrication of top-gate devices [170]. In the R-SoXR experiment, the angle of incidence of the X-ray beam is varied while the intensity of the specularly reflected X-ray beam is monitored (see Supporting Information for further details). The measured reflectance is then plotted as a function of momentum transfer along the surface normal,  $q$  [72]. Here we will scale the reflectance by  $q^4$  to enable features across the full  $q$ -range to be highlighted. So-called Kiessig Fringes are observed that correspond to the thickness of the layers. Encoded in the data is information regarding the interfacial width that can be extracted via numerical model refinement, i.e. fits, of the reflectance profiles. A roughness with a Gaussian distribution is fitted. The procedure yields a root mean square (RMS) value which integrates over all spatial frequencies that correspond to lateral lengths scales smaller than the coherence length of the X-ray beam, i.e.  $\sim 10$   $\mu\text{m}$  [72].

Because the contrast between materials are highly energy-dependent due to the energy-dependent optical properties near an absorption edge, the soft X-ray energy can be tuned to suppress the reflection from the dielectric/vacuum and maximize that from the buried P(NDI2OD-T2)/dielectric interfaces e.g. 285.9 eV for PMMA and 281.4 eV for PS as dielectrics. Energies well below the absorption edge are used to measure the roughness of the top surface of the dielectric in the bilayer structures and of single layer P(NDI2OD-T2) reference samples (typically with an energy of 275.0 eV). The strategy to select appropriate energies has been demonstrated in previous work by Wang et al [72].

Figure 5.1 presents a selection of the obtained experimental R-SoXR data and the corresponding fits, used to determine the buried interfacial widths. For P(NDI2OD-T2)/PMMA bilayer, at 275.0 eV (trace #1), the Kiessig Fringe spacing (as fitted) corresponds to the total

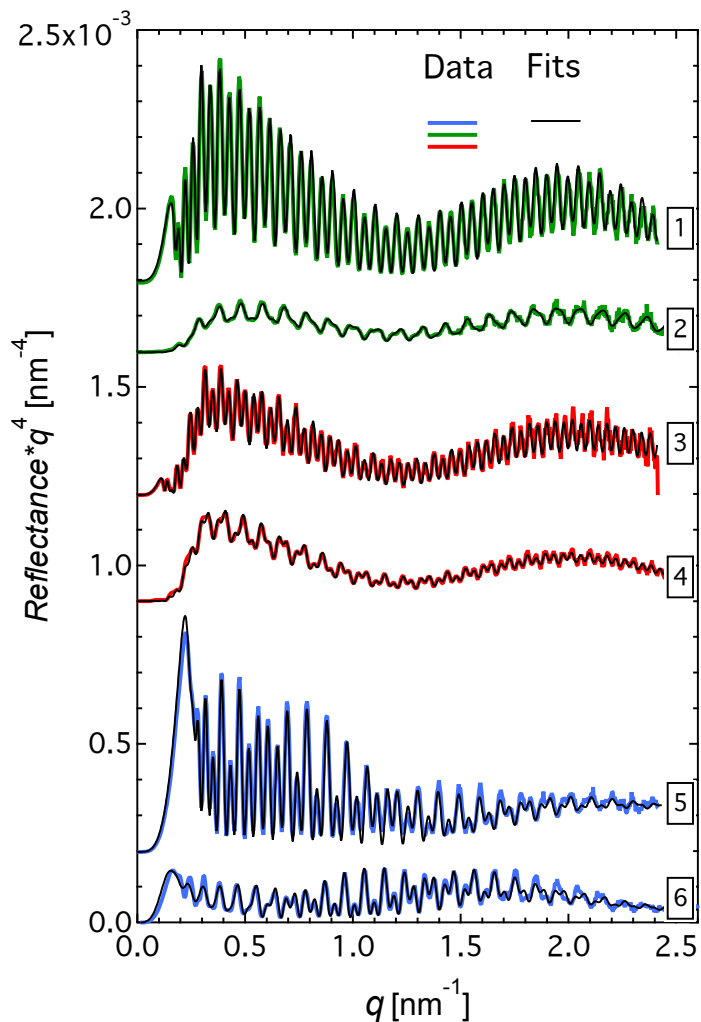


Figure 5.1: R-SoXR data (thicker lines) of bilayers on silicon substrates with various dielectrics as top layers acquired at individual energies: (1) PMMA, 275.0 eV, (2) PMMA, 285.9 eV, (3) PS, 275.0 eV, (4) PS, 281.4 eV, (5) CYTOP, 275.0 eV, and (6) CYTOP, 688.0 eV. The model refinements (fits) to the data are plotted on top of each data traces as thinner black solid lines. Data are offset vertically and (5) and (6) are scaled by a factor of 0.2 and 2, respectively, for clarity.

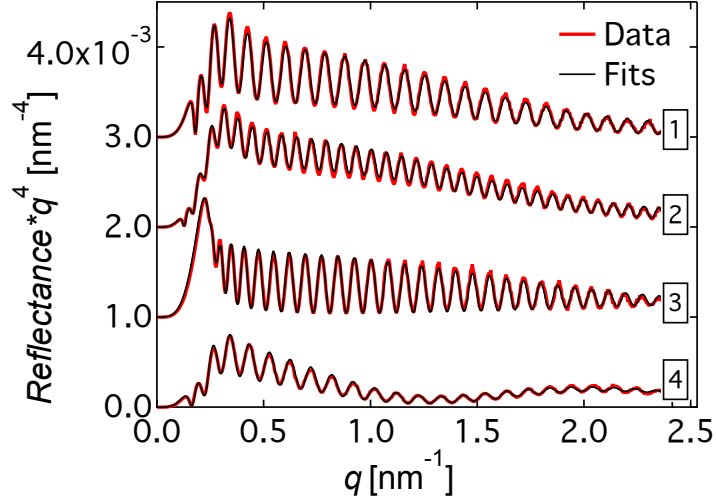


Figure 5.2: R-SoXR data and fits of single layers: (1) PMMA, (2) PS, (3) CYTOP, and (4) P(NDI2OD-T2).

thickness of both the PMMA and P(NDI2OD-T2) layers of  $2\pi/\Delta q = 126.69 \pm 0.12$  nm. At 285.9 eV (trace #2), the top layer is almost transparent to the X-ray beam. Therefore, fringes corresponding to the thickness of the bottom P(NDI2OD-T2) layer, i.e.  $2\pi/\Delta q = 60.16 \pm 0.09$  nm are observed. Data at both energies exhibit very little damping of the fringes, which is indicative of sharp PMMA/vacuum and P(NDI2OD-T2)/PMMA interfaces. Averaged over multiple positions on the investigated sample, the fits yielded interfacial widths of  $0.57 \pm 0.05$  nm and  $0.36 \pm 0.12$  nm for the PMMA/vacuum and P(NDI2OD-T2)/PMMA interfaces, respectively. For P(NDI2OD-T2)/PS bilayers, corresponding energies are 275.0 eV (Figure 5.1, trace #3) and 281.4 eV (Figure 5.2, trace #4) with averaged interfacial widths of the PS/vacuum and P(NDI2OD-T2)/PS interfaces  $0.40 \pm 0.07$  nm and  $0.92 \pm 0.10$  nm, respectively.

The R-SoXR data from the P(NDI2OD-T2)/CYTOP sample are not very selective at the carbon absorption edge. Even at the optimized energy, i.e. 275.0 eV (Figure 5.1, trace #5) both the P(NDI2OD-T2)/CYTOP and the CYTOP/vacuum interfaces contribute and fringes with two characteristic frequencies are observed. In order to provide more selective sensitivity to the polymer/polymer interface, an energy of 688 eV has been employed, which is just below the fluorine absorption edge (see trace #6 in Figure 5.2). The fits yield interfacial widths of  $1.09 \pm 0.12$  nm for the CYTOP/vacuum interface and  $1.06 \pm 0.08$  nm for the P(NDI2OD-T2)/CYTOP interface. For all data sets, the very low frequency modulation of the data corresponding to a thickness of  $\sim 3$  nm is caused by the native oxide layer on top of the silicon substrate.

In order to demonstrate how the deposition of the top dielectric layer affects the P(NDI2OD-T2)/dielectric interfacial width, single layer samples of PMMA, PS, CYTOP, and most impor-

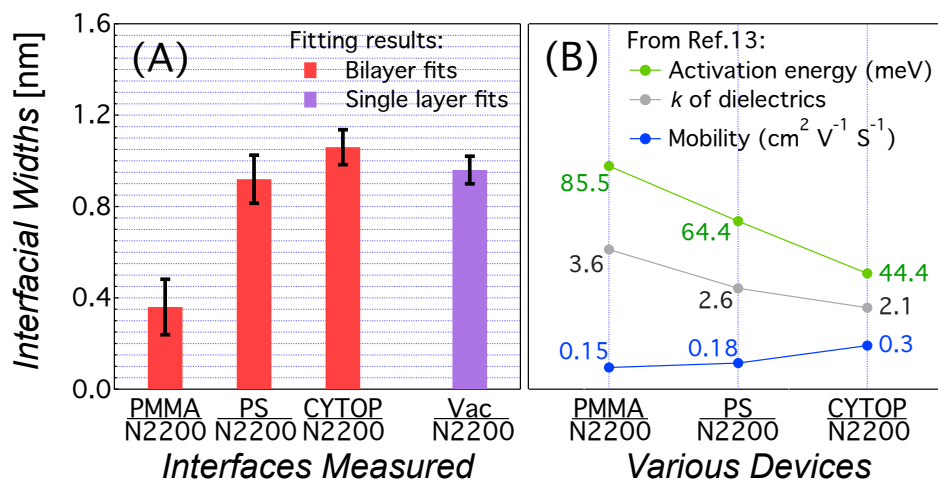


Figure 5.3: (A) Average interfacial widths of the three types of bilayer systems measured and from the surface of the P(NDI2OD-T2) single reference layer. For simplicity, “Vac” stands for “Vacuum” and the commercial name “N2200” is used for “P(NDI2OD-T2)”. The dielectric constants, transport activation energies, and mobilities for OFETs based on each type of dielectric are plotted in (B) to provide context. For clarity, note that they are plotted on their own individual y-axes, with values labeled beside each data point.

tantly P(NDI2OD-T2) were investigated to provide a reference. Representative data and fits are plotted in 5.2. These reflectance curves all show a single characteristic fringe spacing corresponding to the thickness of the single polymer layer with differences in fringe attenuation corresponding to differences in the roughness of the polymer/vacuum interface. As easily discerned by eye, the data show that the P(NDI2OD-T2)/vacuum surface is the roughest. It has been previously characterized to have a near isotropic orientation of the molecules [173]. 5.3 (A) summarizes the comparison of the interfacial widths of the bilayer structures with the single layer P(NDI2OD-T2) results. The error bars are the standard deviations of the fitting results from various spots for each interface and reflect both fitting errors and sample variations.

By comparing the roughness of the P(NDI2OD-T2) film prior to deposition of the dielectric layer to the measured roughness of the buried P(NDI2OD-T2)/dielectric interfaces, it becomes clear that the deposition of the dielectric layer changes the initial surface structure of the P(NDI2OD-T2) layer. Before spin-coating of the dielectric layers the roughness of the bottom P(NDI2OD-T2) layer is  $0.96 \pm 0.06$  nm, while after it the P(NDI2OD-T2) interfaces have widths of  $0.36 \pm 0.12$ ,  $0.92 \pm 0.10$ , and  $1.06 \pm 0.08$  nm corresponding to PMMA, PS, and CYTOP, respectively. The value for CYTOP is close to the initial roughness with a small degree of broadening since the fluorinated polymer and its solvent are known for the small degree of intermixing [174]. Little change is observed for PS, but under identical conditions the deposition

of PMMA results in a smoothing of the interface, despite casting from the *same* solvent (n-butyl-acetate) as for PS. This smoothing may be related to the different concentrations that were used for the spin-coating of the dielectrics, but could also be related to the specific chemical properties of the dielectrics promoting different degrees of phase separation. In the context of a very thin charge accumulation layer in OFETs, the observed variations of interfacial width upon spin-coating of the dielectric are of significance for device performance. The interfacial widths potentially affect the interfacial electronic structure and hence the charge transport properties in the accumulation layer of the P(NDI2OD-T2). While it is difficult to predict how changes in interfacial width will affect charge transport in detail, it is interesting to compare the measured widths with the properties of fabricated P(NDI2OD-T2) transistors.

We have deliberately matched our sample fabrication to the OFET device fabrication used by Caironi et al. [170]. Similar to Yan et al., who also used acetate solvents for deposition of the dielectrics, Caironi et al. observed that the field-effect mobility was largely unaffected by the permittivity of the dielectric material. Transistors with CYTOP were found to have only a slightly higher mobility compared to PS and PMMA, i.e.  $\sim 0.3 \text{ cm}^2 \text{ V}^{-1} \text{ s}^{-1}$  for CYTOP,  $\sim 0.18 \text{ cm}^2 \text{ V}^{-1} \text{ s}^{-1}$  for PS and  $\sim 0.15 \text{ cm}^2 \text{ V}^{-1} \text{ s}^{-1}$  for PMMA based transistors. Caironi et al. also characterized the temperature-dependence of charge transport and used charge modulation spectroscopy (CMS) to examine the polaronic nature of the charge carriers. They observed a strong dependence of the activation energy of the mobility on the type of dielectric used, with CYTOP transistors possessing a significantly lower activation energy (44 meV) than PS (64 meV) and PMMA (86 meV) transistors, meaning that the polaron localization increases significantly from CYTOP transistors to PS and PMMA.

The differences in the dielectric constant of PMMA ( $k = 3.6$ ), PS ( $k = 2.6$ ) and CYTOP ( $k = 2.1$ ) can qualitatively account for the reduced activation energies with decreased dielectric permittivity as a result of the interfacial dipolar disorder effect. Nevertheless, charge localization due to dipolar disorder is expected to significantly affect the mobility of charges in the transistor channel, which has not been observed. However, the physical structure of the semiconductor/dielectric interface inferred from our R-SoXR results can be used to understand the behavior.

The OFET device characteristics are not only affected by the intrinsic dielectric permittivity but also by the physical interface structure between the semiconducting layer and the dielectric. 5.3 demonstrates that while the dielectric constant increases when substituting CYTOP for PS and PMMA, concurrently the quality of the interface is increased, i.e. the interfacial widths decrease. A rough interface introduces trap states and charge barriers that are expected to reduce the mobility of charges in the channel [175]. Furthermore, the percolation pathway along the surface may be larger. The reduction in interfacial roughness therefore counteracts the reduction in mobility due to increased static dipolar disorder, creating the illusion that

charge transport in these OFETs is to a large extent not affected by dipolar disorder. While it is not possible here to completely disentangle the influences of the physical interface structure and the extent of dipolar disorder, our results show that the influence of the interfacial widths for different polymer dielectrics is non-negligible and should be considered as a contributing factor to the observed dielectric-dependence of transistor properties. Indeed, the effect of dipolar disorder in P(NDI2OD-T2) OFETs has recently been unambiguously demonstrated by Li et al [172]. The critical difference between the studies of Caironi et al. and Li et al. is the use of different solvents for the fabrication of the OFETs. This highlights that the choice of solvent is of critical importance for the quality of the interface between semiconductor and dielectric. The advantage of the R-SoXR measurement is that it can discern resulting differences in interface roughness. Therefore, the application of R-SoXR for characterizing the buried interfaces of all-organic FETs will assist in the understanding and optimization of device performance.

## 5.4 Conclusion

In summary, we have used R-SoXR to directly probe the structure of the buried interface in P(NDI2OD-T2)/dielectric bilayers as employed in top-gate OFETs. It has been demonstrated that for the dielectrics PMMA, PS and CYTOP, the deposition of the polymer dielectric on top of the semiconducting polymer significantly affects the interface structure, even when the dielectric is deposited from an orthogonal solvent. The determined interfacial roughnesses explain the relative absence of the effect of dipolar disorder on the mobility in P(NDI2OD-T2) FETs.

## 5.5 Acknowledgements

The authors thank E. Gullikson and A.L.D. Kilcoyne for their support with the experiments. Work at NCSU is supported by NSF (DMR-0906457, ARRA). H. Yan is partially supported by an ALS Doctoral Fellowship. This work was partly supported by the EPSRC (EP/E051804/1) and the ARC (FT100100275). R-SoXR data and reference NEXAFS spectra acquired at beamline 6.3.2. and 5.3.2.2., respectively, at the ALS, which is supported by DOE (DE-AC02-05CH1123).

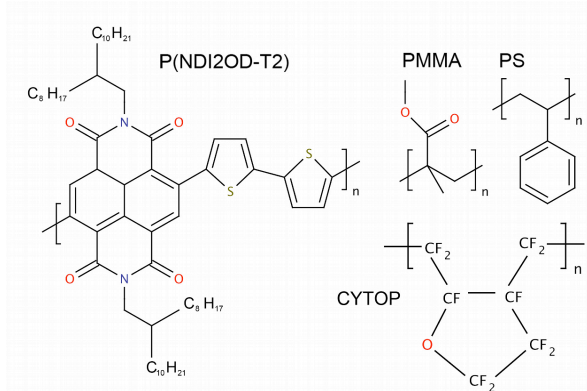


Figure 5.4: Chemical structures of the active layer P(NDI2OD-T2), and the dielectrics PMMA, PS, and CYTOP.

## 5.6 Supporting information

### 5.6.1 Experimental details

P(NDI2OD-T2), specified with a number average molecular weight ( $M_n$ ) of 25.4 kD and polydispersity index (PDI) of 4.03, was purchased from the Polyera Corporation, USA. Poly(methyl methacrylate) (PMMA) and polystyrene (PS) with a weight average molecular weight ( $M_W$ ) of 1,000 kg mol<sup>-1</sup> and 120 kg mol<sup>-1</sup>, respectively, were purchased from Sigma-Aldrich, and CYTOP CTL-809M was used as received from Asahi Glass. P(NDI2OD-T2) thin films were prepared by spin-coating from a 20 mg mL<sup>-1</sup> dichlorobenzene solution onto electron conducting (antimony doped) silicon wafers. The film thickness was determined using a profilometer (Veeco Dektak 3) to be around 55 nm. The P(NDI2OD-T2) films were subsequently annealed at 110 °C for 20 min in nitrogen atmosphere and quickly cooled to room temperature. Deposition of the gate material was also performed by spin-coating from orthogonal solvents (n-butyl-acetate for PS and PMMA and perfluorotributylamine for CYTOP) using spin-conditions that yielded a film thickness of 75 nm measured with the profilometer on a pristine silicon wafer. No further heat treatment was performed on the bilayers after deposition of the gate materials. The fabrication procedures are elaborately designed to mirror the process conditions for the fabrication of top-gate FETs by Caironi et al. [170].

Near edge X-ray absorption fine structure (NEXAFS) spectra of reference pristine single layer samples were acquired at beamline 5.3.2 at the Advanced Light Source (ALS) [41]. These spectra were used to derive the optical constants of the materials. The optical constants were then used to predict contrast and provide initial values for the fits and simulation. R-SoXR data were acquired at beamline 6.3.2 at the ALS in a high vacuum ( $\sim 10^{-7}$  torr) [82], following pre-

viously established protocols [72]. To detect and avoid radiation damage, which can cause mass loss and spectral change [118, 83], multiple scans were taken and the samples were translated to expose a fresh sample area. Simulations and fits were performed using the non-commercial program IMD [84]. The R-SoXR data and fits occasionally showed some discrepancy in the low  $q$ -region that has been traced back to spectral contamination. The  $q$  range used to extract parameters from the fits is therefore occasionally restricted to  $\sim 0.2 - 2.5 \text{ nm}^{-1}$  [74].

## Chapter 6

# Correlating the efficiency and nanomorphology of polymer blend solar cells utilizing resonant soft X-ray scattering

As a promising semiconducting polymer, poly [N,N'- bis(2- octyldodecyl)- naphthalene- 1,4,5,8- bis(dicarboximide)- 2,6-diyl]- alt-5,5'- (2,2'- bithiophene) (P(NDI2OD-T2)) is reported to be a high-mobility electron-transport material that can be used as n-channel material in OFETs or blended with an donor material for use in OPVs. Poly((9,9- dioctylfluorene)- 2,7-diyl-alt-[4,7-bis(3- hexylthien-5-yl)- 2,1,3- benzothiadiazole]- 2',2''-diyl) is another interesting polymer mainly because it is the record-keeper yielding an device efficiency of  $\sim 2\%$  amongst all-polymer organic solar cells. Enhanced scattering contrast afforded by R-SoXS is used to probe the nanomorphology of all-polymer solar cells based on blends of the donor poly(3-hexylthiophene) with either the acceptor (F8TBT) or (P(NDI2OD-T2)). A bimodal distribution of domain sizes is observed for P3HT:P(NDI2OD-T2) blends with smaller domains evolve with annealing while larger domains insensitive to annealing. P3HT:F8TBT blends in contrast show a broader distribution of domain size but with the majority structured on the smaller length scale. For both blends an evolution in device performance is observed that is correlated with a coarsening and purification of domains on the 5 – 10 nm length scale. Grazing-Incidence Wide Angle X-ray Scattering (GI-WAXS) is used to investigate crystal size in these blend thin films. Besides the discoveries of the nanomorphology of the devices, this work highlights the complementarity of R-SoXS and GI-WAXS.

This work has been published on *ACS Nano*, with DOI: 10.1021/nm204150f. This article is

by Hongping Yan, Brian A. Collins, Eliot Gann, Cheng Wang, Torben Schuettfort, Christopher R. McNeill, and Harald W. Ade. In this study, I took the R-SoXS data and the GIWAXS data. I completed the data analysis of R-SoXS data to extract the domain size and purity information under various annealing conditions. To determine the crystal size and to compare the crystallinity across the polymer blend samples, I performed the Sherrer analysis on the GIWAXS data, with the instrumental broadening correction applied. In this study, I also took the NEXAFS data for the polymers and performed optical constants calculations of them. Brian A. Collins and Eliot Gann helped with the R-SoXS and GI-WAXS data taking. Cheng Wang helped with R-SoXS instrumentation. Torben Schuettfort and Christopher R. McNeill provided the samples and device characterizations in this study.

## 6.1 Abstract

Enhanced scattering contrast afforded by resonant soft X-ray scattering (R-SoXS) is used to probe the nanomorphology of all-polymer solar cells based on blends of the donor polymer poly(3-hexylthiophene) (P3HT) with either the acceptor polymer poly((9,9-dioctylfluorene)-2,7-diyl-alt-[4,7-bis(3-hexylthien-5-yl)-2,1,3-benzothiadiazole]-2',2''-diyl) (F8TBT) or poly([N,N'-bis(2-octyldodecyl)-11-naphthalene-1,4,5,8-bis(dicarboximide)-2,6-diyl]-alt-5,5'-(2,2'-12-bithiophene)) (P(NDI2OD-T2)). Both P3HT:F8TBT and P3HT:P(NDI2OD-T2) blends processed from chloroform with subsequent annealing exhibit complicated morphologies with a hierarchy of phase separation. A bimodal distribution of domain sizes is observed for P3HT:P(NDI2OD-T2) blends with small domains of size  $\sim 5-10$  nm that evolve with annealing and larger domains of size  $\sim 100$  nm that are insensitive to annealing. P3HT:F8TBT blends in contrast show a broader distribution of domain size but with the majority of this blend structured on the 10 nm length scale. For both P3HT:P(NDI2OD-T2) and P3HT:F8TBT blends, an evolution in device performance is observed that is correlated with a coarsening and purification of domains on the 5–10 nm length scale. Grazing-incidence wide-angle X-ray scattering (GI-WAXS) is also employed to probe material crystallinity, revealing P(NDI2OD-T2) crystallites 25–40 nm in thickness that are embedded in the larger domains observed by R-SoXS. A higher degree of P3HT crystallinity is also observed in blends with P(NDI2OD-T2) compared to F8TBT with the propensity of the polymers to crystallize in P3HT:P(NDI2OD-T2) blends hindering the structuring of morphology on the sub-10 nm length scale. This work also underscores the complementarity of R-SoXS and GI-WAXS, with R-SoXS measuring the size of compositionally distinguishable domains and GI-WAXS providing information regarding crystallinity and crystallite thickness.

## 6.2 Introduction

Polymer solar cells are an interesting new approach to low-cost solar cells utilizing semiconducting polymers for the conversion of sunlight into electricity [19]. Since tightly bound excitons rather than free charges are the main product of photo-excitation, an important step in the energy conversion process is the dissociation of these excitons into electron-hole pairs at donor/acceptor interfaces. A number of donor/acceptor approaches are used, with fullerene derivatives [19], inorganic nanocrystals [176], along with electron-accepting polymers [177] used as electron acceptors in combination with an electron-donating polymer. The utility of a material as either an electron donor or acceptor depends on the material's electron affinity, with high electron affinity materials (in general) suited as electron acceptors and low electron affinity materials suited as electron donors. The designation is relative, however, with the same material being able to serve as an electron acceptor with one material and an electron donor with another depending on the relative electron affinities of the materials [42]. Limiting the effectiveness of these materials in exciton dissociation is the relatively short exciton diffusion length of  $\sim 10$  nm [178]. In order to absorb sufficient light (film thickness  $\sim 100$  nm or greater) while maintaining short distances to donor/acceptor interfaces, the bulk heterojunction concept has proved to be an effective approach. Here, thin film blends of donor and acceptor materials are produced that have sufficient intermixing between donor and acceptor to maintain charge generation (exciton dissociation) while (ideally) percolating interconnected pathways facilitate charge transport to the electrodes. The influence of morphology on device performance has been a topic of great interest to the organic photovoltaics community [179, 180, 181], with film morphology affecting many device processes including charge generation [127, 145], interfacial charge separation [126, 123], and charge collection [157]. In general, a mixing of donor and acceptor on a length scale finer than the exciton diffusion length optimizes charge generation (exciton diffusion to and dissociation at donor/acceptor interfaces), while coarser morphologies optimize the separation of charges away from the interface and their collection at the device electrodes.

Polymer/fullerene solar cells have, to date, proved to be the most effective blend combination with power conversion efficiencies of over 8% now reported [182]. The efficiency of polymer/polymer solar cells in contrast has remained at  $\sim 2\%$  [42, 183, 184, 185, 186], largely attributed to inefficient interfacial charge separation [146, 187, 188, 189] (that is, the recombination of electron-hole pairs localized at the donor/acceptor interface subsequent to charge transfer). However, the contribution of unoptimized morphology to this lackluster performance is not fully understood. In general, it is thought that a morphology consisting of interconnected pure phases with a characteristic domain size of  $\sim 10$  nm (the exciton diffusion length) is most beneficial for device action [157]. A key challenge in the field of organic photovoltaics is the

ability to provide quantitative information about the morphology of bulk heterojunction blends used in polymer solar cells. Even for polymer/fullerene solar cells whose morphology is easier to characterize due to differences in material density (and hence analysis by traditional techniques such as transmission electron microscopy), new discoveries are being made, such as the existence of a mixed phase in addition to pure polymer and pure fullerene phases in well-studied poly(3-hexylthiophene):[6,6]-phenyl-C61-butyric acid methyl ester blends [46, 190, 191, 192]. Transmission electron microscopy (TEM) [193, 194, 195] and atomic force microscopy (AFM) [196, 197] have been the most common techniques for studying blend morphology; however, standard TEM has relatively poor chemical sensitivity and AFM is limited in being able to only provide information regarding surface topography that may or may not relate to bulk morphology. Energy-filtered TEM is increasingly being utilized that enhances the chemical sensitivity of TEM [198, 199, 200, 201], and neutron-based techniques are also being adopted to probe the structure of polymer/fullerene blends owing to the natural neutron scattering contrast between polymers and fullerenes [192, 109, 202]. X-ray scattering and diffraction using hard X-rays is also a useful technique providing information regarding molecular packing and the size of crystalline regions [203, 204], but scattering contrast from amorphous regions of different materials is low.

An alternative approach for enhanced chemical contrast with high resolution is the use of soft X-rays [112, 113]. Photons with energy close to the 1s ionization energy of carbon are able to promote electrons from the 1s orbital of carbon to unoccupied electronic orbitals. Absorption resonances are observed that are associated with the unoccupied electronic structure of the polymer, providing a means for chemical contrast even when there is no difference in elemental composition. Scanning transmission X-ray microscopy (STXM) [205] that utilizes differences in the near-edge X-ray absorption spectra of materials for chemical contrast has been employed to provide two-dimensional composition maps of bulk heterojunction blends with sub-100 nm resolution [45, 48]. The resolution of STXM is limited by the spot size achievable by zone-plate optics and by the inherent limitations associated with a two-dimensional projection of a 100 nm thick film. One way to overcome the limitations of zone-plate optics and two-dimensional imaging is to use material contrast afforded by soft X-rays in a scattering experiment. Recently, we have demonstrated the ability of resonant soft X-ray scattering (R-SoXS) to provide morphological information on the sub-10 nm length scale in conjugated polymer blends [3]. In this previous communication, blends of the polyfluorene derivatives poly(9,9'-dioctylfluorene-co-bis(N,N'-(4-butylphenyl))bis(N,N'-phenyl-1,4-phenylene)diamine) (PFB) and poly(9,9'-dioctylfluorene-co-benzothiadiazole) (F8BT) were studied that have been extensively studied with STXM. Our results revealed a hierarchy of phase separation in PFB:F8BT blends, with  $\sim 80$  nm sized domains in as-cast samples that are readily observed by STXM, and a finer length scale of intermixing on the sub-10 nm length scale not readily observed by STXM but revealed

by R-SoXS. With annealing, phase coarsening was initially observed on the length scale of a few to tens of nanometers followed by coarsening of the larger domains at higher temperatures [3].

In this contribution, we utilize R-SoXS to study two more recently developed and more efficient polymer/ polymer systems for which little detailed morphological information exists. In particular, we study blends of the donor polymer poly(3-hexylthiophene) (P3HT) with the acceptor polymer poly((9,9-dioctylfluorene)-2, 7-diyl-alt-[4,7-bis(3-hexylthien-5-yl)-2,1,3-benzothiadiazole]-2',2''-diyl) (F8TBT), along with blends of P3HT with the acceptor poly([N,N'-bis(2-octyldodecyl)-11-naphthalene-1,4,5,8-bis(dicarboximide)-2,6-diyl]-alt-5,5'-(2,2'-12-bithiophene)) (P(NDI2OD-T2)). P3HT:F8TBT blends represent one of the most efficient all-polymer solar cell systems to date [42], while P3HT:P(NDI2OD-T2) blends [188] are of interest due to the exceptional electron mobility of P(NDI2OD-T2) [116]. As a complement to the R-SoXS measurement, information about the crystal size and the qualitative degree of crystallization was derived from grazing-incidence wide-angle X-ray scattering (GI-WAXS) data. The combination of R-SoXS and GI-WAXS in particular serves as a powerful demonstration of the additional information derived from R-SoXS and the benefit of using separate techniques to probe amorphous and crystalline structure.

### 6.3 Results and discussion

Figure 6.1 presents the chemical structures of P3HT, F8TBT, and P(NDI2OD-T2) and the optical absorption spectra of neat films. P3HT and F8TBT have overlapping absorption bands in the visible region peaking at  $\sim 550$  nm, while P(NDI2OD-T2) has a low-energy charge-transfer absorption band peaking at 700 nm and extending into the near-infrared. The absorption spectrum of amorphous F8TBT is featureless, while the absorption spectra of semicrystalline P3HT and P(NDI2OD-T2) show features associated with vibronic structure that may be related to film microstructure [206, 173]. Figure 6.2 presents the evolution of the absorption spectra of 1:1 (by weight) blend films of P3HT:F8TBT and P3HT:P(NDI2OD-T2) with annealing. These films were prepared in the same fashion using the same annealing protocol as for films used in devices and films used for structuring characterization, with all blends processed from chloroform. All films were annealed for 10 min followed by quenching to room temperature and subsequent measurements. For P3HT:F8TBT films, there is little vibronic structure in the P3HT absorption component in as-cast films, but with annealing, P3HT vibronic structure appears consistent with ordering of the P3HT phase [207, 208]. The vibronic structure in the UV-vis spectra of the annealed P3HT:F8TBT films is less prominent than that observed in neat P3HT reference shown in Figure 6.1. While overlap of the P3HT and F8TBT absorption spectra will make the P3HT vibronic structure less noticeable in blend spectra, the vibronic structure

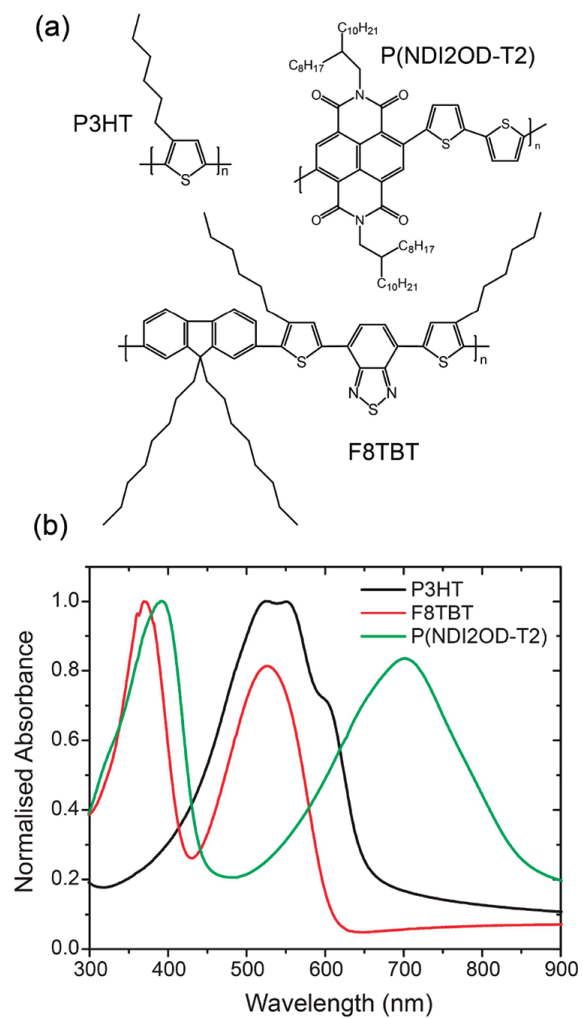


Figure 6.1: (a) Chemical structures of P3HT, F8TBT, and P(NDI2OD-T2). (b) Absorption spectra of neat films.

present in these chloroform-processed films is less prominent than observed in xylene-processed blends [208], suggesting that P3HT crystallization is hindered (see Figure S1 in the Supporting Information). For P3HT:P(NDI2OD-T2) films, a similar evolution in P3HT vibronic structure with annealing is observed, accompanied by changes in the structure of the P(NDI2OD-T2) absorption component. The vibronic structure of the P3HT phase is similar to that observed in neat P3HT, suggesting that P3HT crystallization is not hindered here. Curiously, annealing the P3HT:P(NDI2OD-T2) film at 200 °C results in a loss of structure in the absorption spectrum of both components, suggesting a melting of polymer chains and some loss of crystallinity, which has been confirmed by a comparison of GI-WAXS data of 180 and 200 °C annealed samples (see Figure S2 in Supporting Information). A loss of P3HT crystallinity due to melting with annealing at 200 °C in P3HT:[6,6]-phenyl-C61-butyric acid methyl ester (PCBM) blends has also been observed by Verploegen et al. [209].

Figure 6.3 presents the evolution of the device characteristics of P3HT:F8TBT and P3HT:P(NDI2OD-T2) photovoltaic devices with annealing. All devices were fabricated with PEDOT:PSS-coated ITO glass substrates and aluminum top electrodes (see the Experimental Section for full details). Both P3HT:F8TBT and P3HT:P(NDI2OD-T2) devices show a pronounced evolution of device performance with annealing. P3HT:F8TBT devices show a dramatic 50-fold increase in power conversion efficiency from 0.018% for unannealed devices to 0.90% for devices annealed at 180 °C. This increase is brought about by changes in both short-circuit current (a 20-fold increase) and fill factor (increase from 0.22 to 0.4). P3HT:P(NDI2OD-T2) devices show an increase in power conversion efficiency from 0.16% for unannealed devices to 0.35% for devices annealed at 140 °C. Although the short-circuit current ( $J_{sc}$ ) of P3HT:P(NDI2OD-T2) devices peaks at an annealing temperature of 160 °C, corresponding to a 3-fold increase, device performance is undermined by a monotonic decrease in the fill factor ( $FF$ ) with annealing decreasing from 0.48 for unannealed films to 0.22 for films annealed at 200 °C. Device efficiencies are consistent with previous reports [42, 188], though we note that optimized P3HT:F8TBT devices typically have a slightly thinner active layer (70 nm compared to 100 nm here) and are prepared from xylene rather than chloroform. Chloroform is used here as it results in a more intimate initial mixing of the blend components, producing a more dramatic change in device efficiency and hence facilitating study of the influence of the evolving nanomorphology during annealing on device performance. The lower P3HT crystallinity in chloroform-processed devices may also partially explain the lower efficiency of these devices, with the interplay between nanomorphology and crystallinity discussed further below. Interestingly, the current-voltage ( $J - V$ ) curves of the P3HT:F8TBT and P3HT:P(NDI2OD-T2) devices show a very different shape evolution. Although the  $J_{sc}$  of both P3HT:F8TBT and P3HT:P(NDI2OD-T2) devices is maximized for an anneal temperature of  $\sim 160 - 180$  °C, the FF of the P3HT:F8TBT devices increases monotonically with annealing while it decreases monotonically with annealing for the

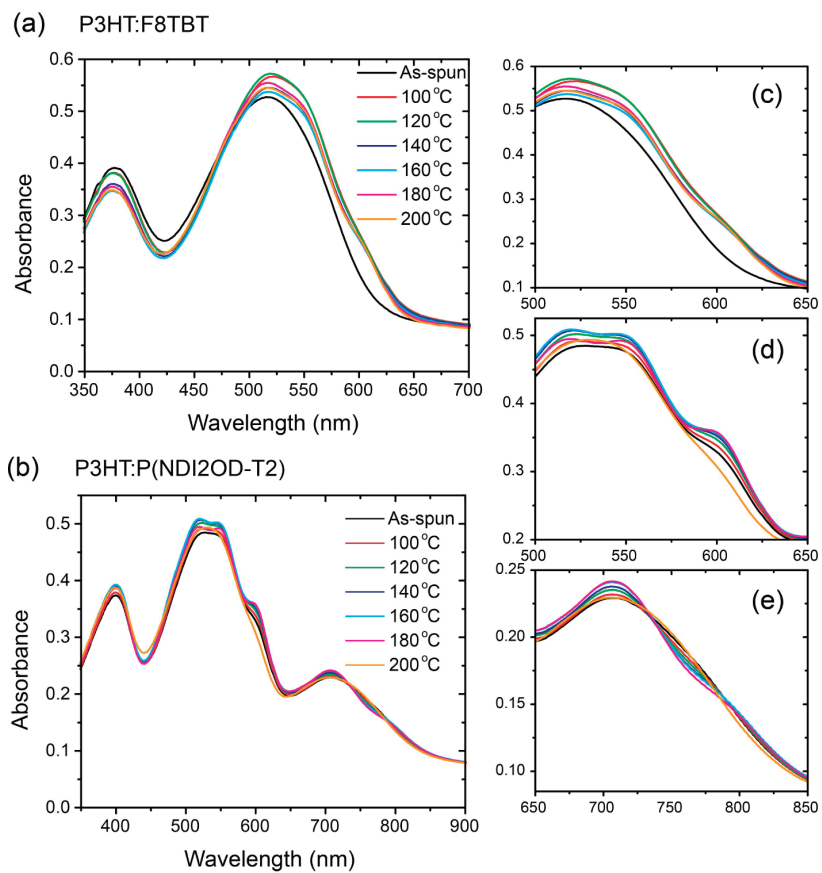


Figure 6.2: Evolution of the absorption spectra of blend films with annealing: (a) P3HT:F8TBT; (b) P3HT: P(NDI2OD-T2). (c) Changes in P3HT vibronic structure with annealing in the P3HT:F8TBT blend; (d,e) changes in P3HT and P(NDI2OD-T2) vibronic structure in the P3HT:P(NDI2OD-T2) blend with annealing.

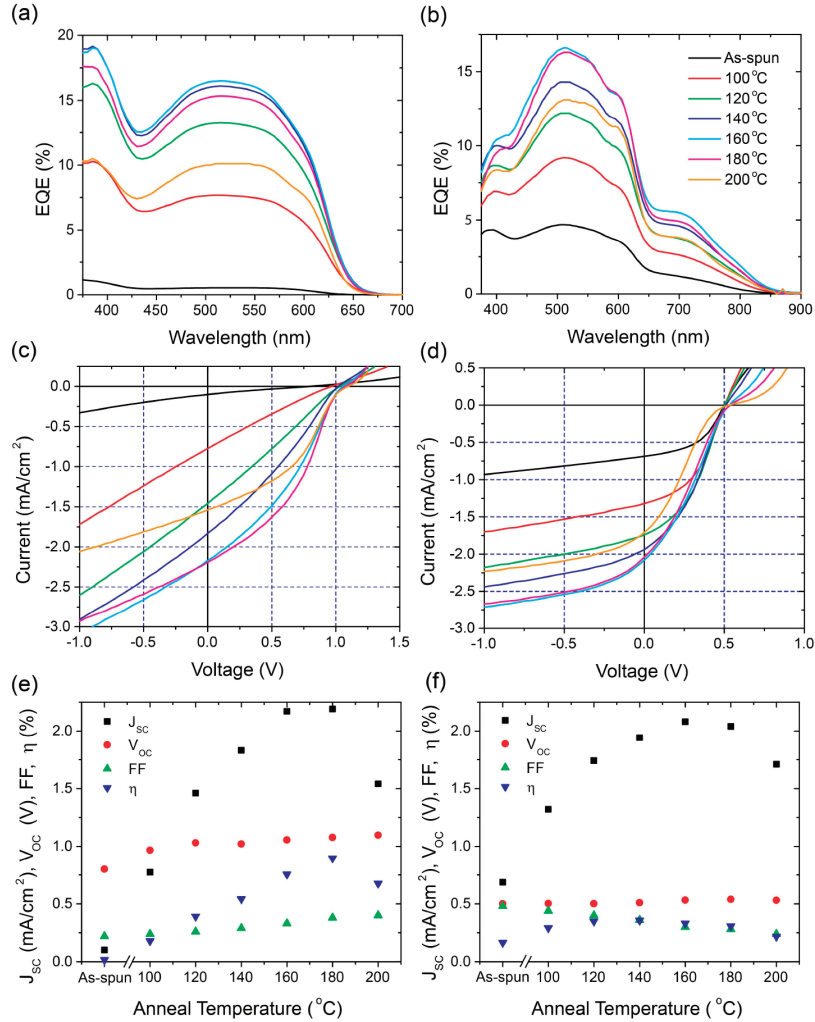


Figure 6.3: Evolution of the device characteristics of ITO / PEDOT:PSS/ P3HT: F8TBT /Al (a,c,e) and ITO/ PEDOT:PSS/ P3HT: P(NDI2OD-T2)/Al (b,d,f) devices with annealing. (a,b) Changes in the external quantum efficiency spectra, (c,d) plot of the current voltage characteristics under 100 mW/cm<sup>2</sup> AM1.5G illumination, and (e,f) summary of the evolution in short-circuit current, open-circuit voltage, fill factor, and power conversion efficiency with annealing temperature.

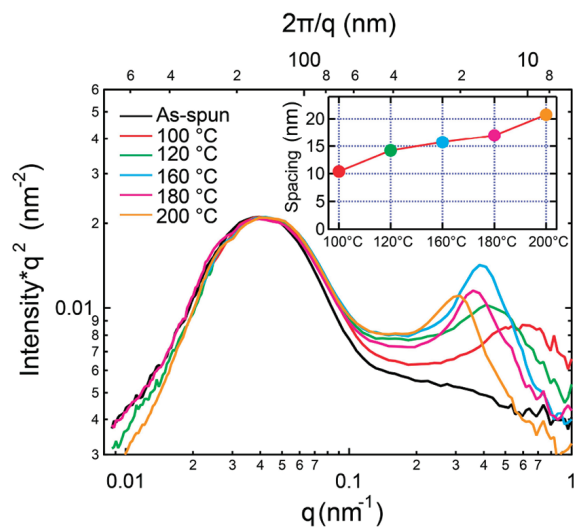


Figure 6.4: R-SoXS of P3HT:P(NDI2OD-T2) blend thin films prepared at various conditions: as-cast, 120, 160, 180, and 200 °C annealed. Inset: Domain spacing calculated from the fitted scattering peak locations of the smaller domains.

P3HT:P(NDI2OD-T2) devices. One reason behind the dramatic improvement in P3HT:F8TBT device efficiency with annealing (both in terms of  $J_{sc}$  and  $FF$ ) is the improvement in P3HT ordering that increases hole mobility [208, 210]. Annealing of P3HT:F8TBT blends spin-coated from xylene leads to an increase in hole mobility of an order of magnitude [210]. A more dramatic enhancement of mobility is expected for P3HT:F8TBT blends processed from chloroform as the P3HT fraction is more disordered in as-cast films from chloroform. This increase in mobility leads to enhanced charge separation efficiency resulting in both increased  $J_{sc}$  and  $FF$ . For P3HT:P(NDI2OD-T2) blends, a significant portion of the P3HT component is already ordered (see also GI-WAXS results below), meaning that there is less likely to be as dramatic an improvement in hole mobility with annealing.

Figure 6.4 shows the R-SoXS scattering profiles of P3HT:P(NDI2OD-T2) blend thin films prepared under various conditions, that is, as-spun and annealed at 100, 120, 160, 180, and 200 °C. The data were acquired at 285.3 eV, an energy for which the chemical contrast between the two polymers is optimized in relation to massthickness differences (see Supporting Information). Scanning transmission X-ray microscopy (STXM) data showed that the average composition of the  $\sim 180$  nm spaced domains does not evolve with annealing (see Figure S5 in the Supporting Information). The R-SoXS data have thus been normalized to the scattering intensity of the low  $q$  peak at  $\sim 0.04$  nm $^{-1}$ . To avoid confusion, some low  $q$  data ( $< 0.02$  nm $^{-1}$ ) that are distorted by parasitic scattering from a few dispersed, large agglomerates or impurities in the 100 and

160 °C samples are removed in the figure. Such sample imperfections are readily observed and correlated with visible light microscopy. The near complete constancy of the shape and position of the low  $q$  peak is a further indication that domains corresponding to this domain size do not evolve in size or average composition. Overall, with the exception of the as-spun film, a bimodal size distribution is observed for all films, with domains corresponding to  $\sim 5-10$  and  $\sim 75-100$  nm, respectively. For the as-spun film, only domains  $\sim 75-100$  nm in size are observed. (We note that the top scale in Figure 6.4 is the domain spacing. Hence, for a morphology with near equal volume fractions, the domain size is a factor of 2 smaller.) Scattering can, by its very nature, not create a reconstruction of the real-space structure. It is thus incapable of differentiating easily (a) if small domains are subdomains of large domains or (b) if different regions in space have large domains and others have small domains. Given the complexity of these system and the limited information, we will discuss the morphology in terms of ensemble averages only and will refrain from explicit interpretation in terms of specific hierarchical structures as have been recently proposed in fullerene based devices [211]. In contrast to the larger domains, the smaller domains show a clear change in size with annealing, with the domain size systematically increasing with annealing temperature (see inset to Figure 6.4). Interestingly, the size of these small domains is generally on the order of the exciton diffusion length, evolving from  $\sim 5$  nm for the 100 °C annealed film to  $\sim 10$  nm for the 200 °C annealed film. Device efficiency is optimized for anneal temperatures of 160 – 180 °C corresponding to a domain spacing of  $\sim 8-9$  nm. In addition to information regarding the domain spacing provided by the position of the scattering peaks, the scattering intensity also provides qualitative information regarding the purity and volume fraction of the domains. The maximum scattering intensity for the small domains is observed for samples annealed at 160 °C, which corresponds to the maximum observed in  $J_{sc}$ . While the scattering data provide information regarding domain spacing and purity, it does not provide information regarding the connectivity of domains. For the 200 °C annealed film, the domain spacing only increases to  $\sim 10-11$  nm with a mild reduction in scattering intensity, yet 200 °C annealed devices exhibit a pronounced drop in efficiency and the appearance of an “S-shape” in the  $J-V$  curve about open circuit. The reduced performance of the 200 °C annealed device could result from domains with poor connectivity, consistent with the production of S-shaped  $J-V$  curves via the accumulation of space charge at material interfaces [212]. Alternatively, the reduced crystallinity in the 200 °C annealed device (see Figure S2 in the Supporting Information) is likely to result in lower charge carrier mobilities and reduced charge separation and collection.

The P3HT:F8TBT blend has a rather different morphology. Figure 6.5 shows the R-SoXS data acquired on this system at 285.5 eV for as-spun, 100, 120, 160, 180, and 200 °C annealed samples. Analogous to P3HT: P(NDI2OD-T2) blends, 285.5 eV is the energy where the polymer/polymer contrast is optimized for P3HT: F8TBT (see Supporting Information).

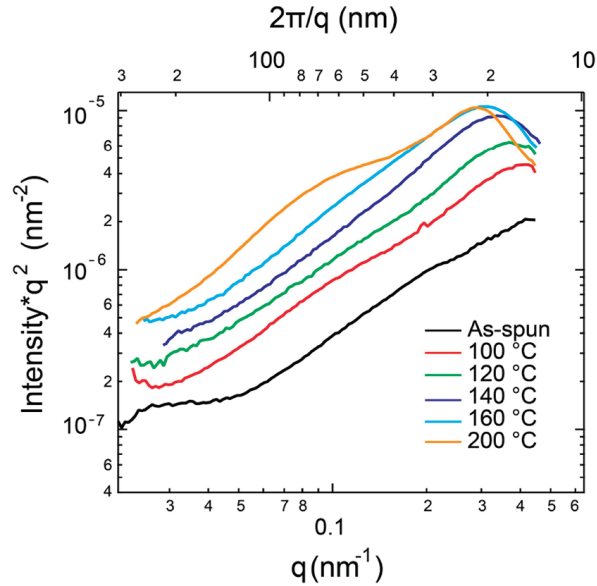


Figure 6.5: R-SoXS of P3HT:F8TBT blend thin films prepared at various conditions: as-cast and annealed at 100, 120, 140, 160, and 200 °C.

Here, we observe a broader domain size distribution than for P3HT: P(NDI2OD-T2). A peak corresponding to  $\sim 7$  nm domains is evident with annealing at 100 °C, with a gradual increase in average domain size to 11 nm for annealing at 200 °C. At the same time, the intensities increase for all but the highest  $q$  values due to uniform coarsening and purification of all the structures. Only at the highest annealing temperature of 200 °C does a clear secondary feature corresponding to  $\sim 30$  nm domains emerge. Furthermore, the smaller domains are significantly more numerous or more pure in relation to large domains as indicated by the high scattering intensity at high  $q$ . Whereas in the P3HT:P(NDI2OD-T2) blend, the high  $q$  peak near  $q = 0.4$   $\text{nm}^{-1}$  has a scattering intensity of only about 50% that of the low  $q$  peak at  $0.04$   $\text{nm}^{-1}$ , the scattering intensity from domains of  $\sim 10$  nm in size in P3HT:F8TBT is more than an order of magnitude higher than those 50 nm or larger. Peak efficiency and peak  $J_{sc}$  are observed at 180 °C, which corresponds (by inference, as this particular temperature is missing in the data set in this sample series, although is confirmed from data of samples with slightly larger thickness) to a saturation of intensity of the  $\sim 10$  nm domains, limited domain growth, and onset of the development of  $\sim 30$  nm domains. Overall, the average domains in the P3HT:F8TBT blend are significantly smaller than in the P3HT:P(NDI2OD-T2) blend and nearly matched to the exciton diffusion length.

Figure 6.6 presents the photoluminescence (PL) spectra of P3HT:F8TBT films as a function of annealing. Due to the characteristic length scale associated with exciton diffusion ( $\sim 10$

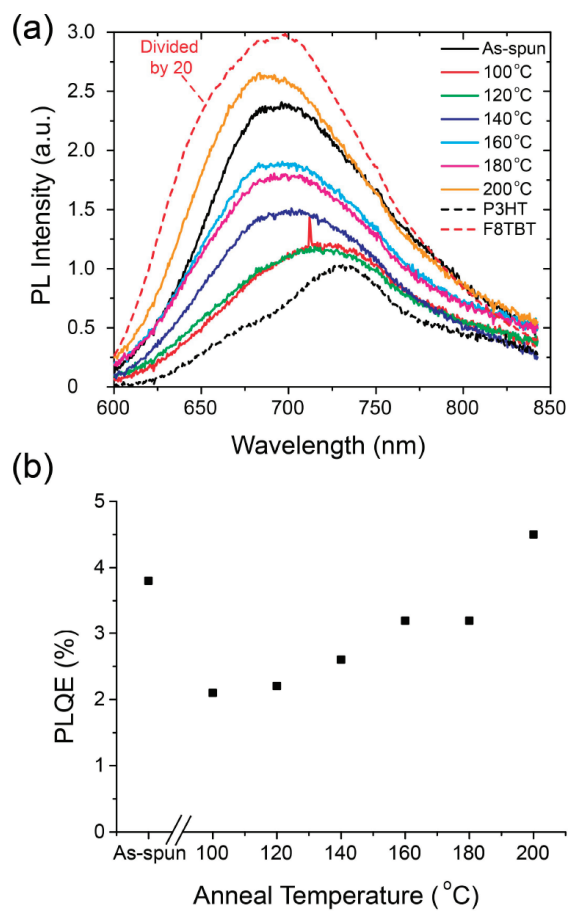


Figure 6.6: Evolution of the photoluminescence spectrum of P3HT:F8TBT blends with annealing. Solid lines depict the blend; while dashed lines correspond to the spectrum of neat films. The magnitude of the F8TBT spectrum has been reduced 20-fold.

nm), PL data provide qualitative information regarding domain size on the 10 nm length scale. Due to the low PL quantum efficiency (PLQE) of P(NDI2OD-T2), a similar analysis could not easily be performed on P3HT:P(NDI2OD-T2) films. Neat F8TBT has a PLQE of 27% and is more luminescent than that of neat regioregular P3HT that is measured to have a PLQE of 1.8%. Examining the data of Figure 6.6, as-spun films have a PLQE of 3.8%, indicating efficient quenching of F8TBT emission via exciton dissociation at P3HT/ F8TBT heterojunctions. With annealing to 100 °C a sharp drop in PLQE to 2.1% is observed that can be attributed to aggregation of P3HT [208]. The photophysics of P3HT is highly sensitive to polymer conformation with disordered, regiorandom P3HT possessing a significantly higher PLQE ( $\sim 15\%$ ) to ordered, regioregular P3HT [208]. Subsequent annealing leads to a monotonic increase in PLQE with annealing consistent with the evolution of morphology on a 10 nm length scale. Even at an annealing temperature of 200 °C, the PLQE of the blend is still well below that of neat F8TBT, suggesting that there is still significant intermixing on the 10 nm length scale. For comparison, PFB:F8BT blends annealed at 200 °C have a PLQE similar to the PLQE neat F8BT (66%), indicating the evolution of pure domains with spacing much larger than the exciton diffusion length, confirmed by STXM and R-SoXS measurements [127, 45]. The PL data of Figure 6.6 are consistent with the R-SoXS data where an evolution in nanostructure on the length scale of 5–10 nm is directly observed but with limited structural evolution beyond the exciton diffusion length. Note that PL measurements are limited in what they can say regarding morphology, as they are sensitive to small minority concentrations and provide no information on length scales much larger than the exciton diffusion length. Thus PL measurements cannot distinguish between large domains with a small minority component that still efficiently quenches PL and efficient PL quenching by pure domains but with domain spacing less than the exciton diffusion length.

To derive information about crystallinity and crystallite thickness in the thin film blends, GI-WAXS data were acquired. Figure 6.7a shows the in-plane scattering intensity of P3HT:P(NDI2OD-T2) as-spun samples and those annealed at 100, 120, 140, 160, and 180 °C. Utilizing reference measurements on pure films, the peaks near  $q = 0.25, 0.37,$  and  $1.7 \text{ \AA}^{-1}$  are indexed as the P(NDI2OD-T2) (100), the P3HT (100), and the P3HT  $\pi - \pi$  (010) peaks, respectively. The relative intensity changes of the P(NDI2OD-T2) (100) peak and the P3HT (100) peak indicate that P(NDI2OD-T2) crystallizes first or more readily in the as-spun films. The out-of-plane scattering shows a similar evolution, but we include here the in-plane GI-WAXS results to allow a comparison to the R-SoXS data which only measures the in-plane morphology. By performing a Scherrer analysis on (100) peaks and correcting the instrumental broadening, the size of the crystals along those crystallographic directions were derived and plotted in Figure 6.7b. Crystal size is observed to evolve with annealing temperature, qualitatively mirroring the R-SoXS observations. However, the size of the P(NDI2OD-T2) crystals even in as-spun films is much larger

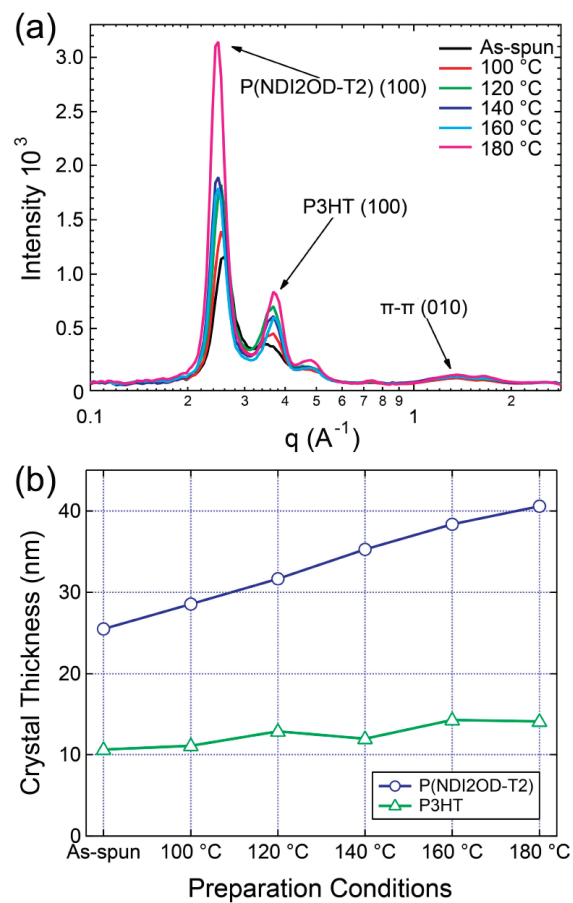


Figure 6.7: In-plane GI-WAXS data of P3HT:P(NDI2OD-T2) samples prepared at various conditions: as-spun, 100, 120, 140, 160, and 180 °C annealed (a), and crystal sizes along the (100) direction derived from a Scherrer analysis (b).

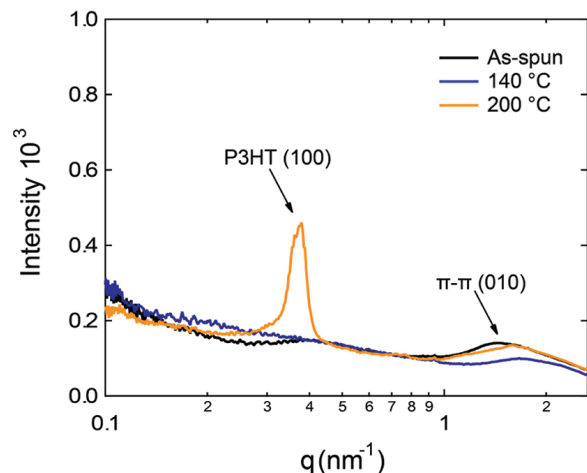


Figure 6.8: In-plane GI-WAXS data of P3HT:F8TBT samples prepared at various conditions: as-spun, 140, and 200 °C annealed.

than the small domains observed in R-SoXS. These crystallites therefore must be embedded in the larger 75–100 nm domains observed by R-SoXS. Similarly, the size of the P3HT crystallites, especially in as-spun and mildly annealed films, are larger than the smaller domains observed by R-SoXS. These observations underscore the fact that R-SoXS measures a different aspect of materials than GI-WAXS and that these two characterization methods are complementary. GI-WAXS only measures the crystal size along the (100) direction, providing little information about the size along the other directions or direct information about whether the crystals are embedded in the same or the complementary material. In contrast, R-SoXS measures the size of the compositionally distinguishable domains, which does not correspond to the size measured with GI-WAXS of either the P3HT or the P(NDI2OD-T2) crystals. Furthermore, GI-WAXS detects crystallization in as-cast films, whereas R-SoXS does not detect structure at the related length scale. The discrepancy observed indicates that most of the crystals are surrounded by the same polymer within the large domains observed in R-SoXS. Consequently, only a fraction of the volume of the P3HT:P(NDI2OD-T2) devices has a favorable domain size that is on the order of the exciton diffusion length. It is also highly likely that the small domains observed with R-SoXS are predominantly composed of amorphous P3HT and P(NDI2OD-T2), although definitive analysis on the relative volume fraction of crystalline and amorphous domains of each polymers cannot be provided at this point. In addition, a direct comparison of the GI-WAXS data from 180 and 200 °C annealed films shows that the latter has much less crystallinity, which explains the loss of structure in the optical absorption spectrum mentioned at the beginning of the Results and Discussion section.

In contrast to the P3HT:P(NDI2OD-T2) blends, significantly less crystallization was revealed in P3HT:F8TBT blends with GI-WAXS, as shown in Figure 6.8, in which data from as-spun, 140, and 200 °C P3HT:F8TBT thin films are plotted. Only a broad and small P3HT (100) diffraction peak at  $q \approx 0.37 \text{ \AA}^{-1}$  is observed for the 200 °C annealed film. Furthermore, the P3HT crystals are so small or ill-formed that the (010) (i.e.,  $\pi - \pi$  stacking) peak is barely detectable. The appearance of vibronic structure in the absorption spectrum of the 140 °C annealed film (Figure 6.2) may be attributed to molecular aggregation of P3HT without the formation of coherent crystallites. In Figure 6.8, there is no diffraction peak that can be attributed to F8TBT.

Annealing at various temperatures causes different structural changes in the two blends. The morphological evolution and the crystallization behavior can be summarized and correlated to device performance as follows. P3HT:F8TBT blends do not exhibit any dominant large-scale phase separation and little crystallization for all annealing temperatures. The vast majority of this material is structured at the  $\sim 10 \text{ nm}$  length scale. The best device performance is correlated to the arrest in growth and purification of the  $\sim 10 \text{ nm}$  domains and just prior to the emergence of domains with a second length scale of about 30 nm, possibly being the result of coalescence. This optimum morphology is consistent with the results of device simulations that indicate that a morphology with domain size slightly larger than the exciton diffusion length balances the processes of charge generation and charge separation [126]. In contrast, P3HT:P(NDI2OD-T2) blends have a more unfavorable morphology if viewed from the conventional bulk heterojunction structure model with dominant domain size of  $\sim 90 \text{ nm}$  even in the as-cast blends. These domains are much larger than the exciton diffusion length resulting in the loss of photo-excitations via exciton recombination. The high crystallinity in the P3HT:P(NDI2OD-T2) blends impedes large-scale evolution of the morphology during annealing. Within the annealing sequence investigated, high scattering intensity for  $\sim 9 \text{ nm}$  domains corresponded to the highest  $J_{sc}$ . Although domains in size on the order of the exciton diffusion length develop, only a fraction of the material is structured at that length scale.

The P3HT:F8TBT blend can and does evolve more than the P3HT:P(NDI2OD-T2) blend since this system is less crystalline at all preparation conditions than the P3HT:P(NDI2OD-T2) blends. The suppression of the crystallization of the P3HT in P3HT:F8TBT blends relative to P3HT:P(NDI2OD-T2) blends implies that there might be a favorable interaction at the molecular level between P3HT and F8TBT that results in partial miscibility of this system. Indeed, a previous X-ray diffraction study of thick P3HT:F8TBT films has found evidence for F8TBT intercalation in P3HT crystallites [207].

If better control of the morphology can be accomplished for P3HT:P(NDI2OD-T2), significant improvement might be achieved for that system. The high crystallinity might allow the morphology to be frozen in, thus making the annealing step relatively insensitive to details

of the fabrication protocol. Such increased processing latitude might be important for large scaling fabrication processes such as roll-to-roll printing. Crystallite size, however, has to be commensurate with the dimensions required for efficient device operation. The 25 – 40 nm size of the P(NDI2OD-T2) crystals in the P3HT:P(NDI2OD-T2) blends precludes their incorporation in the finer nanostructure that is arguably more important for device operation. Indeed, the potential lack of crystallinity within the 5 – 10 nm domains in P3HT:P(NDI2OD-T2) may help to explain the poor performance of P3HT:P(NDI2OD-T2) solar cells that has partly been attributed to fast interfacial recombination following charge transfer [188]. Assuming that a significant proportion of the interfacial area is attributable to the smaller 5 – 10 nm domains, a lack of molecular order in these domains is likely to be detrimental to charge separation. Ordered crystallites should favor charge separation due to increased molecular order and the associated charge mobility. Thus, while neat P(NDI2OD-T2) possesses an electron mobility comparable to that of PCBM, this high electron mobility may not be imparted locally to disordered P(NDI2OD-T2) chains at donor/acceptor interfaces within the smaller domains. These observations highlight that while material crystallinity in general is thought to be favorable, enabling high carrier mobilities, it can be problematic by disabling formation of morphology on the desired length scale.

It is interesting to note that the near-optimal morphology of the P3HT:F8TBT blend does not lead, however, to a much superior  $J_{sc}$  when compared to the P3HT:P(NDI2OD-T2) blend. The  $J - V$  curves of optimized P3HT:F8TBT devices still have a steep gradient even out to  $-1$  V reverse bias (Figure 6.3c), indicating that while near-optimum morphologies have been achieved interfacial charge separation is still limiting device performance. The  $J - V$  curves of P3HT:P(NDI2OD-T2) devices are not as steep in contrast, suggesting that charge separation is not as problematic for P3HT: P(NDI2OD-T2) and that the large domains may also be limiting device performance through incomplete exciton dissociation. Indeed, relatively high fill factors have been achieved for P3HT:P(NDI2OD-T2) blends (up to 67%);<sup>55</sup> however, these fill factors have not been combined with high short-circuit currents. The lower overall performance of the P3HT:P(NDI2OD-T2) system compared to P3HT:F8TBT can be primarily traced to a lower open-circuit voltage and to a lesser extent to reduced fill factor for conditions that produced the higher short-circuit currents. Ultimately, it is the electronic structure and the resultant low open-circuit voltage of the P3HT:P(NDI2OD-T2) blend that is the major difference. While the P(NDI2OD-T2) infrared band extends the absorption of the P3HT:P(NDI2OD-T2) blend relative to the P3HT:F8TBT system, it has insufficient absorption strength in  $\sim 100$  nm thick films to provide a decisive advantage.

## 6.4 Conclusions

Resonant soft X-ray scattering has been employed to directly correlate the device performance of polymer solar cells with the evolution of nanostructure on the length scale of 5 – 20 nm. For the two all-polymer solar cell systems investigated, significant differences in the nature and evolution of nanostructure were observed. For P3HT:P(NDI2OD-T2) blends, a bimodal domain structure was observed with characteristic domain sizes of  $\sim 75 - 100$  and  $\sim 5 - 10$  nm. The size of the larger domains in the P3HT:P(NDI2OD-T2) blends was observed to be invariant under annealing, while the smaller domains were observed to evolve from  $\sim 5$  nm for 100 °C annealed films to  $\sim 10 - 11$  nm for 200 °C annealed films. For P3HT:F8TBT blends, no dominant large-scale phase separation was observed with the vast majority of the material structured at the  $\sim 10$  nm length scale. A broader domain size distribution on the 10 nm length scale was observed for P3HT:F8TBT compared to P3HT:P(NDI2OD-T2), with annealing leading to a gradual increase in the average domain size from  $\sim 7$  nm (100 °C) to  $\sim 11$  nm (200 °C). Only with annealing at 200 °C was a secondary feature corresponding to a  $\sim 30$  nm domain size observed. For both systems, the optimization of device performance with annealing was correlated with a coarsening and purification of domains on the 5 – 10 nm length scale, consistent with the creation of a morphology that balances charge separation/collection with exciton dissociation.

GI-WAXS was used to provide complementary information regarding crystallinity and crystallite size, revealing a higher crystallinity of P3HT in blends with P(NDI2OD-T2) than in blends with F8TBT. Embedded in the larger 75 – 100 nm domains, 25 – 40 nm P(NDI2OD-T2) crystallites were observed significantly larger than the optimum domain size for exciton dissociation. Thus the propensity of P3HT and P(NDI2OD-T2) to crystallize in P3HT:P(NDI2OD-T2) blends hampers the formation of nanostructure on the desired length scale resulting in a suboptimal morphology. The lower crystallinity of P3HT in blends with F8TBT suggests a favorable interaction between P3HT and F8TBT at the molecular level enabling formation of a near-optimum morphology. These observations demonstrate that, while crystallinity is thought to be desirable in enabling high carrier mobilities and arresting large-scale phase separation, control over crystallite size is required to enable formation of domains on the length scale of the exciton diffusion length. The formation of large domains in P3HT:P(NDI2OD-T2) blends driven by crystallization hampers the performance of this system with improved control of nanostructure a route to improved efficiency. Our study also highlights the utility of R-SoXS in providing complementary information to GI-WAXS enable a more complete picture of nanomorphology to be captured.

## 6.5 Experimental section

### 6.5.1 Materials

P3HT was supplied by Merck KGaA with molecular weight ( $M_W$ ) of 25 kg/mol, polydispersity index (PDI) of 2.0, and regioregularity of 94%. P(NDI2OD-T2) was purchased from Polyera Corp. (ActivInk N2200) with a specified number-average molecular weight ( $M_n$ ) of 25.4 kg/mol and PDI of 4.0. F8TBT was supplied by Cambridge Display Technology Ltd. with a peak molecular weight ( $M_p$ ) of 432 kg/mol. Blend films for devices, optical characterization, and X-ray scattering were prepared in identical fashion. P3HT:F8TBT blends were prepared from anhydrous chloroform with a weight ratio of 1:1 and total solution concentration of 12 g/L. Spin-coating at 4000 rpm yielded P3HT: F8TBT films with a thickness of  $100 \pm 20$  nm. P3HT:P(NDI2OD- T2) blends were also prepared from anhydrous chloroform with a 1:1 weight ratio but with a total solution concentration of 19 g/L to produce films  $105 \pm 5$  nm thick when spin-coated at 4000 rpm. Film thicknesses were determined using a Dektak 6 M profilometer.

### 6.5.2 Optical characterization

Films for optical absorption and photoluminescence analysis were prepared on quartz substrates. Absorption spectra were acquired using a Hewlett-Packard 8453 diode-array spectrometer. PL spectra and efficiencies were measured at room temperature in a nitrogen-purged integrating sphere with excitation from an argon ion laser at 488 nm and detection with an Oriel Instaspec IV spectrometer.

### 6.5.3 Device fabrication

Devices were prepared by spin-coating blend films on PEDOT:PSS-coated indium-tin-oxide glass substrates. The ITO-covered glass substrates were initially cleaned by solvent cleaning and oxygen plasma treatment. PEDOT:PSS (40 nm thick) was then deposited by spin-coating onto the plasma-treated substrates and then annealing at 120 °C before being transferred to a nitrogen glovebox for spin-coating of P3HT:F8TBT and P3HT:P(NDI2OD-T2) layers. Previous X-ray photoelectron experiments have shown that P3HT preferentially wets the PEDOT/PSS surface for both P3HT:F8TBT and P3HT:P(NDI2OD-T2) [188, 208]. After the active blend layer was deposited, the samples were transferred to a vacuum evaporator inside the glovebox where 100 nm thick aluminum electrodes were evaporated through a shadow mask. Annealing was performed on a hot plate within the glovebox prior to encapsulation.

#### 6.5.4 Device characterization

External quantum efficiency was measured as a function of wavelength by dispersing light from a tungsten filament (Newport 250 W QTH) through a monochromator (Oriel Cornerstone 130) with a spot size smaller than the device active area. Light intensities of less than  $1 \text{ mW cm}^{-2}$  were used with the short-circuit current recorded using a Keithley 2635 source measure unit. Current–voltage characteristics were measured under an equivalent of  $100 \text{ mW cm}^{-2}$  AM1.5G illumination with an ABET class AAA solar simulator correcting for spectral mismatch.

#### 6.5.5 Resonant soft X-ray scattering measurements

Scattering measurements were performed at beamline 11.0.1.2 at the Advanced Light Source [111]. This undulator beamline is equipped with a variable line spacing plane grating monochromator and a four-bounce harmonic rejection assembly composed of four  $\text{SiO}_2$  substrates coated with 30 nm nickel for the sake of spectral purity. To eliminate most of the beamline parasitic scatter, a set of four-jaw collimating slits were used to define the beam. The scattered intensity was recorded by a back illuminated Princeton PI-MTE CCD thermoelectrically cooled to  $-45^\circ\text{C}$ . Beam centering was completed by imaging the direct beam on the CCD while attenuated with a carbon film. Sample-detector distance was measured from diffraction peaks of the tri-block copolymer poly(isoprene-*b*-styrene-*b*-2-vinyl pyridine), which has a known spacing of 391 Å at 280 eV. The beam size at the sample is approximately  $300 \mu\text{m}$  by  $200 \mu\text{m}$ . A modified version of the NIKA software package was used to process the scattering data to (i) subtract background, (ii) normalize by the I0 provided by photodiode, and (iii) make solid angle corrections. The acquisition time was 60 s for low  $q$  region (below  $0.5 \text{ nm}^{-1}$ ) and 120 s for high  $q$  region (above  $0.5 \text{ nm}^{-1}$ ). These two regions were then stitched together with detector dwell time correction applied.

Removal of parasitic scattering was aided by investigating known isotropic scattering samples and comparing the scattering signals derived by integrated over  $8^\circ$  sectors and eliminating any regions and sectors containing data disagreeing with the others. The parasitic scattering is caused by a few dispersed, large agglomerates or impurities. They are readily observed with visible light microscopy. The scattering intensity profiles were scaled by  $q^2$  to represent total scattered intensity at a given  $q$ .

The sample films used for R-SoXS were spin-cast on NaPSS-covered glass as substrate. To carry out R-SoXS experiment in transmission, the film is floated off in deionized water and picked up with a 1.5 mm by 1.5 mm silicon nitride window. The film is then dried in air before being transferred into the vacuum chamber for R-SoXS.

### 6.5.6 Grazing-incidence wide-angle X-ray scattering (GI-WAXS)

GI-WAXS experiment was performed at beamline 7.3.3 of Advanced Light Source [213]. The blend films were prepared on PEDOT:PSS-covered glass substrates, following the same protocol used preparing samples for other characterizations. Although the data were acquired on samples with slightly larger thickness,  $\sim 140$  nm, instead of  $\sim 100$  nm used for other characterizations, we have confirmed that there is no observable GI-WAXS data difference between samples due to this small thickness difference other than overall intensity. The 10 keV X-ray beam was incident at a grazing angle of  $0.12^\circ$ , which maximized the scattering intensity from the samples. The scattered intensity was detected with an ASDC Quantum 4 CCD.

### 6.5.7 Scanning transmission X-ray microscopy

STXM measurements were performed at beamline 5.3.2 of the Advanced Light Source (ALS), Berkeley, CA [41]. The silicon frame-supported films were mounted in the sample chamber which was evacuated to 0.3 mbar and subsequently refilled with 1/3 atm of helium. The intensity of the focused X-ray beam transmitted through the film was recorded using a scintillator and photomultiplier tube and measured as a function of energy and position.

## 6.6 Acknowledgement

This work was supported in the UK by the EPSRC (EP/E051804/1) and in Australia by the ARC (FT100100275). NCSU's contribution (GI-WAXS, R-SOXS) is supported by DOE, OS, BES, MSE (DE-FG02-98ER45737). Data were acquired at beamlines 11.0.1.2, 7.3.3, and 5.3.2.2 at the ALS, which is supported by DOE (DE-AC02-05CH1123). The authors thank Cambridge Display Technology Ltd. for the supply of F8TBT.

## 6.7 Supplemental information

To demonstrate the loss of crystallinity in 200 °C annealed P3HT: P(NDI2OD-T2) blend film, the GI-WAXS data of both 180 °C and 200 °C annealed samples are plotted in Figure 6.9. The 180 °C data are scaled to the same as in Figure 6.7, for better comparison, and the 200 °C data are scaled accordingly.

In order to predict the right energy optimizing the scattering signal from the blend films, a material contrast is calculated for each combination of materials. For instance, in the P3HT: P(NDI2OD-T2) blend system, the contrast between P3HT and P(NDI2OD-T2), between vacuum and P3HT, and between vacuum and P(NDI2OD-T2) are calculated. The contrasts functions are calculated from the optical constants, i.e.  $\delta$  and  $\beta$  derived from near edge X-ray

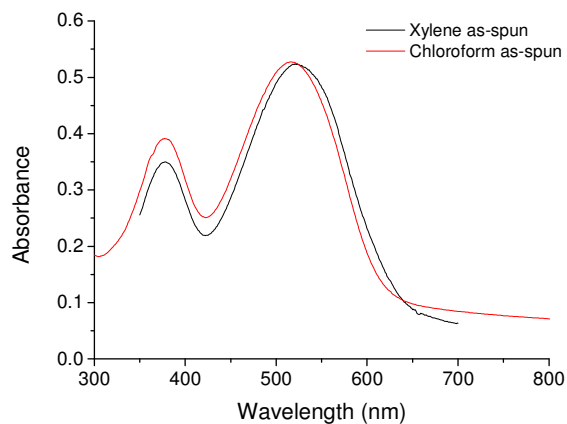


Figure 6.9: Comparison of UV-Vis absorption spectra of as-cast chloroform and xylene P3HT:F8TBT blends. The red-shift in the xylene-processed absorption spectrum is evidence for increased P3HT ordering following spin-coating.

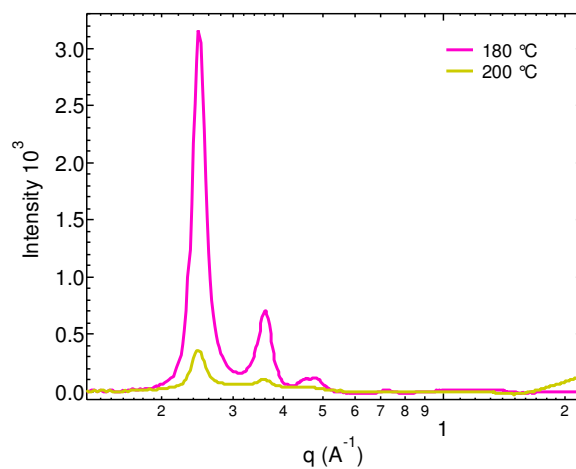


Figure 6.10: In-plane GI-WAXS data of P3HT:P(NDI2OD-T2) blend films annealed at 180 °C and 200 °C, showing that 200 °C annealed sample is much less crystalline. The intensity of 180 °C annealed sample has been scaled to match the other data set in main article text, and the 200 °C annealed sample is then scaled accordingly.

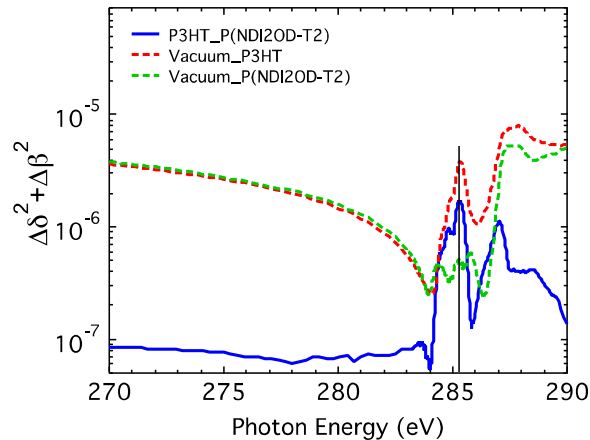


Figure 6.11: Optical contrast plots of P3HT/ P(NDI2OD-T2), vacuum/P3HT, and vacuum / P(NDI2OD-T2). The energy at which the data were acquired is indicated with the vertical dark line.

absorption fine structure (NEXAFS) spectra [71, 3], and are plotted in Figure 6.10, noted as P3HT\_P(NDI2OD-T2), vacuum\_P3HT, and vacuum\_P(NDI2OD-T2), respectively. Similarly in Figure 6.11, the contrast functions of the P3HT:F8TBT system are also plotted and noted in the same way. The dark vertical lines in these two figures show where the resonant soft x-ray scattering data were acquired, at energies for which the contrast between the two polymers in the blends is high, yet the absorption is not so high to significantly reduce the scattering intensity.

In order to examine the composition change of the domains in the P3HT:P(NDI2OD-T2) blend film, scanning transmission x-ray microspectroscopy (STXM) images are acquired and showed in Figure 6.13. As shown in Figure 6.13 (d), at least one  $4 \mu\text{m} \times 6 \mu\text{m}$  sampling area is analyzed and the full-width-half-maximum (FWHM) of the histogram for the images are plotted, showing that there is no contrast difference between the samples investigated, i.e. As-spun (a), 120 °C annealed (b), and 200 °C annealed (c) blend films.

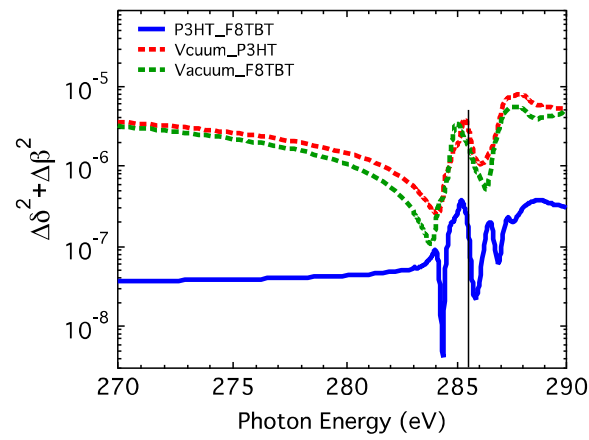


Figure 6.12: Optical contrast plots of P3HT/F8TBT, vacuum / P3HT, and vacuum / F8TBT. The vertical dark line indicates the energy at which the R-SoXS data were acquired.

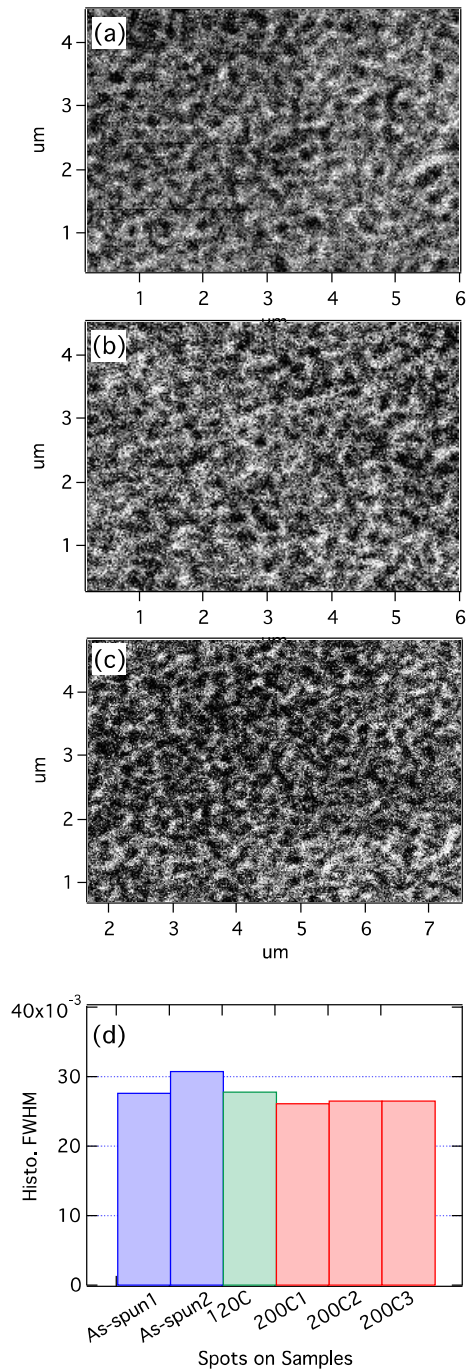


Figure 6.13: STXM images taken at 285.3 eV and histogram results of the images, showing no contrast difference observed for: (a) As-spun, and (b) 120 °C, (c) 200 °C annealed samples.

## Chapter 7

# Future outlook

### 7.1 Polarization-dependent resonant soft X-ray reflectivity for molecular orientation depth profiling of organic thin films

Molecules within matters can disperse in anisotropic or isotropic way in terms of the ordering of them. For molecules with molecular orbitals of distinguishing symmetries in different dimensions, this orientational preference of the alignment of molecules can affect their interaction with the incident polarized electromagnetic field. As a simplified illustration, Figure 7.1 shows several P(NDI2OD-T2) molecules (one repeating unit shown) possessing various orientations relative to the incident polarized soft X-rays. The arrows denotes the polarization direction of the X-rays and the propagating direction of the X-ray is in the plane of and perpendicular to the arrows. Because the transition dipole moment of a P(NDI2OD-T2) molecule is perpendicular to the plane of the molecule, only when the polarization direction of the X-rays are parallel to the transition moment is the resonance absorption maximized. For instance, only group 3 and 4 indicated in the figure has strong absorption, with 3 absorbs more than 4. Group 1 and 2 have the minimum resonant absorption. This kind of orientational order of molecules can often be of critical importance to its properties. Materials such as liquid-crystalline polymers and spider-silk fibers are well-known examples where the orientational order of molecules or the interplay between crystalline and amorphous regions determines their optical and mechanical properties, respectively [214, 215, 216]. The reason for this interesting physical properties is the way in which electrons of highly directional molecular orbitals in soft matter interact with light or are involved in bonding. For aromatic small molecules or polymers, electronic orbitals will delocalize along the polymeric backbone or couple strongly between molecules if molecular packing is sufficient, allowing for efficient charge transport along specific directions in the material and making it suitable for use in devices such as light-emitting diodes, transistors or solar cells [97, 217, 218, 116]. In the case of organic field-effect transistors, the current flows along the

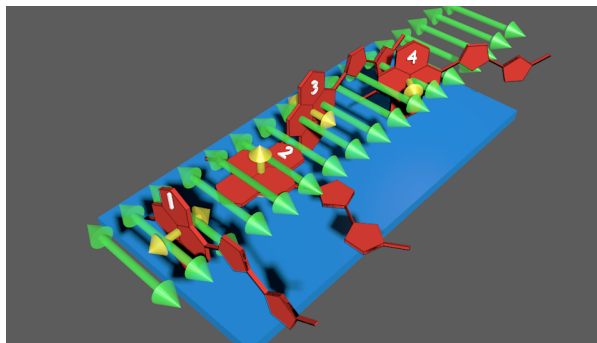


Figure 7.1: Schematic of the molecular orientation of P(NDI2OD-T2) polymer (one repeating unit shown) on a substrate. Green arrows indicate the polarization direction of the soft X-ray beam and the stacking direction of the green arrows is actually the propagating direction of the beam. Yellow arrows represent the transition dipole moment of the molecule.

interface in a nanoscale thin layer between the semiconductive material and the dielectric layer. Considering that the molecular packing in these organic devices influence the charge carrier mobility [97], it is of great interest for researchers to learn more about the orientations of the molecules on these buried interfaces.

Near edge X-ray absorption fine structure (NEXAFS) spectroscopy mentioned from the previous chapters employs the absorption dichroism for X-rays polarized parallel ( $p$ -) and perpendicular ( $s$ -) to the incidence plane, to obtain the orientation of specific molecular bonds. Furthermore, with help of certainly polarized lights, distribution of molecular orientations in the domains of a thin film can be accessed [219]. The specific probing depths of NEXAFS are approximately 1 nm for partial electron yield, up to 10 nm for total electron yield (TEY), and hundreds of nanometers for fluorescence yield or transmission absorption (STXM). In contrast, from the demonstration of the previous chapters, the resonant soft X-ray reflectivity (R-SoXR) data carry full depth-dependent information with nanometer resolution through structures up to several hundreds of nanometer thickness ranging from buried interfaces to the free surfaces.

For our accomplished work as presented in Chapter 5, we have characterized the buried interfacial widths of the OFETs, suggesting better control and consideration of the interfaces when characterizing and comparing the device performances. However, we used a beamline of reflectivity capability only with  $s$ -polarized soft X-rays, so it was not possible to disentangle the physical roughness with the molecular orientation along the buried interface with those reflectivity measurements. I have started to develop the R-SoXR capability of beamline 11.0.1.2 at Advanced Light Source. This beamline is equipped with an undulator as the soft X-ray source which allows the tuning of the polarization of the soft X-rays (comparing to the fixed  $s$ -polarization at beamline 6.3.2 from bending magnets). With the utilization of both the photo-

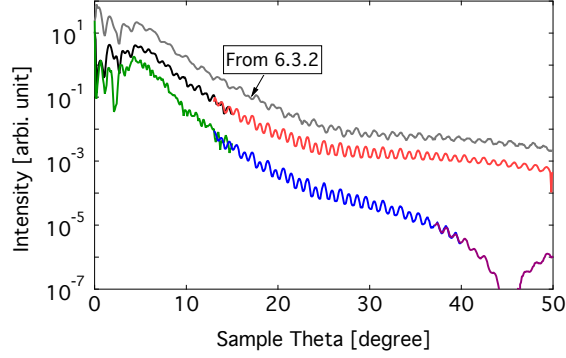


Figure 7.2: Preliminary polarization-dependent R-SoXR data acquired at beamline 11.0.1.2 comparing with data from 6.3.2 with *s*-polarized X-ray. Data are acquired at 281.4 eV on PS/P(NDI2OD-T2) bilayer. From top to bottom: reflectivity data from beamline 6.3.2 for comparison (*s*-polarized); data from beamline 11.0.1.2 with *s*-polarized X-ray; and data from beamline 11.0.1.2 with *p*-polarized X-ray. The various colors indicate the data acquired at several angle ranges and they are stitched to obtain the whole range data.

diode and the single-photon-count CCD camera as the detectors to cover the required dynamic range, we are able to adding the capability of polarization-dependent reflectivity experiments to beamline 11.0.1.2, which is designed for scattering experiment at the beginning.

Some preliminary data from PS/P(NDI2OD-T2) bilayer acquired at 281.4 eV are shown in Figure 7.2. In this plot, both the *s*- and the *p*-polarized soft X-rays are used for a reflectivity experiment on a bilayer sample with PS on top of P(NDI2OD-T2) bottom layer on a silicon substrate. For the sake of comparison, one set of data acquired at beam line 6.3.2 (*s*-polarized x-ray) is also displayed. The photodiode is used to acquire the data at lower sample angles (lower-*q*, hence intensity too high to use CCD as detector). The CCD detector is used to acquired the data at higher sample angles (higher-*q*) and then normalize and stitch with the lower-*q* part. It is clear that for the *p*-polarized data, there is a Brewster's angle as expected when the sample angle is at around 45 degrees, which is where the reflected ray is supposed to be orthogonal of the diffracted ray. The analysis (numerical fitting) of these reflectivity profiles is much more complicated than processing data from *s*-polarized X-rays. That is because the optical constants keep changing with the change of incident angle, resulting from the orientation change of the transition dipole moment relative to the soft X-ray polarization direction. In order to access the molecular orientation information carried by these data, a data fitting algorithm with the ability of taking the optical constants variation into consideration needs to be developed.

## 7.2 Polarization-dependent resonant soft X-ray scattering for molecular ordering study in organic thin films

As shown in the above section, the orientation of the molecules influences its sensitivity to the polarized soft X-rays to a large extent due to the anisotropic molecular orbitals in soft matters. When these molecules pack into domains in an organic thin film, polarized electric field can be the utilized to identify the domains. Because of the orientation-dependent optical constants of the domains, the contrast between domains composed of differently oriented molecules, even within the same material, can be probed with polarized X-rays. When these incident X-rays are scattered, besides the scattering from the density or compositional fluctuations, there is scattering from ordering in molecular orientation added. Moreover, as a result of the energy dependence of the optical constants (thus the contrast  $\Delta\delta^2 + \Delta\beta^2$ ), the energy can be tuned to selectively probe the density, compositional fluctuations, or the ordering fluctuations in the sample.

As one of my co-authored work, P-SoXS has been employed to investigate the molecular orientation in organic semiconductors and correlated to the OFET device performance, which has been published in *Nature Materials* [4]. As part of this work, we studied the P3HT: P(NDI2OD-T2) polymer blend system again. The NEXAFS spectra of both P3HT and P(NDI2OD-T2) show orientational resonant absorption, as can be seen in Figure 7.3. In this figure, again, the green arrows in the insets show the polarization direction of the incident soft X-ray beam, and the stacking direction of the arrows is the propagating direction of the beam. These spectra demonstrate clearly the polarization dependent of the absorption fine structures of both polymers. P3HT and P(NDI2OD-T2) has very different absorption at energy 285.3 eV, so this energy has been used to acquire STXM images to obtain the composition map. Figure 7.4 shows normalized STXM images with three different polarizations, namely horizontal (*s*-), vertical (*p*-) and circular (indicated in the top-left corner of each image) in Figure 7.4(a), 7.4(b) and 7.4(c) respectively. Fourier transform of each image has also been presented as insets to show the ordering of the patterns in the images. The zoomed in area clearly shows the complementary brightness of the domains marked with dashed lines for linear polarizations. Comparing the absorption ability of the two components in this blend, we can identify that the darker domains are P(NDI2OD-T2) rich and the brighter ones are P3HT rich. Due to the resolution limitation of the STXM, we cannot zoom in further to get further domain information.

With the help of P-SoXS, we can further examine domain properties in smaller length scale accessed through reciprocal space. Figure 7.5 shows the scattering images for horizontally and vertically polarized soft X-rays at 285.4 eV. The scattering from these films is anisotropic, meaning stronger scattering along certain azimuthal directions than others. The anisotropy follows the X-ray polarization (Figure 7.5(a),(b)), occurs only at resonance (Figure 7.5(c)) and

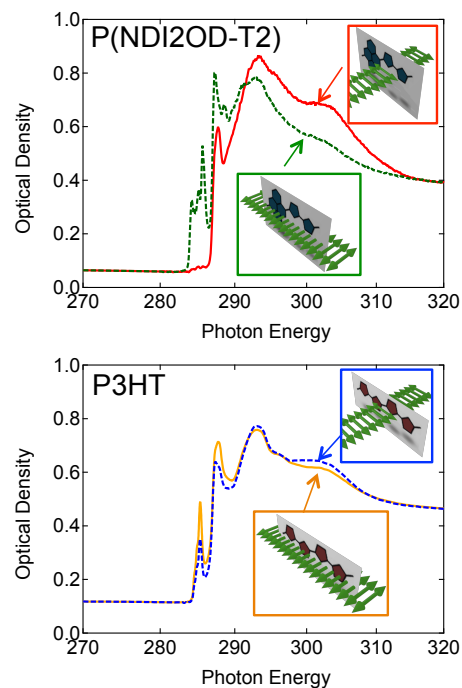


Figure 7.3: Angle-dependent NEXAFS of P3HT and P(NDI2OD-T2). The insets illustrate the relative orientations of the molecules to the incident soft X-ray beam. Green arrows in the insets indicate the polarization direction of the beam and the stacking direction of these arrows is actually the propagating direction of the beam. It is worth noting that the insets just show the extreme situations. Practically in a real film, the large population of molecules employ orientational preferences of alignment rather than aligning perfectly.

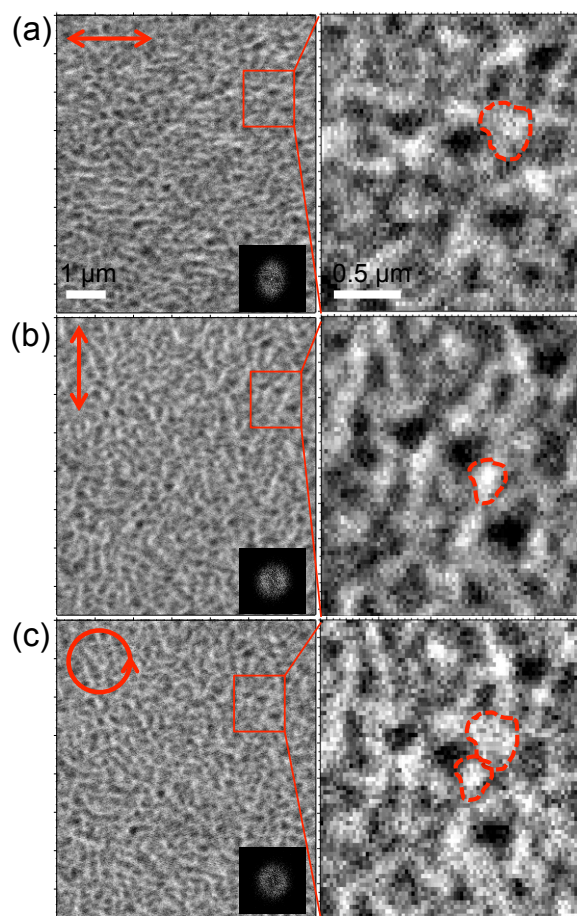


Figure 7.4: Polarization-dependent STXM images of P3HT: P(NDI2OD-T2) blend acquired at photon energy of 285.3 eV. Polarizations of the soft X-rays are (from top to bottom)  $s$ -,  $p$ - and circular, respectively, indicated with arrows in the images. The insets in each images show the Fourier transformation of each image to show the ordering of the patterns observed in the images. Zoomed-in images are shown beside the images from each polarization, with dashed lines highlighting some of the domains to show how the domain brightness varies from linear polarizations to circular.

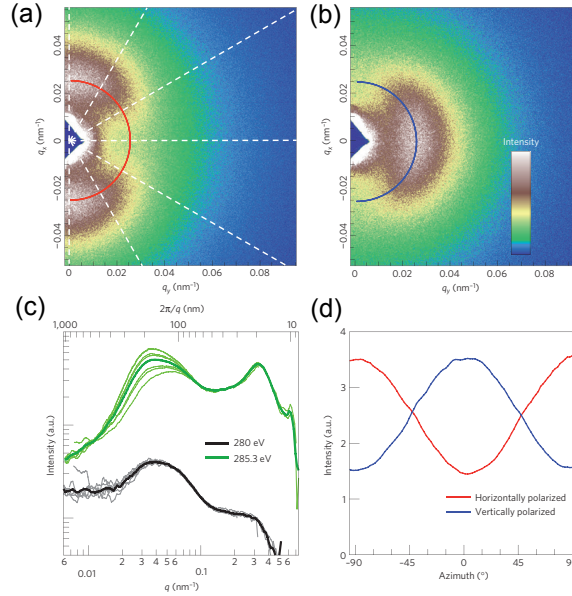


Figure 7.5: P-SoXS of P3HT:P(NDI2OD-T2) blend films. (a),(b), Anisotropic scattering patterns obtained using linear horizontally (a) and vertically (b) polarized photons at an energy of 285.3 eV. The linear intensity scale bar is in arbitrary units, blue represents low intensity and white represents high intensity. (c), Radial scattering profiles at non-resonant (black) and resonant (green) energies. Darker lines are averages over the entire azimuth whereas lighter lines are from  $30^\circ$  sectors along the azimuth as indicated by white dashes in (a). (d),  $I(\phi)$  for  $q = 0.04 \text{ nm}^{-1}$  (colour-coded circles in (a) and (b)). Figure authorized by and reproduced from Reference [4].

produces a sinusoidal intensity variation with the azimuth as shown in Figure 7.5(d). The pattern is also independent of sample rotation, demonstrating that the sample is itself isotropic with no preferential alignment of the molecules or domains as is the case for zone cast samples, for example [220]. This is remarkable as anisotropic scattering has not been reported before for globally isotropic samples. The circularly averaged scattering profiles (dark line in Figure 7.5(c)) in shape or location between resonant (285.3 eV) and non-resonant (280 eV) energies and represent the spacing between the two domains of phase-separated materials as observed in STXM images shown in Figure 7.4. In contrast to the low- $q$  peak, the presence of a scattering peak at higher  $q$  is significantly enhanced at resonance, and does not exhibit any scattering anisotropy. This indicates that this peak is due to small domains not linked to the ordering that gives rise to the anisotropy at  $q = 0.04 \text{ nm}^{-1}$ , yet are domains that exhibit orientation-enhanced contrast. The  $\sim 20 \text{ nm}$  spacing of these domains puts them well outside the reach of being observed with STXM or visible microscopy methods.

Combining the analysis of the P-SoXS data and the anisotropic contrast functions of both

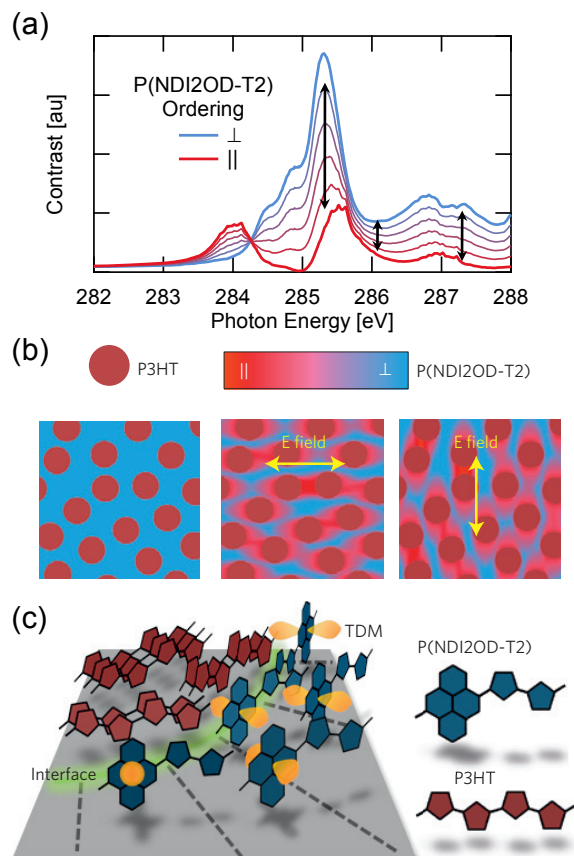


Figure 7.6: Morphology and mechanism of scattering anisotropy in P3HT: P(NDI2OD-T2) films. (a), Scattering contrast between randomly oriented P3HT and oriented P(NDI2OD-T2) as a function of the photon electric-field alignment with the P(NDI2OD-T2) transition dipole moment (TDM). Two data sets from actual optical constants are shown as red and blue and intermediate traces are calculated and coloured using a linear interpolation. Energy used for scattering is shown with the arrow. (b), Top-down schematics depicting (left to right) a view of the mesoscale phase composition of the film, a view of the contrast for horizontally polarized X-rays and a view of the contrast for vertically polarized X-rays. Colours for P(NDI2OD-T2) represent TDMs orientation mimicking those used in (a). Blue regions, therefore, have TDMs oriented perpendicular to the electric field. (c), Molecular-scale perspective at the blend interface formed in the phase-separated materials. The green line on the grey substrate represents the interface between material phases. P(NDI2OD-T2) TDMs (shown in yellow) determine how the molecules scatter resonant X-ray photons and in this sample are aligned radially along the curved interface. Figure authorized by and reproduced from Reference [4].

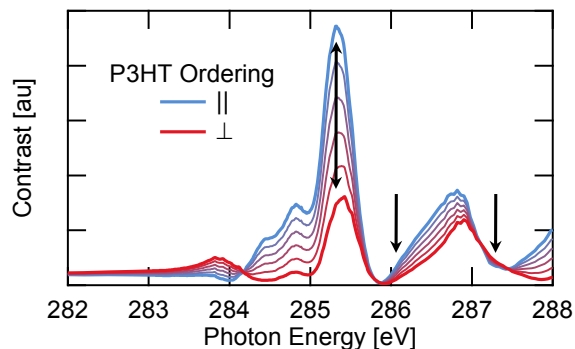


Figure 7.7: Angle-dependent contrast functions between P3HT and P(NDI2OD-T2) for an ordered matrix of P3HT. Angles are defined to be between the ordered molecule’s transitions dipole moment and that of the photon electric field. Arrows indicate the photon energies used in scattering data presented in Figure 7.8. Figure authorized by and reproduced from Reference [4].

component materials reveals the film morphology and the source of the scattering anisotropy. The following rules for interpretation apply: if the anisotropy is localized to the low- $q$  peak corresponding to the overall compositional morphology, the orientation is in the matrix phase; and if the anisotropy is present at higher  $q$  than this peak, it is a result of interdomain scattering from within the dispersion. In the present sample, the anisotropic signal observed is localized at the scattering peak associated with compositional phase separation as shown in Figure 7.5(c) and therefore, is from a matrix phase scattering across the dispersions. The identity of the matrix phase material is furthermore revealed through the energy dependence of the anisotropic signal. Shown in Figure 7.6(a) are the contrast functions for aligned P(NDI2OD-T2) molecules with P3HT dispersions of randomly oriented molecules. Scattering intensity at photon energies above approximately 285 eV will depend significantly on the P(NDI2OD-T2) orientation giving rise to the scattering anisotropy seen in the present system. This is not the case if the signal originates from ordered P3HT molecules (Figure 7.7) whose contrast functions are free of orientation dependence at approximately 286 and 287 eV. As shown in Figure 7.8, significant anisotropic signal was recorded at these energies. Thus, the anisotropy must originate from within a P(NDI2OD-T2) matrix phase with randomly oriented P3HT molecules in a dispersed phase. STXM microscopy confirms this conclusion (Figure 7.4).

Now that we have been managed to interpret the P-SoXS data to understand the ordering details of the nanomorphology of P3HT: P(NDI2OD-T2) blend system, it is extremely interesting to investigate the origin and evolution of the ordering phenomena in terms of the weight ratio of P3HT over P(NDI2OD-T2) and the sample preparing conditions such as annealing temperature and solvent annealing. As mentioned at the beginning of this section, the molecular

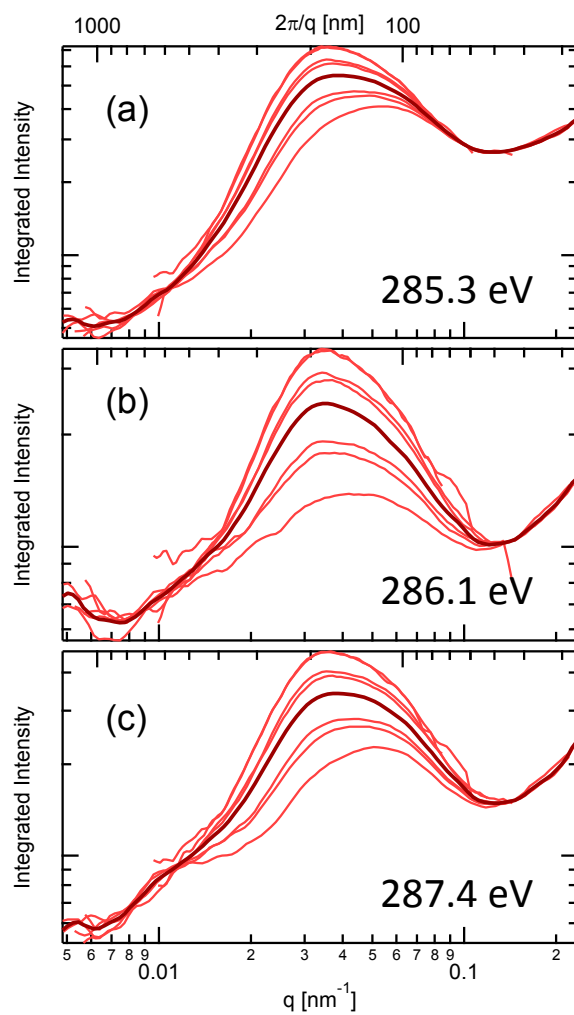


Figure 7.8: Radial scattering profiles processed identically as in Figure 7.5 at different photon energies. Figure authorized by and reproduced from Reference [4].

ordering are critical to the performance of the organic electronic devices. It will be significantly intriguing if the relationship between the ordering of the molecules and the performance of the devices can be revealed. This technique will certainly open another significant field of understanding the physics of organic electronics.

### 7.3 Quantatively determination of the domain purity by scattering invariant calculation

Resonant soft X-ray scattering has been proved to be able to provide domain information such as domain sizes, distribution and domain purity. Although the domain size can be accessed to as low as several nanometers with high enough phase contrast thanks to the high resolution tunability of the soft X-ray energies, the domain purity information is still limited to be qualitative. Considering that the device performance is affected not only by the domain size but also the domain purity in each phase [3], it will benefit the understanding of both device physics and engineering. Related study have been done in our group on a high efficiency blend system for organic solar cells [221]. The blend systems of P3HT: F8TBT and P3HT: P(NDI2OD-T2) exhibit good models for this type of study because of the easy control of the evolution of domain properties with annealing temperatures.

According to the definition of the Porod's invariant [51, 222, 223], the scattering profiles can be processed further to derive the domain purity. Starting with a two phase system, the total scattering intensity can be written as

$$TSI = \int_0^\infty I(q)q^2 dq = 2\pi^2 \Delta\rho^2 v_1 v_2 V \quad (7.1)$$

where  $I(q)$  is the angle dependent scattering intensity at certain momentum transfer  $q = 4\pi \sin \theta / \lambda$ ,  $\Delta\rho$  is the difference in electron density between the two phases,  $v_1$  and  $v_2$  are the volume fraction of domain 1 and 2 respectively, and  $V$  is the total illuminated volume by the incident X-ray beam. The material contrast affect the TSI and thus can be an measure of the domain purity. Considering the electron density

$$\rho = \frac{f_1 - \mathbf{i}f_2}{V} = \sum_j n_j (f_{1,j} - \mathbf{i}f_{2,j}) = \alpha E^2 (\delta - \mathbf{i}\beta) \quad (7.2)$$

where  $f_{1,j} - \mathbf{i}f_{2,j}$  are the complex elemental scattering factors,  $n_j$  are the number densities for the  $j^{th}$  element in each component molecule, and  $\alpha$  is a factor containing only universal constants, i.e.  $\alpha \equiv 2\pi / (r_e h^2 c^2)$ , where  $R_e$  is the classical electron radius,  $h$  is Plank's constant and  $c$  is the speed of light in vacuum. The left equality comes from the fact that the scattering factor is equivalent to the effective number of electrons that scatter, while the middle equality

converts from atomic view to that of a molecule. The final equality converts from scattering factors to optical constants. Thus

$$\Delta\rho_{12}^2 = \alpha^2 E^4 \Delta n_{12}^2 = \alpha^2 C_{12} \quad (7.3)$$

with the subscripts indicating contrast between domains (not materials). If the materials are mixed within the domains, this contrast will be reduced accordingly, and so will the TSI. By integrating the TSI over  $q$  from a scattering intensity profile, the domain purity information can be accessed and compared across samples.

## 7.4 Index-matched soft X-ray scattering

R-SoXR and R-SoXS have been proved to be extremely useful to access the interfacial information in planar geometry and domain information in BHJ nanomorphology. Despite the accuracy of the measurement of the bare surface or, more importantly, buried interfacial width with R-SoXR method, the values derived are root-mean-square averages with the interfacial profile being assumed as an error function. However, the interfacial nanostructure can be much more complicated in practical than an error function math model and R-SoXR has the difficulty of revealing the details of interfacial nanostructures. For instance, as in the diagram showing the definition of interfacial width ( $2\sigma$ ) for two very unlike interfacial profiles in Figure 4.1, R-SoXR can not distinguish the difference between these two types of profiles but can only measure an averaged width as defined. Considering how much the interfaces can influence the device performance, it is worth investigating the buried interfacial nanostructure in detail with more straightforward methods. As demonstrated in Chapter 6, R-SoXS has been successfully utilized to access the domain size distribution and qualitative purity information. In this transmission experimental geometry, however, the domain information acquired is constrained to the in-plane averaged structure. There is no out-of-plane nanostructure assessed in this geometry.

Motivated by the ability of accessing both in-plane and out-of-plane information possessed by techniques employing a grazing incidence, such as GI-WAXS, GI-SAXS (grazing-incidence wide/small angle X-ray scattering), and GI-SANS (grazing-incidence small angle neutron scattering), we have been developing a novel method to characterize the buried interfaces in grazing geometry, i.e. index-matched soft X-ray scattering (IM-SoXS). The experiment setup is shown in Figure 7.9. A soft X-ray beam hits the sample at a grazing angle ( $\alpha$  as shown in figure), gets scattered by the materials in the sample and the scatter intensity is recorded using a CCD detector. With this geometry, the recorded scattering data contains not only the in-plane structure information (as can be derived from the line cut indicated in Figure 7.9 aligned with the red arrows) but also the out-of-plane information that can not be accessed with simple

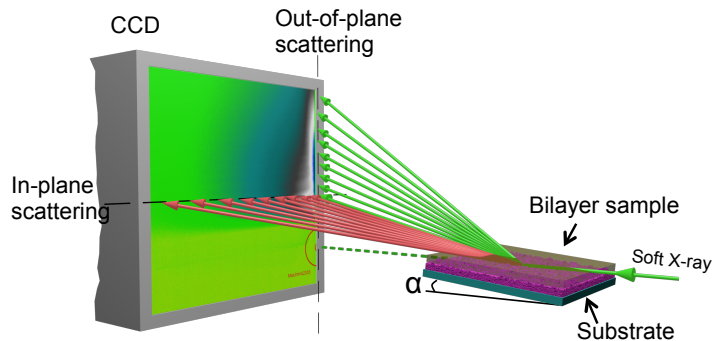


Figure 7.9: Schematic diagram of an IM-SoXS setup. A polymer bilayer on a substrate is illustrated as the sample examined. The green arrows indicates the out-of-plane scattering and the red ones indicates the in-plane scattering. The center of the red circle is where the direct beam should reach the detector.

transmission geometry. Most significantly, with the tunability of the soft X-ray energy, we can selectively enhance the contrast between the media at interfaces, ensuring the ability of probing the nanostructure of a buried interface underneath an organic top layer.

As mentioned in the preceding chapters, the contrast between two media at an interface can be measured by  $\Delta\delta^2 + \Delta\beta^2$ . As an example, a bilayer system composed of PMMA as the top layer is considered here. The optical constants  $\delta$  and  $\beta$  are plotted in Figure 7.10. In order to penetrate the top layer and probe the buried interface, the absorption and the scattering of the top layer has to be minimized. The use of the energies below the absorption edge will essentially reduce the absorption, allowing more X-ray to get through the top layer at grazing angles. Because the PMMA top layer in this case is an amorphous homogenous layer, the scattering from this layer due to density variation does not dominate and that due to crystalline or other bulk nanostructure is not applicable here. The scattering from the top layer is majorly due to the surface (vacuum/PMMA interface) roughness. With the absorption suppressed by choosing below-edge energies, another important factor to take into consideration is the critical angle when the X-ray is reflected by the PMMA surface. The critical angle,  $\theta_c$ , is the incident angle when the total reflection happens, meaning all the light is reflected and no light gets penetrated into the surface. It is known that  $\theta_c \approx \sqrt{\delta}$  [2], which is usually very low ( $\sim 0.15^\circ$ ) for hard X-rays but can be as high as several degrees and varies with the X-ray energy in the case of soft X-rays. Consequently, in order to reduce the scattering from the surface of the top layer, the energy at which  $\delta$  possess small magnitude is preferred. According to the plots in Figure 7.10, the energy of 286.4 eV is the best, where  $\delta$  equals zero and  $\beta$  is equally small as other below-edge energies. This is the so-called index-matched point which is the origin of the name IM-SoXS. At this point, the contrast  $\Delta\delta^2 + \Delta\beta^2$  is simultaneously minimized so the soft X-ray

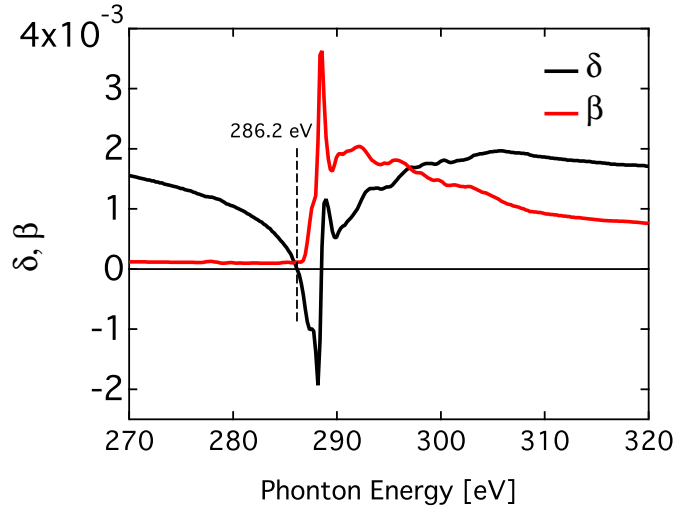


Figure 7.10: Optical constants of PMMA.

is not sensitive to the top surface.

The in-plane and out-of-plane scattering profiles then can be analyzed to extract the interfacial roughness by Inverse Fourier Transform the scattering profile ( $I \cdot q^2$ ) to get the real space autocorrelation of the original surface [51]. As a result, the nanostructure of the buried layer can be decomposed from the complexity of the scattering in grazing incidence and be characterized directly. Furthermore, the polarizability of the incident beam adds the capability of studying the molecular ordering at the buried interface and in the bulk of the buried layer, although the analysis of the scattering profile will be largely complicated, which is still under developing.

In the case of bilayer systems based on semiconductive polymer P(NDI2OD-T2), e.g. PMMA/P(NDI2OD-T2), IM-SoXS can be employed to investigate the buried PMMA/P(NDI2OD-T2) interfacial nanostructure. By examining the in-plane scattering profile, the interfacial roughness can be obtained and the nanostructure, i.e. either physically rough or diffused, can be determined. On the other hand, the out-of-plane scattering can be analyzed to infer the nanomorphology in the direction normal to the sample surface. Since dielectric/P(NDI2OD-T2) bilayer system poses an excellent model of studying the relationship between the device performance and the nanomorphology of the buried interface and bulk of active layer involving molecular ordering phenomena [117, 172, 4], the use of IM-SoXS is expected to reveal in-depth physics in those transistor devices based on these materials and to provide comprehensive knowledge of organic semiconductors.

## 7.5 R-SoXS at high- $q$ range for interfacial study of the domain boundaries

As discussed in Chapter 1, the working mechanism of organic solar cells base on BHJ active layers indicates that the interfaces between the donor and the acceptor materials are essentially important for the performance of the device, because the excitons need to be separated at the interfaces and charges need to drift from the interfaces into the donor or acceptor materials and reach the electrodes to be collected as photocurrent. The importance of the interfaces in a planar geometry has been investigated and assured in the study of PFB/F8BT bilayer organic solar cells in Chapter 3. As in the case of BHJ, R-SoXS can be used to examine the quality of the domain boundaries.

According to Porod [223], the limiting behavior of the scattering from an ideal two-phase system with sharp boundaries and a constant density inside the boundaries is expected to decrease with an  $q^{-4}$  law,

$$\lim_{q \rightarrow \infty} [I_p(q)] = \frac{K_p}{q^4} \quad (7.4)$$

where  $K_p$  is the so-called Porod-law constant, which is related to certain structural parameters of the system,

$$K_p = (S/V)Q/8\pi^3\phi_1\phi_2 = Q/2\pi^3l_p, \quad (7.5)$$

where

$$Q = 4\pi \int_0^\infty q^2 I(q) dq = V\phi_1\phi_2(\rho_1 - \rho_2)^2 \quad (7.6)$$

and  $(S/V)$  is the area of interface per unit volume,  $\phi_1$  and  $\phi_2$  are the volume fractions of the phases and  $\rho_1$  and  $\rho_2$  the respective electron densities.  $Q$  is the Porod invariant and  $l_p$  is the Porod inhomogeneity length, a parameter which serves as a measure of the average sized of the phases. Polymers often exhibit systematic deviations from Porod's law, that is, the product of  $I_p(q)q^4$  does not reach a constant value, maybe due to the thermal density fluctuations or mixing within phases, resulting in an enhancement of scattering at high angles causing a plot of  $Iq^4$  vs  $q^2$  to have a positive slope. This is known as the positive deviations from Porod's law [224].

Furthermore, in the case of BHJ practically, the two phases are not 100% pure and the phase boundaries are diffused in addition. The non-ideal boundary causes a depletion of high- $q$  scattering resulting in a negative slope for a  $Iq^4$  vs  $q^2$  plot, which is referred to as negative deviations from Porod's law. Ruland [225] has developed a method with modified Porod's law

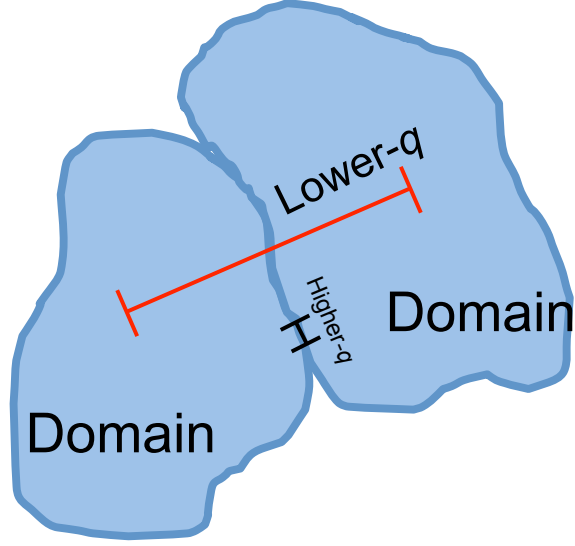


Figure 7.11: An illustration of the comparison between the length scales probed in low- $q$  and high- $q$  scattering data.

to extract the diffused domain boundary width from a  $Iq^4$  vs  $q^2$  plot .

Considering the scattering intensity in the Porod region after removing contributions due to density fluctuations within the phases is given by

$$I_{obs}(q) = I_p(q)H^2(q) \quad (7.7)$$

where  $H^2(q)$  is the Fourier transform of the autocorrelation of the smoothing function which represents the negative deviations from Porod's law due to the diffuse interface [224]. The form of the smoothing function used is dependent on the geometrical model for the interphase gradient. For example, the sigmoidal-gradient model has been treated by Ruland [225], with a smoothing function of Gaussian and thus  $H(q)$  is given by

$$H(q) = e^{-2\pi^2\sigma^2q^2}, \quad (7.8)$$

where  $\sigma$  is the standard deviation of the Gaussian smoothing function and is a measure of the tradition-layer width or the boundary width. The corresponding Porod-law relation becomes

$$I_{obs}(q) = (K_p/q^4)e^{-2\pi^2\sigma^2q^2} \quad (7.9)$$

and has been used in the determination of the diffuse-boundary widths in polystyrene- polyisoprene block copolymers [226]. This method is easier to understand qualitatively with the illustration in Figure 7.11. Because of  $q = 2\pi/d$  with  $d$  the spacing in the real space length

scale, lower- $q$  scattering data reflects a larger correlated real space length scale (which can be length scale of domain sizes), while higher- $q$  reflects a smaller correlated real space length scale (which can be the nanostructures in the scale of domain boundaries). Therefore, the scattering data at higher- $q$  carry the nanomorphology information of the interfacial areas between domains. Thanks to the contrast that can be probed by soft X-rays with the right energies, it is possible to examine the domain boundaries according to the theories and models that are developed as mentioned above. To do this, higher- $q$  data is required, which can be accessed by rotating the CCD detector with respect to the axis parallel to the sample plane in a transmission geometry and stitching the data acquired with CCD at different positions [227]. To carry out a quantitative measurement, the main challenge would be to normalize the data and perform the background subtraction correctly. The experimental and mathematical details need to be addressed carefully.

## REFERENCES

- [1] B. Kippelen and J.-L. Brédas, “Organic photovoltaics,” *Energy and Environmental Science*, vol. 2, no. 3, p. 251, 2009.
- [2] D. Attwood, *Soft X-rays and Extreme Ultraviolet Radiation, Principles and Applications*. Cambridge: Cambridge University Press, 2000.
- [3] S. Swaraj, C. Wang, H. Yan, B. Watts, J. Luning, C. R. McNeill, H. Ade, H. Yang, J. Lüning, and J. Luening, “Nanomorphology of bulk heterojunction photovoltaic thin films probed with resonant soft X-ray scattering,” *Nano Letters*, vol. 10, pp. 2863–2869, Jan. 2010.
- [4] B. A. Collins, J. E. Cochran, H. Yan, E. Gann, C. Hub, R. Fink, C. Wang, T. Schuettfort, C. R. McNeill, M. L. Chabinye, and H. Ade, “Polarized X-ray scattering reveals non-crystalline orientational ordering in organic films,” *Nature Materials*, vol. 11, pp. 536–543, Apr. 2012.
- [5] L. Dou, J. You, J. Yang, C. Chen, Y. He, S. Murase, T. Moriarty, K. Emery, G. Li, and Y. Yang, “Tandem polymer solar cells featuring a spectrally matched low-bandgap polymer,” *Nature Photonics*, vol. 6, pp. 180–185, 2012.
- [6] G. Heimel, L. Romaner, E. Zojer, and J.-L. Brédas, “Toward control of the metal-organic interfacial electronic structure in molecular electronics: a first-principles study on self-assembled monolayers of pi-conjugated molecules on noble metals.,” *Nano letters*, vol. 7, pp. 932–40, Apr. 2007.
- [7] R. H. Bube, *Photovoltaic materials*. London: Imperial College Press, 1998.
- [8] P. Würfel, *Physics of solar cells: from basic principle to advanced concepts*. Weinheim: Wiley-VCH, 2009.
- [9] M. A. Green, *Solar cells: operating principles, technology and system applications*. Kensington, NSW: Univ. of New South Wales, 1998.
- [10] B. P. Rand, D. P. Burk, and S. R. Forrest, “Offset energies at organic semiconductor heterojunctions and their influence on the open-circuit voltage of thin-film solar cells,” *Physical Review B*, vol. 75, no. 11, pp. 115311–115327, 2007.
- [11] M. C. Scharber, D. Mühlbacher, M. Koppe, P. Denk, C. Waldauf, A. J. Heeger, and C. J. Brabec, “Design Rules for Donors in Bulk-Heterojunction Solar Cells - Towards 10 % Energy-Conversion Efficiency,” *Advanced Materials*, vol. 18, no. 6, pp. 789–794, 2006.
- [12] T. Sekitani, S. Iba, Y. Kato, Y. Noguchi, T. Sakurai, and T. Someya, “Submillimeter radius bendable organic field-effect transistors,” *Journal of Non-Crystalline Solids*, vol. 352, pp. 1769–1773, June 2006.

- [13] H. Ishii, K. Sugiyama, E. Ito, and K. Seki, "Energy level alignment and interfacial electronic structures at organic/metal and organirganic interfaces," *Advanced Materials*, vol. 11, no. 8, pp. 605–625, 1999.
- [14] J. E. Malinsky, J. G. C. Veinot, G. E. Jabbour, S. E. Shaheen, J. D. Anderson, P. Lee, A. G. Richter, A. L. Burin, M. a. Ratner, T. J. Marks, N. R. Armstrong, B. Kippelen, P. Dutta, and N. Peyghambarian, "Nanometer-Scale Dielectric Self-assembly Process for Anode Modification in Organic Light-Emitting Diodes. Consequences for Charge Injection and Enhanced Luminous Efficiency," *Chemistry of Materials*, vol. 14, pp. 3054–3065, July 2002.
- [15] J. Cui, Q. Huang, J. Veinot, H. Yan, and T. Marks, "Interfacial Microstructure Function in Organic Light-Emitting Diodes: Assembled Tetraaryldiamine and Copper Phthalocyanine Interlayers," *Advanced Materials*, vol. 14, p. 565, Apr. 2002.
- [16] J. G. C. Veinot and T. J. Marks, "Toward the Ideal Organic Light-Emitting Diode. The Versatility and Utility of Interfacial Tailoring by Cross-Linked Siloxane Interlayers," *Accounts of Chemical Research*, vol. 38, pp. 632–643, Aug. 2005.
- [17] N. R. Armstrong, W. Wang, D. M. Alloway, D. Placencia, E. Ratcliff, and M. Brumbach, "Organic/Organic' heterojunctions: organic light emitting diodes and organic photovoltaic devices.," *Macromolecular Rapid Communications*, vol. 30, pp. 717–31, May 2009.
- [18] M. T. Bernius, M. Inbasekaran, J. O'Brien, and W. S. Wu, "Progress with light-emitting polymers," *Advanced Materials*, vol. 12, pp. 1737–1750, Jan. 2000.
- [19] C. J. Brabec, S. Gowrisanker, J. J. M. Halls, D. Laird, S. Jia, and S. P. Williams, "Polymer-fullerene bulk-heterojunction solar cells," *Advanced Materials*, vol. 22, pp. 3839–56, Sept. 2010.
- [20] C. J. Brabec, M. Heeney, I. McCulloch, and J. Nelson, "Influence of blend microstructure on bulk heterojunction organic photovoltaic performance.," *Chemical Society Reviews*, vol. 40, pp. 1185–99, Mar. 2011.
- [21] S. Braun, W. R. Salaneck, and M. Fahlman, "Energy-Level Alignment at Organic/Metal and Organic/Organic Interfaces," *Advanced Materials*, vol. 21, no. 14-15, pp. 1450–1472, 2009.
- [22] K. Jandt, "Developments and perspectives of scanning probe microscopy (SPM) on organic materials systems," *Materials Science and Engineering: R: Reports*, vol. 21, pp. 221–295, 1998.
- [23] S. N. Magonov and D. H. Reneker, "CHARACTERIZATION OF POLYMER SURFACES WITH ATOMIC FORCE MICROSCOPY," *Annual Review of Materials Science*, vol. 27, pp. 175–222, Aug. 1997.
- [24] S. Sheiko, "Imaging of polymers using scanning force microscopy: From superstructures to individual molecules," *Advances in Polymer Science*, vol. 151, p. 61, 2000.

- [25] D. C. Coffey and D. S. Ginger, "Time-resolved electrostatic force microscopy of polymer solar cells," *Nature materials*, vol. 5, pp. 735–40, Sept. 2006.
- [26] D. C. Coffey, O. G. Reid, D. B. Rodovsky, G. P. Bartholomew, and D. S. Ginger, "Mapping local photocurrents in polymer/fullerene solar cells with photoconductive atomic force microscopy," *Nano letters*, vol. 7, pp. 738–44, Mar. 2007.
- [27] T. P. Russell, A. Karim, A. Mansour, and G. P. Felcher, "Specular reflectivity of neutrons by thin polymer films," *Macromolecules*, vol. 21, no. 6, pp. 1890–1893, 1988.
- [28] V. Arrighi and J. S. Higgins, "Structural investigation of polymers by neutron scattering," *Plastics, Rubber and Composites*, vol. 33, pp. 313–330, Oct. 2004.
- [29] J. Dudowicz, K. F. Freed, and M. Lifschitz, "Towards a Molecular-Basis for Understanding the Behavior of Isotopic Polymer Blends - Lattice Cluster Theory Computations for Psh Psh Blends," *Macromolecules*, vol. 27, no. 19, pp. 5387–5398, 1994.
- [30] T. Russell, "Changes in Polystyrene and Poly(methyl methacrylate) Interactions with Isotopic Substitution," *Macromolecules*, vol. 26, p. 5819, 1993.
- [31] T. P. Russell, "On the reflectivity of polymers: Neutrons and X-rays," *Physica B*, vol. 221, no. 1-4, pp. 267–283, 1996.
- [32] B. E. Warren, *X-ray diffraction*. New York: Dover Publications, 1990.
- [33] A. Guinier, *X-ray diffraction in crystals, imperfect crystals, and amorphous bodies*. New York: Dover Publications, 1994.
- [34] Y. D. Park, D. H. Kim, Y. Jang, J. H. Cho, M. Hwang, H. S. Lee, J. A. Lim, and K. Cho, "Effect of side chain length on molecular ordering and field-effect mobility in poly(3-alkylthiophene) transistors," *Organic Electronics*, vol. 7, pp. 514–520, Dec. 2006.
- [35] D. H. Kim, Y. D. Park, Y. Jang, H. Yang, Y. H. Kim, J. I. Han, D. G. Moon, S. Park, T. Chang, C. Chang, M. Joo, C. Y. Ryu, and K. Cho, "Enhancement of Field-Effect Mobility Due to Surface-Mediated Molecular Ordering in Regioregular Polythiophene Thin Film Transistors," *Advanced Functional Materials*, vol. 15, pp. 77–82, Jan. 2005.
- [36] J.-F. Chang, B. Sun, D. W. Breiby, M. M. Nielsen, T. I. Sölling, M. Giles, I. McCulloch, and H. Sirringhaus, "Enhanced Mobility of Poly(3-hexylthiophene) Transistors by Spin-Coating from High-Boiling-Point Solvents," *Chemistry of Materials*, vol. 16, pp. 4772–4776, Nov. 2004.
- [37] H. Sirringhaus, "Device Physics of Solution-Processed Organic Field-Effect Transistors," *Advanced Materials*, vol. 17, pp. 2411–2425, Oct. 2005.
- [38] A. Salleo, "Charge transport in polymeric transistors," *Materials Today*, vol. 10, pp. 38–45, Mar. 2007.
- [39] J. Stöhr, *NEXAFS spectroscopy*. New York: Springer-Verlag, 1992.

- [40] B. Watts, S. Swaraj, D. Nordlund, J. Luening, and H. Ade, "Calibrated NEXAFS spectra of common conjugated polymers," *Journal of Chemical Physics*, vol. 134, p. 24702, Jan. 2011.
- [41] A. L. D. Kilcoyne, T. Tylizszczak, W. F. Steele, S. Fakra, P. Hitchcock, K. Franck, E. Anderson, B. Harteneck, E. G. Rightor, G. E. Mitchell, A. P. Hitchcock, L. Yang, T. Warwick, and H. Ade, "Interferometer-controlled scanning transmission X-ray microscopes at the Advanced Light Source," *Journal of Synchrotron Radiation*, vol. 10, no. 2, pp. 125–136, 2003.
- [42] C. R. McNeill, A. Abrusci, J. Zaumseil, R. Wilson, M. J. McKiernan, J. H. Burroughes, J. J. M. Halls, N. C. Greenham, and R. H. Friend, "Dual electron donor/electron acceptor character of a conjugated polymer in efficient photovoltaic diodes," *Applied Physics Letters*, vol. 90, p. 193506, Jan. 2007.
- [43] B. Watts and C. R. McNeill, "Simultaneous Surface and Bulk Imaging of Polymer Blends with X-ray Spectromicroscopy," *Macromolecular Rapid Communications*, vol. 31, pp. 1706–1712, Jan. 2010.
- [44] B. Watts, W. J. Belcher, L. Thomsen, H. Ade, and P. C. Dastoor, "A Quantitative Study of PCBM Diffusion during Annealing of P3HT: PCBM Blend Films," *Macromolecules*, vol. {ASAP}, pp. 8392–8397, Jan. 2009.
- [45] C. R. McNeill, B. Watts, S. Swaraj, H. Ade, L. Thomsen, W. Belcher, and P. C. Dastoor, "Evolution of the nanomorphology of photovoltaic polyfluorene blends: Sub-100 nm resolution with X-ray spectromicroscopy," *Nanotechnology*, vol. 19, p. 424015, Jan. 2008.
- [46] B. A. Collins, E. Gann, L. Guignard, X. He, C. R. McNeill, and H. Ade, "Molecular miscibility of polymer-fullerene blends," *The Journal of Physical Chemistry Letters*, vol. 1, pp. 3160–3166, Jan. 2010.
- [47] B. A. Collins, Z. Li, C. R. McNeill, and H. Ade, "Fullerene-dependent miscibility in the silole-containing copolymer PSBTBT-08," *Macromolecules*, p. (in press), 2011.
- [48] C. R. McNeill, B. Watts, L. Thomsen, W. J. Belcher, A. L. D. Kilcoyne, N. C. Greenham, and P. C. Dastoor, "X-ray spectromicroscopy of polymer/fullerene composites: Quantitative chemical mapping," *Small*, vol. 2, p. 1432, Jan. 2006.
- [49] T. Araki, H. Ade, J. M. Stubbs, D. C. Sundberg, G. Mitchell, J. Kortright, and A. Kilcoyne, "Soft X-ray resonant scattering of structured polymer nanoparticles," *Applied Physics Letters*, vol. 89, no. 12, p. 124106, 2006.
- [50] G. E. Mitchell, B. G. Landes, J. Lyons, B. J. Kern, M. J. Devon, I. Koprinarov, E. M. Gullikson, and J. B. Kortright, "Molecular bond selective x-ray scattering for nanoscale analysis of soft matter," *Applied Physics Letters*, vol. 89, no. 4, p. 044101, 2006.
- [51] O. Glatter and O. Kratky, *Small angle X-ray scattering*. London: New York: Academic Press, 1982.

- [52] B. L. Henke, E. M. Gullikson, and J. C. Davis, “X-Ray interactions: photoabsorption, scattering, transmission, and reflection at  $E=50\text{--}30,000$  eV,  $Z=1\text{--}92$ ,” *Atomic Data and Nuclear Data Tables*, vol. 54, no. 2, pp. 181–342, 1993.
- [53] O. Dhez, H. Ade, and S. Urquhart, “Calibrated NEXAFS spectra of some common polymers,” *Journal of Electron Spectroscopy and Related Phenomena*, vol. 128, no. 1, pp. 85–96, 2003.
- [54] J. Kikuma and B. P. Tonner, “XANES spectra of a variety of widely used organic polymers at the C K-edge,” *Journal of Electron Spectroscopy and Related Phenomena*, vol. 82, no. 1-2, pp. 53–60, 1996.
- [55] S. Urquhart, A. Hitchcock, A. Smith, H. Ade, W. Lidy, E. Rightor, and G. Mitchell, “NEXAFS spectromicroscopy of polymers: Overview and quantitative analysis of polyurethane polymers,” *Journal of Electron Spectroscopy and Related Phenomena*, vol. 100, pp. 119–135, 1999.
- [56] S. Urquhart and H. Ade, “Trends in the carbonyl core (C 1s, O 1s)  $\pi^*\text{C}=\text{O}$  transition in the near edge X-ray absorption fine structure spectra of organic molecules,” *The Journal of Physical Chemistry B*, vol. 106, no. 34, pp. 8531–8538, 2002.
- [57] P. L. Cook, X. Liu, W. Yang, and F. J. Himpsel, “X-ray absorption spectroscopy of biomimetic dye molecules for solar cells,” *Journal of Chemical Physics*, vol. 131, p. 194701, Nov. 2009.
- [58] K. Kaznatcheyev, A. Osanna, C. Jacobsen, O. Plashkevych, O. Vahtras, and H. Agren, “Innershell absorption spectroscopy of amino acids,” *The Journal of Physical Chemistry A*, vol. 106, no. 13, pp. 3153–3168, 2002.
- [59] S. Dambach, H. Backe, T. Doerk, N. Eftekhari, H. Euteneuer, F. Görgen, F. Hagenbuck, K. H. Kaiser, O. Kettig, G. Kube, W. Lauth, H. Schöpe, A. Steinhof, T. Tonn, and T. Walcher, “Novel interferometer in the soft X-ray region,” *Physical Review Letters*, vol. 80, no. 25, pp. 5473–5476, 1998.
- [60] D. Joyeux, F. Polack, and D. Phalippou, “An interferometric determination of the refractive part of optical constants for carbon and silver across soft x-ray absorption edges,” *Review of Scientific Instruments*, vol. 70, no. 7, p. 2921, 1999.
- [61] C. Jacobsen, S. Wang, W. Yun, and S. Frigo, “Calculation of x-ray refraction from near-edge absorption data only,” in *Proceedings of the SPIE*, vol. 5538, pp. 23–30, 2004.
- [62] H. Ade, A. P. Smith, H. Zhang, G. R. Zhuang, J. Kirz, E. Rightor, and A. Hitchcock, “X-ray spectromicroscopy of polymers and tribological surfaces at beamline X1A at the NSLS,” *Journal of Electron Spectroscopy and Related Phenomena*, vol. 84, no. 1-3, pp. 53–71, 1997.
- [63] E. M. Gullikson, P. DENHAM, S. MROWKA, and J. H. UNDERWOOD, “Absolute photoabsorption measurements of Mg, Al, and Si in the soft X-ray region below the L<sub>2,3</sub> edges,” *Physical Review B*, vol. 49, pp. 16283–16288, Jan. 1994.

- [64] B. Sae-Lao and R. Soufli, "Measurements of the refractive index of yttrium in the 50-1300 eV energy region," *Applied Optics*, vol. 41, no. 34, pp. 7309–7316, 2002.
- [65] R. Soufli and E. M. Gullikson, "Absolute photoabsorption measurements of molybdenum in the range 60-930 eV for optical constant determination," *Applied Optics*, vol. 37, no. 10, pp. 1713–1719, 1998.
- [66] K. Rosfjord, C. Chang, R. Miyakawa, H. Barth, and D. Attwood, "Direct index of refraction measurements at extreme-ultraviolet and soft-x-ray wavelengths.," *Applied Optics*, vol. 45, pp. 1730–6, Mar. 2006.
- [67] H.-J. Hagemann, W. Gudat, and C. Kunz, "Optical constants from the far infrared to the x-ray region : Mg, Al, Cu, Ag, Au, Bi, C, and Al<sub>2</sub>O<sub>3</sub>," *Journal of the Optical Society of America*, vol. 65, no. 6, pp. 742–744, 1975.
- [68] J. Svatos, D. Joyeux, D. Phalippou, and F. Polack, "Soft-x-ray interferometer for measuring the refractive index of materials.," *Optics Letters*, vol. 18, p. 1367, Aug. 1993.
- [69] R. Soufli and E. M. Gullikson, "Reflectance measurements on clean surfaces for the determination of optical constants of silicon in the extreme ultraviolet-soft-X-ray region," *Applied Optics*, vol. 36, pp. 5499–5507, Jan. 1997.
- [70] C. Chang, E. Anderson, P. Naulleau, E. Gullikson, K. Goldberg, and D. Attwood, "Direct measurement of index of refraction in the extreme-ultraviolet wavelength region with a novel interferometer," *Optics Letters*, vol. 27, no. 12, pp. 1028–1030, 2002.
- [71] C. Wang, T. Araki, and H. Ade, "Soft X-ray resonant reflectivity of low Z material thin films," *Applied Physics Letters*, vol. 87, p. 214109, Jan. 2005.
- [72] C. Wang, T. Araki, B. Watts, S. Harton, T. Koga, S. Basu, and H. Ade, "Resonant soft x-ray reflectivity of organic thin films," *Journal of Vacuum Science & Technology A*, vol. 25, pp. 575–586, Jan. 2007.
- [73] J. M. Virgili, Y. F. Tao, J. B. Kortright, N. P. Balsara, and R. A. Segalman, "Analysis of order formation in block copolymer thin films using resonant soft X-ray scattering," *Macromolecules*, vol. 40, pp. 2092–2099, Jan. 2007.
- [74] H. Yan, S. Swaraj, C. Wang, I. Hwang, N. C. Greenham, C. Groves, H. Ade, and C. R. McNeill, "Influence of annealing and interfacial roughness on the performance of bilayer donor/acceptor polymer photovoltaic devices," *Advanced Functional Materials*, vol. 20, no. 24, pp. 4329–4337, 2010.
- [75] M. Nayak, G. S. Lodha, T. T. Prasad, P. Nageswararao, and A. K. Sinha, "Probing porosity at buried interfaces using soft x-ray resonant reflectivity," *Journal of Applied Physics*, vol. 107, no. 2, p. 23529, 2010.
- [76] S. P. Singh, M. H. Modi, and P. Srivastava, "Growth kinetics and compositional analysis of silicon rich a-SiN(x):H film: A soft x-ray reflectivity study," *Applied Physics Letters*, vol. 97, no. 15, p. 151906, 2010.

- [77] M. Mezger, B. Jérôme, J. Kortright, M. Valvidares, E. Gullikson, A. Giglia, N. Mahne, and S. Nannarone, “Molecular orientation in soft matter thin films studied by resonant soft x-ray reflectivity,” *Physical Review B*, vol. 83, no. 15, p. 155406, 2011.
- [78] M. Beckers, T. Senkbeil, T. Gorniak, M. Reese, K. Giewekemeyer, S.-C. Gleber, T. Salditt, and A. Rosenhahn, “Chemical Contrast in Soft X-Ray Ptychography,” *Physical Review Letters*, vol. 107, p. 208101, Nov. 2011.
- [79] R. D. L. Kronig, “On the theory of dispersion of x-rays,” *Journal of the Optical Society of America*, vol. 12, pp. 547–556, June 1926.
- [80] R. Bachrach and F. Brown, “Exciton-optical properties of TlBr and TlCl,” *Physical Review B*, vol. 1, pp. 818–831, Jan. 1970.
- [81] K. F. Palmer, M. Z. Williams, and B. A. Budde, “Multiply subtractive Kramers-Kronig analysis of optical data,” *Applied Optics*, vol. 37, p. 2660, May 1998.
- [82] J. H. Underwood and E. M. Gullikson, “High-resolution, high-flux, user friendly VLS beamline at the ALS for the 50-1300 eV energy region,” *Journal of Electron Spectroscopy and Related Phenomena*, vol. 92, no. 1-3, pp. 265–272, 1998.
- [83] T. Coffey, S. G. Urquhart, and H. Ade, “Characterization of the effects of soft X-ray irradiation on polymers,” *Journal of Electron Spectroscopy and Related Phenomena*, vol. 122, no. 1, pp. 65–78, 2002.
- [84] D. L. Windt, “IMD–Software for modeling the optical properties of multilayer films,” *Computers in Physics*, vol. 12, no. 4, pp. 360–370, 1998.
- [85] H. Klauk, *Organic Electronics. Materials, Manufacturing and Applications*. New York: Wiley-VCH, 2006.
- [86] C. Brabec, V. Dyakonov, J. Parisi, and N. S. Sariciftci, *Organic Photovoltaics: Concepts and Realization*. New York: Springer, 2003.
- [87] J. Kido, M. Kimura, and K. Nagai, “Multilayer White Light-Emitting Organic Electroluminescent Device,” *Science*, vol. 267, pp. 1332–1334, Jan. 1995.
- [88] W. L. Ma, P. K. Iyer, X. Gong, B. Liu, D. Moses, G. C. Bazan, and A. J. Heeger, “Water/methanol-soluble conjugated copolymer as an electron-transport layer in polymer light-emitting diodes,” *Advanced Materials*, vol. 17, pp. 274–277, Jan. 2005.
- [89] X. Gong, S. Wang, D. Moses, G. C. Bazan, and A. J. Heeger, “Multilayer polymer light-emitting diodes: White-light emission with high efficiency,” *Advanced Materials*, vol. 17, pp. 2053–2058, Jan. 2005.
- [90] R. Yang, H. Wu, Y. Cao, and G. C. Bazan, “Control of Cationic Conjugated Polymer Performance in Light Emitting Diodes by Choice of Counterion,” *Journal of the American Chemical Society*, vol. 128, pp. 14422–14423, Jan. 2006.

- [91] S. Guenes, H. Neugebauer, N. S. Sariciftci, and S. Gunes, “Conjugated polymer-based organic solar cells,” *Chemical Reviews*, vol. 107, pp. 1324–1338, Jan. 2007.
- [92] S. H. Park, A. Roy, S. Beaupré, S. Cho, N. Coates, J. S. Moon, D. Moses, M. Leclerc, K. Lee, S. Beaupre, and A. J. Heeger, “Bulk heterojunction solar cells with internal quantum efficiency approaching 100%,” *Nature Photonics*, vol. 3, pp. 297–302, Jan. 2009.
- [93] W. L. Ma, C. Y. Yang, X. Gong, K. Lee, and A. J. Heeger, “Thermally stable, efficient polymer solar cells with nanoscale control of the interpenetrating network morphology,” *Advanced Functional Materials*, vol. 15, pp. 1617–1622, Jan. 2005.
- [94] Y. Liang, Z. Xu, J. Xia, S. Tsai, Y. Wu, G. Li, C. Ray, and L. Yu, “For the Bright Future-Bulk Heterojunction Polymer Solar Cells with Power Conversion Efficiency of 7.4%,” *Advanced Materials*, vol. 22, pp. E135–E138, Jan. 2010.
- [95] G. Horowitz, “Organic field-effect transistors,” *Advanced Materials*, vol. 10, pp. 365–377, Jan. 1998.
- [96] L.-L. Chua, J. Zaumseil, J.-F. Chang, E. C.-W. Ou, P. K.-H. Ho, H. Sirringhaus, and R. H. Friend, “General observation of n-type field-effect behaviour in organic semiconductors,” *Nature*, vol. 434, pp. 194–199, Jan. 2005.
- [97] A. Salleo, R. J. Kline, D. M. DeLongchamp, and M. L. Chabiny, “Microstructural Characterization and Charge Transport in Thin Films of Conjugated Polymers,” *Advanced Materials*, vol. 22, pp. 3812–3838, Jan. 2010.
- [98] S. E. Fritz, T. W. Kelley, and C. D. Frisbie, “Effect of dielectric roughness on performance of pentacene TFTs and restoration of performance with a polymeric smoothing layer,” *The Journal of Physical Chemistry B*, vol. 109, pp. 10574–10577, Jan. 2005.
- [99] M. L. Chabiny, R. Lujan, F. Endicott, M. F. Toney, I. McCulloch, and M. Heeney, “Effects of the surface roughness of plastic-compatible inorganic dielectrics on polymeric thin film transistors,” *Applied Physics Letters*, vol. 90, no. 23, p. 233508, 2007.
- [100] Y. Jung, R. J. Kline, D. a. Fischer, E. K. Lin, M. Heeney, I. McCulloch, and D. M. DeLongchamp, “The Effect of Interfacial Roughness on the Thin Film Morphology and Charge Transport of High-Performance Polythiophenes,” *Advanced Functional Materials*, vol. 18, pp. 742–750, Mar. 2008.
- [101] R. A. L. Jones, *Polymers at Surfaces and Interfaces*. New York: Cambridge University Press, 1999.
- [102] A. M. Higgins, S. J. Martin, M. Geoghegan, S. Y. Heriot, R. L. Thompson, R. Cubitt, R. M. Dalgliesh, I. Grizzi, and R. A. L. Jones, “Interfacial structure in conjugated polymers: Characterization and control of the interface between poly(9,9-dioctylfluorene) and poly(9,9-dioctylfluorene-alt-benzothiadiazole),” *Macromolecules*, vol. 39, no. 19, pp. 6699–6707, 2006.

- [103] Y. J. Lee, H. Lee, Y. Byun, S. Song, J. E. Kim, D. Eom, W. Cha, S. S. Park, J. Kim, and H. Kim, "Study of thermal degradation of organic light emitting device structures by X-ray scattering," *Thin Solid Films*, vol. 515, no. 14, pp. 5674–5677, 2007.
- [104] Y. J. Lee, X. Li, D. Y. Kang, S. S. Park, J. Kim, J. W. Choi, and H. Kim, "Surface morphology and interdiffusion of LiF in Alq(3)-based organic light-emitting devices," *Ultramicroscopy*, vol. 108, no. 10, pp. 1315–1318, 2008.
- [105] O. Seeck, I. Kaendler, M. Tolan, M. Shin, M. Rafailovich, J. Sokolov, and R. Kolb, "Analysis of X-Ray Reflectivity Data from Low-Contrast Polymer Bilayer Systems using a Fourier Method," *Applied Physics Letters*, vol. 76, no. 19, pp. 2713–2715, 2000.
- [106] H. Ade, C. Wang, A. Hexemer, A. Garcia, T. Q. Nguyen, G. C. Bazan, K. E. Sohn, and E. J. Kramer, "Characterization of multicomponent polymer trilayers with resonant soft x-ray reflectivity," *Journal of Polymer Science, Part B: Polymer Physics*, vol. 47, pp. 1291–1299, 2009.
- [107] A. M. Higgins, A. Cadby, D. C. Lidzey, R. M. Dalgliesh, M. Geoghegan, R. A. L. Jones, S. J. Martin, and S. Y. Heriot, "The impact of Interfacial Mixing on Forster Transfer at Conjugated Polymer Heterojunctions," *Advanced Functional Materials*, vol. 19, no. 1, pp. 157–163, 2009.
- [108] A. M. Higgins, S. J. Martin, P. C. Jukes, M. Geoghegan, R. A. L. Jones, S. Langridge, R. Cubitt, S. Kirchmeyer, A. Wehrum, and I. Grizzi, "Interfacial structure in semiconducting polymer devices," *Journal of Material Chemistry*, vol. 13, no. 11, pp. 2814–2818, 2003.
- [109] J. W. Kiel, A. P. R. Eberle, and M. E. Mackay, "Nanoparticle agglomeration in polymer-based solar cells," *Physical Review Letters*, vol. 105, p. 168701, Jan. 2010.
- [110] J. W. Kiel, M. E. Mackay, B. J. Kirby, B. B. Maranville, and C. F. Majkrzak, "Phase-sensitive neutron reflectometry measurements applied in the study of photovoltaic films," *Journal of Chemical Physics*, vol. 133, p. 74902, Jan. 2010.
- [111] Z. C. Wang, A. Hexemer, J. Nasiatka, E. R. Chan, A. T. Young, H. A. Padmore, W. F. Schlotter, J. Lüning, S. Swaraj, B. Watts, E. Gann, H. Yan, and H. Ade, "Resonant Soft X-ray Scattering of Polymers with a 2D Detector: Initial Results and System Developments at the Advanced Light Source," *IOP Conference Series.: Materials Science and Engineering*, vol. 14, p. 12016, 2010.
- [112] H. Ade and A. P. Hitchcock, "NEXAFS microscopy, resonant scattering and resonant reflectivity: composition and orientation probed in real and reciprocal space," *Polymer*, vol. 49, no. 3, pp. 643–675, 2008.
- [113] S. Swaraj, C. Wang, T. Araki, G. Mitchell, L. Liu, S. Gaynor, B. Deshmukh, H. Yan, C. R. McNeill, H. Ade, and C. R. McNeill, "Extension of the utility of resonant soft x-ray scattering and reflectivity for nanoscale characterization of polymers," *European Physical Journal Special Topics*, vol. 168, pp. 121–126, Jan. 2009.

- [114] D. W. Steuerman, A. Garcia, M. Dante, R. Yang, J. P. Lofvander, and T. Q. Nguyen, "Imaging the interfaces of conjugated polymer optoelectronic devices," *Advanced Materials*, vol. 20, no. 3, pp. 528–534, 2008.
- [115] C. Wang, A. Garcia, H. Yan, K. E. Sohn, A. Hexemer, T. Nguyen, G. C. Bazan, E. J. Kramer, and H. Ade, "Interfacial widths of conjugated polymer bilayers," *Journal of the American Chemical Society*, vol. 131, no. 35, pp. 12538–12539, 2009.
- [116] H. Yan, Z. Chen, Y. Zheng, C. Newman, J. R. Quinn, F. Dötz, M. Kastler, A. Facchetti, and F. Dotz, "A high-mobility electron-transporting polymer for printed transistors," *Nature*, vol. 457, pp. 679–686, Jan. 2009.
- [117] J. Rivnay, M. F. Toney, Y. Zheng, I. V. Kauvar, Z. Chen, V. Wagner, A. Facchetti, and A. Salleo, "Unconventional Face-On Texture and Exceptional In-Plane Order of a High Mobility n-Type Polymer," *Advanced Materials*, vol. 22, pp. 4359–4363, Jan. 2010.
- [118] E. G. Rightor, A. P. Hitchcock, H. Ade, R. D. Leapman, S. G. Urquhart, A. P. Smith, G. Mitchell, D. Fisher, H. J. Shin, and T. Warwick, "Spectromicroscopy of Poly(ethylene terephthalate): Comparison of Spectra and Radiation Damage Rates in X-ray Absorption and Electron Energy Loss," *The Journal of Physical Chemistry B*, vol. 101, no. 11, pp. 1950–1960, 1997.
- [119] M. Sferrazza, C. Xiao, R. A. L. Jones, D. G. Bucknall, J. Webster, and J. Penfold, "Evidence for capillary waves at immiscible polymer/polymer interfaces," *Physical Review Letters*, vol. 78, no. 19, pp. 3693–3696, 1997.
- [120] P. W. M. Blom, V. D. Mihailetschi, L. Koster, and D. Markov, "Device Physics of Polymer:Fullerene Bulk Heterojunction Solar Cells," *Advanced Materials*, vol. 19, pp. 1551–1566, June 2007.
- [121] V. D. Mihailetschi, L. J. A. Koster, J. C. Hummelen, and P. W. M. Blom, "Photocurrent generation in polymer-fullerene bulk heterojunctions," *Physical Review Letters*, vol. 93, no. 21, 2004.
- [122] P. Peumans and S. R. Forrest, "Separation of geminate charge-pairs at donor-acceptor interfaces in disordered solids," *Chemical Physics Letters*, vol. 398, no. 1-3, pp. 27–31, 2004.
- [123] D. Veldman, O. Ipek, S. C. J. Meskers, J. Sweelssen, M. M. Koetse, S. C. Veenstra, J. M. Kroon, S. S. V. Bavel, J. Loos, and R. a. J. Janssen, "Compositional and electric field dependence of the dissociation of charge transfer excitons in alternating polyfluorene copolymer/fullerene blends," *Journal of the American Chemical Society*, vol. 130, pp. 7721–7735, June 2008.
- [124] M. Wojcik and M. Tachiya, "Accuracies of the empirical theories of the escape probability based on Eigen model and Braun model compared with the exact extension of Onsager theory," *The Journal of Chemical Physics*, vol. 130, p. 104107, Mar. 2009.

- [125] R. A. Marsh, C. R. McNeill, A. Abrusci, A. R. Campbell, and R. H. Friend, “A unified description of current-voltage characteristics in organic and hybrid photovoltaics under low light intensity,” *Nano letters*, vol. 8, pp. 1393–8, May 2008.
- [126] C. Groves, R. a. Marsh, and N. C. Greenham, “Monte Carlo modeling of geminate recombination in polymer-polymer photovoltaic devices,” *Journal of Chemical Physics*, vol. 129, p. 114903, Sept. 2008.
- [127] C. R. McNeill, S. Westenhoff, C. Groves, R. H. Friend, and N. C. Greenham, “Influence of nanoscale phase separation on the charge generation dynamics and photovoltaic performance of conjugated polymer blends: Balancing charge generation and separation,” *The Journal of Physical Chemistry C*, vol. 111, no. 51, pp. 19153–19160, 2007.
- [128] C. Groves, L. J. a. Koster, and N. C. Greenham, “The effect of morphology upon mobility: Implications for bulk heterojunction solar cells with nonuniform blend morphology,” *Journal of Applied Physics*, vol. 105, no. 9, p. 094510, 2009.
- [129] C. R. McNeill, B. Watts, L. Thomsen, H. Ade, N. C. Greenham, P. C. Dastoor, and P. C. Dastoor, “X-ray microscopy of photovoltaic polyfluorene blends: Relating nanomorphology to device performance,” *Macromolecules*, vol. 40, pp. 3263–3270, Jan. 2007.
- [130] D. G. Stearns, “The Scattering of X-Rays from Nonideal Multilayer Structures,” *Journal of Applied Physics*, vol. 65, no. 2, pp. 491–506, 1989.
- [131] E. Helfand and Y. Tagami, “Theory of the Interface between Immiscible Polymers. II,” *Journal of Chemical Physics*, vol. 56, no. 7, pp. 3592–3601, 1972.
- [132] C. L. Donley, J. Zaumseil, J. W. Andreasen, M. M. Nielsen, H. Sirringhaus, R. H. Friend, and J.-s. Kim, “Effects of Packing Structure on the Optoelectronic and Charge Transport Properties in Poly(9,9-di-n-octylfluorene-alt-benzothiadiazole),” *Journal of American Chemistry Society*, vol. 127, no. 37, pp. 12890–12899, 2005.
- [133] T.-W. Lee, M.-G. Kim, S. Y. Kim, S. H. Park, O. Kwon, T. Noh, and T.-S. Oh, “Hole-transporting interlayers for improving the device lifetime in the polymer light-emitting diodes,” *Applied Physics Letters*, vol. 89, no. 12, p. 123505, 2006.
- [134] C. Groves, J. C. Blakesley, and N. C. Greenham, “Effect of charge trapping on geminate recombination and polymer solar cell performance,” *Nano letters*, vol. 10, pp. 1063–9, Mar. 2010.
- [135] R. G. E. Kimber, A. B. Walker, G. E. Schröder-Turk, and D. J. Cleaver, “Bicontinuous minimal surface nanostructures for polymer blend solar cells,” *Physical Chemistry Chemical Physics*, vol. 12, pp. 844–51, Jan. 2010.
- [136] R. a. Marsh, C. Groves, and N. C. Greenham, “A microscopic model for the behavior of nanostructured organic photovoltaic devices,” *Journal of Applied Physics*, vol. 101, no. 8, p. 083509, 2007.

- [137] L. Meng, Y. Shang, Q. Li, Y. Li, X. Zhan, Z. Shuai, R. G. E. Kimber, and A. B. Walker, "Dynamic Monte Carlo Simulation for Highly Efficient Polymer Blend Photovoltaics," *The Journal of Physical Chemistry B*, vol. 114, pp. 36–41, Jan. 2010.
- [138] R. A. Marcus, "Electron Transfer Reactions in Chemistry: Theory and Experiment (Nobel Lecture)," *Angewandte Chemie International Edition in English*, vol. 32, pp. 1111–1121, Aug. 1993.
- [139] J. Lukkien, J. Segers, P. Hilbers, R. Gelten, and A. Jansen, "Efficient Monte Carlo methods for the simulation of catalytic surface reactions," *Physical Review E*, vol. 58, pp. 2598–2610, Aug. 1998.
- [140] C. Groves, R. G. E. Kimber, and A. B. Walker, "Simulation of loss mechanisms in organic solar cells: A description of the mesoscopic Monte Carlo technique and an evaluation of the first reaction method.," *Journal of Chemical Physics*, vol. 133, p. 144110, Oct. 2010.
- [141] C. Deibel, T. Strobel, and V. Dyakonov, "Origin of the Efficient Polaron-Pair Dissociation in Polymer-Fullerene Blends," *Physical Review Letters*, vol. 103, pp. 1–4, July 2009.
- [142] J. Zaumseil, C. Groves, J. M. Winfield, N. C. Greenham, and H. Sirringhaus, "Electron-Hole Recombination in Uniaxially Aligned Semiconducting Polymers," *Advanced Functional Materials*, vol. 18, pp. 3630–3637, Nov. 2008.
- [143] Y.-s. Huang, S. Westenhoff, I. Avilov, P. Sreearunothai, J. M. Hodgkiss, C. Deleener, R. H. Friend, and D. Beljonne, "Electronic structures of interfacial states formed at polymeric semiconductor heterojunctions.," *Nature Materials*, vol. 7, pp. 483–489, June 2008.
- [144] S. Athanasopoulos, E. Hennebicq, D. Beljonne, and A. B. Walker, "Trap Limited Exciton Transport in Conjugated Polymers," *The Journal of Physical Chemistry C*, vol. 112, pp. 11532–11538, July 2008.
- [145] S. Westenhoff, I. A. Howard, J. M. Hodgkiss, K. R. Kirov, H. A. Bronstein, C. K. Williams, N. C. Greenham, and R. H. Friend, "Charge recombination in organic photovoltaic devices with high open-circuit voltages," *Journal of the American Chemical Society*, vol. 130, pp. 13653–13658, Oct. 2008.
- [146] J. M. Hodgkiss, A. R. Campbell, R. A. Marsh, A. Rao, S. Albert-Seifried, and R. H. Friend, "Subnanosecond geminate charge recombination in polymer-polymer photovoltaic devices," *Physical Review Letters*, vol. 104, p. 177701, Jan. 2010.
- [147] J. C. Blakesley, H. S. Clubb, and N. C. Greenham, "Temperature-dependent electron and hole transport in disordered semiconducting polymers: Analysis of energetic disorder," *Physical Review B*, vol. 81, pp. 1–9, Jan. 2010.
- [148] R. Khan, D. Poplavskyy, T. Kreouzis, and D. Bradley, "Hole mobility within arylamine-containing polyfluorene copolymers: A time-of-flight transient-photocurrent study," *Physical Review B*, vol. 75, pp. 1–14, Jan. 2007.

- [149] J. K. Grey, D. Y. Kim, C. L. Donley, W. L. Miller, J. S. Kim, C. Silva, R. H. Friend, and P. F. Barbara, "Effect of Temperature and Chain Length on the Bimodal Emission Properties of Single Polyfluorene Copolymer Molecules," *The Journal of Physical Chemistry B*, vol. 110, pp. 18898–18903, Sept. 2006.
- [150] S. R. Scully and M. D. McGehee, "Effects of optical interference and energy transfer on exciton diffusion length measurements in organic semiconductors," *Journal of Applied Physics*, vol. 100, no. 3, p. 034907, 2006.
- [151] N.-K. Persson, H. Arwin, and O. Inganäs, "Optical optimization of polyfluorene-fullerene blend photodiodes," *Journal of Applied Physics*, vol. 97, no. 3, p. 034503, 2005.
- [152] L. a. a. Pettersson, L. S. Roman, and O. Inganäs, "Modeling photocurrent action spectra of photovoltaic devices based on organic thin films," *Journal of Applied Physics*, vol. 86, no. 1, p. 487, 1999.
- [153] C. M. Ramsdale and N. C. Greenham, "The optical constants of emitter and electrode materials in polymer light-emitting diodes," *Journal of Physics D: Applied Physics*, vol. 36, pp. L29–L34, Feb. 2003.
- [154] R. I. R. Blyth, S. a. Sardar, F. P. Netzer, and M. G. Ramsey, "Influence of oxygen on band alignment at the organic/aluminum interface," *Applied Physics Letters*, vol. 77, no. 8, p. 1212, 2000.
- [155] N. Koch, a. Kahn, J. Ghijsen, J.-J. Pireaux, J. Schwartz, R. L. Johnson, and a. Elschner, "Conjugated organic molecules on metal versus polymer electrodes: Demonstration of a key energy level alignment mechanism," *Applied Physics Letters*, vol. 82, no. 1, p. 70, 2003.
- [156] P. Peumans, S. Uchida, and S. R. Forrest, "Efficient bulk heterojunction photovoltaic cells using small-molecular-weight organic thin films.," *Nature*, vol. 425, p. 158, Sept. 2003.
- [157] P. K. Watkins, A. B. Walker, and G. L. B. Verschoor, "Dynamical Monte Carlo modelling of organic solar cells: The dependence of internal quantum efficiency on morphology," *Nano Letters*, vol. 5, no. 9, pp. 1814–1818, 2005.
- [158] J. Nelson, J. J. Kwiakowski, J. Kirkpatrick, and J. M. Frost, "Modeling charge transport in organic photovoltaic materials.," *Accounts of Chemical Research*, vol. 42, pp. 1768–78, Nov. 2009.
- [159] C. V. Hoven, A. Garcia, G. C. Bazan, and T. Q. Nguyen, "Recent Applications of Conjugated Polyelectrolytes in Optoelectronic Devices," *Advanced Materials*, vol. 20, no. 20, pp. 3793–3810, 2008.
- [160] R. Steyrleuthner, S. Bange, and D. Neher, "Reliable electron-only devices and electron transport in n-type polymers," *Journal of Applied Physics*, vol. 105, no. 6, p. 064509, 2009.

- [161] A. Facchetti, "Semiconductors for organic transistors," *Materials Today*, vol. 10, no. 3, pp. 28–37, 2007.
- [162] H. Sirringhaus and M. Ando, "Materials challenges and applications of solution-processed organic field-effect transistors," *MRS Bulletin Y*, vol. 33, no. 7, pp. 676–682, 2008.
- [163] H. Sirringhaus, M. Bird, T. Richards, and N. Zhao, "Charge Transport Physics of Conjugated Polymer FieldEffect Transistors," *Advanced Materials*, vol. 22, no. 34, pp. 3893–3898, 2010.
- [164] J. Veres, S. Ogier, S. W. Leeming, D. C. Cupertino, and S. Mohialdin Khaffaf, "Low-k Insulators as the Choice of Dielectrics in Organic Field-Effect Transistors," *Advanced Functional Materials*, vol. 13, pp. 199–204, Mar. 2003.
- [165] J. Veres, S. Ogier, and G. Lloyd, "Gate Insulators in Organic Field-Effect Transistors," *Chemistry of Materials*, vol. 16, no. 23, pp. 4543–4555, 2004.
- [166] A. F. Stassen, R. W. I. de Boer, N. N. Iosad, and A. F. Morpurgo, "Influence of the gate dielectric on the mobility of rubrene single-crystal field-effect transistors," *Applied Physics Letters*, vol. 85, no. 17, p. 3899, 2004.
- [167] I. N. Hulea, S. Fratini, H. Xie, C. L. Mulder, N. N. Iossad, G. Rastelli, S. Ciuchi, and A. F. Morpurgo, "Tunable Frohlich polarons in organic single-crystal transistors," *Nature Materials*, vol. 5, pp. 982–986, Jan. 2006.
- [168] S. S. Chang, A. B. Rodríguez, A. M. Higgins, C. Liu, M. Geoghegan, H. Sirringhaus, F. Cousin, R. M. Dalgleish, and Y. Deng, "Control of roughness at interfaces and the impact on charge mobility in all-polymer field-effect transistors," *Soft Matter*, vol. 4, no. 11, p. 2220, 2008.
- [169] N. Zhao, Y.-Y. Noh, J.-F. Chang, M. Heeney, I. McCulloch, and H. Sirringhaus, "Polaron Localization at Interfaces in High-Mobility Microcrystalline Conjugated Polymers," *Advanced Materials*, vol. 21, pp. 3759–3763, Oct. 2009.
- [170] M. Caironi, M. Bird, D. Fazzi, Z. Chen, R. Di Pietro, C. Newman, A. Facchetti, and H. Sirringhaus, "Very Low Degree of Energetic Disorder as the Origin of High Mobility in an n-channel Polymer Semiconductor," *Advanced Functional Materials*, vol. 21, no. 17, pp. 3371–3381, 2011.
- [171] H. Yan, C. Wang, A. Garcia, S. Swaraj, Z. Gu, C. R. McNeill, T. Schuettfort, K. E. Sohn, E. J. Kramer, G. C. Bazan, T.-Q. Nguyen, and H. Ade, "Interfaces in organic devices studied with resonant soft x-ray reflectivity," *Journal of Applied Physics*, vol. 110, no. 10, p. 102220, 2011.
- [172] J. Li, J. Du, J. Xu, H. L. W. Chan, and F. Yan, "The influence of gate dielectrics on a high-mobility n-type conjugated polymer in organic thin-film transistors The influence of gate dielectrics on a high-mobility n-type conjugated polymer in organic thin-film transistors," *Applied Physics Letters*, vol. 100, no. 3, p. 033301, 2012.

- [173] T. Schuettfort, S. Huettner, S. Lilliu, J. E. Macdonald, L. Thomsen, and C. R. McNeill, "Surface and bulk structural characterization of a high-mobility electron-transporting polymer," *Macromolecules*, vol. 44, pp. 1530–1539, Jan. 2011.
- [174] J.-F. Chang, M. C. Gwinner, M. Caironi, T. Sakanoue, and H. Sirringhaus, "Conjugated-Polymer-Based Lateral Heterostructures Defined by High-Resolution Photolithography," *Advanced Functional Materials*, vol. 20, pp. 2825–2832, Sept. 2010.
- [175] K. Suemori, S. Uemura, M. Yoshida, S. Hoshino, N. Takada, T. Kodzasa, and T. Kamata, "Influence of fine roughness of insulator surface on threshold voltage stability of organic field-effect transistors," *Applied Physics Letters*, vol. 93, no. 3, p. 033308, 2008.
- [176] S. Dayal, N. Kopidakis, D. C. Olson, D. S. Ginley, and G. Rumbles, "Photovoltaic devices with a low band gap polymer and CdSe nanostructures exceeding 3% efficiency," *Nano Letters*, vol. 10, pp. 239–242, Jan. 2010.
- [177] C. McNeill and N. C. Greenham, "Conjugated polymer blends for optoelectronics," *Advanced Materials*, Jan. 2009.
- [178] D. E. Markov, E. Amsterdam, P. W. M. Blom, A. B. Sieval, and J. C. Hummelen, "Accurate measurement of the exciton diffusion length in a conjugated polymer using a heterostructure with a side-chain cross-linked fullerene layer.," *The Journal of Physical Chemistry A*, vol. 109, pp. 5266–74, June 2005.
- [179] X. Yang and J. Loos, "Toward high-performance polymer solar cells: The importance of morphology control," *Macromolecules*, vol. 40, pp. 1353–1362, Jan. 2007.
- [180] A. J. Moule, K. Meerholz, and A. J. Moulé, "Morphology control in solution-processed bulk-heterojunction solar cell mixtures," *Advanced Functional Materials*, vol. 19, pp. 3028–3036, Jan. 2009.
- [181] S. C. Veenstra, J. Loos, and J. M. Kroon, "Nanoscale structure of solar cells based on pure conjugated polymer blends," *Progress in Photovoltaics*, vol. 15, pp. 727–740, Jan. 2007.
- [182] Z. He, C. Zhong, X. Huang, W.-Y. Wong, H. Wu, L. Chen, S. Su, and Y. Cao, "Simultaneous enhancement of open-circuit voltage, short-circuit current density, and fill factor in polymer solar cells.," *Advanced Materials*, vol. 23, pp. 4636–4643, Oct. 2011.
- [183] M. Granstrom, K. Petritsch, A. C. Arias, A. Lux, M. R. Andersson, R. H. Friend, and M. Granström, "Laminated fabrication of polymeric photovoltaic diodes," *Nature*, vol. 395, pp. 257–260, Jan. 1998.
- [184] T. W. Holcombe, C. H. Woo, D. F. J. Kavulak, B. C. Thompson, and J. M. J. Frechet, "All-polymer photovoltaic devices of poly(3-(4-n-octyl)-phenylthiophene) from grignard metathesis (GRIM) polymerization," *Journal of the American Chemical Society*, vol. 131, p. 14160, Jan. 2009.

- [185] T. Kietzke, H. H. Horhold, D. Neher, and H. Hörhold, “Efficient polymer solar cells based on M3EH-PPV,” *Chemistry of Materials*, vol. 17, pp. 6532–6537, Jan. 2005.
- [186] M. M. Koetse, J. Sweelssen, K. T. Hoekerd, H. F. M. Schoo, S. C. Veenstra, J. M. Kroon, X. N. Yang, and J. Loos, “Efficient polymer : polymer bulk heterojunction solar cells,” *Applied Physics Letters*, vol. 88, p. 83504, Jan. 2006.
- [187] M. M. Mandoc, W. Veurman, L. J. A. Koster, B. de Boer, and P. W. M. Blom, “Origin of the reduced fill factor and photocurrent in MDMO-PPV : PCNEPV all-polymer solar cells,” *Advanced Functional Materials*, vol. 17, pp. 2167–2173, Jan. 2007.
- [188] J. R. Moore, S. Albert-Seifried, A. Rao, S. Massip, B. Watts, D. J. Morgan, R. H. Friend, C. R. McNeill, and H. Sirringhaus, “Polymer blend solar cells based on a high-mobility naphthalenediimide-based polymer acceptor: Device physics, photophysics and morphology,” *Advanced Energy Materials*, vol. 1, pp. 230–240, Jan. 2011.
- [189] C. Yin, T. Kietzke, D. Neher, H. Horhold, H. H. Horhold, and H. Hoerhold, “Photovoltaic properties and exciplex emission of polyphenylenevinylene-based blend solar cells,” *Applied Physics Letters*, vol. 90, p. 92117, Jan. 2007.
- [190] A. J. Parnell, A. J. Cadby, O. O. Mykhaylyk, A. D. F. Dunbar, P. E. Hopkinson, A. M. Donald, and R. a. L. Jones, “Nanoscale phase separation of P3HT PCBM thick films as measured by small-angle X-ray scattering,” *Macromolecules*, vol. 44, pp. 6503–6508, Aug. 2011.
- [191] N. D. Treat, M. A. Brady, G. Smith, M. F. Toney, E. J. Kramer, C. J. Hawker, and M. L. Chabinye, “Plastic solar cells: interdiffusion of PCBM and P3HT reveals miscibility in a photovoltaically active Blend,” *Advanced Energy Materials*, vol. 1, pp. 1–1, Jan. 2011.
- [192] W. Yin and M. Dadmun, “A new model for the morphology of P3HT/PCBM organic photovoltaics from small-angle neutron scattering: Rivers and streams,” *ACS Nano*, vol. 5, pp. 4756–4768, Jan. 2011.
- [193] T. Martens, J. D’Haen, T. Munters, Z. Beelen, L. Goris, J. Manca, M. D’Olieslaeger, D. Vanderzande, L. D. Schepper, R. Andriessen, and L. De Schepper, “Disclosure of the nanostructure of MDMO-PPV : PCBM bulk hetero-junction organic solar cells by a combination of SPM and TEM,” *Synthetic Metals*, vol. 138, pp. 243–247, Jan. 2003.
- [194] S. S. van Bavel, E. Sourty, G. With, J. Loos, and G. de With, “Three-dimensional anoscale organization of bulk heterojunction polymer solar cells,” *Nano Letters*, vol. 9, pp. 507–513, Jan. 2008.
- [195] X. N. Yang, J. Loos, S. C. Veenstra, W. J. H. Verhees, M. M. Wienk, J. M. Kroon, M. A. J. Michels, and R. A. J. Janssen, “Nanoscale morphology of high-performance polymer solar cells,” *Nano Letters*, vol. 5, pp. 579–583, Jan. 2005.
- [196] G. Li, V. Shrotriya, J. S. Huang, Y. Yao, T. Moriarty, K. Emery, and Y. Yang, “High-efficiency solution processable polymer photovoltaic cells by self-organization of polymer blends,” *Nature Materials*, vol. 4, pp. 864–868, Jan. 2005.

- [197] S. E. Shaheen, C. J. Brabec, N. S. Sariciftci, F. Padinger, T. Fromherz, and J. C. Hummelen, "2.5% efficient organic plastic solar cells," *Applied Physics Letters*, vol. 78, pp. 841–843, Jan. 2001.
- [198] L. F. Drummy, R. J. Davis, D. L. Moore, M. Durstock, R. A. Vaia, and J. W. P. Hsu, "Molecular-scale and nanoscale morphology of P3HT:PCBM bulk heterojunctions: energy-filtered TEM and low-dose HREM," *Chemistry of Materials*, vol. 23, pp. 907–912, Jan. 2011.
- [199] A. A. Herzing, L. J. Richter, and I. M. Anderson, "3D nanoscale characterization of thin-film organic photovoltaic device structures via spectroscopic contrast in the TEM," *The Journal of Physical Chemistry C*, vol. 114, pp. 17501–17508, Oct. 2010.
- [200] S. C. Veenstra, W. J. H. Verhees, J. M. Kroon, M. M. Koetse, J. Sweelssen, J. Bastiaansen, H. F. M. Schoo, X. Yang, A. Alexeev, J. Loos, U. S. Schubert, M. M. Wienk, and Others, "Photovoltaic properties of a conjugated polymer blend of MDMO-PPV and PCNEPV," *Advanced Materials*, vol. 15, pp. 2503–2508, Jan. 2003.
- [201] D. R. Kozub, K. Vakhshouri, L. M. Orme, C. Wang, A. Hexemer, and E. D. Gomez, "Polymer crystallization of partially miscible polythiophene/fullerene mixtures controls morphology," *Macromolecules*, vol. 44, pp. 5722–5726, July 2011.
- [202] D. Chen, F. Liu, C. Wang, A. Nakahara, and T. P. Russell, "Bulk heterojunction photovoltaic active layers via bilayer interdiffusion," *Nano Letters*, vol. 11, pp. 2071–2078, Jan. 2011.
- [203] T. Agostinelli, S. Lilliu, J. G. Labram, M. Campoy-Quiles, M. Hampton, E. Pires, J. Rawle, O. Bikondoa, D. D. C. Bradley, T. D. Anthopoulos, J. Nelson, and J. E. Macdonald, "Real-time investigation of crystallization and phase-segregation dynamics in P3HT:PCBM solar cells during thermal annealing," *Advanced Functional Materials*, vol. 21, pp. 1701–1708, Jan. 2011.
- [204] E. D. Gomez, K. P. Barteau, H. Wang, M. F. Toney, and Y.-L. Loo, "Correlating the scattered intensities of P3HT and PCBM to the current densities of polymer solar cells.," *Chemical Communications*, vol. 47, pp. 436–8, Jan. 2011.
- [205] H. Ade, X. Zhang, S. Cameron, C. COSTELLO, J. KIRZ, and S. Williams, "Chemical contrast in X-ray microscopy and spatially resolved XANES spectroscopy of organic specimens," *Science*, vol. 258, pp. 972–975, Jan. 1992.
- [206] J. Clark, C. Silva, R. H. Friend, and F. C. Spano, "Role of intermolecular coupling in the photophysics of disordered organic semiconductors: Aggregate emission in regioregular polythiophene," *Physical Review Letters*, vol. 98, p. 206406, Jan. 2007.
- [207] H. G. Flesch, R. Resel, and C. R. McNeill, "Charge transport properties and microstructure of polythiophene/polyfluorene blends," *Organic Electronics*, vol. 10, pp. 1549–1555, Jan. 2009.

- [208] C. R. McNeill, A. Abrusci, I. Hwang, M. A. Ruderer, P. Mueller-Buschbaum, N. C. Greenham, and P. Muller-Buschbaum, “Photophysics and photocurrent generation in polythiophene/polyfluorene copolymer blends,” *Advanced Functional Materials*, vol. 19, pp. 3103–3111, Jan. 2009.
- [209] E. Verploegen, R. Mondal, C. J. Bettinger, S. Sok, M. F. Toney, and Z. Bao, “Effects of thermal annealing upon the morphology of polymer-fullerene blends,” *Advanced Functional Materials*, vol. 20, pp. 3519–3529, Oct. 2010.
- [210] C. R. McNeill, J. J. M. Halls, R. Wilson, G. L. Whiting, S. Berkebile, M. G. Ramsey, R. H. Friend, and N. C. Greenham, “Efficient polythiophene/polyfluorene copolymer bulk heterojunction photovoltaic devices: device physics and annealing effects,” *Advanced Functional Materials*, vol. 18, no. 16, pp. 2309–2321, 2008.
- [211] W. Chen, T. Xu, F. He, W. Wang, C. Wang, J. Strzalka, Y. Liu, J. Wen, D. J. Miller, J. Chen, K. Hong, L. Yu, and S. B. Darling, “Hierarchical nanomorphologies promote exciton dissociation in polymer/fullerene bulk heterojunction solar cells,” *Nano Letters*, vol. 11, no. 9, pp. 3707–3713, 2011.
- [212] a. Wagenpfahl, D. Rauh, M. Binder, C. Deibel, and V. Dyakonov, “S-shaped current-voltage characteristics of organic solar devices,” *Physical Review B*, vol. 82, pp. 1–8, Sept. 2010.
- [213] A. Hexemer, W. Bras, J. Glossinger, E. Schaible, E. Gann, R. Kirian, A. MacDowell, M. Church, B. Rude, and H. Padmore, “A SAXS/WAXS/GISAXS beamline with multilayer monochromator,” *XIV International Conference on Small-Angle Scattering (SAS09)*, vol. 247, p. 12007, 2010.
- [214] a. H. Simmons, C. a. Michal, and L. W. Jelinski, “Molecular orientation and two-component nature of the crystalline fraction of spider dragline silk,” *Science*, vol. 271, pp. 84–7, Jan. 1996.
- [215] F. Vollrath and D. P. Knight, “Liquid crystalline spinning of spider silk,” *Nature*, vol. 410, pp. 541–8, Mar. 2001.
- [216] L. Schmidt-Mende, A. Fechtenkötter, K. Müllen, E. Moons, R. H. Friend, and J. D. MacKenzie, “Self-organized discotic liquid crystals for high-efficiency organic photovoltaics,” *Science*, vol. 293, no. 5532, pp. 1119–1122, 2001.
- [217] R. H. Friend, R. W. Gymer, A. B. Holmes, J. H. Burroughes, R. N. Marks, C. Taliani, D. D. C. Bradley, D. A. Dos Santos, J. L. Br—[eacute]—das, M. L—[ouml]—gdlund, and W. R. Salaneck, “Electroluminescence in conjugated polymers,” *Nature*, vol. 397, pp. 121–128, Jan. 1999.
- [218] H. Sirringhaus, T. Kawase, R. H. Friend, T. Shimoda, M. Inbasekaran, W. Wu, and E. P. Woo, “High-resolution inkjet printing of all-polymer transistor circuits,” *Science*, vol. 290, pp. 2123–6, Dec. 2000.

- [219] T. Schuettfort, B. Watts, L. Thomsen, M. Lee, H. Siringhaus, and C. R. McNeill, "Microstructure of polycrystalline PBTTT films: domain mapping and structure formation.," *ACS nano*, vol. 6, pp. 1849–64, Feb. 2012.
- [220] M. J. Lee, D. Gupta, N. Zhao, M. Heeney, L. McCulloch, and H. Siringhaus, "Anisotropy of Charge Transport in a Uniaxially Aligned and Chain-Extended, High-Mobility, Conjugated Polymer Semiconductor," *Advanced Functional Materials*, vol. 21, no. 5, pp. 932–940, 2011.
- [221] B. Collins, Z. Li, J. Tumbleston, E. Gann, C. McNeill, and H. Ade, "Absolute measurement of domain composition and nanoscale size distribution explains performance in PTB7:PC<sub>71</sub>BM solar cells," *Advanced Energy Materials*, 2012 submitted.
- [222] H. Brumberger, ed., *Modern aspects of small-angle scattering*. Dordrecht: Kluwer Academic Publishers, 1995.
- [223] G. Porod, "Die Röntgenkleinwinkelstreuung von dichtgepackten kolloiden Systemen," *Colloid and Polymer Science*, vol. 125, pp. 51–57, Jan. 1952.
- [224] J. T. Koberstein, B. Morra, and R. S. Stein, "The determination of diffuse-boundary thicknesses of polymers by small-angle X-ray scattering," *Journal of Applied Crystallography*, vol. 13, pp. 34–45, Feb. 1980.
- [225] W. Ruland, "Small-angle scattering of two-phase systems: determination and significance of systematic deviations from Porod's law," *Journal of Applied Crystallography*, vol. 4, pp. 70–73, Feb. 1971.
- [226] A. Todo, T. Hashimoto, and H. Kawai, "Small-angle X-ray scattering from block copolymers as an ideal model system for a pseudo two-phase solid texture," *Journal of Applied Crystallography*, vol. 11, pp. 558–563, Oct. 1978.
- [227] E. Gann, a. T. Young, B. a. Collins, H. Yan, J. Nasiatka, H. a. Padmore, H. Ade, a. Hexemer, and C. Wang, "Soft x-ray scattering facility at the Advanced Light Source with real-time data processing and analysis," *Review of Scientific Instruments*, vol. 83, no. 4, p. 045110, 2012.

## APPENDIX

## Appendix A

# Kramers-Kronig relations

To derive the Kramers-Kronig relations, we can start with the expression of the atomic scattering factor

$$f^0(\omega) = \sum_s \frac{g_s \omega^2}{\omega^2 - \omega_s^2 + i\gamma\omega} \quad (\text{A.1})$$

where the oscillator strength  $g_s$  in this semi-classical model sum to the total number of atomic electrons,  $Z$ , and where for small  $\gamma$  the poles lie in the lower half plane (LHP) at  $\omega = \pm\omega_s - i\gamma/2$  (As shown in Figure A.1). Multiplying the numerator and denominator of  $f^0(\omega)$  by the complex conjugate of the scattering factor, we obtain the real and imaginary parts

$$f_1^0(\omega) = \sum_s \frac{g_s \omega^2 (\omega^2 - \omega_s^2)}{(\omega^2 - \omega_s^2)^2 + \gamma^2 \omega^2} \quad (\text{A.2})$$

and

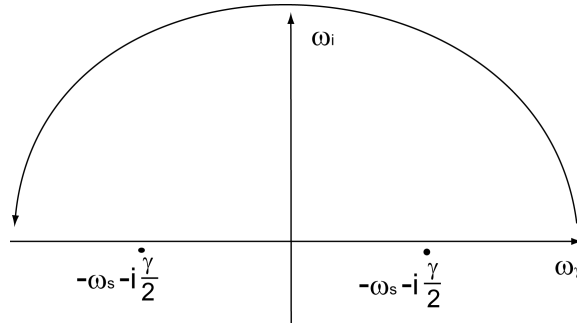


Figure A.1:  $f^0$  represented in the complex  $\omega$ -plane. for  $\gamma \ll \omega_s$ , the function  $f^0(\omega)$  has poles at  $\pm\omega_s - i(\gamma/2)$  in the lower half plane and is analytic in the upper half plane.

$$f_2^0(\omega) = \sum_s \frac{g_s \gamma \omega^3}{(\omega^2 - \omega_s^2)^2 + \gamma^2 \omega^2}, \quad (\text{A.3})$$

where

$$f^0 = f_1^0(\omega) - i f_2^0(\omega). \quad (\text{A.4})$$

Using the Cauchy residue theorem, we can represent the complex function  $f^0(\omega)$ , which has poles only in the lower half plane, in terms of a function  $f(u)$  which is analytic in the upper half plane (UHP),

$$f^0(\omega) = \frac{1}{2\pi i} \oint \frac{f^0(u)}{u - \omega} du. \quad (\text{A.5})$$

For a function that has a limiting value  $Z$  as  $\omega$  approaches infinity, this can be written as

$$f^0(\omega) - Z = \frac{1}{2\pi i} \oint \frac{f^0(u) - Z}{u - \omega} du. \quad (\text{A.6})$$

Knowing the normalization condition for  $g_s$

$$\sum_s g_s = Z \quad (\text{A.7})$$

Equation A.6 can be written as

$$f^0(\omega) - Z = \sum_s \frac{g_s (\omega_s^2 - i\gamma\omega)}{\omega^2 - \omega_s^2 + i\gamma\omega}. \quad (\text{A.8})$$

This sum goes to zero as  $\omega$  approaches infinity, and thus does not contribute to the integral in Equation A.6 along the semicircle of infinite radius in the UHP. Thus only the integral along the real axis remains, which can be written as

$$f^0(\omega) - Z = \frac{1}{2\pi i} \int_{-\infty}^{+\infty} \frac{f^0(u) - Z}{u - \omega} du. \quad (\text{A.9})$$

Using the principal value theorem

$$\lim_{\epsilon \rightarrow 0} \frac{1}{x \mp i\epsilon} = \mathcal{P}_c(1/x) \pm i\pi\delta(x), \quad (\text{A.10})$$

where the principal value  $\mathcal{P}_c(1/x)$  refers to a function that behaves like  $1/x$  everywhere except at  $x = 0$ , with the discontinuous behavior separated out and described by the Dirac delta function,  $\delta(x)$ . We can then write

$$f^0(\omega) - Z = \frac{1}{2\pi i} \int_{-\infty}^{+\infty} [\mathcal{P}_c(\frac{1}{u-\omega}) + \pi i \delta(u-\omega)] [f^0(u) - Z] du \quad (\text{A.11})$$

or

$$f^0(\omega) - Z = \frac{1}{2\pi i} \int_{-\infty}^{+\infty} \frac{f^0(u) - Z}{u-\omega} du + 12[f^0(\omega) - Z]. \quad (\text{A.12})$$

Combining like terms,

$$f^0(\omega) - Z = \frac{1}{\pi i} \mathcal{P}_c \int_{-\infty}^{+\infty} \frac{f^0(u) - Z}{u-\omega} du. \quad (\text{A.13})$$

Recalling that  $f^0(\omega) = f_1^0(\omega) - i f_2^0(\omega)$ , we can equate real and imaginary components to obtain

$$f_1^0(\omega) - Z = -\frac{1}{\pi} \mathcal{P}_c \int_{-\infty}^{+\infty} \frac{f_2^0(u)}{u-\omega} du \quad (\text{A.14})$$

and

$$f_2^0(\omega) - Z = \frac{1}{\pi} \mathcal{P}_c \int_{-\infty}^{+\infty} \frac{f_1^0(u) - Z}{u-\omega} du \quad (\text{A.15})$$

where the integration is along the real axis, from minus infinity to plus infinity. To rewrite these equations in terms of only positive frequencies, we divide Equation A.14 into two parts as follows:

$$f_1^0(\omega) - Z = -\frac{1}{\pi} [\mathcal{P}_c \int_{-\infty}^0 \frac{f_2^0(u)}{u-\omega} du + \mathcal{P}_c \int_0^{+\infty} \frac{f_2^0(u)}{u-\omega} du].$$

Replacing  $u$  by  $-u$  in the first integral, and noting from Equation A.3 that  $f_2^0(-u) = -f_2^0(u)$  and that in general reversing the limits of integration causes a sign change, the integration can be rewritten in terms of positive frequencies only as

$$f_1^0(\omega) - Z = -\frac{1}{\pi} \mathcal{P}_c \int_0^{+\infty} [\frac{1}{u+\omega} + \frac{1}{u-\omega}] f_2^0(u) du$$

or more concisely

$$f_2^0(\omega) - Z = -\frac{2}{\pi} \mathcal{P}_c \int_0^{+\infty} \frac{u f_2^0(u)}{u^2 - \omega^2} du, \quad (\text{A.16})$$

which gives a solution for  $f_1^0(\omega)$ , and thus  $\delta$ , at some specific frequency  $\omega$  in terms of an integral of  $f_2^0(\omega)$ , or equivalently  $\beta$ , over all real positive frequencies. In similar fashion we can separate Equation A.15 into integrals from minus infinity to zero and from zero to infinity, make the substitution  $-u$  for  $u$  in the first integral, and observe that in this case according to Equation A.2 we have  $f_1^0(-u) = f_1^0(u)$ , and that

$$\frac{1}{u-\omega} - \frac{1}{u+\omega} = \frac{u+\omega}{u^2-\omega^2} - \frac{u-\omega}{u^2-\omega^2} = \frac{2\omega}{u^2-\omega^2}.$$

With these substitutions Equation A.15 becomes

$$f_2^0(\omega) = \frac{2\omega}{\pi} \mathcal{P}_c \int_0^\infty \frac{f_1^0(u) - Z}{u^2 - \omega^2} du. \quad (\text{A.17})$$

Showing that  $f_2^0$ , and  $\beta$ , could in complementary fashion be obtained by an integration of  $f_1^0(u)$ , if  $f_1^0(u)$ ,  $\delta$  that can be more easily measured.

The Kramers-Kronig relations provide the desired integral relationship between the real and imaginary parts of the atomic scattering factor,  $f_1^0$  and  $f_2^0$ , or equivalently between  $\delta$  and  $\beta$ . Since it is easier to determine  $\beta$  for a wide range of photon energies (frequencies) through absorption measurements, this provides a technique for numerically determining values of  $\delta(\omega)$ .